

A STUDY OF TWO-DIMENSIONAL UNSTEADY BREAKING WAVES IN FINITE-DEPTH WATER

by

Zhigang Tian

A dissertation submitted in partial fulfillment
of the requirements for the degree of
Doctor of Philosophy
(Naval Architecture and Marine Engineering)
in The University of Michigan
2010

Doctoral Committee:

Professor Marc Perlin, Co-Chair
Professor Wooyoung Choi, Co-Chair, New Jersey Institute of Technology
Professor Steven L. Ceccio
Professor William W. Schultz

Report Documentation Page			Form Approved OMB No. 0704-0188		
Public reporting burden for the collection of information is estimated to average 1 hour per response, including the time for reviewing instructions, searching existing data sources, gathering and maintaining the data needed, and completing and reviewing the collection of information. Send comments regarding this burden estimate or any other aspect of this collection of information, including suggestions for reducing this burden, to Washington Headquarters Services, Directorate for Information Operations and Reports, 1215 Jefferson Davis Highway, Suite 1204, Arlington VA 22202-4302. Respondents should be aware that notwithstanding any other provision of law, no person shall be subject to a penalty for failing to comply with a collection of information if it does not display a currently valid OMB control number.					
1. REPORT DATE 2010		2. REPORT TYPE		3. DATES COVERED 00-00-2010 to 00-00-2010	
4. TITLE AND SUBTITLE A Study of Two-Dimensional Unsteady Breaking Waves in Finite-Depth Water				5a. CONTRACT NUMBER	
				5b. GRANT NUMBER	
				5c. PROGRAM ELEMENT NUMBER	
6. AUTHOR(S)				5d. PROJECT NUMBER	
				5e. TASK NUMBER	
				5f. WORK UNIT NUMBER	
7. PERFORMING ORGANIZATION NAME(S) AND ADDRESS(ES) University of Michigan, Ann Arbor, MI, 48109				8. PERFORMING ORGANIZATION REPORT NUMBER	
9. SPONSORING/MONITORING AGENCY NAME(S) AND ADDRESS(ES)				10. SPONSOR/MONITOR'S ACRONYM(S)	
				11. SPONSOR/MONITOR'S REPORT NUMBER(S)	
12. DISTRIBUTION/AVAILABILITY STATEMENT Approved for public release; distribution unlimited					
13. SUPPLEMENTARY NOTES					
14. ABSTRACT					
15. SUBJECT TERMS					
16. SECURITY CLASSIFICATION OF:			17. LIMITATION OF ABSTRACT Same as Report (SAR)	18. NUMBER OF PAGES 4	19a. NAME OF RESPONSIBLE PERSON
a. REPORT unclassified	b. ABSTRACT unclassified	c. THIS PAGE unclassified			

© Zhigang Tian

2010

To my family

Acknowledgements

I would like to express my sincere gratitude to my advisor Professor Marc Perlin for his guidance and support throughout my stay at the University of Michigan. His patience and trust in my capabilities has allowed me to grow and accomplish more than what I expected. His scope of knowledge keeps amazing and guiding me during my study. His keenness on research has impressed me deeply and I hope to apply the same attitude to my study in future.

Sincere gratitude is also given to Professor Wooyoung Choi for being my advisor and co-chair in the committee. Discussions and meetings with him have always been precious opportunities to advance my knowledge. His guidance on the numerical part of this study and effort on helping me to continue my study after graduation is highly appreciated.

Thanks are extended to my committee members Professor Ceccio and Professor Schultz. I am very grateful to their effort on monitoring my work. Their valuable suggestions are essential to the completion of this dissertation.

During my Ph.D. study, Department of Naval Architecture and Marine Engineering has given me tremendous support, both academically and financially. Without the support, I could not have completed my degree. I would like to thank all faculty and staff members at the department. Specially, many tanks are due to Professor Beck, Professor Karr, Professor Meadows, Professor Nwogu, Professor Sun, Professor Troesch, Professor

Vlahopoulos and Professor Young for their care and advice to my study and research. I would like to thank Betty Bonde, Kathy Brochner, Kay Drake, Nathalie Fiveland, Shanna Jessee, Warren Noone, Kristina Owens, Timothy Peters, Suzanne Taylor and Kathy Stolaruk for helping my academic life in the department. Thanks are extended to Ed Celkis, David Parsons, Joe Wild and Nick Wild at the Marine Hydrodynamics lab for their help on my experiments.

I would like to acknowledge all my friends and colleagues that I met at the University of Michigan; my experience as a Ph.D. student would be incomplete without them. An incomplete list includes (roughly in alphabetical order by last name) Sina Aragh, Pitor Bandyk, James Bretl, Che-Chun Chang, Weiwei Yu, Jian Chen, Nabaanita Datta, Jinting Guo, Elisha Garcia, Christopher Hart, Zheyu Hong, Daehyun Kim, Keary Lay, Jonghun Lee, Sheng Li, Yaning Li, Zhen Li, Yang Lin, Yi Liao, Zhao Lu, Kevin Marki, Steven Zalek, Javid Moraveji, Ellie Nick, Kamaldev Raghavan, Xiaoyan Yan, Oscar Tascon, Hui Tang, Aimin Wang, Rong Wu, Ying Jin, Wei Wu, Handa Xi, Yanhui Xie, Yunyun Ni, Ryo Yakushiji, Binbin Yu, Xiaotong Zhang, Xinshu Zhang and Yan Zhou.

This research was partially funded by the Office of Naval Research under ONR Contract Number N00014-05-1-0537, an MURI contract awarded to the University of Michigan. The content of this document does not necessarily reflect the position or the policy of the United States Government, and no official endorsement should be inferred.

My family has been a tremendous source of support over the years. My parents, Wenzhong Tian and Sulan Wang, have done some much for me and their support is so generous. I want to thank them for everything they gave to me. My wife, Ying Wang,

sacrificed the most for me and the family. She gave up her own career to keep me company throughout my Ph.D. study. Her love and support have always been the source of strength in difficult times. I highly appreciate what she has done for the family and I love her, forever. The arrival of my son and daughter, Rubin and Luna, made so lovely a family and they have brought so much fun to the family. The time we stay and play together has always been the most pleasant moments to me. I would also like to thank my mother-in-law, Liye Wang, who has taken me in as her own child and has put tremendous time and effort on helping raise Rubin and Luna.

The material presented in Chapter II has been published in the *Physics of Fluids* as “Evaluation of a deep-water wave breaking criterion” with co-authors Marc Perlin and Wooyoung Choi in 2008. Chapter III in full is the manuscript that has been accepted to the *Journal of Fluid Mechanics* for publication (pending minor revisions) with co-authors Marc Perlin and Wooyoung Choi.

Table of Contents

Dedication.....	ii
Acknowledgements.....	iii
List of Figures.....	ix
List of Tables	xv
List of Appendices	xvi
Abstract.....	xvii
Chapter I Introduction	1
1 Background.....	1
2 Objectives	2
3 Summary of the current study.....	4
References.....	10
Chapter II Evaluation of a Deep-Water Wave Breaking Criterion	12
Abstract.....	12
1 Introduction.....	13
2 Experiments	17
2.1 Temporal surface elevation measurements	20
2.2 Spatial surface profile measurements	25
3 Numerical simulations	29
4 Computation of associated breaking parameters	35
4.1 Song and Banner’s criterion revisited	35
4.2 Surface elevation profiles	37
4.3 Local wave number computation	38

4.4 Local energy	42
5 Experimental evaluation of the breaking criterion	45
5.1 Examination of the wave steepness as a breaking criterion	45
5.2 Examination of Song and Banner's wave breaking criterion	47
5.3 Energy dissipation due to wave breaking	51
6 Conclusions.....	55
Appendix.....	57
References.....	60
Chapter III Energy Dissipation in Two-Dimensional Unsteady Plunging Breakers and an Eddy Viscosity Model	62
Abstract.....	62
1 Introduction.....	64
2 Experiments	71
2.1 Facilities	71
2.2 Breaking wave generation	72
2.3 Temporal surface elevation measurements	75
2.4 High-speed imager measurements.....	76
3 Experimental results	80
3.1 Characteristic wave parameters	80
3.2 Energy loss	91
3.3 Energy dissipation rate due to wave breaking.....	99
3.4 Eddy viscosity	106
4 Eddy viscosity parameterization and numerical simulations.....	110
4.1 Eddy viscosity parameterization.....	110
4.2 Comparison of numerical solutions with laboratory measurements	113
5 Conclusions.....	126
Appendix A Nonlinear group velocity	129

Appendix B Derivation of (4.5).....	131
Appendix C Integral velocity estimation based on the turbulent energy dissipation analysis by Melville (1994)	133
References.....	135
Chapter IV Wave Spectra Evolution of Two-Dimensional Unsteady Breaking Waves.....	139
Abstract.....	139
1 Introduction.....	141
2 Experiments	144
3 Experimental results	150
3.1 Spatial evolution of wave frequency spectra.....	150
3.2 Temporal evolution of wavenumber spectra	165
4 Numerical Simulations	172
4.1 The eddy viscosity model for breaking waves	172
4.2 Evolution of the wave spectra	174
5 Conclusions.....	183
References.....	185
Chapter V Conclusions.....	187
Appendices	195

List of Figures

Figure II-1 Typical command signal sent to the wavemaker.....	19
Figure II-2 Sketch of the experimental setup for the temporal (a) and spatial imaging (b) of the sea-surface elevation. FOV indicates the field of view.	21
Figure II-3 Measured surface elevations at the first wave probe located at $x_l = 6.88\text{m}$..	23
Figure II-4 Measured surface elevations (solid line) compared with the predictions (dashed line) based on linear wave theory at the second wave probe.	24
Figure II-5 Illustration of the spatial surface-elevation-measurement error due to a time alignment inaccuracy for a sine wave. $\Delta t = 1/60$ s. Note that the differences of the elevation around the maxima are small.	27
Figure II-6 Measured surface elevations (Gain: 2020) as a function of space and time. The asterisk on the uppermost profile shows where incipient breaking occurs. For clarity the surface profiles are offset 2.5cm for each successive measurement. The time delay between profiles is 1/30 sec.	28
Figure II-7 A comparison of the linear predictions, the numerical solutions, and the measured surface profiles for the four wave groups. For clarity, one of every six experimental data points is plotted. (a) Gain 900 results for every $0.5T$ between $70T$ and $77T$ are shown (T is the period of the carrier wave); (b) Gain 1265 results for every $0.5T$ between $65.8T$ and $72.8T$ are shown; (c) Gain 1690 results for every $0.5T$ between $61T$ and $68T$ are shown; (d) Gain 2020, and results for every $0.5T$ between $58.7T$ and $65.7T$ are shown. Each profile is offset 15cm for clarity.	34
Figure II-8 Local wave number, k_h , versus dimensionless time. k_h is computed from the numerical solution for Gain 900 using the Hilbert transform at the maximum surface displacement at each time step.....	39
Figure II-9 Definitions of local wave number, k_g , at the wave crest. The numerical subscripts on k_g represent the number of lengths used in their determination.....	40
Figure II-10 Local wave number, k_{gl} , as a function of dimensionless time. k_{gl} is computed from the numerical solution for Gain 900 based on local wave geometry at the maximum surface displacement. Number of points used for the simulation is 2^{11} . k_g obtained from the simulation results with 2^{10} points is virtually the same.	41
Figure II-11 Ratio of local potential energy to local total energy at maximum surface elevations. The abscissa represents the normalized time to wave breaking (or to the focus	

point if not breaking); the ordinate is the energy ratio. ‘o’ symbols represent the maximum surface elevations at crests; ‘+’ symbols represent the maximum surface elevations at troughs. 43

Figure II-12 Ratio of local potential energy (LPE) to local total energy (LTE) at crests and troughs for steady 3rd order Stokes waves. At very small wave steepness ($ka=0.00628$), the ratios are approximately equal to 0.667, the same result as given by linear theory. 44

Figure II-13 The growth rate of the breaking parameter, $\delta(t)$, for the wave group with Gain 900. Graphs (a) and (b) are the linear results while (c) and (d) are the numerical ones. In addition, the breaking parameters determined from direct measurements are presented in (c) and (d). Also shown as a function of dimensionless time are the relevant variables used to determine δ . The horizontal region in the figures (b) and (d) denotes the threshold range of $\delta(t)$ 49

Figure II-14 Evolution of breaking parameters for the breaking wave groups with Gains 1265, 1690, and 2020. The horizontal region in the lower figure denotes the threshold range of $\delta(t)$ 50

Figure II-15 Estimation of the energy loss due to wave breaking. Wave train measurements with Gain 900, ‘x’; Gain 1265, ‘Δ’; Gain 1690, ‘□’ ; Gain 2020, ‘o’, are shown. Dashed lines represent the linear least-square fits. $\langle \eta^2 \rangle$ is the integration of η^2 with respect to time. E_0 is the integrated energy flux just prior to wave breaking based on the linear least-square fit, and ΔE is the estimated energy loss due to wave breaking, shown only for the Gain 2020 experiment. 53

Figure II-16 Non-dimensionalized total energy loss versus breaking parameter, $\delta(t)_{max}$ (determined from experimental measurements), for the three breaking cases. The horizontal region in the figure denotes the threshold range of $\delta(t)$ 54

Figure II-17 Same as Figure II-10 but for k_{g3} and k_{g6} . See Figure II-9 for definitions of k_{g3} and k_{g6} 59

Figure III-1 Sketch of the experimental setup for the surface elevation measurements. FOV indicates field of view. (Not to scale.) 71

Figure III-2 Shown are the different wave trains of the various groups. In the figure the non-breaking wave groups measured at the first wave station are presented. In (a), for clarity, an increment of 10 cm is applied to separate the measurements vertically. The wave trains have been time shifted so that they can be shown in the same graph. Shown in (b) are the amplitude spectra of the wave groups (computed with a 40.95 s measurement, corresponding to 4096 data points). Four wave trains with varying components are implemented. In addition, measurements of the experiments conducted in Tian et al. (2008) are included. 73

Figure III-3 Recorded surface profiles during active wave breaking for W4G3. The time sequence is referenced to the first image in the top left photograph. The vertical black

bars on the images represent the horizontal location of the surface disturbance front, which is used to define the active breaking time and length scales (see section 3.3.1).... 79

Figure III-4 Measured time series of surface elevation (W3G3, see Table III-1 for designations) at various spatial locations. This graph demonstrates that the wave group propagates closer to the spectral weighted group velocity, C_{gs} (solid line); the group velocity associated with the center wave frequency, C_{gc} (dash line), significantly underestimates wave group travel speed. f_s and k_s are the characteristic wave frequency and wave number, respectively, as shown in table 1. For clarity the surface elevation is exaggerated by a factor of three (i.e. $3*\eta(t)$ is shown. The spatial locations, $k_s x$, remain its original scale on the vertical axis) as shown in Table III-1. For clarity the surface elevation is exaggerated by a factor of three (i.e. $3* \eta(t)$ is shown. The spatial locations, $k_s x$, remain its original scale on the vertical axis). 84

Figure III-5 Global wave steepness, S , versus local wave steepness, S_b . The solid line represents a linear least-squares fit: $S_b = 1.237S$ 88

Figure III-6 Correlation between S_b and δ_{br} . The solid line represents a linear least-squares fit and the slope is 8.77×10^{-3} 90

Figure III-7 Estimation of energy loss due to friction, contact-line damping, and wave breaking, shown only for Wave 3. The thick dash lines are the exponential best fits; the vertical dash dot lines denote the active breaking length scale. Non-breaking losses are estimated from the exponential fit of the non-breaking wave measurements (lowest, W3G1). E_0 is the estimated total energy just prior to wave breaking based on the exponential fit; ΔE is the estimated energy loss due to wave breaking, both shown only for W3G4. 93

Figure III-8 Normalized energy loss versus S and δ_{br} . Banner and Peirson (2007) data (open symbols in the figure) are reproduced for comparison. The solid lines in (a) and (b) represent linear least-squares fits. The thick vertical line in (c) illustrates the threshold, $\delta_c = (1.4 \pm 0.1) \times 10^{-3}$, for wave breaking onset, as discussed in Song and Banner (2002) and Tian et al. (2008). 96

Figure III-9 Time scale t_{br} and length scale l_{br} associated with active wave breaking. ω_b and k_b are the wave frequency and the wave number associated with the breaking wave (see section 3.1.4 for details). ω_s and k_s are the spectrally-weighted wave frequency and wave number. Solid lines represent linear least-squares fits. In (c), the dash line illustrates the characteristic wave speed, c_b , based on local wave number, k_b , measurement; the solid line represents the estimated horizontal breaking crest speed as $u_{br} = 0.836c_b$. And in (d), the dash line represents the characteristic wave speed, c_s , based on the spectrally-weighted wave frequency ω_s ; the solid line represents the estimated horizontal breaking crest speed as $u_{br} = 0.750c_s$ 101

Figure III-10 Normalized energy dissipation rate versus S_b and δ_{br} . Solid lines represent linear least-squares fits. 105

Figure III-11 Eddy viscosity as a function of the wave breaking strength is presented. Solid symbols denote estimations using (3.6) and open symbols using (3.7). The two

equations provide estimations close to each other. In this study, estimations with (3.6) are used in the numerical simulations. Solid lines represent linear least-square fits (only estimations with (3.6) are included in the best fits. 109

Figure III-12 In graphs (a - e), comparisons of the total energy as a function of space are presented. Symbols represent experimental measurements and solid lines represent numerical results. The vertical dash lines indicate the wave breaking region..... 120

Figure III-13 (a - e) show the comparison of surface elevations measured from three wave stations. Solid line: experimental measurements; dash line: numerical results. In each of the five sets of graphs, figures in the left column are from the nonbreaking wave groups; figures of the most violent breaking wave groups are in the right column. Breaking regions are: [11.28 m, 12.57m] for W1G3 in (a), [12.53m, 13.71m] for W2G4 in (b), [13.09m, 14.24m] for W3G4 in (c), [14.11m, 15.54m] for W4G4 in (d), and [11.72m, 12.59m] for W5G2 in (e). 125

Figure III-14 Normalized integral speed ($\chi = u/c_b$) as a function of wave breaking strength, b_b . As expected, the integral speed increases as wave breaking intensifies..... 134

Figure IV-1 Sketch of the experimental setup (not to scale). 144

Figure IV-2 Typical surface elevations measured with wave probes along the tank (W1G3). The horizontal axis is normalized time, $f_s t$. Locations of measurements, $k_s x$, are shown on the figure. Here, f_s is the characteristic wave frequency; k_s is the characteristic wavenumber; x is the horizontal distance to the wavemaker's front face intersection with calm water. For clarity, an increment of 12.5 cm is applied to the ordinate to separate different measurements. 148

Figure IV-3 Examples of recorded image for surface profile measurement (W4G3). The time stamps referenced to the top image. For images without breaking crests, the water-air interface is well defined and can be easily tracked with a simple MATLAB program (after some brightness and contrast ratio adjustments). When active breaking crests are present, a 'mean' water-air interface is also obvious. However, the entrained bubbles/air clouds have to be manually removed to use the MATLAB program to detect the surface profile. 149

Figure IV-4 Wave frequency spectra of typical non-breaking (first column) and breaking wave groups. Locations of measurements, $k_s x$, are shown in the first column of the figure. The dash lines indicate the reference spectrum measured at the first wave station ($k_s x = 28.7$ for this case). For clarity, an increment of three is applied along the ordinate to separate the wave spectra at different locations. 151

Figure IV-5 Energy dissipation as a function of space for non-breaking wave groups. Solid symbols: $\Delta E_0(x)/E_0(x_1)$; open symbols: $\Delta E_1(x)/E_0(x_1)$. Here, $\Delta E_i(x) = E_i(x) - E_i(x_1)$ with $i = 0$ and 1 . $E_0(x)$ and $E_1(x)$ are the total energy and the energy near the spectral peak ($f/f_p = 0.95 \sim 1.1$), respectively. x_1 indicates the location of the first measurement station. For clarity, an increment of 0.2 is applied to separate different wave groups along the ordinate. 154

Figure IV-6 Frequency bandwidth effect on spectral peak dissipation. ΔE_I and ΔE_0 are the total spectral peak dissipation and the total non-breaking dissipation, respectively, both averaged over the last four measurements for each non-breaking wave group in Figure IV-8. 155

Figure IV-7 In the right column of the figure, energy dissipation as a function of space for breaking wave groups (only five most violent breaking wave groups) are shown. For comparison, results of the non-breaking wave groups are also provided (left column). Open circles: $\Delta E_0(x)/E_0(x_1)$; triangles: $\Delta E_2(x)/E_0(x_1)$; plusses: $\Delta E_3(x)/E_0(x_1)$. Here, $\Delta E_i(x) = E_i(x) - E_i(x_1)$ with $i = 0, 2$ and 3 . $E_0(x)$: the total energy; $E_2(x)$: energy in frequency range $f/f_p = 0.65 \sim 0.95$; $E_3(x)$: energy in frequency range $f/f_p = 1.1 \sim 2.0$. x_1 indicates the location of the first measurement station. 158

Figure IV-8 Spectral distribution of the non-breaking dissipation. $S_I(f)_{max}$ indicates the spectral peak of the reference wave spectrum measured at the first wave station. For clarity, an increment of 0.2 is applied to separate different wave groups. 161

Figure IV-9 Spectral distribution of energy dissipation due to wave breaking. $S_I(f)_{max}$ indicates the spectral peak of the reference wave spectrum measured at the first station. For clarity, an increment of 0.5 is applied to separate the five wave packets. Results of wave groups in each wave packet are plotted together and distinguished by the gain value, i.e. G2, G3 and G4. 163

Figure IV-10 Temporal evolution of the measured wavenumber spectra. Nondimensional time relative to wave breaking/focusing, i.e. $f_s(t-t_b)$, is provided and shown in the results of W4G1. Here, t_b represents wave breaking/focusing time. Dash lines represent the reference wavenumber spectra measured at $f_s(t-t_b) = -3.6$. For clarity, an increment of 2.5 is applied to the ordinate values to separate the measured spectra. 166

Figure IV-11 Mean wavenumber spectral differences before and after wave breaking/focusing. $S(k)_p$ represents the mean of the wavenumber spectral peak before wave breaking. 168

Figure IV-12 Comparison of the measured and the linear-wave-theory-predicted surface profiles before and after wave breaking for W4G4. Nondimensional time relative to wave breaking/focusing is provided on each figure. Solid lines are the measured profile at these nondimensional times and dash lines are the predicted profile at corresponding spatial locations. The profiles are used as input to the Fourier analysis, which give the wave number spectra shown later. The peaks in the linear-wave-theory predictions have been aligned to the measurements for these figures; however this does not affect the wavenumber spectra based on linear-wave-theory predictions. 170

Figure IV-13 Comparison of the measured (solid lines) and the transformed (dash lines) wavenumber spectra before and after wave breaking/focusing. Nondimensional time is shown on the graphs. For clarity, an increment of 3 is applied to the ordinates in each of the four graphs. 171

Figure IV-14 (a) through (e) provide a comparison of all the wave frequency spectra. Solid lines are based on probe measurements and dash lines are the numerical results.

Nondimensional locations of the probes are provided and shown in the first column of the figures. For clarity, an increment of three is applied to the ordinates to separate the frequency spectra.	180
Figure IV-15 Comparison of the wavenumber spectra evolution. Solid lines are the experimental measurements and dash lines are the numerical results. Nondimensional time relative to wave breaking/focusing are provided and shown in W4G1. For clarity, an increment of three is applied to the ordinates to separate the wavenumber spectra.	181
Figure IV-16 Same as Figure IV-9 but based on numerical simulations.....	182
Figure A1-1 Observed global wave steepness of two-dimensional incipient wave breaking, S_0 . Open symbols indicate wave breaking is produced by focusing wave groups with constant amplitude wave spectra; solid symbols are used for constant steepness wave spectra. S_0 from Drazen et al. (2008) are based on our observations of their figure 8.	198
Figure A1-2 Illustration of the determination of α for W1G1. The area under the thick solid line represents E_p and the area within the box defined by the dash lines represents E_{ref} . f_1 and f_2 are the one-half maximum energy associated frequencies.	200
Figure A1-3 Energy loss due to wave breaking as a function of S_{eqv} . Results from Rapp and Melville (1990) are reproduced with data from their Figure 15; only measurements for wave groups with center frequency 1.08 Hz and 1.28 Hz are shown, as both center frequencies are comparable to ours; non-breaking energy loss is deducted from their measured total energy loss to obtain energy loss due to wave breaking. Results from Lamarre (1993) are based on their Figure C.3 and their wave spectrum in Figure 3.2, which gives $\alpha \approx 0.77$. Results from Wu and Nepf (2002) are obtained from their Tables 2 and 3 and their wave spectrum in Figure 3(b), which produces $\alpha \approx 0.73$	201
Figure A2-1 Sketch of the wind wave tunnel (not to scale).	208
Figure A2-2 Experimental set-up for flow visualization (not to scale).	209
Figure A2-3 (a) through (d) are four typical images recorded during the experiments. The air flow direction and wind speed are shown on the images. These waves are generated by driving the wavemaker with a sinusoidal electric signal of frequency 1.8 Hz with different strokes. Waves are traveling in the same direction as the wind. The two vertical black strips on the left side of each image are due to a malfunction of the CCD in the imager.	211

List of Tables

Table II-1 Local wave steepness immediately before the onset of wave breaking.	46
Table II-2 Comparison of the breaking parameters.	48
Table II-3 δ_{max} determined with k_h and the numerical results.	58
Table III-1 Summary of the primary wave parameters. f_p : peak wave frequency; Δf : frequency bandwidth based on one-half the maximum energy associated frequencies; S : global wave steepness; C_{gs} : spectrally-weighted group velocity; f_s : spectrally-weighted wave frequency; k_s : spectrally-weighted wave number; E_0 : total energy just prior to wave breaking; ΔE : energy loss due to wave breaking; δ_{max} : maximum wave breaking criterion parameter, $\delta(t)$, for non-breaking wave groups; δ_{br} : $\delta(t)$ immediately prior to breaking for breaking wave groups; k_b : local wave number just prior to wave breaking; c_b : breaking wave phase speed; t_{br} : breaking time scale; l_{br} : breaking horizontal length scale; h : falling wave crest/jet height (breaking vertical length scale); b_b : breaking strength parameter; ν_{eddy} : estimated eddy viscosity with (3.6).	81
Table IV-1 Summary of primary wave parameters. f_c : center wave frequency specified in the input signal to the wavemaker; f_p : peak wave frequency; Δf : frequency bandwidth based on one-half the maximum energy associated frequencies; f_s : spectrally-weighted wave frequency (for definition see Chapter III, equation (3.2) on page 85) ; k_s : spectrally-weighted wave number; $S = k_s(\sum a_n)$: global wave steepness; $k_s x_b$: wave group focusing/breaking point relative to the mean position of the wavemaker; $f_s t_b$: wave group focusing/breaking time relative to the initial motion of the wavemaker; ν_{eddy} : estimated eddy viscosity used in the numerical simulations.	147
Table IV-2 Normalized energy loss and gain due to wave breaking. ΔE_{pos} represents integration of the positive portion of the spectral distribution of energy dissipated due to wave breaking (essentially all energy gain in low frequency band) and ΔE_{neg} for negative portion (essentially all energy loss in high frequency band). ΔE_{tot} represents the overall energy loss due to wave breaking. ΔE_{pos} , ΔE_{neg} and ΔE_{tot} are all normalized by the total energy at the reference wave station, $E_0(x_1)$	164

List of Appendices

Appendix 1 Wave Breaking Onset Prediction Using a Modified Global Wave Steepness	195
Appendix 2 Observation of Air Flow Separation over Steep Wave Crests	204

Abstract

Laboratory experiments are conducted to study two-dimensional unsteady breaking waves in finite-depth water. An eddy viscosity model to simulate energy dissipation in breaking waves is proposed. Numerical simulations are performed to compare to the experimental results and good agreement is found.

An energy-convergence rate based wave breaking criterion is evaluated. Our study revealed that the breaking criterion is sensitive to the choice of local wavenumber, but a particular local wavenumber based on local wave geometry distinguishes breaking waves groups from non-breaking ones. This study is published in *Physics of Fluids* (Tian Z., Perlin, M. & Choi, W. 2008, **20**, 066604).

Kinematics and dynamics of breaking wave groups are studied. Characteristic time and length scales associated with the wave groups and the breaking waves are defined and determined. Correlations among the characteristic scales are demonstrated. Energy dissipation in breaking waves is quantified and is shown to scale accurately with the characteristic scales. Time and length scales of the breaking crests are used to determine and parameterize the energy dissipation rate. The resulting normalized dissipation rate is on the order of 10^{-3} . This study has been accepted to the *Journal of Fluid Mechanics* for publication.

In experimental studies, spatial evolution of wave frequency spectra is observed, as is temporal evolution of wavenumber spectra. For non-breaking wave groups, energy loss near the spectral peak appears to depend on frequency spectral bandwidth. In breaking wave groups, higher frequency wave components lose energy while lower frequency ones gain to 50% of the energy loss in the higher frequency band. Transformation of wave frequency to wavenumber spectra using wave probe measurements and the linear dispersion relation is discussed.

An eddy viscosity model is proposed to simulate energy dissipation in two-dimensional unsteady plunging breakers. Numerical simulations with the model are performed to compare to the experimental measurements. Both the magnitude and the trend of the total energy measured in the experiments are approximated reasonably well. Good agreement as regards energy dissipation due to wave breaking and surface profiles after wave breaking is achieved. This work is part of the study mentioned above that has been accepted to the *Journal of Fluid Mechanics* for publication.

In the appendices, wave breaking onset and breaking strength prediction using the global wave steepness is revisited. In addition, air flow separation over non-breaking waves is observed in flow visualization experiments.

Chapter I

Introduction

1 Background

Breaking waves have a significant role in air-sea interaction. They enhance gas and heat exchange between air and sea by entraining air and generating turbulence; they also limit surface wave height and dissipate wave energy. In addition, these waves have tremendous impact on engineering design; they are usually much higher and steeper than the average waves present, and can wreak havoc with ships and offshore structures.

According to the review on the origins of water wave theory by Craik (2004), the first to attempt a theory of water waves was Isaac Newton, who deduced the frequency of deep-water waves must be proportional to the inverse of the square root of the wave length in 1687. Much later, Louis Lagrange, in 1781 and 1786, derived the linearized governing equations for small-amplitude waves.

George Gabriel Stokes completed his first study on weakly nonlinear wave theory in 1847 and later showed a limiting two-dimensional periodic wave (1880), which was possibly the first scientific study of the wave stability problem. It was much later that analytical and numerical studies of nonlinear surface wave interactions were completed

and revealed various wave instabilities (Phillips, 1960; Benjamin, 1967; Benjamin and Feir, 1967; Longuet-Higgins, 1978a, b; Mclean, 1982a, b; Tanaka, 1983, 1985, to name a few). Numerous experiments and numerical studies on deep water breaking waves have been conducted since then (for reviews see Banner and Peregrine, 1993; Melville, 1996; Perlin and Schultz, 2000; Duncan, 2001). One seminal research effort on breaking waves was that of Rapp and Melville (1990). More recently, investigations with flow visualization techniques (Perlin et al., 1996; Chang and Liu, 1998; Jiang et al., 1996, 1998; Banner and Peirson, 1998; Duncan et al., 1999; Melville et al., 2002) have provided significant insight on the kinematics and dynamics of wave breaking.

Although we have gained much appreciation through the abovementioned studies, our ability to predict wave breaking onset and breaking strength, our understanding of the kinematics and dynamics of breaking waves, and robust and effective numerical models of breaking waves remain very limited, primarily due to the complicated mechanisms that wave breaking involves, such as strong nonlinearity, intermittent breaking patterns, wave groups, and the wide range of breaking scales.

2 Objectives

Lab experiments serve as the most reliable method in the study of breaking waves, as numerical simulations fail or cannot fully represent the physics subsequent to wave breaking while field observations lack the control required for detailed studies. In lab experiments, breaking waves are generated often by focusing wave energy at desired time and space (e.g. Rapp and Melville, 1990) and by Benjamin-Feir (1967) instability (e.g.

Tulin and Waseda, 1999). Both methods use wave-wave interaction, but the intrinsic governing mechanism for wave breaking may be different.

In this study, experiments are conducted to investigate two-dimensional unsteady breaking waves generated by frequency focusing wave groups in finite-depth water in the laboratory. In addition, numerical simulations are performed to facilitate a comparison to the experimental results.

The objective of this research is to further improve our understanding of breaking waves. Specifically, this study intends to

- evaluate and further develop breaking onset criteria for two-dimensional unsteady breaking waves in finite-depth water;
- investigate the kinematics of both nonlinear frequency focusing wave groups (global scale) and breaking waves (local scale);
- quantify and parameterize energy dissipation and dissipation rate in nonlinear wave groups, including breaking wave groups;
- examine wave spectra evolution and quantify spectral distribution of energy dissipation in nonlinear wave groups;
- develop an eddy viscosity model to simulate energy dissipation for two-dimensional unsteady plunging breakers.

3 Summary of the current study

Major contributions of this study are presented in Chapter II through IV, which are written so that each of them stands on its own and presents both major research findings and detailed literature reviews relevant to specific topics in that chapter. Summaries of the chapters are provided as follows.

In Chapter II, we conducted an experimental study to evaluate the performance of a wave breaking criterion based on the local wave energy convergence rate (Song and Banner, 2002). For this purpose, four separate wave groups of progressive surface gravity waves with slowly decreasing frequency are generated mechanically in a two-dimensional wave tank. Surface elevations as a function of time are measured using capacitance wave probes; surface elevations as a function of space prior to and during breaking are obtained by recording sub-regions with an imaging system, and combining the measurements from repeated experiments. In addition, nonlinear numerical solutions for the surface elevation profiles for the four wave groups are obtained by solving a set of nonlinear evolution equations using a pseudo-spectral method, and are compared with experiments and linear predictions. It is found that the breaking criterion of Song and Banner is sensitive to the choice of the local wave number, but that a particular local wave number based on local wave geometry distinguishes wave groups leading to breaking from wave groups that do not break. It is shown that the lead time between the parameter exceeding the threshold and incipient wave breaking increases as wave breaking intensifies. The total energy loss is related strongly to this parameter immediately prior to breaking. This chapter is a reprint in full of the research work contained in Tian et al. (2008).

In Chapter III, an experimental study of energy dissipation in two-dimensional unsteady plunging breakers and an eddy viscosity model to simulate the dissipation due to wave breaking are reported. This chapter is the complete manuscript that has been accepted (pending minor revisions) to the *Journal of Fluid Mechanics*.

Measured wave surface elevations are used to examine the characteristic time and length scales associated with wave groups and local breaking waves, and to estimate and parameterize the energy dissipation and dissipation rate due to wave breaking. Numerical tests using the eddy viscosity model are performed and we find that the numerical results capture well the measured energy loss.

In our experiments, three sets of characteristic time and length scales are defined and obtained: global scales associated with the wave groups, local scales immediately prior to breaking onset, and post-breaking scales. Correlations among these time and length scales are demonstrated, which to the best of our knowledge, have not been reported before. Measured surface elevations are used to estimate the total energy and the energy loss due to wave breaking. The total energy and the energy loss are non-dimensionalized with the characteristic scales and we find that they scale well with the global and local wave steepnesses. In addition, for our wave groups, wave breaking onset predictions using the global and local wave steepnesses are found based on experimental results. The universality of these predictions for wave breaking requires further study.

Breaking time and breaking horizontal-length scales are defined, and they are determined from high-speed imaging. The time and length scales depend approximately linearly on the local wave steepness. The two scales are used then to determine the horizontal

breaking-wave crest speed and the energy dissipation rate, which is the ratio of the energy loss to the breaking time scale. The dissipation rate is parameterized with the wave characteristics of local breaking waves; the resulting normalized dissipation rate is on the order of 10^{-3} . In general this is consistent with previous results, subject to proper data interpretation, but is one to two orders of magnitude greater than field measurements. Our experimental results show that the local wave steepness is correlated highly with the measured dissipation rate, indicating that the local wave steepness may serve as a good wave-breaking-strength indicator.

To simulate the energy dissipation due to wave breaking, a simple eddy viscosity model is proposed and validated with our experimental measurements. Under the small viscosity assumption, the leading-order viscous effect is incorporated into the free surface boundary conditions. Then, the kinematic viscosity is replaced with an eddy viscosity to account for energy loss. The breaking time and length scales, which depend weakly on wave breaking strength, are applied to evaluate the magnitude of the eddy viscosity using dimensional analysis. In addition, the value of eddy viscosity is assessed through a turbulence energy dissipation rate analysis, which provides estimations very close to those of the first method. The estimated eddy viscosity is on the order of $10^{-3} \text{ (m}^2\text{s}^{-1}\text{)}$ and demonstrates a strong dependence on wave breaking strength. Numerical simulations with the eddy viscosity estimation are performed to compare to the experimental results. Both the magnitude and the trend of the total energy measured in the experiments as a function of space are approximated reasonably well by the numerical results. Good agreement as regards energy dissipation due to wave breaking and surface profiles after

wave breaking is achieved, which illustrates that the simple eddy viscosity model functions effectively.

Chapter IV presents an experimental study on spectral evolution of laboratory generated breaking waves. Spatial evolution of wave frequency spectra and temporal evolution of wavenumber spectra of breaking wave groups are examined. Spectral content following energy dissipation due to wave breaking is presented.

Spatial evolution of wave frequency spectra is examined for non-breaking wave groups. Nonlinear energy transfer across the frequency spectra is obvious as wave groups focus and defocus. A large energy loss due to viscous effects and contact-line damping is observed in the non-breaking wave groups. Depending on spectral bandwidth, 20% to 70% of this non-breaking energy loss is from the spectral peak region ($f/f_p = 0.95 \sim 1.1$). Here, f_p is the peak energy frequency. In addition, the energy loss near the spectral peak rises as frequency spectral bandwidth decreases. To the best of our knowledge, a similar observation has not been reported previously.

Observations of the evolution of the frequency spectra for breaking wave groups are also reported. From these the spectral distribution of energy dissipated due to wave breaking is determined then as the spectral difference between the before and after wave breaking value less the corresponding spectral difference of the non-breaking wave group. Wave components in the frequency range $1.1 f_p$ to $2.0 f_p$ lose significant energy, which contributes to most of the energy loss due to wave breaking; wave components between $0.65 f_p$ and $0.95 f_p$ gain to 50% of the energy loss in the higher frequency band. The ratio of the energy gain to loss across the wave spectrum due to wave breaking shows no

apparent dependence on breaking strength, and is higher than others, previous experimental results. Due to wave breaking, energy near the spectral peak may increase or decrease, depending on the initial wave frequency spectrum.

Surface profile measurement is used to examine the temporal evolution of the wavenumber spectra before and after breaking. Consistent with the observation on the frequency spectra, shorter wave components ($k/k_p = 1.2 \sim 4.0$) lose energy during wave breaking while longer wave components ($k/k_p = 0.4 \sim 0.9$) gain energy. Here, k_p is the wavenumber associated with the peak frequency component. Surface elevation measurements and the linear dispersion relation are used to transform the wave frequency spectra to wavenumber spectra. As nonlinearity increases, as expected, the transformed wavenumber spectra demonstrate larger discrepancies from the measured ones, indicating that not surprisingly this transformation has limited application for highly nonlinear and breaking wave groups.

Numerical tests using a simple eddy viscosity model to simulate energy dissipation in breaking waves are conducted. Although the eddy viscosity model fails to simulate detailed spectral changes after wave breaking, the character of the energy loss and gain across the spectrum is captured.

In Appendix 1, an equivalent global wave steepness that accounts for wave spectral shape to predict wave breaking onset is proposed. A coefficient that accounts for wave spectral shape is proposed and used to modify a global wave steepness, which is shown to relate closely to total energy loss due to wave breaking, but has a different wave breaking onset threshold for different wave spectra. After modification, the global steepness has a

threshold close to 0.25 for wave breaking onset prediction and correlates approximately linearly with energy dissipation due to wave breaking for wave groups with both constant amplitude and constant steepness wave spectra.

In Appendix 2, a preliminary investigation of the separation of air flow over water waves is presented. It is found that air flow separation does occur over non-breaking wave crests, indicating that the presence of wave breaking is a sufficient but not necessary condition for the air flow separation over water waves. Similar observations in laboratory studies have been seldom reported. Furthermore, higher wind speed is necessary to initiate the air flow separation over non-breaking wave crests, implying that a robust air flow separation criterion may depend on both the local wave crest geometry and the wind speed above the wave crest.

References

- BANNER, M. L. & PEREGRINE, D. H. 1993 Wave breaking in deep-water. *Annu. Rev. Fluid Mech.* **25**, 373-97.
- BANNER, M. L. & PEIRSON, W. L. 1998 Tangential stress beneath wind-driven air-water interfaces. *J. Fluid Mech.* **364**, 115-145.
- BENJAMIN, T. B. 1967 Instability of periodic wavetrains in nonlinear dispersive systems. *Proc. R. Soc. London Ser. A-Math. Phys. Sci.* **299**, 59-76.
- BENJAMIN, T. B. & FEIR, J. E. 1967 Disintegration of wave trains on deep water. 1. Theory. *J. Fluid Mech.* **27**, 417-430.
- CHANG, K. A. & LIU, P. L. F. 1998 Velocity, acceleration and vorticity under a breaking wave. *Phys. Fluids* **10**, 327-329.
- CRAIK, A. D. D. 2004 The origins of water wave theory. *Annu. Rev. Fluid Mech.* **36**, 1-28.
- DUNCAN, J. H. 2001 Spilling breakers. *Annu. Rev. Fluid Mech.* **33**, 519-547.
- DUNCAN, J. H., QIAO, H., PHILOMIN, V. & WENZ, A. 1999 Gentle spilling breakers: crest profile evolution. *J. Fluid Mech.* **379**, 191-222.
- JIANG, L., PERLIN, M. & SCHULTZ, W. W. 1998 Period tripling and energy dissipation of breaking standing waves. *J. Fluid Mech.* **369**, 273-299.
- JIANG, L., TING, C. L., PERLIN, M. & SCHULTZ, W. W. 1996. Moderate and steep Faraday waves: Instabilities, modulation and temporal asymmetries. *J. Fluid Mech.* **329**, 275-307.
- LONGUET-HIGGINS, M. S. 1978a Instabilities of gravity-waves of finite-amplitude in deep-water .1. superharmonics. *Proc. R. Soc. London Ser. A-Math. Phys. Sci.* **360**, 471-488.
- LONGUET-HIGGINS, M. S. 1978b Instabilities of gravity-waves of finite-amplitude in deep-water .2. subharmonics. *Proc. R. Soc. London Ser. A-Math. Phys. Sci.* **360**, 489-505.
- MCLEAN, J. W. 1982a Instabilities of finite-amplitude gravity-waves on water of finite depth. *J. Fluid Mech.* **114**, 331-341.
- MCLEAN, J. W. 1982b Instabilities of finite-amplitude water-waves. *J. Fluid Mech.* **114**, 315-330.
- MELVILLE, W. K. 1996 The role of surface-wave breaking in air-sea interaction. *Annu. Rev. Fluid Mech.* **28**, 279-321.

- MELVILLE, W. K., VERON, F. & WHITE C. J. 2002 The velocity field under breaking waves: coherent structures and turbulence. *J. Fluid Mech.* **454**, 203-233.
- PERLIN, M., HE, J. H. & BERNAL, L. P. 1996 An experimental study of deep water plunging breakers. *Phys. Fluids* **8**, 2365-2374.
- PERLIN, M. & SCHULTZ, W. W. 2000 Capillary effects on surface waves. *Ann. Rev. Fluid Mech.* **32**, 241-274.
- PHILLIPS, O. M. 1960 On the dynamics of unsteady gravity waves of finite amplitude .1.The elementary interactions. *J. Fluid Mech.* **9**,193-217.
- RAPP, R. J. & MELVILLE, W. K. 1990 Laboratory measurements of deep-water breaking waves. *Philos. Trans. R. Soc. Lond. Ser. A-Math. Phys. Sci.* **331**, 735-800.
- STOKES. G. G. 1880 Supplement to a paper on the theory of oscillatory waves. *Math. Phys. Papers.* **1**, 314–326.
- TANAKA, M. 1983 The stability of steep gravity-waves. *J. Phys. Soc. Jpn.* **52**, 3047-3055.
- TANAKA, M. 1985 The stability of steep gravity-waves 2. *J. Fluid Mech.* **156**, 281-289.
- TULIN, M. P. & WASEDA, T. 1999 Laboratory observations of wave group evolution, including breaking effects. *J. Fluid Mech.* **378**, 197–232.

Chapter II

Evaluation of a Deep-Water Wave Breaking Criterion

Abstract

An experimental and numerical study is presented to investigate the breaking criterion of Song and Banner [J. Phys. Oceanogr. 32, 2541 (2002)] who suggested a threshold range of $(1.4 \pm 0.1) \times 10^{-3}$ for a predictive wave breaking parameter, measuring the rate of change of the local energy maximum and the local wave number, to differentiate between wave trains that lead to breaking and those that do not. To examine the breaking criterion experimentally, four separate wave groups of progressive surface gravity waves with slowly decreasing frequency are generated mechanically in a two-dimensional wave tank. Surface elevations as a function of time are measured using capacitance wave probes; surface elevations as a function of space prior to and during breaking are obtained by recording sub-regions with an imaging system, and combining the measurements from repeated experiments. In addition, nonlinear numerical solutions for the surface elevation profiles for the four wave groups are obtained by solving a set of nonlinear evolution equations using a pseudo-spectral method, and are compared with experiments and linear predictions. It is found that the breaking criterion of Song and Banner is sensitive to the choice of the local wave number, but that a particular local wave number based on local

wave geometry distinguishes wave groups leading to breaking from wave groups that do not break. It is shown that the lead time between the parameter exceeding the threshold and incipient wave breaking increases as wave breaking intensifies. The total energy loss is related strongly to this parameter immediately prior to breaking.

1 Introduction

Many criteria for predicting the onset of breaking and breaking severity of deep water surface waves have been reported based on field observations, lab experiments, and numerical studies. A literature review of work prior to 1998 can be found in the study by Nepf *et al.*¹. Later, Wu and Nepf² segregated these criteria into three classes (i.e. geometric, kinematic, and dynamic criteria) based on relevant wave characteristics, such as local wave geometry, wave steepness, wave crest particle velocity and phase speed, wave crest acceleration, and rate of change of momentum and energy. Their experimental study suggested that the kinematic criterion is the most robust while the other two classes are affected readily by wave directionality.

The aforementioned kinematic criterion is used often to predict wave breaking and simply states that breaking occurs when the horizontal crest particle velocity, U , exceeds the phase speed, C . Application of this criterion to irregular waves is complicated due to ambiguity in defining the phase velocity, and difficulty in measuring the crest particle velocity. Particle image velocimetry (PIV) measurements by Perlin *et al.*³ showed that the horizontal velocity at the tip of an overturning jet of their deep water plunger was 1.3 times the phase speed, while Chang and Liu⁴ provided a horizontal particle velocity 68%

greater than the phase velocity. Wu and Nepf² experimentally validated the kinematic criterion and for three-dimensional seas reported that wave directionality, as well as wave focusing and diffracting, has little affect on the criterion. However, Stansell and MacFarlane⁵ reported $U/C \leq 0.95$ for spilling breakers and $U/C \leq 0.81$ for plunging breakers, which indicate that the kinematic criterion is in general unable to predict the onset of breaking. In addition, Oh *et al.*⁶ recently conducted experiments to examine breaking criteria for deep water wind waves under strong wind action using a PIV system. They also concluded that the kinematic criterion is an inadequate predictor of breaking for wind waves under strong wind action.

Another group of breaking criteria is that of geometric classification. The geometric criteria generally use wave steepness and local wave geometry as characteristic parameters to predict breaking onset. Criteria based on wave steepness, ka , with values of 0.443⁷, 0.31⁸, 0.43⁹, and 0.41(Ref. 10) have been reported to indicate the onset of wave breaking. Commonly, the disparity in the breaking ka value is attributed to the various mechanisms responsible for wave breaking and the manner in which the responsible process is generated. In addition, instability¹¹, three dimensional effects¹, and wave directionality^{2, 12} are known to have significant influence on the breaking onset. Another factor that strongly affects breaking is the presence of currents, as can be seen at inlet entrances during ebb tide. In particular, Yao and Wu¹³ investigated the effects of shear current on the incipient breaking of unsteady waves and found that the steepness at incipient breaking is decreased by a positive shear and increased by a negative shear.

Rapp and Melville¹⁴ showed global spectrum-based wave steepness, ka_c , is a good indicator of breaking onset as well as breaking severity for two dimensional unsteady

breakers. Chaplin¹⁵ and Kway *et al.*¹⁶ examined deep water breaking waves of different wave spectra. Both results illustrated that the steepness is sensitive to wave spectral shape. Nepf *et al.*¹ and Wu and Nepf² reported similar observations, and they also demonstrated that wave directionality has an effect on the breaking steepness criterion.

Several researchers have demonstrated also that profile asymmetry is important regarding breaking. Wave steepness defined simply as ka cannot represent the horizontal and the vertical wave crest asymmetries that appear as waves approach incipient breaking. Kjeldsen and Myrhaug¹⁷ introduced the crest front steepness, the crest rear steepness, the vertical asymmetry, and the horizontal asymmetry, to describe the asymmetries. However, their parameters were reported to vary considerably, and are also sensitive to wave directionality and shape of the wave spectrum^{2, 12}. Additionally, Yao and Wu¹³ showed that sheared currents have pronounced effects on the wave crest asymmetry, and hence on breaking.

Criteria based on energy and energy gradients have created more and more excitement. Schultz *et al.*¹⁸ proposed that the local mean RMS potential energy can function as a breaking criterion for regular two-dimensional deep water waves based on numerical experiments of fully nonlinear irrotational flow in a periodic domain. They found that the energy input rate can indicate the breaking severity, and suggested a breaking criterion of the potential energy exceeding 52% of the total energy of a limiting Stokes wave.

Focusing also on energy, Banner and Tian¹⁹ investigated the evolution of the local mean energy and momentum densities of modulating surface gravity water waves with the numerical code of Dold and Peregrine²⁰. They developed two dimensionless growth rates,

β_E and β_M , that are diagnostic parameters of their wave breaking criterion. A threshold of $\beta_{(E/M)}$ equal to 0.2 is reported as a universal criterion, independent of wave group structures, initial wave group configurations, and surface shears. The criterion can also provide information on when wave breaking will occur, as it monitors the evolution of the predictive parameters.

Following similar reasoning, Song and Banner²¹ extended the Banner and Tian investigation by considering a dimensionless growth rate, $\delta(t)$, constructed from the evolution of the local energy density and the local wave number at the envelope maxima of three types of deep water wave groups. A threshold range for $\delta(t)$ of $(1.4 \pm 0.1) \times 10^{-3}$ was suggested to differentiate wave breaking from non-breaking. Numerical experiments showed that the initial wave group structures, as well as the number of waves in the wave groups, wind forcing and surface shear²², have no effect on the threshold, which suggests that the criterion is universal. For the first time, they systematically reported the lead time between $\delta(t)$ exceeding the threshold value and the onset of wave breaking. In addition, a strong correlation was presented between the breaking parameter, $\delta(t)$, and the breaking intensity observed by Rapp and Melville¹⁴.

During the course of this study, it was discovered that Banner and Peirson²³ had conducted detailed lab experiments aimed at validating the breaking criterion proposed by Song and Banner. Their intent was to generate and examine two types of wave group structures with the same (equivalent) initial conditions as in Song and Banner's numerical simulations. The total local energy density and the local wave number were inferred based on measurements from six wave probes, designed in a special configuration of two

in-line sets of three probes. Experimental results were found in good agreement with the numerical results of Song and Banner, despite small differences in the conditions.

In this study, there is no intent to examine the evolution of the breaking parameter of the wave groups with the same initial conditions. Rather, the study is designed to validate or not the breaking criterion through experiments on wave groups of differing configuration. Additionally numerical solutions of the Euler equations are obtained using a pseudo-spectral method by initializing the numerical model with laboratory measurements and are compared carefully with experiments to test the validity of the numerical results near the onset of wave breaking. The remainder of the paper is as follows: Section 2 describes the experimental strategy, the breaking wave generation method, the physical setup, and the measurement error analysis. Numerical simulations and computation of breaking parameters are presented in Section 3 and 4, respectively. Results and discussion are provided in Section 5. Section 6 communicates our concluding remarks.

2 Experiments

Experiments are conducted in a 2-D wave tank of length 35 meters, width 0.7 meters, and water depth 0.62 meters. The walls and bottom of the tank are glass; thus, surface elevation profiles can be viewed and recorded unimpeded using imaging systems positioned outside the tank. A servo-controlled wavemaker (oscillating wedge) with a feedback loop and auxiliary electronics is used to generate the wave trains.

The technique to generate breaking waves used by Perlin *et al.*³ is employed in the experiments. First, a time history of the water surface elevation required at the wavemaker to produce a steep wave at a desired position in the tank is generated. Second, a wavemaker transfer function is applied to obtain the command signal. The local wave steepness, ka , is further modified such that it approximately remains constant for every zero-upcrossing wave in the wave group. As demonstrated by Perlin *et al.*³, the technique helps ensure that the phase speed of each component in the wave group, as well as the local wave steepness, ka , will vary equally when the gain of the command signal is altered. One advantage of this method is that it can generate ‘clean’ breaking waves. Here, ‘clean’ indicates the absence of upstream breaking. This technique is also able to produce breaking waves with strong spatial and temporal repeatability, which is important in this study.

The range of frequencies that comprises the wave group is 1.0 to 2.0 Hz; therefore, deep water conditions are maintained as predicted by linear theory for the set water depth. However, a finite-depth effect was observed when predicting the surface elevations, and is addressed subsequently. A typical command signal to the wavemaker is shown in Figure II-1. Gains (i.e. relative voltages) of 900, 1265, 1650 and 2020 are used, corresponding to waves of non-breaking, breaking, strong breaking, and severe breaking, respectively. The three breakers are plungers and break essentially once, though a following gentle spiller was observed in the Gain 2020 case.

The study is designed to use measured surface elevations (temporal and spatial) to construct the surface profile as a function of time and space, and then to examine the evolution of the parameters that determine the wave breaking onset. In particular, spatial

measurements of the surface elevation required to test Song and Banner's breaking criterion²¹ are made using video imaging (see Section 2.2).

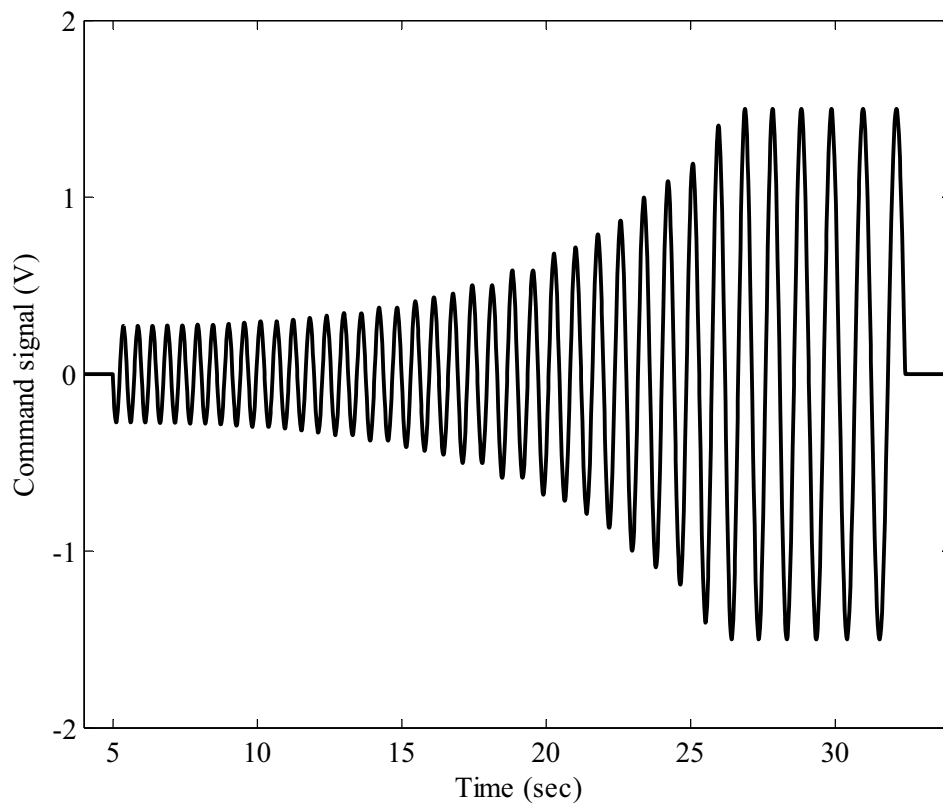


Figure II-1 Typical command signal sent to the wavemaker.

2.1 Temporal surface elevation measurements

To measure temporal surface elevations, capacitance wave probes are positioned at desired measurement locations along the tank. The first probe is 6.88m downstream from the mean wavemaker position (unless specified otherwise, distance, x , is relative to the mean wavemaker position, and time, t , refers to the start of the wavemaker). Positions of the second and the third gages are chosen so that the former is upstream and the latter is downstream relative to the wave breaking location. The distance between these two probes is 1.1 m. We note that the positions of the second and the third gages are not fixed as the breaking location of the wave trains with different gains varies. (The change of breaking locations was observed also by others^{14, 16}). A sketch of the arrangement is shown in Figure II-2(a). A Dell PC, a National Instruments PCI-6034 board and a SCB-68 box (NIDAQ-instruments) serve as the data acquisition system to record the temporal measurements.

The recorded temporal surface elevations at the first wave probe are shown in Figure II-3. Based on linear wave theory (LWT), after it is Fourier decomposed into N (256) sinusoidal components, the measured surface elevation can be used to predict the surface elevation as a function of time and space by means of

$$\eta(t, x) = \sum_{n=1}^N A_n \cos[\omega_n t - k_n(x - x_m) - \varepsilon_n] \quad (1)$$

where x_m is the position of the wave probe and the n^{th} Fourier component has radian frequency, ω_n , wave amplitude, A_n , and phase shift, ε_n . The temporal surface elevations

are measured for a sufficiently long period to ensure that the periodicity in the Fourier analysis does not affect the prediction (i.e. there is only one wave group propagating in the spatial domain). The linear dispersion relation, $\omega_n^2 = k_n g \tanh(k_n h)$, is used to obtain the wave number, k_n .

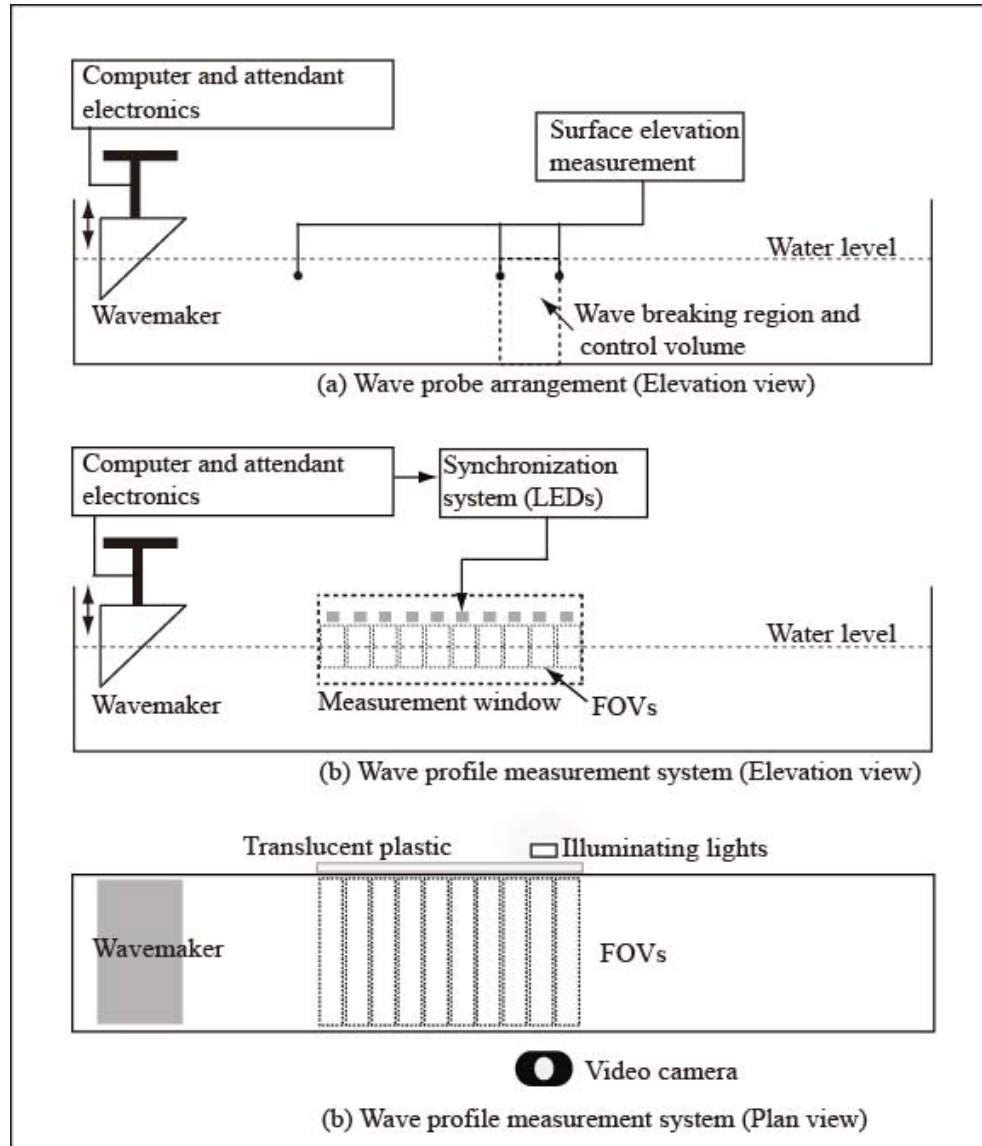


Figure II-2 Sketch of the experimental setup for the temporal (a) and spatial imaging (b) of the sea-surface elevation. FOV indicates the field of view.

To provide comparisons of the measured and the predicted surface elevations at the second wave probe, Figure II-4 is presented. In Figure II-4(a), linear theory predicts this profile adequately as the wave steepness is small and nonlinearity effects are negligibly small. As expected, nonlinearity increases with increased wavemaker command signal, and predictions based on LWT become less accurate as the command signal is increased and waves approach breaking. Figure II-4(b) illustrates the measured and predicted surface elevation for the severe breaking case. Discrepancies are found in both surface elevation and phase, and therefore, nonlinear theory needs to be introduced.

One problem that attracted our attention was the finite-depth effect in both LWT predictions and numerical simulations. Surface elevations generated according to deep water conditions deviated from the experimental measurements. Although the carrier wave (frequency 1.5Hz) has a wave length of 0.694m, which satisfies the deep water condition ($kh > \pi$) based on LWT, the wave groups exhibit much longer length scales; hence the groups apparently “feel” the tank bottom. Therefore, the linear predictions/simulations are computed using finite-water-depth equations.

For the low command-signal cases, linear theory does an adequate job of describing the surface elevation; thus, the evolution of the breaking parameter may be examined with the predicted surface elevation profiles. However, the parameter, $\delta(t)$, for waves of large steepness (the strong and the severe breaking cases), can only be determined from accurate spatial measurements as discussed subsequently. That is, to rectify the discrepancies in surface elevation and phase shown to exist using only the temporal probe measurements, spatial measurements are essential.

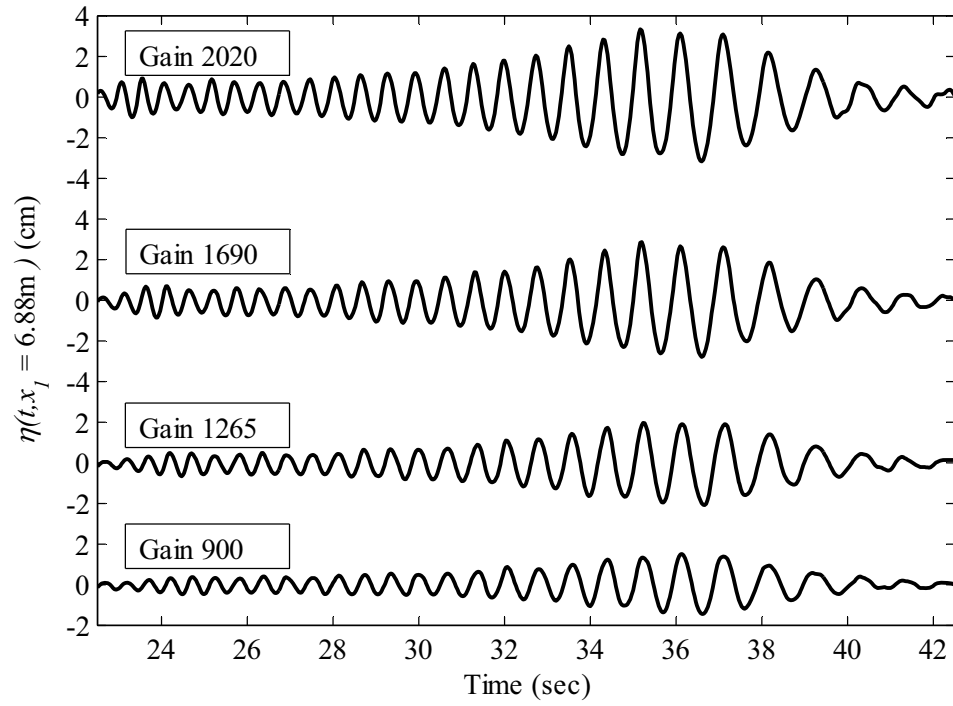


Figure II-3 Measured surface elevations at the first wave probe located at $x_l = 6.88\text{m}$.

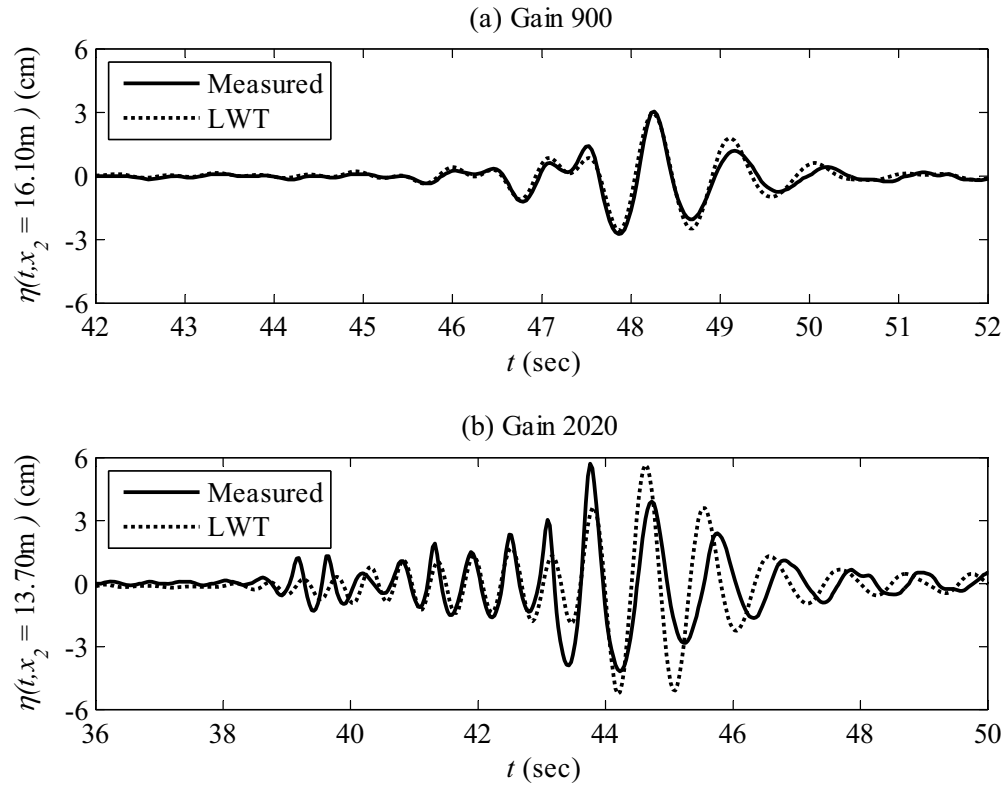


Figure II-4 Measured surface elevations (solid line) compared with the predictions (dashed line) based on linear wave theory at the second wave probe.

2.2 Spatial surface profile measurements

As discussed, for an accurate description of the evolution of the breaking parameter $\delta(t)$, in particular, for large steepness waves, measurements of spatial surface profiles are conducted using the experimental setup depicted in Figure II-2(b). To obtain the surface elevation profiles for this purpose, only those in the final stages of the approach to breaking are recorded, which are related to the total energy dissipation by wave breaking according to Song and Banner ²¹. We use spatial information of the surface elevation profiles from approximately the last $7.5T$ (T is the period of the carrier wave with frequency 1.5Hz) prior to wave breaking.

The measurement window must be of sufficient length to include as a minimum the entire wave group, approximately $8.5L$ (L is the wavelength of the carrier wave with frequency 1.5Hz) in the experiments. It is not possible for us to use a single field of view to achieve this; therefore, the measurement window is divided into 10 sub regions, each of length 61 cm. Relying on the demonstrated repeatability of the generated breaking wave process and the measurements in each sub region from repeated runs, we combined the data to construct the surface elevation profile across the entire measurement window.

To facilitate the spatial measurements, a back lighting illumination technique is adopted. This is achieved using a pair of 500W halogen lights, a sheet of translucent high-density polyethylene and a video imager. The lights are seated 61cm from the opposite sidewall with the translucent plastic sheet attached directly to the outer sidewall to diffuse the light and thus backlight the liquid-gas interface. The imager is positioned on the front sidewall of the tank with its axis oriented slightly downward for a better image of the field of view.

The imager is framing a field of view of 704 x 480 pixels at 30 frames per second. Using a precise optical target, the spatial resolution is determined to be 0.866 mm/pixel and the image distortion is shown to be negligible.

This simple method works well for our purposes. The water surface is defined clearly and can be identified easily in the recorded images. When the surface waves become very steep, there is some uncertainty in the wave-crest region. However, the uncertainty is limited to ± 3 pixels. Considering that the wave height in the final stage is about 120 mm, this measurement precision (better than 5%) is sufficient for the purposes of this study. (In fact, this method can be used to determine the surface elevation through the breaking process to provide the local potential energy density as we will present in a subsequent publication.)

A synchronization system made of LEDs is utilized to identify simultaneously recorded images. An illumination signal is sent to the LEDs when the wavemaker is initiated, facilitating the synchronization. Since the temporal error from the LEDs is on the order of a microsecond, the measurement error due to time alignment is caused primarily by the framing rate (30fps). To minimize this error, time alignment is carried out carefully by comparing the water surface in the measurement overlap regions. Assuming that the image from the first sub region is measured at time t_0 and measurement of the second sub region starts at time t_1 , then the worst scenario is that $\Delta t = t_1 - t_0 = 1/60$ s. A simple analysis for a sinusoidal wave of frequency 1.5 Hz (i.e. the carrier wave frequency), and wave height 100 mm (on the order of the maximum wave height in the breaking wave trains) reveals that the error is 7.8% at zero-crossings and is 0.1% at maxima, as shown in

Figure II-5. Therefore, the experimental technique presented can capture the wave profile with reasonable precision, especially the wave maxima, which are more important in the calculation of the breaking-prediction parameters.

A series of surface elevation profiles measured with this technique is presented in Figure II-6. The initial profile is measured $7.5T$ before wave breaking ensues, and the time delay between each profile presented is $1/30$ s. The asterisk denotes where wave breaking occurs. This waterfall graph presents a clear picture of the temporal evolution of the spatial elevation changes that occur.

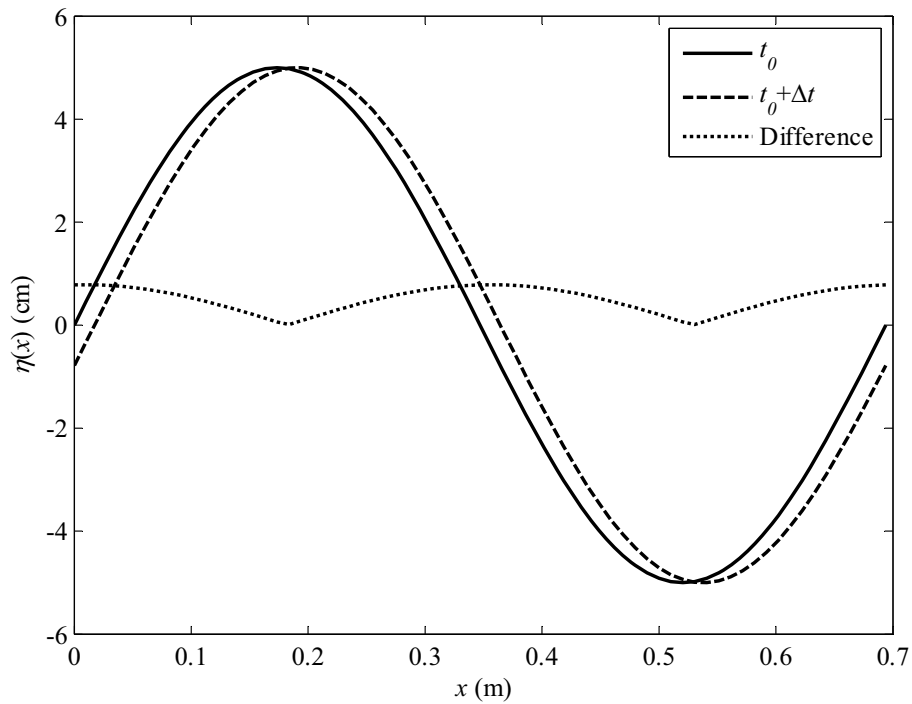


Figure II-5 Illustration of the spatial surface-elevation-measurement error due to a time alignment inaccuracy for a sine wave. $\Delta t = 1/60$ s. Note that the differences of the elevation around the maxima are small.

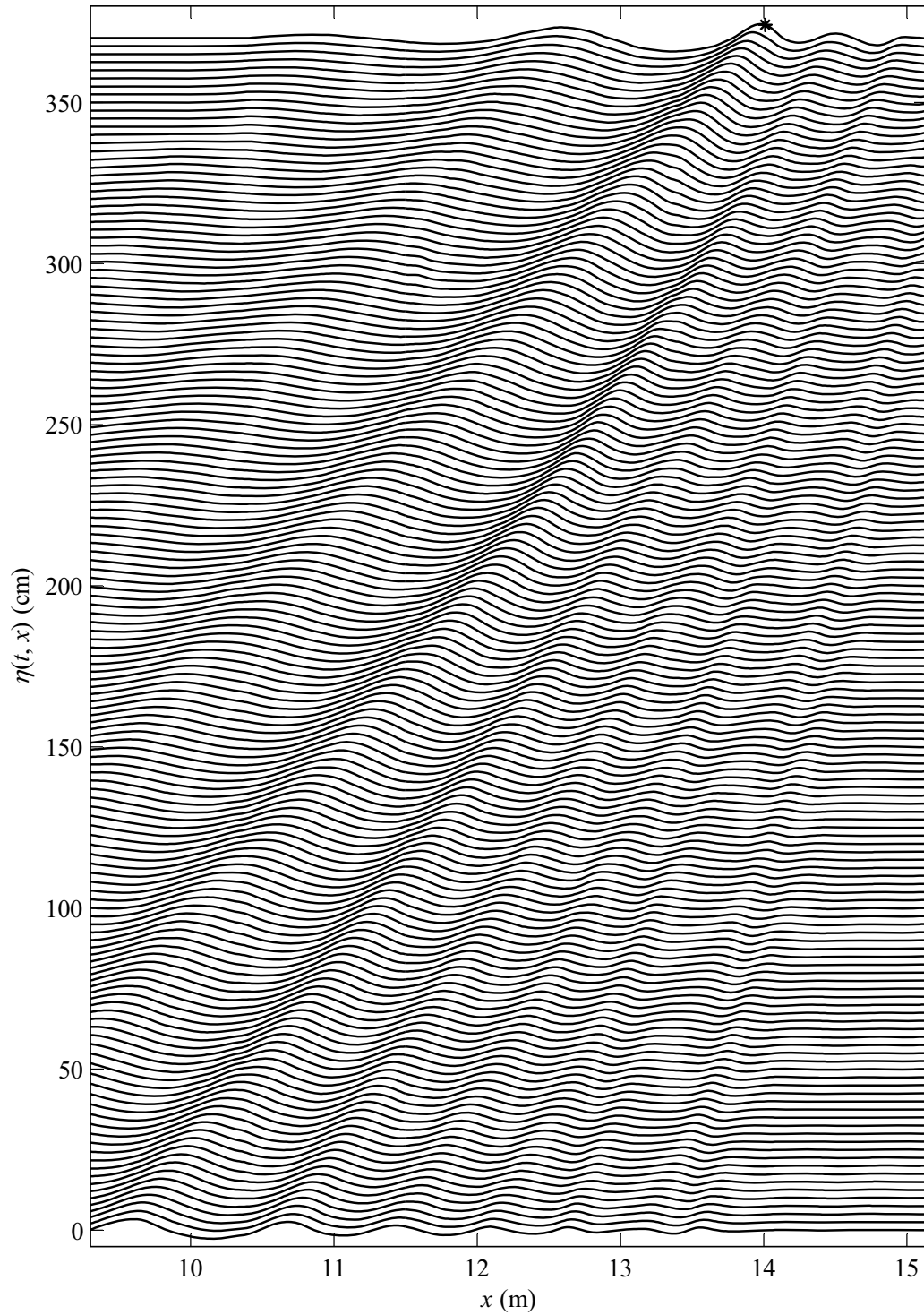


Figure II-6 Measured surface elevations (Gain: 2020) as a function of space and time. The asterisk on the uppermost profile shows where incipient breaking occurs. For clarity the surface profiles are offset 2.5cm for each successive measurement. The time delay between profiles is 1/30 sec.

3 Numerical simulations

Under the ideal-fluid assumption, using a systematic asymptotic expansion in small wave steepness, it was shown^{24, 25} that the Euler equations with the nonlinear free surface boundary conditions can be reduced to the following nonlinear evolution equations for the surface elevation, $\eta(t,x)$, and the velocity potential evaluated at the free surface, $\Phi(t,x)$,

$$\frac{\partial \eta}{\partial t} = \sum_{n=1}^{\infty} Q_n[\eta, \Phi] , \quad \frac{\partial \Phi}{\partial t} = \sum_{n=1}^{\infty} R_n[\eta, \Phi] , \quad (2)$$

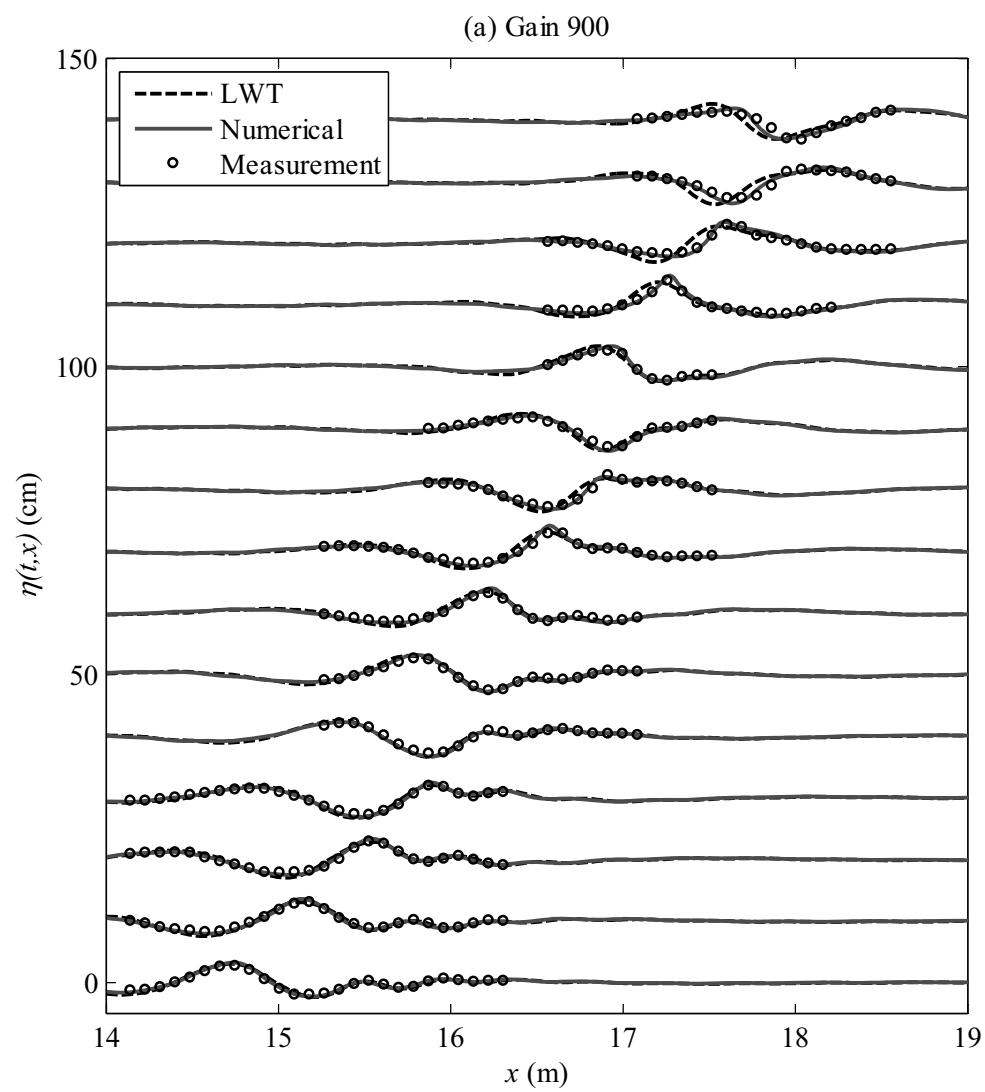
where Q_n and R_n of $O(ka)^n$ represent the n^{th} order nonlinear terms that can be found through explicit recursion formulae²⁶. This system can be considered as an unsteady generalization of the classical Stokes expansion for traveling waves.

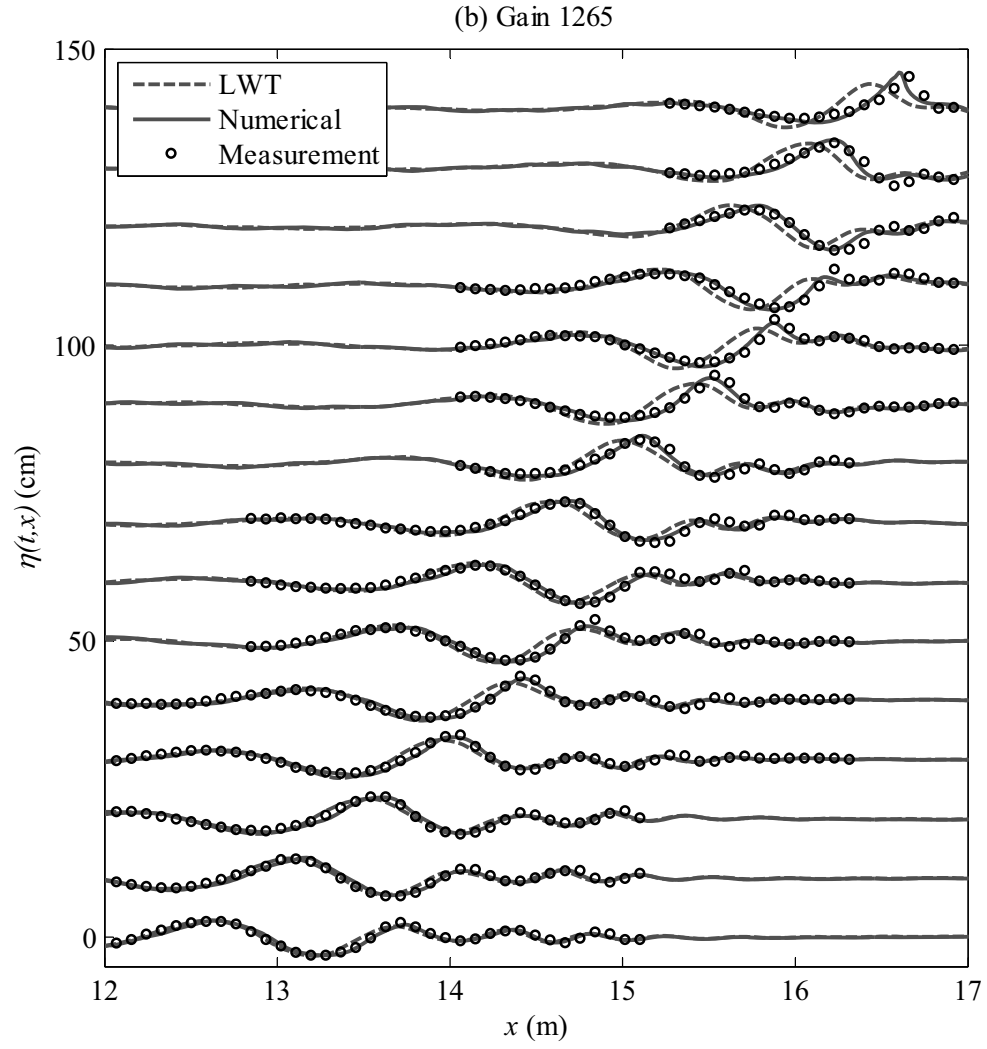
After the right-hand sides are truncated to the third order, the system is solved numerically using a pseudo-spectral method based on the fast Fourier transform to evaluate the right-hand sides, and a fourth-order Runge-Kutta method to integrate in time. Since only one wave group is present in the computational domain, the periodic boundary conditions have little effect on the numerical solutions. Higher-order nonlinear computational results show little difference from the third-order solutions even for the strong and severe breaking cases, and will not be presented. For details of our numerical method, see Choi *et al.*²⁶.

To compare the surface elevation profiles with experimental measurements, initial conditions for η and Φ are generated at $t=36$ sec using Eq. (1). The computations are

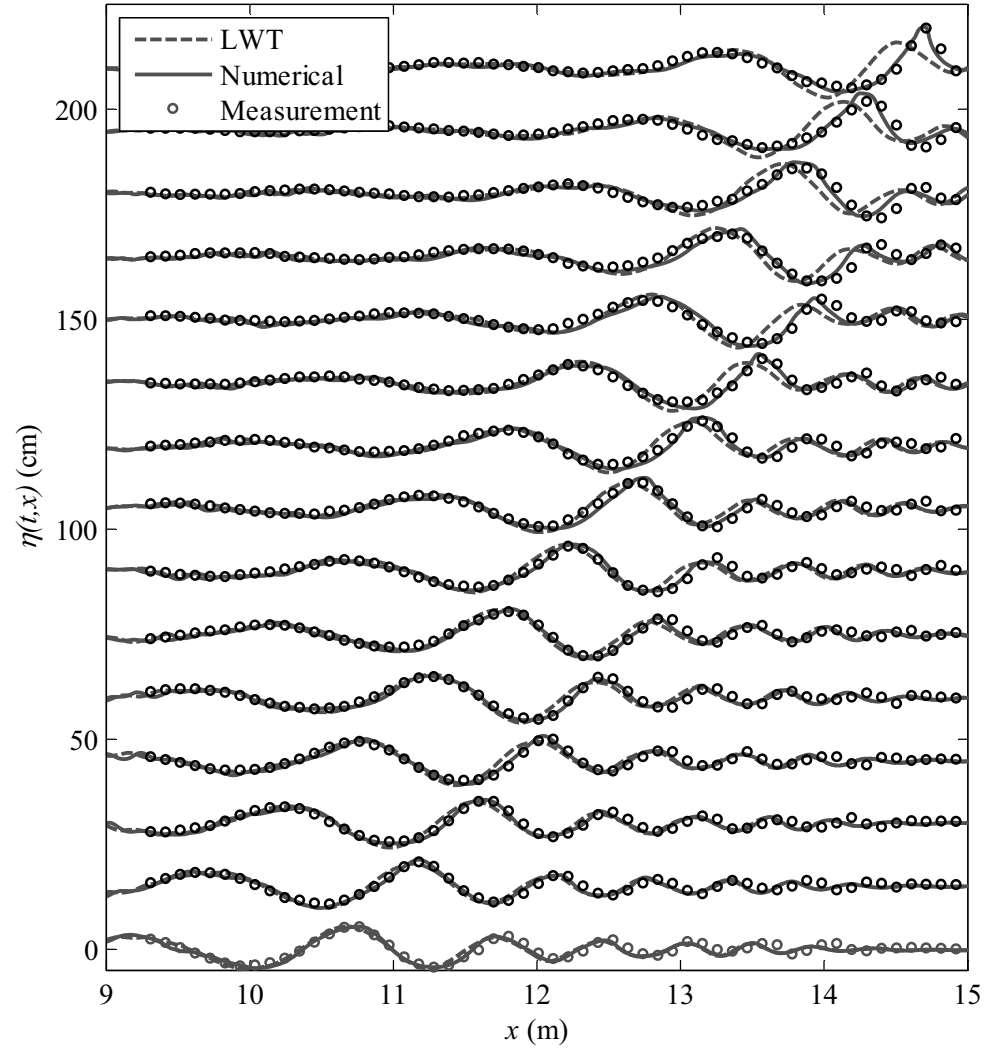
performed for a spatial domain of 24 meters. Convergence tests illustrate that using 2^{10} points to discretize the domain (i.e. $dx = 0.0234\text{m}$) with a time step of $1/60$ sec is sufficient for the simulation.

A comparison of the computed and the measured surface elevation profiles is completed, and the results are presented in Figure II-7 along with the surface elevation profiles predicted by linear theory, as discussed in Section 3.1. For each of the four simulations, as the wave groups approach breaking/near-breaking, linear wave predictions become less accurate in terms of both wave heights and phases as a result of the increasing nonlinearity; the agreement between the numerical results and the measurements remains adequate till immediately prior to wave breaking, when the wave crest motion becomes most energetic. For the four wave groups, the disparity between the LWT predictions and the measurements become more pronounced as gain value is increased; contrastingly, numerical simulations consistently provide results closer to the measured values even though the truncated system is obtained under the assumption of small wave steepness.





(c) Gain 1690



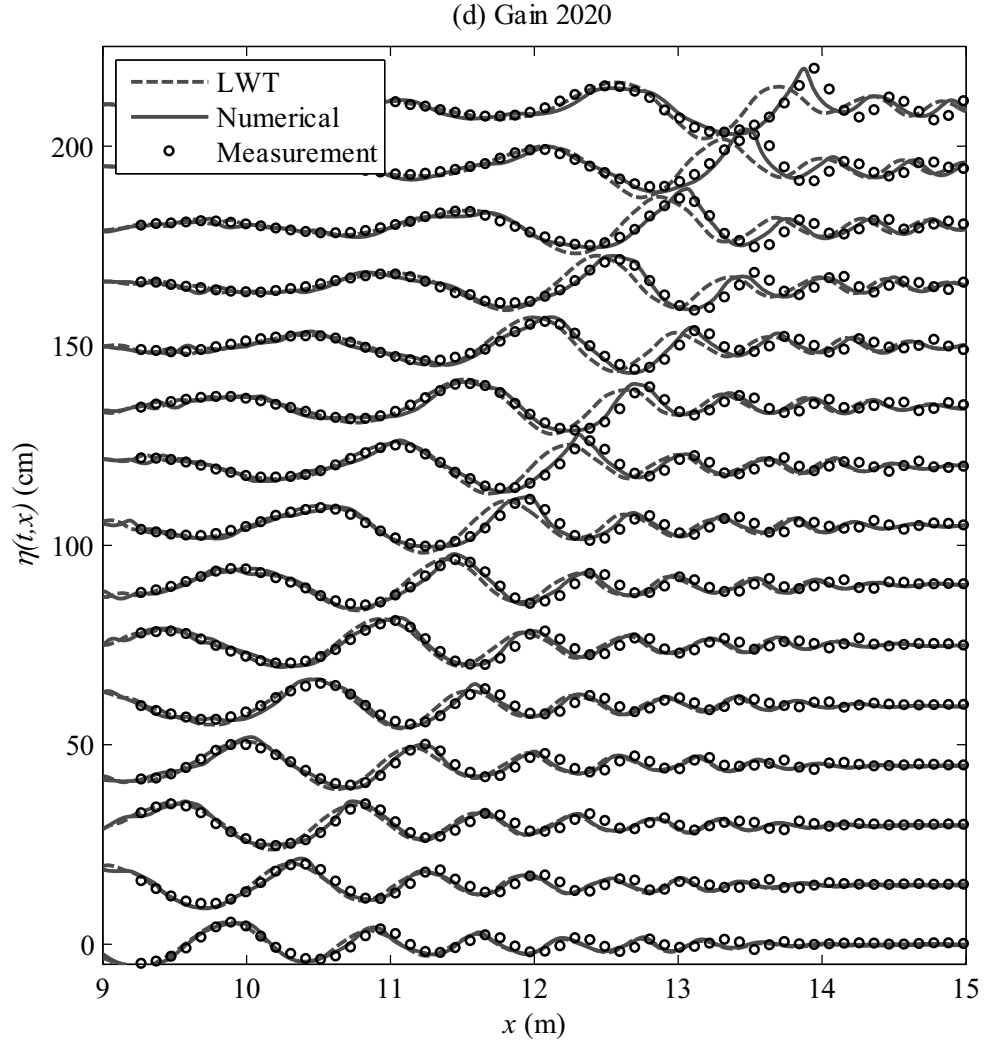


Figure II-7 A comparison of the linear predictions, the numerical solutions, and the measured surface profiles for the four wave groups. For clarity, one of every six experimental data points is plotted. (a) Gain 900 results for every $0.5T$ between $70T$ and $77T$ are shown (T is the period of the carrier wave); (b) Gain 1265 results for every $0.5T$ between $65.8T$ and $72.8T$ are shown; (c) Gain 1690 results for every $0.5T$ between $61T$ and $68T$ are shown; (d) Gain 2020, and results for every $0.5T$ between $58.7T$ and $65.7T$ are shown. Each profile is offset 15cm for clarity.

4 Computation of associated breaking parameters

4.1 Song and Banner's criterion revisited

Song and Banner²¹ proposed a predictive dimensionless parameter, $\delta(t)$, which can forecast the onset of wave breaking. A threshold, $\delta_c = (1.4 \pm 0.1) \times 10^{-3}$, is suggested to distinguish a group of waves that will eventually break from a group that will not break, and the threshold is claimed to be independent of wave group structure. Additionally the parameter is suggested as an indicator of the subsequent breaking intensity that will occur.

In their criterion, the two-dimensional depth-integrated local wave energy density is first found by summing the kinetic and the potential energy components of the fluid particles along a vertical line at position x and time t ,

$$E(t, x) = \int_{-h}^{\eta} \frac{1}{2} \rho_w (u^2 + w^2) dz + \frac{1}{2} \rho_w g \eta^2 \quad (3)$$

where u and w are the x and z water particle velocity components, g is the gravitational acceleration, ρ_w is the density of the water, h is the still water depth, and $\eta(t, x)$ is the free surface elevation.

Continuing with their analysis, the parameter, s , is defined as $s^2 = [E/(\rho_w g)]k^2$. As pointed out by Song and Banner, the wave number, k , is the local wave number, which can be calculated from the x derivative of the unfolded phase function computed from the Hilbert transform of the free surface profile. Another method to obtain the local wave number is to average the physical wave numbers determined from the surface elevation

profile by direct measurement of successive crests, troughs, and zero-crossings. These two different methods to compute the local wave number will be discussed in detail later.

Of interest are the extreme values of s^2 , i.e. $\mu(t) \equiv \max(s^2)$, at each time step. It is known that the maximum of s^2 can be determined either from the maximum of the wave envelope, calculated from the Hilbert Transform of the free surface, or from the maximum surface displacement (in this case, $\mu(t)$ is defined as: $\mu(t) \equiv (E_{\max}/\rho_w g)k^2$). As the nonlinear waves approach breaking, the wave envelope and the carrier waves become strongly coupled (i.e. both location and magnitude of the wave envelope maxima approximately match those of the maximum surface displacement); therefore, the wave breaking criterion using the wave properties associated with either wave envelope maxima or maximum surface displacement will result in little difference. In fact, Song and Banner have demonstrated that the resulting values of the breaking parameter obtained by tracking either wave envelope maxima or maximum surface displacement are virtually identical. In this paper, following Song and Banner, the latter definition is used to calculate $\mu(t)$ and spline interpolation is used to determine the upper and lower envelopes of $\mu(t)$.

Finally, the local mean, $\langle \mu(t) \rangle$ is found by averaging the upper and the lower envelopes.

(For details on how to calculate the local average value of $\mu(t)$ and $\langle \mu(t) \rangle$, refer to the

work of Song and Banner²¹.) Then the parameter, $\delta(t)$, is defined as $\delta(t) = \frac{1}{\omega_c} \frac{D \langle \mu(t) \rangle}{Dt}$,

where ω_c is the center radian frequency of the wave group. As pointed out by Song and

Banner, $\langle \mu(t) \rangle$ rather than $\mu(t)$ is used as the primary parameter to compute $\delta(t)$ as the

oscillating components of $\mu(t)$ (as seen in both Figure II-11 and Figure II-12) are the results of the strong asymmetry of wave crest and trough, which can not represent explicitly the energy convergence rate.

4.2 Surface elevation profiles

Surface elevation profiles are needed to examine whether the proposed threshold of the breaking parameter can distinguish wave breaking from non-breaking. As described in Section 3, the surface elevation profiles are obtained using linear wave theory with single point wave-probe measurements, numerical simulations with generated initial conditions, and direct spatial measurements.

With the surface elevation profiles, one can easily detect the maximum surface displacement and its location, and the local wave number can be computed readily once a calculation method is chosen. In the recent work by Banner and Peirson²³, six wave probes arranged in a special configuration were used to measure the surface elevations. Then the local wave number was deduced from the phase difference in these measurements. Through this strategy, they avoided the issue of measuring the surface elevation field although to apply the approach the crest and trough maxima of the wave group still need to be found as the group evolves. Notice that their measurement method does not provide spatial zero-crossings-based local wave numbers that are necessary to compute the breaking criterion parameter in the current study.

4.3 Local wave number computation

The breaking parameter $s^2(t)$ is proportional to k^2 ; therefore accurate computation of local wave number, k , is extremely important to the wave breaking criterion. In the numerical work by Song and Banner²¹, the local wave number, k_h , is defined as the derivative of the unfolded phase of the Hilbert transform of the wave group. Although k_h is used in their wave breaking criterion, they applied a low-pass filter to eliminate ‘spurious’ wave numbers with the intention of matching k_h to the local wave number based on local wave geometry. A similar low-pass filter was applied in the time domain in Banner and Peirson’s study²³, thus limiting the ratio of the local wave number at crest and trough maxima to that of the carrier wave to the range (1, 1.3). Since the choice of filter is somewhat arbitrary, no filter is applied here. The computed k_h at the maximum surface elevation at each time step, for example, for Gain 900, is shown in Figure II-8. Banner and Tian¹⁹ and Song and Banner²¹ also demonstrated that, when filtered properly, the local wave number determined from the Hilbert transform agree well with that based on successive zero-crossings, crests and troughs. However, the local wave numbers based on the two methods exhibit little agreement for our wave groups, as shown below and in the Appendix.

In this study, the local wave number based on local wave geometry, k_{gl} , is used and it is defined in Figure II-9. The evolution of k_{gl} at the maximum surface displacement for wave train with Gain 900 is provided in Figure II-10. Note that the intermittent pattern visible in the figure is a result of the maximum surface displacement switching from one wave crest or trough to another during evolution. Other definitions of the local wave number such as k_{g3} and k_{g6} depicted in Figure II-9 are also considered, but, as described

in the Appendix, the breaking parameter $\mu(t)$ based on k_{g3} and k_{g6} shows larger time fluctuations. Therefore, k_{gl} is employed to define the local wave number.

As for comparison of k_h and k_{gl} , neither magnitude nor phase is in agreement. The disparity might be due to the application of the Hilbert transform, which only applies to narrow band processes. Wave groups generated in the experiments may not be narrow-banded. This problem is known to occur in experiments with breaking wave groups. A discussion on how the breaking parameters vary depending on the choice of local wave number is presented also in the Appendix.

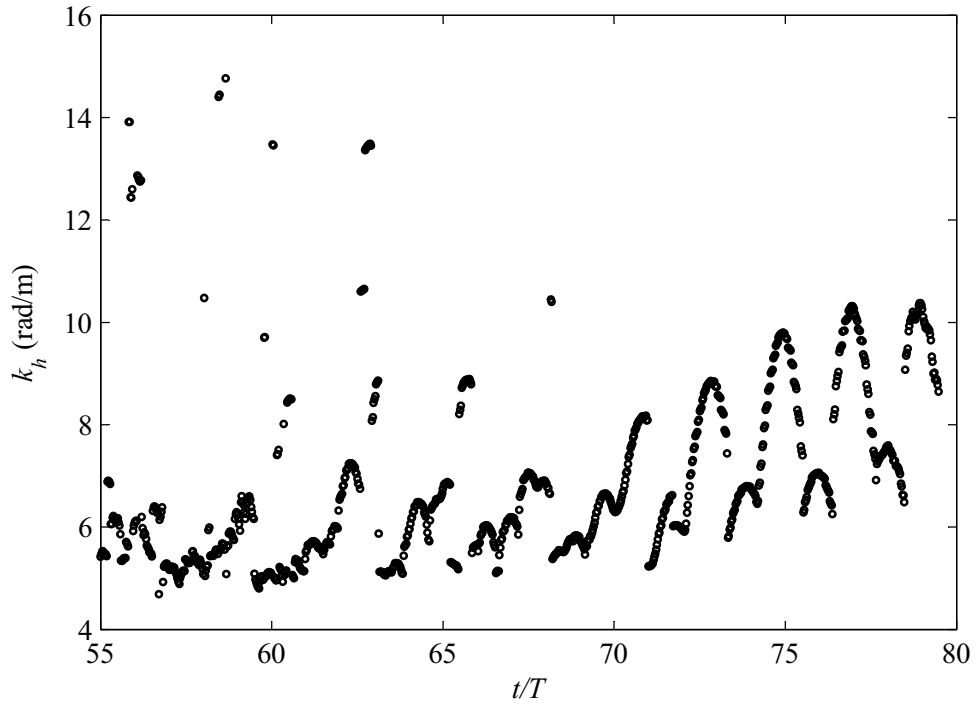
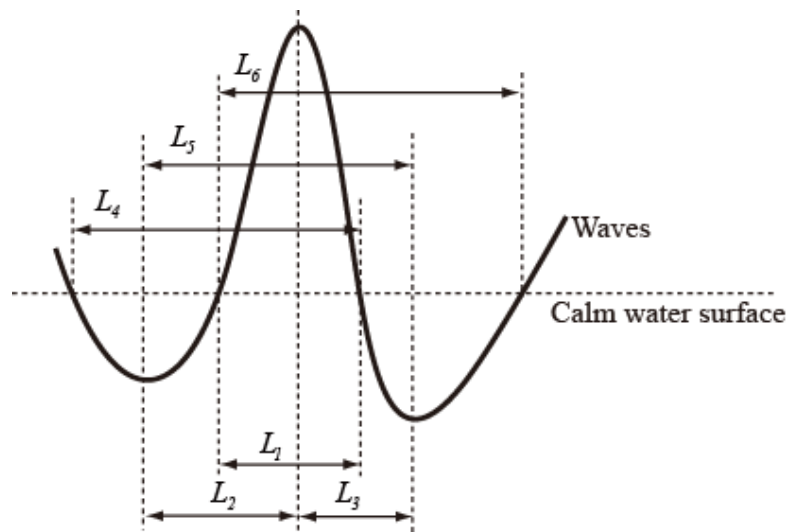


Figure II-8 Local wave number, k_h , versus dimensionless time. k_h is computed from the numerical solution for Gain 900 using the Hilbert transform at the maximum surface displacement at each time step.



$$\begin{aligned}
 k_{g1} &= \frac{\pi}{L_1} \\
 k_{g3} &= \frac{2\pi}{L_{m3}} \quad \text{and} \quad L_{m3} = \frac{2(L_1 + L_2 + L_3)}{3} \\
 k_{g6} &= \frac{2\pi}{L_{m6}} \quad \text{and} \quad L_{m6} = \frac{2(L_1 + L_2 + L_3) + L_4 + L_5 + L_6}{6}
 \end{aligned}$$

Figure II-9 Definitions of local wave number, k_g , at the wave crest. The numerical subscripts on k_g represent the number of lengths used in their determination.

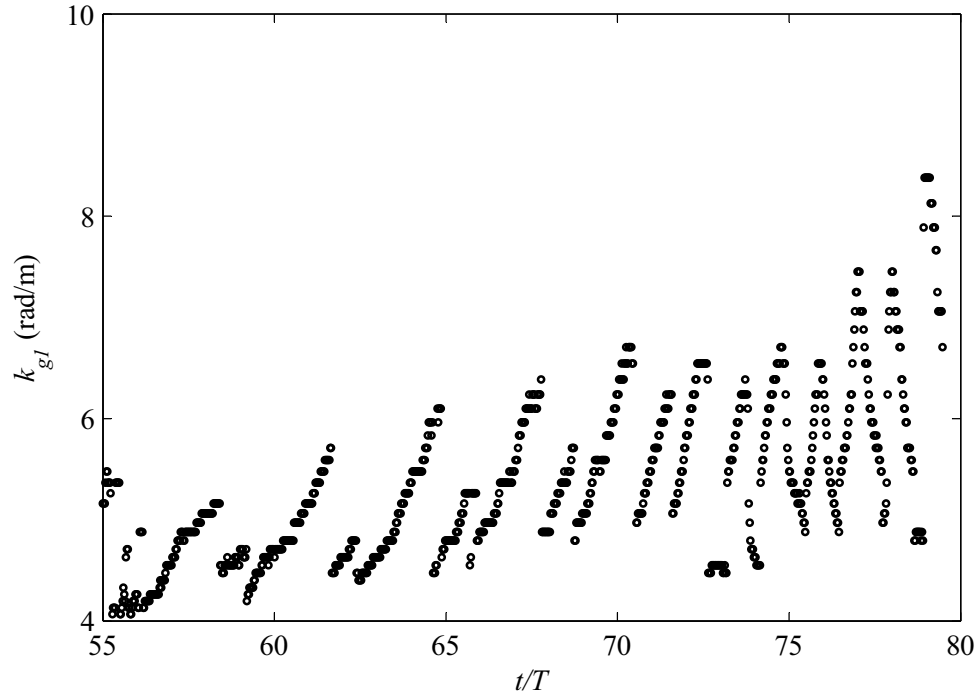


Figure II-10 Local wave number, k_{gl} , as a function of dimensionless time. k_{gl} is computed from the numerical solution for Gain 900 based on local wave geometry at the maximum surface displacement. Number of points used for the simulation is 2^{11} . k_g obtained from the simulation results with 2^{10} points is virtually the same.

4.4 Local energy

This experimental study is intended to examine Song and Banner's breaking wave criterion, where both local potential and local kinetic energy densities are needed. However, simultaneous measurement of both energy densities in such a large domain is very difficult to achieve. In addition, during active breaking, optical techniques to measure particle velocities (e.g. PIV and PTV) in the immediate vicinity are rendered difficult by the opacity of the (two-phase) flow. Therefore, it is common practice, see experiments on breaking waves by Rapp and Melville¹⁴ for instance, to obtain total energy by measuring the surface elevations (to determine the potential energy) and by inferring kinetic energy based on wave theory and/or its relationship to potential energy. (A recent work by Banner and Peirson²³ provides experimental validation of their criterion by examining laboratory-generated waves with the same initial conditions as Song and Banner's numerical ones. They also limited their energy measurements to surface elevation measurements.) This method is used for the present study.

In the current investigation, local potential energy can be computed easily based on the obtained surface elevations, i.e. $E_p = \rho g \eta^2 / 2$. To infer local total energy based on local potential energy for the experiments, we rely on the numerical simulation results. (Banner and Peirson²³ also used this strategy to determine their local total energy.) Figure II-11 presents the numerical results of the ratio of local potential energy to local total energy at the maximum surface displacements as the wave group evolves. As wave groups focus, this energy ratio at crest maxima decreases, which means that the local kinetic energy increases. Our results are consistent with Banner and Peirson²³. However, if the maximum surface displacement is a wave trough, the ratio of local potential energy to

local total energy as the wave group evolves is quite different than our computations. In the current study, the local potential energy represents approximately 68% of the total local energy at trough maxima, while Banner and Peirson observed that the ratio at trough maxima decreases from approximately 0.62 to 0.50 as waves evolve to breaking.

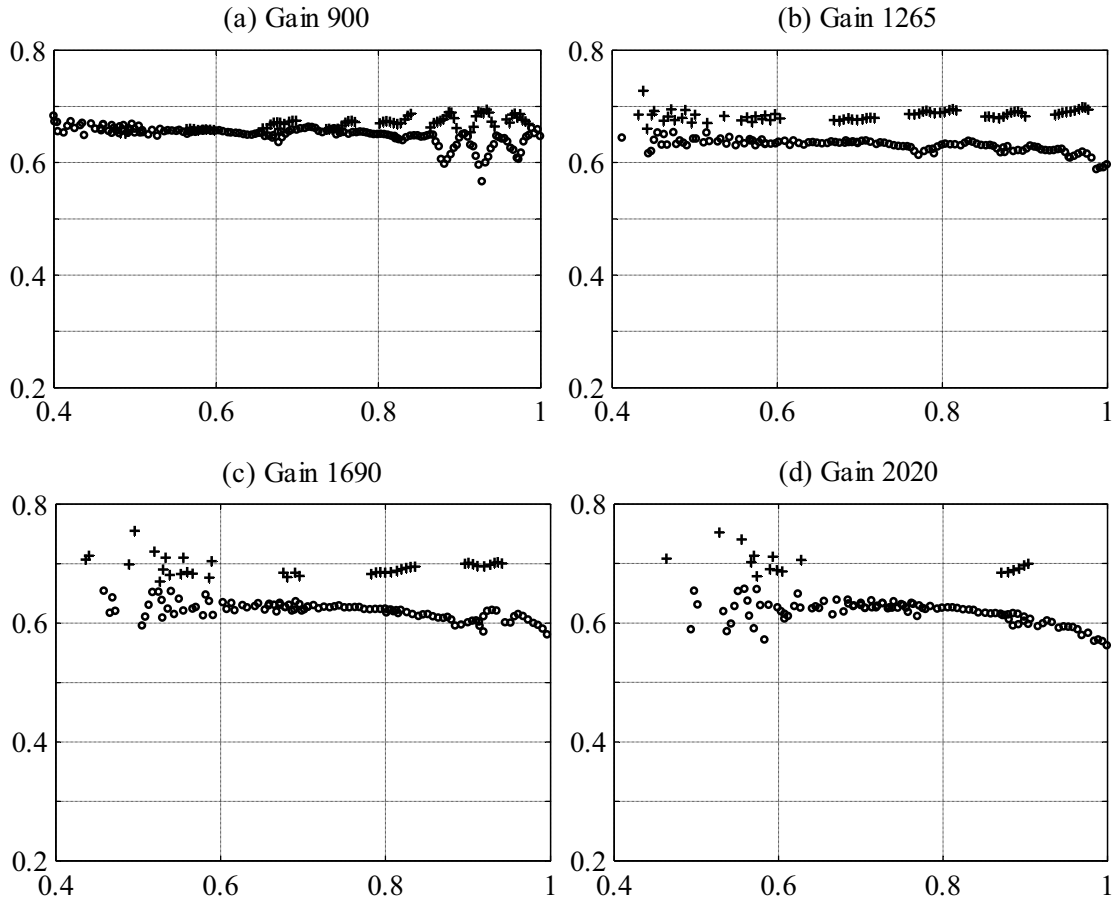


Figure II-11 Ratio of local potential energy to local total energy at maximum surface elevations. The abscissa represents the normalized time to wave breaking (or to the focus point if not breaking); the ordinate is the energy ratio. 'o' symbols represent the maximum surface elevations at crests; '+' symbols represent the maximum surface elevations at troughs.

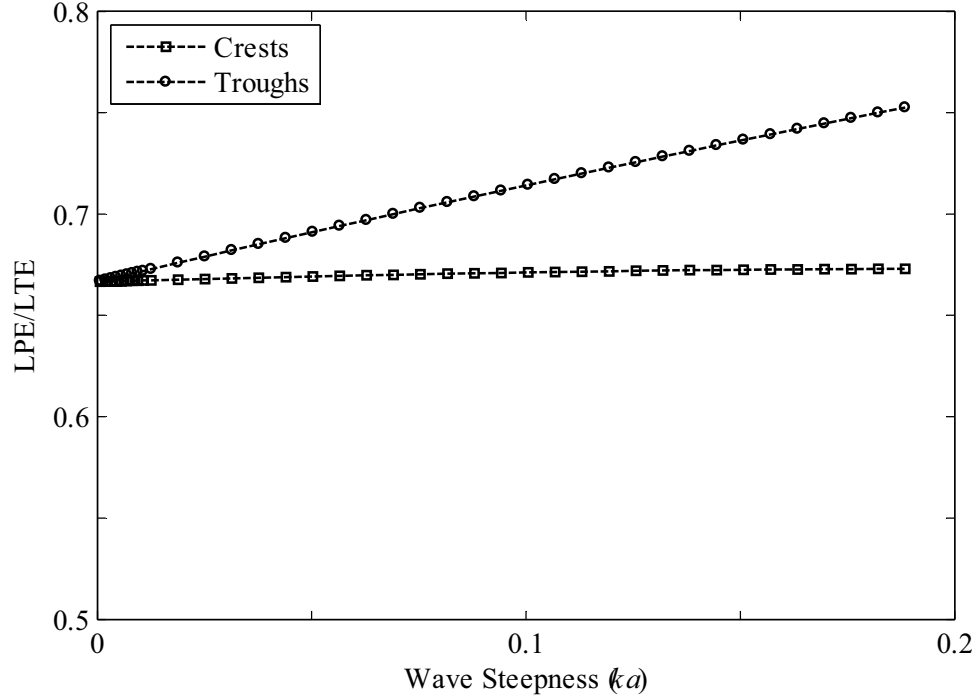


Figure II-12 Ratio of local potential energy (LPE) to local total energy (LTE) at crests and troughs for steady 3rd order Stokes waves. At very small wave steepness ($ka=0.00628$), the ratios are approximately equal to 0.667, the same result as given by linear theory.

As we are somewhat unfamiliar with local analyses as regards water waves, an investigation of a steady 3rd order Stokes wave was made to provide a comparison of the ratios of local potential energy to local total energy at wave crests and troughs. Figure II-12 presents those ratios at crests and troughs of waves with different steepness. As shown, the ratio at the crests remains about 66.7 % (the ratio from linear theory for deep water waves is 66.7%), and dwindles slightly as the wave becomes steeper; conversely, the ratio at the troughs varies significantly, from 66.7% to 75.0% for the cases considered. Based on this observation, one may conclude that the ratio of local potential energy to local total energy at crests and troughs can be affected by both wave steepness and the

configuration of the wave groups. Having investigated the different ratios for the Stokes solution, we see that the trend is in general agreement with our numerical solution. Therefore, in this paper, the local total energy for the experimental study is inferred based on the ratio of local potential energy and total energy found from our numerical results. To do so, we used a 3rd order polynomial to fit the data (ratio of local potential energy to local total energy in Figure II-11) for each wave group, and then the local total energy at the wave maxima is computed based on the experimental measurements for local potential energy.

5 Experimental evaluation of the breaking criterion

5.1 Examination of the wave steepness as a breaking criterion

To check the breaking criterion based on local wave steepness, ka , one can use the measured surface elevation just prior to breaking or at the focus point if there is no breaking. We note that the incipient breaking in this study is defined as when the forward side of the wave crest becomes very steep/vertical, but prior to when the crest falls. The wave-steepness results are listed in Table II-1 along with $\mu_{\max}^{1/2}$ and $\langle \mu \rangle_{\max}^{1/2}$, the value and the averaged value of the square root of μ immediately prior to wave breaking. Since $\mu(t)$ is defined as $(E_{\max}/\rho_w g)k_{gt}^2$, the square root of $\mu(t)$ and of $\langle \mu \rangle(t)$ is similar to ka , but they are determined from local properties. In the table abackward, aforward are calculated as one half of the trough-to-subsequent crest and crest-to-subsequent trough elevations respectively. Although the wave breaks, the local wave steepness just prior to

breaking for the Gain 1265 case is well below the reported criterion threshold^{7, 9, 10}. Although the steepness determined from $k_{g1}a_{backward}$ for the Gain 1690 group is close to the reported breaking criterion^{7, 9, 10}, the criterion also fails for the maximum dissipation case, Gain 2020 (see Figure II-15). Therefore, we conclude that the wave steepness criterion based on ka does not apply to our wave groups. On the other hand, as one would expect, $\mu_{\max}^{1/2}$ and $\langle \mu \rangle_{\max}^{1/2}$ immediately prior to breaking increase monotonically with increasing gain, and seem to be good indicators of nonlinearity.

Table II-1 Local wave steepness immediately before the onset of wave breaking.

Gain	900	1265	1690	2020
$k_{g1}a_{backward}$	0.2028	0.2893	0.4294	0.4087
$k_{g1}a_{forward}$	0.1870	0.2243	0.3488	0.3146
$\mu_{\max}^{1/2}$	0.2681	0.3705	0.4680	0.5258
$\langle \mu \rangle_{\max}^{1/2}$	0.2093	0.2781	0.3414	0.4057

5.2 Examination of Song and Banner's wave breaking criterion

With the surface elevation profiles and local energy, one can examine whether the threshold of the breaking parameter proposed by Song and Banner can distinguish wave breaking from non-breaking in the four wave groups considered here. Results for the nonbreaking wavetrain, Gain 900, are presented in Figure II-13. The evolution of the breaking parameters, $\mu(t)$ and $\delta(t)$, are computed based on LWT (figures a and b) and on numerical simulations (figures c and d); in addition, the parameters obtained from experimental measurements are presented also in (c) and (d). Recall that the breaking parameters are computed with k_{gl} as the local wave number. As shown in Figure II-13, for the non-breaking experiment, $\delta(t)$ decreases after it achieves its maximum, which is well below the threshold given by Song and Banner. Comparison reveals that linear theory underestimates the energy convergence rate. In addition, an oscillation in $\mu(t)$ caused by wave crest-trough asymmetry²¹ is observed; however, the oscillating period based on linear theory is approximately T ; while the numerical and experimental results provide an oscillating period of $2T$, which is consistent with Song and Banner.

For the three breaking wavetrains, evolution of the $\langle\mu(t)\rangle$ and $\delta(t)$ are obtained from numerical simulations and direct measurements of the surface profiles, as provided in Figure II-14. For all cases, the $\delta(t)$ parameter achieves its maximum at the initiation of wave breaking, and it is greater than the threshold. The numerical results show reasonably good agreement with the measurements before wave breaking occurs. It is noteworthy that the numerical model ran beyond the physical time of breaking (with some energy dissipation due to a low-pass filter that is used primarily to reduce aliasing

errors and effectively removes physical energy of high-wavenumber components). These experimental results validate that $\delta(t)$ can distinguish breaking wave groups from non-breaking ones, and verify the Song and Banner prediction although careful choices of local wave number and local total energy are required.

In Table II-2, detailed comparisons of the breaking parameters are presented. Here, threshold time is defined as when $\delta(t)$ crosses the threshold value; the breaking time is the actual time (referenced to the start of wave generation) when waves break in the experiments. The lead time between the parameter exceeding the threshold and wave breaking varies significantly for the three breakers. This might indicate that a stronger breaking condition has a longer lead time. However, no similar conclusion is proposed by Song and Banner²¹.

Table II-2 Comparison of the breaking parameters.

	Gain	$\delta_{max} \times 10^3$	Threshold time (t/T)	Breaking time (t/T)	Lead time (t/T)
Linear Theory	900	0.92			
	1265	1.41			
Numerical Simulations	900	0.69			
	1265	2.14	70.70		
	1690	5.39	64.50		
	2020	7.64	61.02		
Experiments	900	0.61			
	1265	2.52	70.63	72.57	1.94
	1690	4.05	64.25	67.95	3.70
	2020	5.41	60.40	65.70	5.30

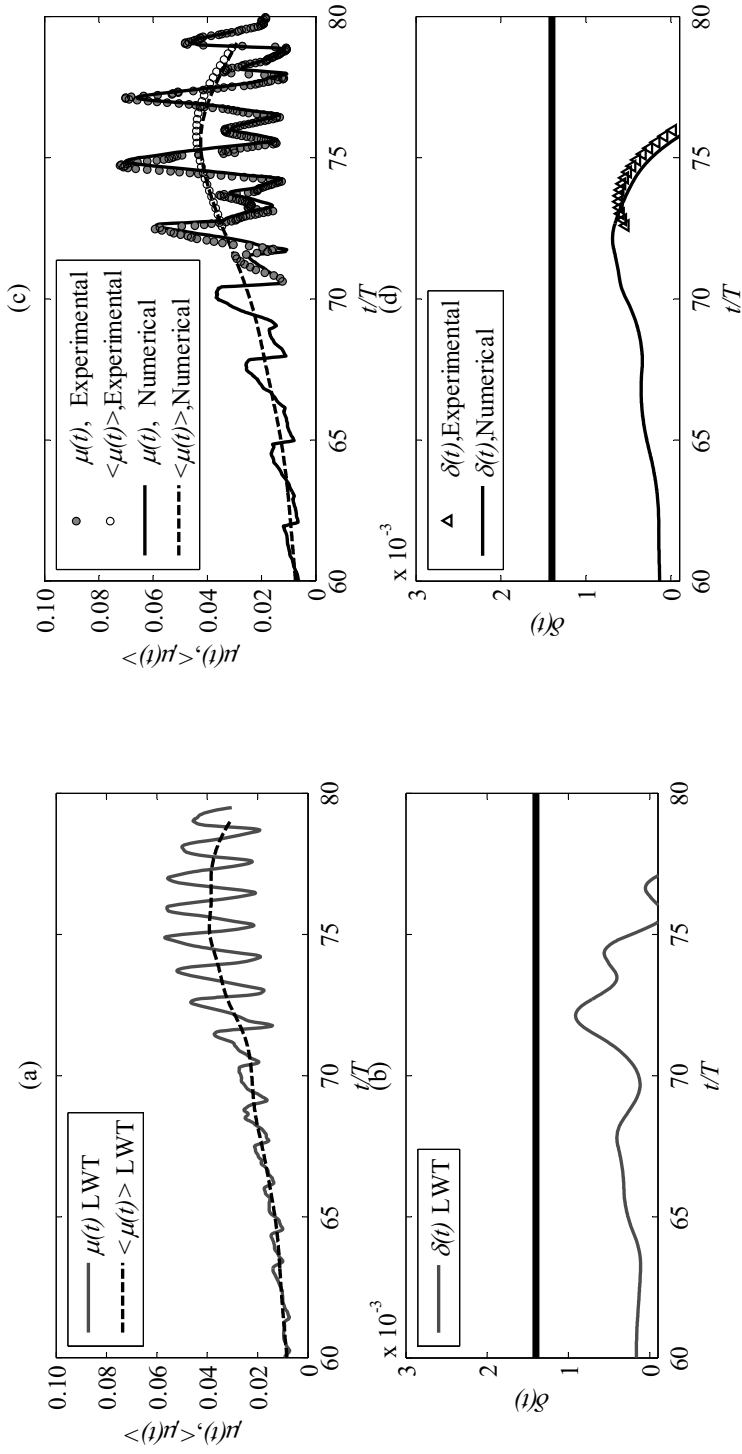


Figure II-13 The growth rate of the breaking parameter, $\delta(t)$, for the wave group with Gain 900. Graphs (a) and (b) are the linear results while (c) and (d) are the numerical ones. In addition, the breaking parameters determined from direct measurements are presented in (c) and (d). Also shown as a function of dimensionless time are the relevant variables used to determine δ . The horizontal region in the figures (b) and (d) denotes the threshold range of $\delta(t)$.

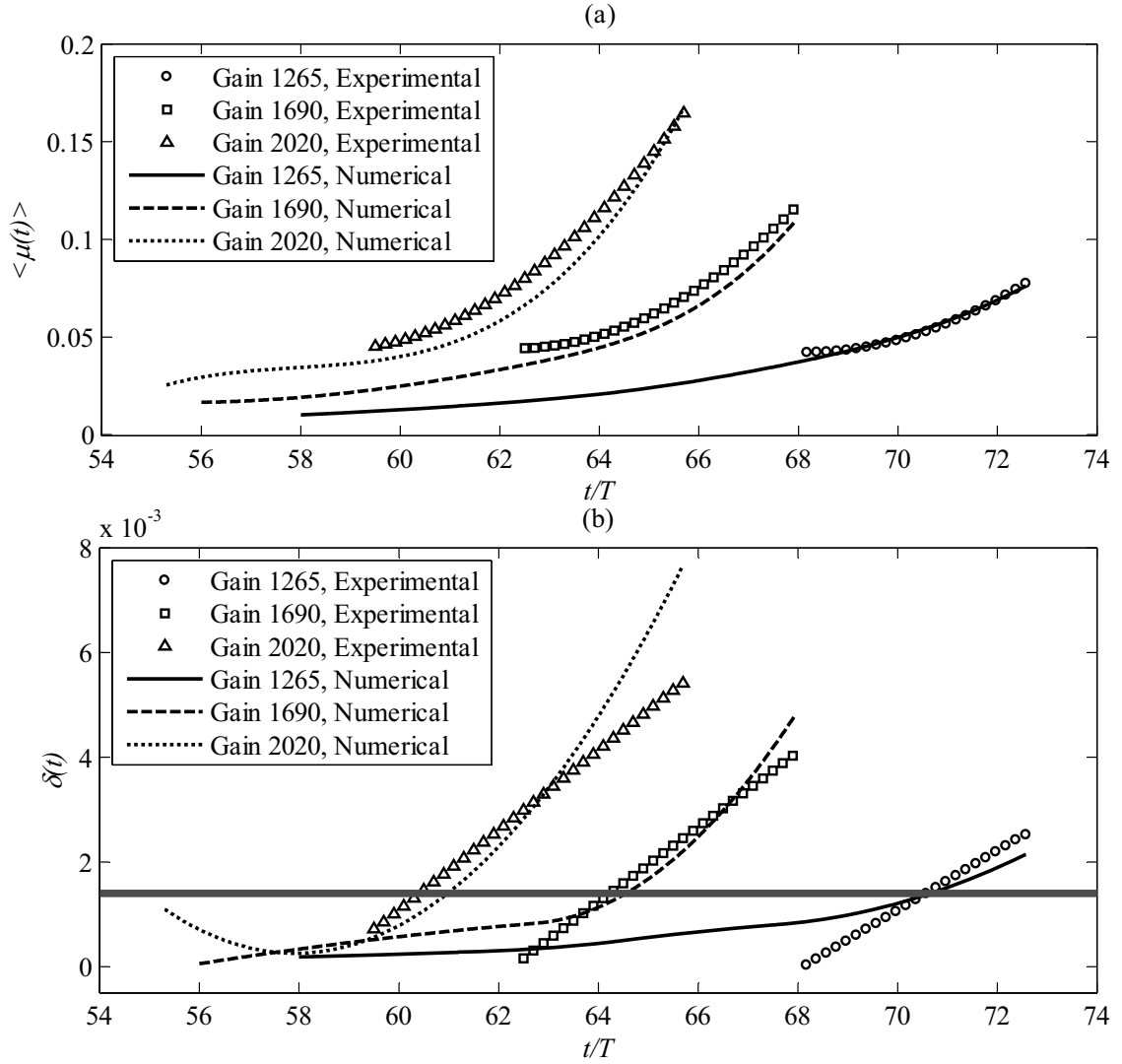


Figure II-14 Evolution of breaking parameters for the breaking wave groups with Gains 1265, 1690, and 2020. The horizontal region in the lower figure denotes the threshold range of $\delta(t)$.

5.3 Energy dissipation due to wave breaking

Another obvious quantity of interest is the total energy dissipation due to the breaking process. Following Rapp and Melville¹⁴, the total energy loss due to wave breaking is estimated via surface elevation measurements from the second and the third wave probes. To compute the total energy dissipated, one determines the total energy flux in and out the control volume shown in (a) of Figure II-2. The energy flux is defined as

$$F(t, x) = \int_{-h}^{\eta} \left[\frac{1}{2} \rho_w (u^2 + w^2) + \rho_w g z + P \right] u dz, \quad (4)$$

where P is the water-wave pressure. For deep water, under the linear assumption, the flux can be approximated by

$$F(t, x) = \frac{1}{2} \rho_w g c_g \eta^2, \quad (5)$$

where c_g is the group velocity. This simplification holds except for the breaking (focus) points, and it has an accuracy to the second order, $O((ka)^2)$ (Rapp and Melville¹⁴). If the measurement is initiated from quiescent conditions and continues till the return of quiescent conditions, the total energy dissipation equals the difference of the integrations of energy flux with respect to time

$$E_{loss} = \int_{t_0}^{t_1} [F(t, x_2) - F(t, x_3)] dt = \frac{1}{2} \rho g c \int_{t_0}^{t_1} [\eta(t, x_2)^2 - \eta(t, x_3)^2] dt, \quad (6)$$

where E_{loss} is the total energy loss, t_0 and t_1 are the beginning and ending times, and x_2 and x_3 are the locations of the second and the third wave gages. For 2-D waves, in the SI system, E_{loss} has units of J/m.

The wave packet energy obtained by means of integration of energy flux just prior to and after wave breaking has been known to show significant variability^{14, 16}; therefore, energy loss estimated with Eq. (6) may contain large errors. To minimize the errors, wave probe measurements are made at 23 stations along the wave tank; results of the integrated energy flux at these stations are presented in Figure II-15. A similar method to that used by Banner and Peirson²⁷ is applied to determine the energy loss due to wave breaking. As shown in Figure II-15, for the breaking cases, the measurements upstream and downstream of wave breaking are fitted with linear least-square regressions, respectively; then the energy losses are estimated by the difference of the data fitted lines across the break point. Viscous dissipation is represented by the fitted curves of the measurements for the nonbreaking wave train.

Accordingly, the computed total energy loss is non-dimensionalized (i.e. $\Delta E/E_0$, where E_0 is the integrated energy flux immediately prior to breaking and ΔE is the estimated energy loss) and compared with the maximum breaking parameter for each of the three breaking cases, as shown in Figure II-16. For these three experiments, the breaking parameter increases as total energy dissipation increases. Similar dependence on the energy loss due to wave breaking of the predictive parameter is also reported by Banner and Peirson²⁷. However, for a comparable δ_{max} , our energy loss is almost twice that of Banner and Peirson. The discrepancy may be attributed to generally smaller local wave number (See Figure II-8 and Figure II-10 and the impact of the choice of local wave

number on the breaking parameter in the Appendix). Another possible cause of the energy dissipation discrepancy is the type of breaking wave that occurs. In the current study, the three breakers are all plungers and break only once; while the wave trains of Banner and Peirson exhibit multiple breaking.

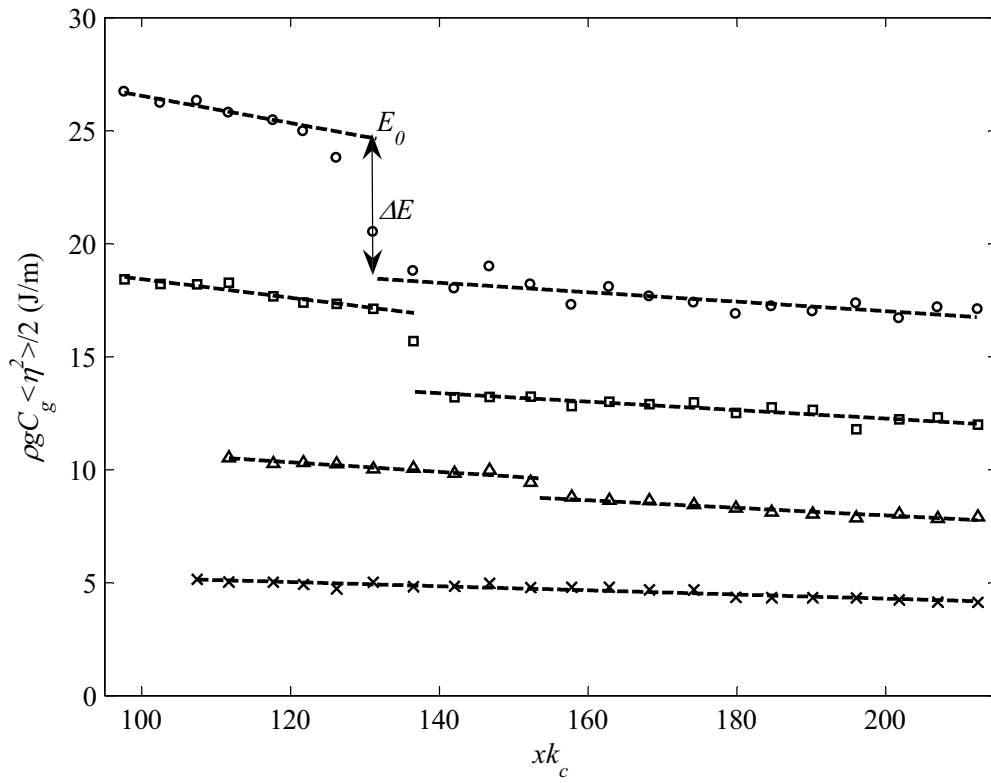


Figure II-15 Estimation of the energy loss due to wave breaking. Wave train measurements with Gain 900, 'x'; Gain 1265, '\$\Delta\$'; Gain 1690, '\$\square\$'; Gain 2020, 'o', are shown. Dashed lines represent the linear least-square fits. $\langle \eta^2 \rangle$ is the integration of η^2 with respect to time. E_0 is the integrated energy flux just prior to wave breaking based on the linear least-square fit, and ΔE is the estimated energy loss due to wave breaking, shown only for the Gain 2020 experiment.

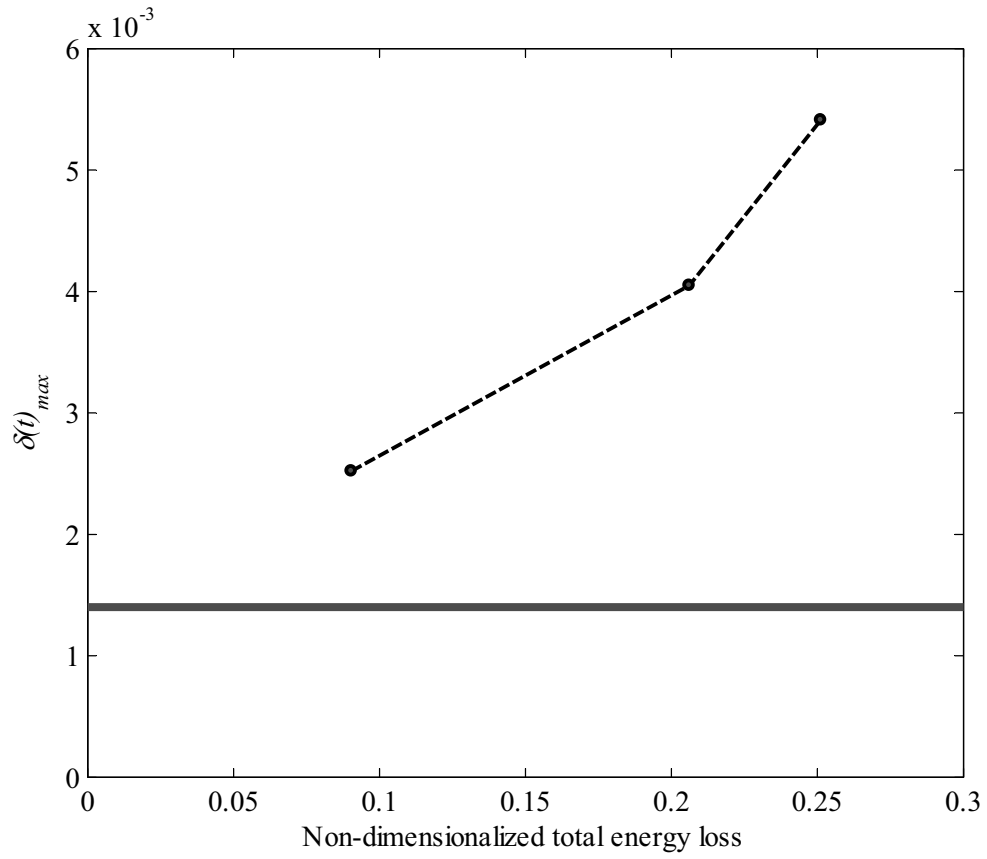


Figure II-16 Non-dimensionalized total energy loss versus breaking parameter, $\delta(t)_{max}$ (determined from experimental measurements), for the three breaking cases. The horizontal region in the figure denotes the threshold range of $\delta(t)$.

6 Conclusions

An experimental and numerical study of the wave breaking criterion proposed by Song and Banner is presented by examining the growth rate of the breaking parameter, $\delta(t)$, constructed from the evolution of the total local energy density and the local wave number at the maximum surface displacement of wave groups. It is found that the breaking criterion of Song and Banner is sensitive to the choice of the local wave number, but that a particular local wave number based on local wave geometry distinguishes wave groups leading to breaking from wave groups that do not break.

The breaking/non-breaking wave generation technique used in the experiments is capable of producing wave groups with reasonable spatial and temporal repeatability. The repeatability of the generated wave groups enables us to divide the spatial domain into smaller sub regions, each of which can be measured individually. Measurements from different runs are combined to obtain the surface elevation spatial profile during the final stages of breaking. Error analysis showed that the measurement technique can provide reasonable precision.

Local wave number computation based on both the Hilbert transform and the local wave profile is discussed; using one of the wavenumber construction techniques and the local wave profile in conjunction with the Song and Banner parameter produced reliable wave breaking predictions for our wave groups. Ratios of local potential energy to local total energy at crest maxima and trough maxima are obtained based on numerical simulations. The ratios at crest maxima decrease as the wave groups focus, while there is little

variation of the ratios at trough maxima. Local energy at wave maxima for the experimental study is inferred based on numerical simulations.

For the criterion based on local wave geometry, measured surface profiles just prior to incipient breaking are used to determine the local wave steepness. Results show that the wave steepness criterion is unable to differentiate wave breaking from non-breaking for our wave groups. For Song and Banner's criterion, experimental results illustrate that the energy convergence rate at the maxima increases, and that the corresponding wave geometry steepens. The breaking parameter, $\delta(t)$, constructed from the energy convergence rate and the local wave geometry decreases after it achieves a maximum, which is smaller than the threshold for non breaking waves; on the other hand, the parameter continues growing once it surpasses the threshold for breaking conditions.

It is shown that the lead time between the parameter exceeding the threshold and incipient wave breaking increases as wave breaking intensifies. The total energy loss is related strongly to this parameter immediately prior to breaking. A similar relationship exists between the total energy loss and the value of the breaking parameter just prior to wave breaking.

Appendix

Figure II-17 provides the evolution of k_{g3} and k_{g6} (as in Figure II-10 in the text, the evolution is also from the maximum surface displacement). Along with Figure II-10, it is obvious that the three k_g 's behave similarly to $t/T=70$, after which their evolutions change; the variation of k_{g1} is less than that of k_{g3} and k_{g6} . Careful inspection of the wave profiles reveals that a considerable short wave perturbation occurs just above or below the mean water level after $t/T=70$.

When k_{g6} and k_{g3} rather than k_{g1} are adopted to compute the local wave number, the resulting breaking parameter $\mu(t)$ shows larger time fluctuations, and hence, the resulting breaking criterion parameter does not differentiate breaking waves from nonbreaking ones via Song and Banner's criterion. One possible explanation for this is that not all components of k_{g6} and k_{g3} represent the local character of the geometry, and thus the resulting breaking parameter does not represent the physics.

To test the breaking criterion using the local wave number based on the Hilbert transform, δ_{max} is computed with k_h for both the non-breaking and breaking cases and the numerical results are shown in Table II-3. Since k_h is in general greater than k_g , δ_{max} for the non-breaking case is much larger than the threshold value of Song and Banner²¹, and almost one order of magnitude larger than the one determined with k_{g1} (see Table II-2) for the same wave group. For the three breaking cases, the determined δ_{max} are surprisingly close to each other, which means that the parameter obtained with k_h is not a good indicator of the breaking strength. Noticing the significant difference in δ_{max} between the nonbreaking and breaking wave trains, we suspect that a proper threshold for

δ , other than $\delta_c=(1.4 \pm 0.1) \times 10^{-3}$, may be valid for our wave groups if the local wave number is determined with the Hilbert transform without any artificial filtering.

Table II-3 δ_{max} determined with k_h and the numerical results.

Gain	900	1265	1690	2020
$\delta_{max} \times 10^3$	5.20	22.07	21.84	22.18

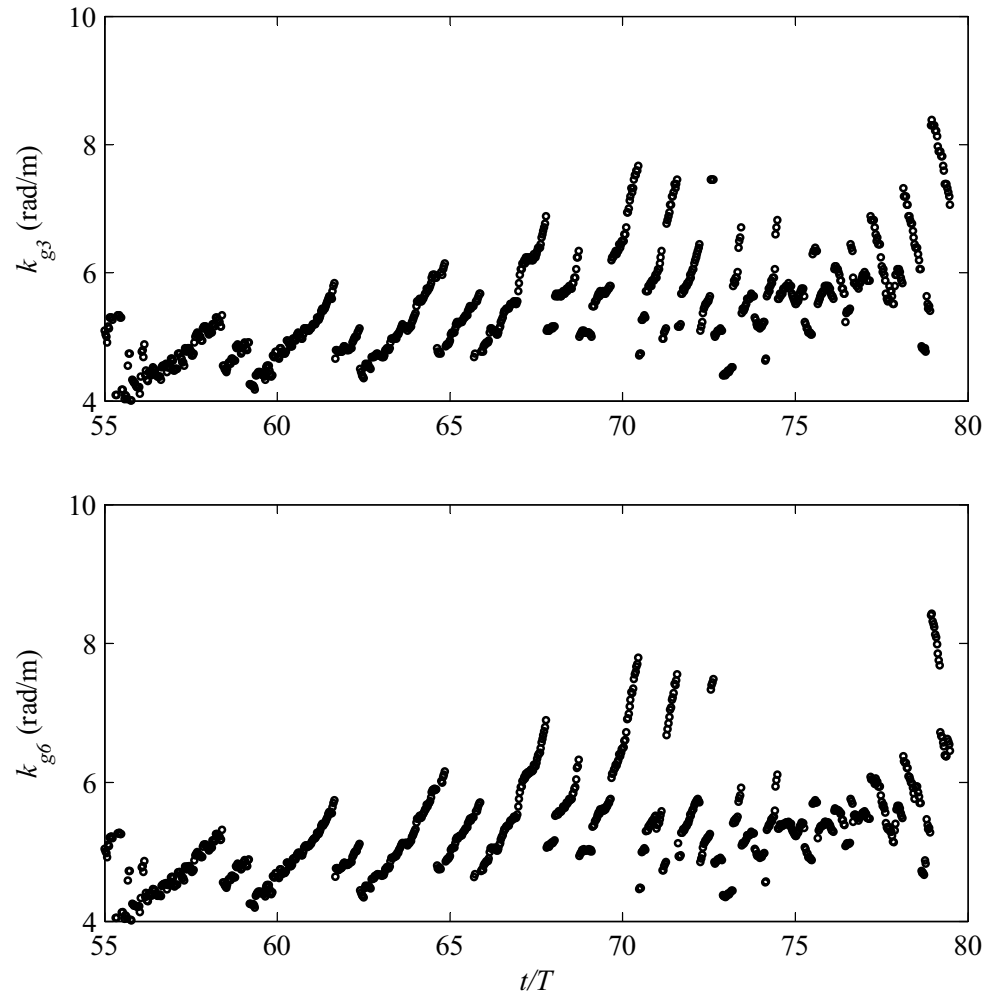


Figure II-17 Same as Figure II-10 but for k_{g3} and k_{g6} . See Figure II-9 for definitions of k_{g3} and k_{g6} .

References

- [1] H. M. Nepf, C. H. Wu and E. S. Chan, "A comparison of two- and three-dimensional wave breaking," *J. Phys. Oceanog.* 28, 1496 (1998).
- [2] C. H. Wu and H. M. Nepf, "Breaking criteria and energy losses for three-dimensional wave breaking," *J. Geophys. Res.* 107(C10), 3177 (2002).
- [3] M. Perlin, J. H. He and L. P. Bernal, "An experimental study of deep water plunging breakers," *Phys. Fluids* 8(9), 236 (1996).
- [4] K. A. Chang and P. L. F. Liu, Velocity, acceleration and vorticity under a breaking wave, *Phys. Fluids* 10, 327 (1998).
- [5] P. Stansell and C. MacFarlane, "Experimental investigation of wave breaking criteria based on wave phase speeds," *J. Phys. Oceanog.* 32(5), 1269 (2002).
- [6] S. H. Oh, N. Mizutani, K. D. Suh and N. Hashimoto, "Experimental investigation of breaking criteria of deepwater wind waves under strong wind action," *Appl. Ocean Res.* 27, 235 (2005).
- [7] G. G. Stokes, "Supplement to a paper on the theory of oscillatory waves," *Math. Phys. Papers* 1, 314 (1880).
- [8] J. H. Duncan, "An experimental investigation of breaking waves produced by a towed hydrofoil," *Proc. R. Soc. London, Ser. A* 377, 331(1981).
- [9] M. Tanaka, "The stability of steep gravity waves," *J. Phys. Soc. Jpn.* 52, 3047 (1983).
- [10] S. E. Ramberg and O. M. Griffin, "Laboratory study of steep and breaking deep water waves," *J. Water. Port Coastal Ocean Eng.* 113, 493 (1987).
- [11] W. K. Melville, "The instability and breaking of deep-water waves," *J. Fluid Mech.* 115, 163 (1982).
- [12] K. She, C. A. Greated and W. J. Easson, "Experimental study of three dimensional wave breaking," *J. Water. Port Coastal Ocean Eng.* 120(1), 20 (1994).
- [13] Yao and C. H. Wu, "Incipient breaking of unsteady waves on sheared currents," *Phys. Fluids* 17(8), 08210 (2005).
- [14] R. J. Rapp and W. K. Melville, "Laboratory measurements of deep water breaking waves." *Philos. Trans. R. Soc. London Ser. A* 331, 735 (1990).
- [15] J. Chaplin, "On frequency-focusing unidirectional waves," *Int. J. Offshore Polar Eng.* 6(2), 131 (1996).

- [16] J. H. L Kway, Y. S. Loh and E. S. Chan, "Laboratory study of deep water breaking waves," *Ocean Eng.* 25(8), 657 (1998).
- [17] S. P. Kjeldsen and D. Myrhaug, "Wave-wave and wave-current interactions in deep water," *Proc.5th POAC Conference, Trondheim, Norway, Vol. III*, 179 (1979).
- [18] W. W. Schultz, J. Huh and O. M. Griffin, "Potential energy in steep and breaking waves," *J. Fluid Mech.* 278, 201 (1994).
- [19] M. L. Banner and X. Tian, "On the determination of the onset of wave breaking for modulating surface gravity water waves," *J. Fluid Mech.* 367, 107(1998).
- [20] J. W. Dold, "An efficient surface-integral algorithm applied to unsteady gravity waves," *J. Comp. Phys.* 103, 90 (1992).
- [21] J. B. Song and M. L. Banner, "On determining the onset and strength of breaking for deep water waves. Part I: Unforced irrotational wave groups," *J. Phys. Oceanog.* 32, 2541 (2002).
- [22] M. L. Banner and J. B. Song, "On determining the onset and strength of breaking for deep water waves. Part II: Influence of wind forcing and surface shear," *J. Phys. Oceanog.* 32, 2559 (2002).
- [23] M. L. Banner and W. L. Peirson, "Wave breaking onset and strength for two-dimensional deep water wave groups," *J. Fluid Mech.* 585, 93 (2007).
- [24] B. J. West, K. A. Brueckner, R. S. Janda, D. M. Milder and R. L. Milton, "A new numerical method for Surface Hydrodynamics," *J. Geophys. Res.*, 92, 11803 (1987).
- [25] W. Choi, "Nonlinear evolution equations for two-dimensional surface waves in a fluid of finite depth," *J. Fluid Mech.* 295, 381 (1995).
- [26] W. Choi, C. P. Kent and C. Schillinger, Numerical modeling of nonlinear surface waves and its validation," *Advances in Engineering Mechanics*, 94, World Scientific (2005).

Chapter III

Energy Dissipation in Two-Dimensional Unsteady Plunging Breakers and an Eddy Viscosity Model

Abstract

An experimental study of energy dissipation in two-dimensional unsteady plunging breakers and an eddy viscosity model to simulate the dissipation due to wave breaking are reported. Measured wave surface elevations are used to examine the characteristic time and length scales associated with wave groups and local breaking waves, and to estimate and parameterize the energy dissipation and dissipation rate due to wave breaking. Numerical tests using the eddy viscosity model are performed and we find that the numerical results capture well the measured energy loss.

In our experiments, three sets of characteristic time and length scales are defined and obtained: global scales associated with the wave groups, local scales immediately prior to breaking onset, and post-breaking scales. Correlations among these time and length scales are demonstrated, which to the best of our knowledge, have not been reported before. Measured surface elevations are used to estimate the total energy and the energy loss due to wave breaking. The total energy and the energy loss are non-dimensionalized with the characteristic scales and we find that they scale well with the global and local

wave steepnesses. In addition, for our wave groups, wave breaking onset predictions using the global and local wave steepnesses are found based on experimental results. The universality of these predictions for wave breaking requires further study.

Breaking time and breaking horizontal-length scales are defined, and they are determined with high-speed imaging. The time and length scales depend approximately linearly on the local wave steepness. The two scales are then used to determine the horizontal breaking-wave crest speed and the energy dissipation rate, which is the ratio of the energy loss to the breaking time scale. The dissipation rate is parameterized with the wave characteristics of local breaking waves; the resulting normalized dissipation rate is on the order of 10^{-3} . In general this is consistent with previous results, subject to proper data interpretation, but is one to two orders of magnitude greater than field measurements. Our experimental results show that the local wave steepness is correlated highly with the measured dissipation rate, indicating that the local wave steepness may serve as a good wave-breaking-strength indicator.

To simulate the energy dissipation due to wave breaking, a simple eddy viscosity model is proposed and validated with our experimental measurements. Under the small viscosity assumption, the leading-order viscous effect is incorporated into the free surface boundary conditions. Then, the kinematic viscosity is replaced with an eddy viscosity to account for energy loss. The breaking time and length scales, which depend weakly on wave breaking strength, are applied to evaluate the magnitude of the eddy viscosity using dimensional analysis. In addition, the value of eddy viscosity is assessed through a turbulence energy dissipation rate analysis, which provides estimations very close to those of the first method. The estimated eddy viscosity is on the order of $10^{-3} \text{ (m}^2\text{s}^{-1}\text{)}$ and

demonstrates a strong dependence on wave breaking strength. Numerical simulations with the eddy viscosity estimation are performed to compare to the experimental results. Both the magnitude and the trend of the total energy measured in the experiments as a function of space are approximated reasonably well by the numerical results. Good agreement as regards energy dissipation due to wave breaking and surface profiles after wave breaking is achieved, which illustrates that the simple eddy viscosity model functions effectively.

1 Introduction

Wave breaking has been of interest since the very beginning of the scientific study of water waves. Due to its significant role in air-sea interaction and its important effects on upper ocean dynamics and possibly climate change, wave breaking has received more and more attention recently. The laboratory study by Rapp and Melville (1990) provided remarkable insight on wave breaking. Banner and Peregrine (1993) presented a comprehensive review of both field measurements and laboratory studies of breaking waves and wave-breaking-associated secondary effects were discussed in their study. Later, Melville (1996) focused on the role of surface-wave breaking in air-sea interaction and presented a thorough discussion on wave breaking dynamics. More recently, Perlin and Schultz (2000) reviewed capillary effects on surface waves and discussed breaking onset and breaking models of forced standing waves. Duncan (2001) provided experimental measurements of the surface profiles of spilling breakers and revealed important kinematics associated with them.

Although extensive research on breaking waves has been reported, the kinematics and dynamics of breaking waves remain an open question. For example, a robust wave breaking criterion remains an enigma; measuring the velocity field during active wave breaking continues to be a formidable challenge; and robust and reliable methods to characterize, quantify, and simulate the energy dissipation due to wave breaking have not been developed yet.

As regards wave breaking criteria, the limiting wave steepness, $ka \approx 0.44$, has been used to indicate wave breaking onset since the study by Stokes (1880). However, this criterion is sensitive to three-dimensional effects (Nepf, Wu and Chan, 1998) and wave directionality (Wu and Nepf, 2002). A second type of wave criterion is based on local wave kinematics and states that wave breaking occurs when the horizontal crest particle velocity exceeds the linear wave phase speed. Particle image velocimetry (PIV) measurements by Perlin, He and Bernal (1996) and Chang and Liu (1998) support this criterion; however, Stansell and MacFarlane's (2002) study demonstrates that wave breaking can occur even when the horizontal crest particle velocity is less than the phase speed. Recently, wave breaking criteria based on local wave energy provided promising results (Schultz, Huh and Griffin, 1994; Banner and Tian, 1998). Particularly, the numerical study by Song and Banner (2002) presents a dimensionless growth rate, $\delta(t)$, based on the local wave energy density and the local wave number to predict the onset of wave breaking. A threshold for $\delta(t)$ of $(1.4 \pm 0.1) \times 10^{-3}$ is proposed to distinguish wave groups that lead to breaking from those that do not. Banner and Peirson (2007) reproduced experimentally the numerical tests by Song and Banner and provided an experimental validation of the criterion. Tian, Perlin and Choi (2008) performed

experimental measurements of wave groups with different group structure than Song and Banner. They found that the criterion is sensitive to the choice of local wave number, but that a particular wave number based on local wave geometry differentiates wave groups that lead to breaking from those that do not.

Measurement of surface profiles and velocity fields associated with wave breaking is very important in understanding wave breaking kinematics and in providing validation of numerical simulations of breaking waves (Longuet-Higgins and Cokelet, 1976; Dommermuth et al., 1988; Skyner, 1996; Grue et al., 2003; Grue and Jensen, 2006). Duncan et al. (1999) managed to capture breaking crest profile histories of gentle spillers with high-speed imaging using a thin laser sheet. The profile histories suggest that the wave breaking process begins with a bulbous formation at the front-face toe of the breaking crest. Further development of the bulge (a moving pressure disturbance) generates capillary waves. Similar parasitic capillary waves were observed previously on the lower front face of plunging breakers by Perlin et al. (1996), who conducted a detailed experimental study on deep-water plungers. Their PIV measurements show that the velocity fields under the breaking crests decay rapidly with depth and that they are essentially irrotational until incipient breaking occurs. Chang and Liu (1998) did similar experiments, but focused on velocity, acceleration, and vorticity measurements. They reported that the overturning jet has a horizontal velocity 68% greater than the linear phase speed and that its acceleration is as high as 1.1g as the jet collapses near perpendicularly to the horizontal water surface. Melville, Veron and White (2002) used digital PIV to measure the velocity field under breaking waves. Their measurements reveal that wave breaking produces at least one coherent vortex, which propagates slowly

downstream and may suppress short waves. Their experimental study also confirms that 90% of the total energy loss occurs within the first four wave periods, consistent with the study by Rapp and Melville (1990). Although these experiments provide valuable measurements of the velocity field prior to and/or after active wave breaking, they were unable to measure the velocity field beneath the breaking crest during active breaking, as the PIV technique is rendered ineffective due to the opacity of the two phase flow and the laser sheet scattering by the entrained bubbles and the free surface.

Estimation of the energy dissipation rate due to wave breaking remains another challenging problem. The most reliable method to estimate the energy dissipation rate requires direct measurement of the velocity field and the surface profile over a fairly large field of view throughout the breaking process, and it has proved impractical for both laboratory and field measurements. Alternatively, one may first estimate the energy loss due to wave breaking with surface elevation measurements and control volume analysis, and then evaluate the dissipation rate with proper breaking time scale. Lowen and Melville (1991) measured the duration of the acoustic sound generated by wave breaking; Melville (1994) applied their measurements to deduce the associated energy dissipation rate. Similarly, Drazen, Melville and Lenain (2008) estimated the energy loss due to plunging breakers and recorded the acoustic sound to infer the breaking time scale, based on which the energy loss rate was assessed. This method assumes implicitly that the dissipation rate is constant throughout the breaking process. However, wave breaking is unsteady (Melville, 1994) and the dissipation rate may not remain constant. As demonstrated by Lamarre and Melville (1991), entraining air into water, that occurs within a small fraction of a wave period, expends 30% to 50% of the energy dissipated;

on the other hand, 90% of the total energy loss is dissipated within the first four wave periods after wave breaking, and the remainder decays as t^{-1} (Rapp and Melville, 1990; Melville et al., 2002). Nevertheless, a large amount of energy is dissipated rapidly over a short period so that a constant dissipation rate assumption may be a reasonable approximation.

Seminal work on characterizing the energy loss rate arose from the experimental work of Duncan (1981, 1983), who measured the drag per unit length due to quasi-steady breaking waves generated with a submerged hydrofoil. His measurements illustrated that the drag per unit width scales with the fourth power of the breaking crest speed: $F_b \sim u_{br}^4$, where u_{br} is the breaking wave crest velocity. Thus, the energy dissipation rate was determined to be $\varepsilon \sim u_{br}^5$ (Phillips, 1985; Thorpe, 1993; Melville, 1994). Recently, Banner and Peirson (2007) rewrote the proportional relation as $\varepsilon = bc_b^5$ with c_b the breaking wave phase speed and b a proportional parameter, which is related to wave breaking strength. They argued that the new proportional relation is consistent with energy and momentum flux transfers while the original one is not.

The proportional parameter, b , in the above relation is considered usually as an indication of wave breaking strength; and hence it is termed the wave breaking strength parameter (Banner and Peirson, 2007; Drazen et al., 2008). Extensive laboratory experiments and field measurements have been conducted to quantify this constant (Duncan, 1981 and 1983; Phillips, 1985; Thorpe, 1993; Melville, 1994; Phillips, Posner and Hansen, 2001; Melville and Matusov, 2002; Banner and Peirson, 2007; Drazen et al., 2008; Gemmrich, Banner and Garret, 2008). However, reported results span two orders of magnitude. In

general, field measurements provide a much smaller estimation than laboratory experiments. This discrepancy remains unresolved (Gemmrich et al., 2008).

A second wave breaking strength parameter, δ_{br} , has been proposed recently by Song and Banner (2002), whose study suggests that the magnitude of the breaking criterion parameter, $\delta(t)$, just prior to wave breaking, indicates wave breaking strength. Banner and Peirson (2007) and Tian et al. (2008) performed experiments and demonstrated that δ_{br} increases as wave breaking intensifies. In addition, an approximately linear relationship between δ_{br} and b is shown in figure 8 (b) of Banner and Peirson (2007).

Along with the difficulties of wave breaking onset prediction, energy dissipation rate estimation, and wave breaking strength quantification, robust numerical studies of breaking waves in deep water are few. One of the first numerical studies of breaking waves was completed by Longuet-Higgins and Cokelet (1976) using the boundary integral method (BIM). Their computation was successful to wave-crest overturning, but as expected failed when the overturning jet collapsed on the water surface. The success of the volume of fluid method (VoF) provides an alternative way to simulate wave breaking. Chen et al. (1999) used the VoF method to simulate a two-dimensional plunging breaker. Their numerical study captured key kinematic characteristics of wave breaking, including the overturning motion, the gas entrainment and the surface splash-up phenomena. In addition, 80% of the pre-breaking energy was dissipated within the first three wave periods following breaking. More recently, Sullivan, McWilliams and Melville (2004) developed a stochastic wave breaking model based on laboratory experiments and field measurements, and employed direct numerical simulation (DNS) to evaluate the model with an isolated breaking event to estimate wave breaking effects on the ocean surface

boundary layer. With the breaker model, they reproduced some key dynamic features of a breaking event, such as the mean kinetic energy decay rate and the coherent vortex structure (Melville et al., 2002).

In this study, we have no intention of developing or using complicated numerical models of wave breaking to model the breaking process; rather, we apply a simple eddy viscosity model to simulate energy dissipation in two-dimensional unsteady plunging breakers. In addition, detailed experiments are performed to: determine wave characteristics associated with wave groups and local breaking waves; further validate the wave breaking criterion of Song and Banner (2002); measure the time and length scales of active wave breaking; estimate the energy dissipation and dissipation rate due to breaking waves; quantify the wave breaking strength. The measured time and length scales associated with active wave breaking are used to determine the eddy viscosity using dimensional analysis and/or the turbulence energy dissipation rate analysis according to Melville (1994).

The remainder of the paper is as follows. Subsequent to the Introduction, we describe the experimental setup and surface profile measurements with wave probes and high-speed imaging. Detailed experimental results on breaking-wave time and length scale measurements, energy loss and energy loss rate estimation, and eddy viscosity assessment are provided in section 3. Section 4 presents an eddy viscosity model for weakly damped waves in which the small viscous effect is incorporated into the inviscid free surface boundary conditions; in addition, numerical simulations using the eddy viscosity model to determine energy dissipation due to wave breaking are presented and compared with experimental measurements. The final section presents our conclusions.

2 Experiments

2.1 Facilities

Experiments are performed at the University of Michigan in a two-dimensional wave channel with glass bottom and sidewalls. The tank is 35 m long, 0.7 m wide, and has a water depth as used of 0.62 m. At one end of the wave tank, wave trains are generated with a servo-controlled wedge-type wavemaker and auxiliary electronics. Two stacks of horsehair mats are placed at the downstream end to help damp the incident waves and minimize reflections. A sketch of the facility is presented in Figure III-1.

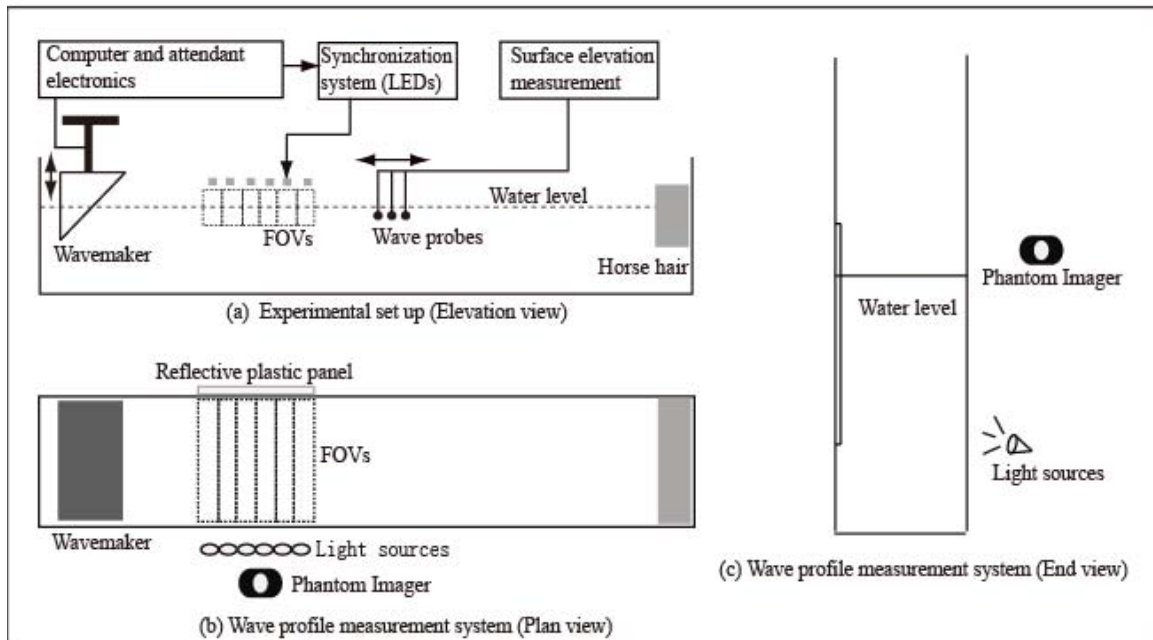


Figure III-1 Sketch of the experimental setup for the surface elevation measurements. FOV indicates field of view. (Not to scale.)

The tank is filled initially with tap water; the water surface is cleaned with a closed-loop system composed of a pump, a reservoir, a filter, and connecting hoses. The system can remove efficiently dirt and floating materials from the water surface. When a complete drain and refill is required, the tank is allowed to equilibrate for about one day prior to any measurements to let the water temperature and/or other uncertain factors (e.g. water aging, Mei, 1983) adjust, thus helping to insure the repeatability of the experiments. The water depth is monitored throughout the experiment and the calm water level variation is limited to less than ± 1 mm.

2.2 Breaking wave generation

Following Perlin et al. (1996) and Tian et al. (2008), a similar technique is employed to produce dispersive focusing wave trains that lead to wave breaking. Individual wave steepness during generation remains virtually constant. As demonstrated by Perlin et al. (1996), this wave train configuration ensures that the phase speed, as well as the local wave steepness of each wave component in the wave group changes accordingly when the gain value (i.e., relative voltage of the signal sent to wavemaker) is altered. This method can minimize the presence of premature breaking. Details on the generation of breaking waves using this technique can be found in Perlin et al. (1996).

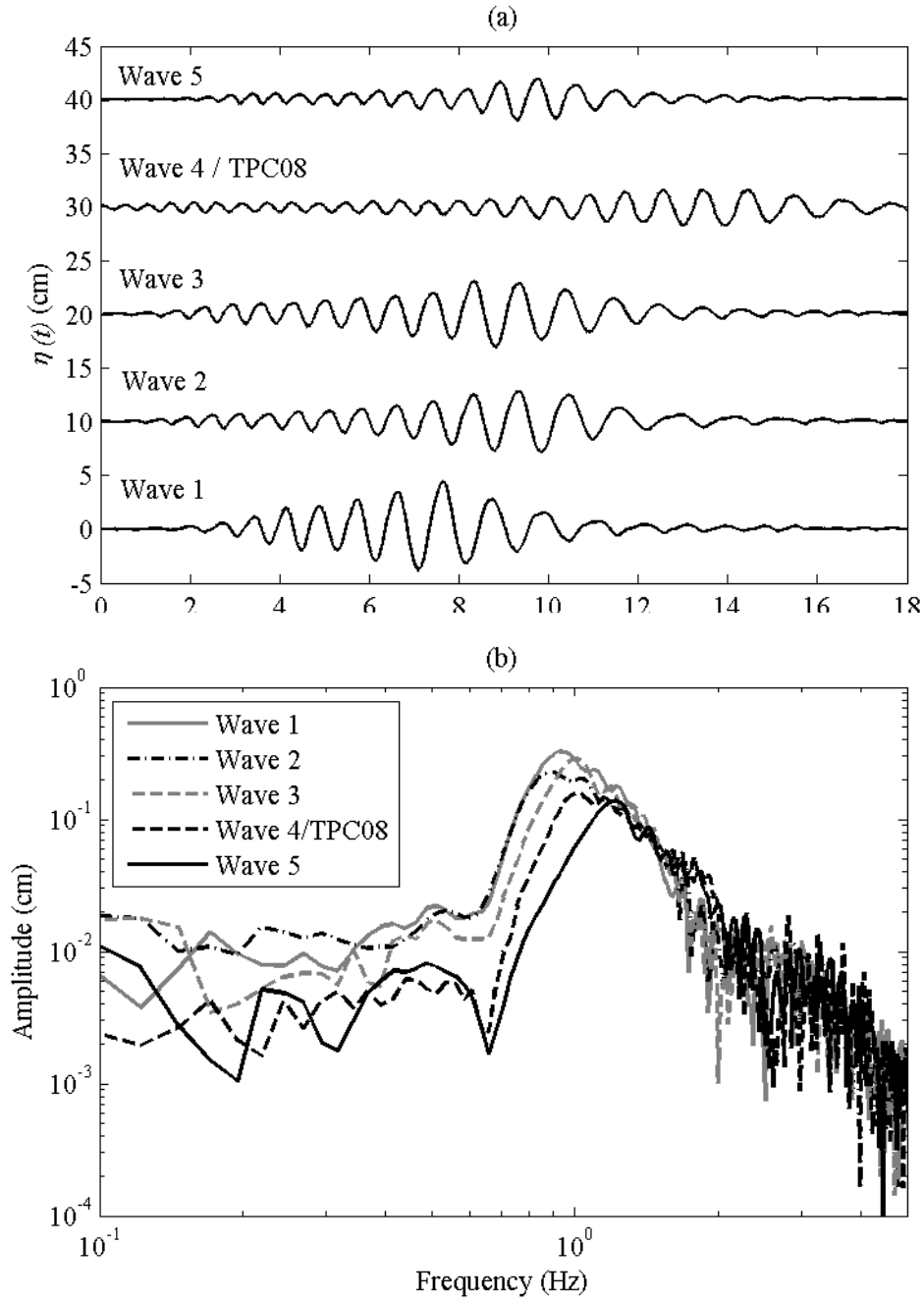


Figure III-2 Shown are the different wave trains of the various groups. In the figure the non-breaking wave groups measured at the first wave station are presented. In (a), for clarity, an increment of 10 cm is applied to separate the measurements vertically. The wave trains have been time shifted so that they can be shown in the same graph. Shown in (b) are the amplitude spectra of the wave groups (computed with a 40.95 s measurement, corresponding to 4096 data points). Four wave trains with varying components are implemented. In addition, measurements of the experiments conducted in Tian et al. (2008) are included.

Figure III-2 provides the different wave train structures. Gains are adjusted for each of the wave trains to lead to both non-breaking (five cases) and breaking waves (12 cases). Detailed wave parameters associated with the wave groups are listed in Table III-1. Measurements of the non-breaking wave groups are used to compute the non-breaking loss due to surface damping, friction on the sidewalls and the bottom of the tank, and contact-line dissipation (Jiang, Perlin and Schultz, 2004), as this non-breaking loss can be important in the determination of energy dissipation (Rapp and Melville, 1990; Banner and Peirson, 2007; Tian et al., 2008; Drazen et al., 2008). While it is simple to generate breaking waves using high gain values, significant effort is necessary to find a proper gain and group structure to generate a wave group that leads to a single breaker. In this paper, most of the wave groups that evolve to breaking are characterized with one single plunging breaker, although in some cases very limited spilling occurs either upstream, or of less importance downstream.

Breaking waves generated with the aforementioned technique demonstrate strong temporal and spatial repeatability (Tian et al., 2008). Observations with high-speed imaging and an accurate synchronization system confirm that the horizontal locations of wave breaking onset vary within only ± 2.5 cm, and that the time is within ± 0.03 s (both better than 0.5%, considering that breaking usually occurs more than 12 m downstream from the wavemaker and more than 20 seconds following the initial motion of the wave maker). A calm water surface (initial condition prior to wave generation) is necessary to achieve the high repeatability; therefore, at least 10 minutes is allowed between experiments to obtain a near quiescent state, which is confirmed also by visual inspection before each test.

2.3 Temporal surface elevation measurements

Capacitance wave probes, transducer power supply, low pass Krohn-Hite filters, National Instruments data acquisition hardware (i.e. PCI-6034e board and SCB-68 connector block), and Dell PCs are used to record the temporal surface elevations at desired stations along the wave tank. Wave probes are composed of two 25 cm long copper wires, one of which is a sensing wire located within a 1.5 mm diameter glass tube and the other is placed directly in the water. Electronic circuits detect the capacitance between the sensing wire and the water. The sampling rate for each probe is chosen as 100Hz in this experiment. The low-pass filters are set at 25Hz. Dynamic calibrations are made before and after each experiment, and are used to convert the measured electric signal to surface elevation. The calibrations confirm that the wave probes exhibit long-term stability. In addition, static calibrations are performed daily to help ensure that no probe malfunction has occurred. To maintain their measurement accuracy, the wave probes are cleaned with alcohol at least twice a day.

An in-line set of three capacitance wave probes are mounted mid-stream (streamwise) from above by a mechanical mount. The distance between adjacent probes is adjustable and is maintained between 30 and 55 cm. Visual inspections confirmed that surface disturbances by the upstream wave probe(s) have little influence on the downstream one(s). Figure III-1 (a) provides an illustration of the arrangement of the wave probes. With accurate repeatability of an experiment, we chose to obtain surface elevation measurements at 33 stations along the tank. For each station, three repeated measurements for each of the wave groups considered are used (i.e. a total of more than 450 runs are achieved). For each measurement, a DC signal synchronized with the initial

motion of the wavemaker is recorded and is utilized to align the measurements in time from other runs.

The first station is located 6.81 m downstream of the mean position of the wavemaker (i.e. the wedge's front face intersection with the water). Unless specified otherwise, the distance x is relative to this mean position, and time t refers to the initial motion of the wavemaker. The surface elevation measurements at the first station are used to generate initial conditions for our numerical simulations (see section 4.2). Based on linear wave theory (LWT), the measurement is decomposed first into 128 Fourier components; then the surface elevation is expressed analytically from a summation of these sinusoidal waves (functions of time and space). Detailed discussions can be found in Tian et al. (2008).

2.4 High-speed imager measurements

Surface profiles prior to and during active wave breaking are captured by a Phantom high-speed imager (Model 9.1), which has a full resolution of 1632×1200 pixels and can capture images to 144k frames per second (fps) with reduced resolution (1,000 fps at full resolution).

Surface profile measurement has been achieved with high-speed cameras and thin laser light sheets in numerous experiments (Perlin, Lin, and Ting, 1993; Perlin, et al., 1996; Duncan et al., 1999; Yao and Wu, 2005). We initially attempted to use a thin laser sheet as an illuminating source for our tests but abandoned it due to two difficulties encountered. First, laser light sheets usually illuminate a small field of view (to ~ 0.5 m)

while our study involves measurement windows of lengths to 1.1 m. Second, laser light sheet illumination can be rendered useless by the opacity of the two-phase flow in active wave breaking.

Bonmarin (1989) managed to capture the breaking surface profile with high power flash lamps and high speed cameras with a field of view of 1 m. On the other hand, Yao and Wu (2005) and Tian et al. (2008) used a backlighting illumination technique to measure surface wave profiles with relatively large field of views.

In this study, we employ a backlighting illumination technique to facilitate the surface profile measurement prior to and during active wave breaking. Figure III-1 (b) and (c) show the experimental setup. Two high intensity light sources (each has a maximum output of 2000 W) are seated 30 cm from the corner of the front sidewall and the tank bottom with their mean beam oriented slightly upward to illuminate the water surface. A reflective and translucent, high-density polyethylene sheet (approximately 6 mm thick) is attached directly to the back sidewall to reflect the light and thus backlight the liquid-gas interface. The imager, equipped with a 28 mm – 80 mm focal length Nikon lens, is positioned about 1.5 m from the front sidewall of the tank with its axis oriented slightly downward for a better image of the field of view (1632×304 pixels), recording at 100 fps. With a precise target of known geometry, the spatial resolution is determined to be 0.683 mm/pixel while the image distortion is shown to be negligible.

Following Tian et al. (2008), a synchronization system of light emitting diodes (LEDs) is used to identify simultaneous recorded images and to temporally align measurements from different field of views. This system functions as follows: A DC signal is generated

and sent to the LEDs to illuminate them at a specific time relative to the initial motion of the wavemaker. The off-on/on-off status of the LEDs is captured with the high-speed imager and applied to determine the start of wave generation. Analysis (Tian et al., 2008) has shown that the system can provide sufficient accuracy for our purpose.

As demonstrated by Tian et al. (2008), this backlighting technique works well for wave surface profile measurement, especially for a large field of view (about 1.1 m long). A few typical images recorded during active wave breaking are presented in Figure III-3. As shown, the water surface is defined clearly (the bright interface) and the mean wave profile during active breaking can be identified easily in the recorded images. We note that the wave profile in the absence of breaking can be tracked readily with brightness and contrast adjustments and a MATLAB program; however, when active breaking occurs, the mean profile is extracted manually as a necessity.

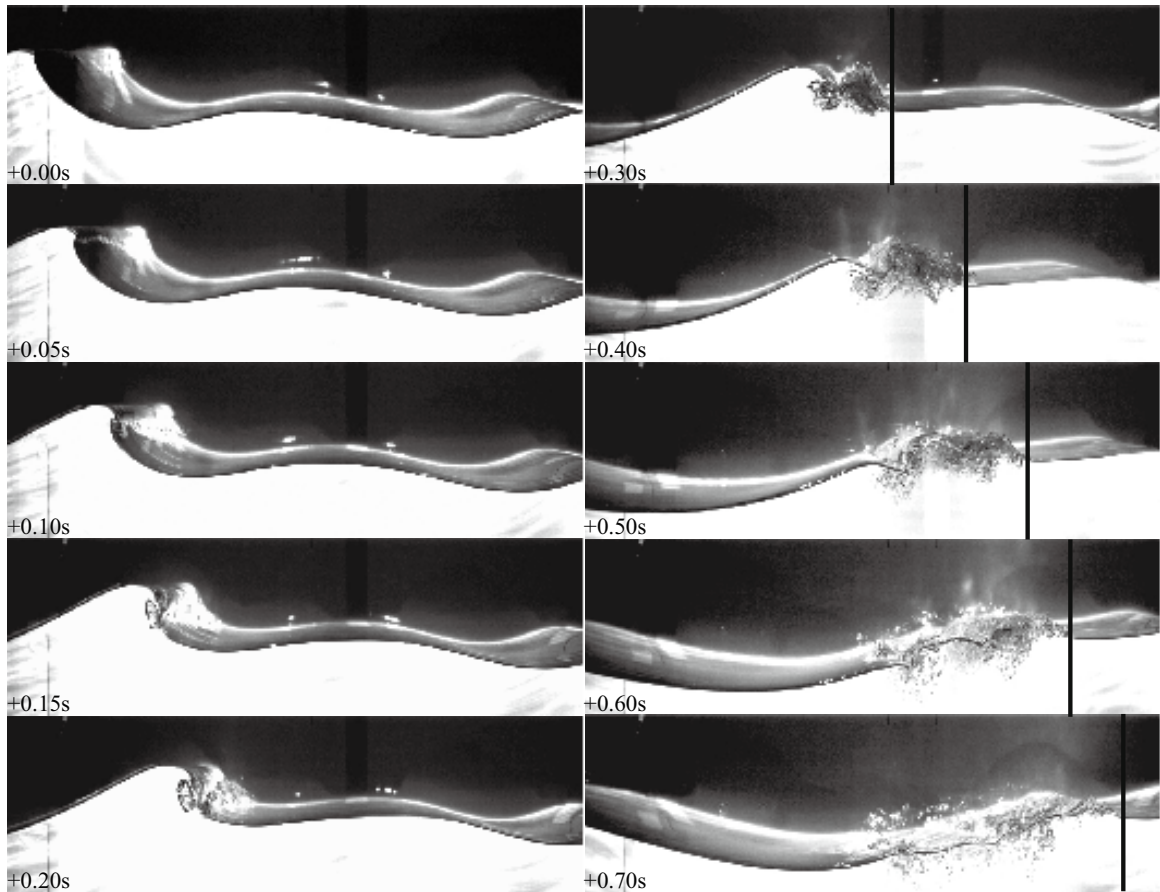


Figure III-3 Recorded surface profiles during active wave breaking for W4G3. The time sequence is referenced to the first image in the top left photograph. The vertical black bars on the images represent the horizontal location of the surface disturbance front, which is used to define the active breaking time and length scales (see section 3.3.1)

3 Experimental results

3.1 Characteristic wave parameters

Described below are details on the determination of wave parameters associated with the wave groups and the breaking waves, such as characteristic group velocity; characteristic wave frequencies and wave numbers; global wave steepness; local breaking wave characteristics; breaking criterion parameter. Unless otherwise noted, most of the wave characteristics associated with the wave group (rather than the wave characteristics associated with wave breaking) are determined from surface elevation measured at the first wave station. Table III-1 summarizes these characteristic parameters of the wave groups considered in this study.

3.1.1 Characteristic group velocity

It is essential to estimate accurately the characteristic group velocity to compute energy loss from wave probe measurements (Drazen et al., 2008). The linear group velocity associated with the center wave frequency in a wave group is used frequently for this purpose. However, in wave groups with constant wave steepness distribution, wave components with low frequencies have more energy than those with high frequencies. Hence, one may expect that a weighted group velocity rather than a center frequency group velocity may better characterize the wave group.

Table III-1 Summary of the primary wave parameters. f_p : peak wave frequency; Δf : frequency bandwidth based on one-half the maximum energy associated frequencies; S : global wave steepness; C_{gs} : spectrally-weighted group velocity; f_s : spectrally-weighted wave frequency; k_s : spectrally-weighted wave number; E_0 : total energy just prior to wave breaking; ΔE : energy loss due to wave breaking; δ_{max} : maximum wave breaking criterion parameter, $\delta(t)$, for non-breaking wave groups; $\delta(t)$ immediately prior to breaking for breaking wave groups; k_b local wave number just prior to wave breaking; c_b : breaking wave phase speed; t_{br} : breaking time scale; l_{br} : breaking horizontal length scale; h : falling wave crest/jet height (breaking vertical length scale); b_b : breaking strength parameter; v_{eddy} : estimated eddy viscosity with (3.6).

Wave group	Wave ID	f_p (Hz)	$\Delta f/f_p$	S	C_{gs} (ms ⁻¹)	f_z (Hz)	k_z (radm ⁻¹)	E_0 (Jm ⁻¹)	$\Delta E/E_0$	δ_{max} or $\delta_b \times 10^3$	k_b (radm ⁻¹)	c_b (ms ⁻¹)	t_{br} (s)	l_{br} (m)	h (m)	$b_b \times 10^3$	$v_{eddy} \times 10^3$ (m ² s ⁻¹)
W1	W1G1			0.315	0.85	1.019	4.223	—	—	1.08	—	—	—	—	—	—	—
	W1G2	0.952	0.307	0.381	0.84	1.022	4.247	29.91	0.101	3.39	5.347	1.35	1.11	1.28	0.044	5.91	1.011
	W1G3			0.463	0.84	1.026	4.279	41.62	0.154	6.23	5.878	1.29	1.18	1.30	0.055	14.83	1.196
	W2G1			0.268	0.86	1.024	4.263	—	—	0.9	—	—	—	—	—	—	—
W2	W2G2			0.346	0.86	1.021	4.239	21.50	0.084	3.43	5.464	1.34	0.91	1.04	0.038	4.52	0.855
	W2G3	0.903	0.351	0.413	0.86	1.023	4.255	30.57	0.122	6.09	6.283	1.25	0.99	1.05	0.055	12.15	1.174
	W2G4			0.468	0.86	1.025	4.271	38.94	0.184	6.7	6.203	1.26	1.07	1.19	0.075	20.94	1.651
	W3G1			0.293	0.79	1.073	4.662	—	—	1.19	—	—	—	—	—	—	—
W3	W3G2			0.356	0.79	1.073	4.662	18.96	0.088	4.14	5.643	1.32	0.95	1.03	0.032	4.36	0.706
	W3G3	1.025	0.214	0.442	0.78	1.080	4.721	28.37	0.129	5.76	6.315	1.25	1.00	1.08	0.052	11.94	1.122
	W3G4			0.497	0.78	1.082	4.738	35.16	0.168	6.32	5.911	1.29	1.08	1.15	0.070	15.17	1.499
	W4G1			0.277	0.71	1.192	5.727	—	—	0.77	—	—	—	—	—	—	—
W4/ TPC08	W4G2			0.393	0.71	1.192	5.727	12.32	0.090	3.17	5.502	1.33	0.59	0.55	0.033	4.36	0.615
	W4G3	1.025	0.381	0.544	0.71	1.201	5.813	21.56	0.206	5.06	6.491	1.23	1.08	1.03	0.054	14.4	1.027
	W4G4			0.669	0.70	1.210	5.900	31.20	0.251	6.71	6.670	1.21	1.36	1.43	0.059	21.58	1.234
	W5G1			0.263	0.66	1.282	6.618	—	—	0.54	—	—	—	—	—	—	—
W5	W5G2	1.245	0.196	0.483	0.64	1.295	6.752	10.52	0.186	4.93	7.805	1.12	1.01	0.88	0.031	10.75	0.549

Drazen et al. (2008) defined a *spectrally-weighted group velocity*, C_{gs} , as

$$C_{gs} = \frac{\sum (C_{gn} a_n^2)(\Delta f)_n}{\sum (a_n^2)(\Delta f)_n}, \quad (3.1)$$

and demonstrated that wave trains propagated at a speed close to this characteristic group velocity. In (3.1), a_n and C_{gn} are the amplitude and linear group velocity of the n th component of the wave train, respectively; $(\Delta f)_n$ is the frequency difference between components, which is constant here. We note that in the spectral weighting a_n^2 rather than a_n is used based on an energy argument (i.e. group velocity is the speed of wave energy propagation and a_n^2 is proportional to wave energy).

To evaluate the effectiveness of this spectrally-weighted group velocity, C_{gs} , we measured experimentally the group velocity by tracking the wave group maxima. To achieve this, Hilbert analysis is applied to the surface elevation measurements to determine their envelopes, and then the maxima are identified. As can be seen in figure 4, compared with the speed of the wave group maxima, the spectrally-weighted group velocity, C_{gs} , appears to be slightly smaller. A nonlinear correction to the group velocity (see Appendix A) is added to C_{gn} , but is found to be too small to appreciably change C_{gs} . Notice that C_{gs} remains virtually constant for wave groups with the same input time series but different gains, as shown in Table III-1. This indicates that the discrepancy should be explained by the nonlinear interaction between different wave components rather than the nonlinear correction to the linear group velocity of each wave component. Despite this small discrepancy, as shown in Figure III-4, the spectrally-weighted group velocity, C_{gs} ,

indeed provides a good prediction of the wave group propagation speed; on the other hand, the group velocity associated with the center wave frequency that has been often used in the literature provides a significantly smaller and worse prediction, which is consistent with Drazen et al. (2008). The group velocity associated with the peak frequency is an alternative, but C_{gs} can be computed more consistently without ambiguity.

We note further that the spectrally-weighted group velocity obtained with surface elevation measurements at different wave stations along the tank remains virtually constant for non-breaking wave groups. For breaking wave groups, observations made upstream and downstream of wave breaking exhibit a jump and about a 5% to 10% increase in the spectrally-weighted group velocity after wave breaking is observed. This increase is caused possibly by the spectral change due to wave breaking, which often dissipates energy in high frequency wave components (Rapp and Melville, 1990; Kway, Loh and Chan, 1998) and may introduce a frequency downshift (Lake et al., 1977; Melville, 1982; Hara & Mei, 1991; Trulsen & Dysthe, 1997; Dias and Kharif, 1999; Tulin and Waseda, 1999). On the other hand, this jump is not reported by Drazen et al. (2008), who argued that their spectrally-weighted group velocity remains unchanged within their experimental accuracy.

To remain consistent with other wave characteristics employed in our study, we use the spectrally-weighted group velocity computed at the first wave station to estimate the total energy and total energy loss due to wave breaking. By doing so, the energy loss and energy loss rate are likely overestimated.

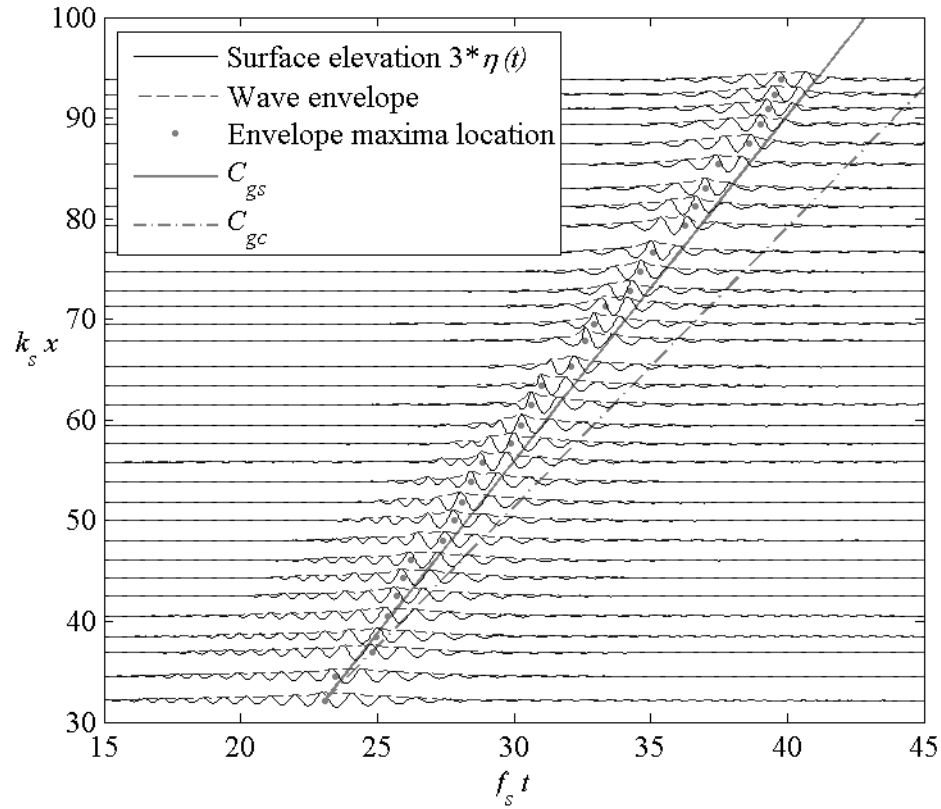


Figure III-4 Measured time series of surface elevation (W3G3, see Table III-1 for designations) at various spatial locations. This graph demonstrates that the wave group propagates closer to the spectral weighted group velocity, C_{gs} (solid line); the group velocity associated with the center wave frequency, C_{gc} (dash line), significantly underestimates wave group travel speed. f_s and k_s are the characteristic wave frequency and wave number, respectively, as shown in table 1. For clarity the surface elevation is exaggerated by a factor of three (i.e. $3*\eta(t)$ is shown. The spatial locations, $k_s x$, remain its original scale on the vertical axis) as shown in Table III-1. For clarity the surface elevation is exaggerated by a factor of three (i.e. $3* \eta(t)$ is shown. The spatial locations, $k_s x$, remain its original scale on the vertical axis).

3.1.2 Wave characteristics associated with the wave group

We now discuss the characteristic wave parameters (i.e. the characteristic wave frequency and wave number) associated with our wave groups. The options we used to determine the characteristic wave frequency are: (1) the center frequency, (2) the peak frequency, and (3) a spectrally weighted frequency defined in a similar manner as C_{gs} . Among these three trial candidates, the *spectrally-weighted wave frequency* defined by

$$f_s = \frac{\sum (f_n a_n^2) (\Delta f)_n}{\sum (a_n^2) (\Delta f)_n} \quad (3.2)$$

appears to be the best for our wave groups since it provides the best data collapse. In addition, this definition of a characteristic wave frequency is consistent with that of the characteristic group velocity (i.e. both are spectrally weighted).

We note further that the spectrally-weighted wave frequency is close to the frequency associated with the spectrally-weighted group velocity C_{gs} (i.e. the frequency provides a group velocity that equals C_{gs} based on linear wave theory and the finite-water-depth dispersion relation; less than 5% difference for most of the wave groups) and that the latter also produces good collapse of the data. However, to be consistent with the spectral weighting argument (i.e. our wave group's components with low frequencies have more energy than those with high frequencies), the spectrally-weighted wave frequency, f_s , is chosen as our characteristic frequency. The linear finite-water-depth dispersion relation is applied to obtain the corresponding characteristic wave number, k_s and the characteristic wave phase speed c_s , which are termed the *spectrally-weighted wave number* and

spectrally-weighted wave phase speed, respectively. We remark that both f_s and k_s remain virtually constant for wave groups with the same input time series regardless of the gain.

3.1.3 Global wave steepness

A measure of global wave steepness was first proposed by Rapp and Melville (1990) to measure wave breaking strength. In their experimental study, they generated repeatable focusing wave trains with constant amplitude distribution (i.e. a top-hat wave spectrum) to study breaking waves; their study demonstrated that the global wave steepness parameter, $S=k_c \sum a_n$, is correlated strongly with wave breaking strength. Here, a_n is the amplitude of the n th wave component (a total of 32 wave components were specified in their study) and k_c is the wave number associated with the center frequency in their wave group. Subsequent studies (Lowen and Melville, 1991; Melville, 1994; and Drazen et al., 2008) drew similar conclusions, although a different definition, $S=\sum(k_n a_n)$, is used for wave groups with constant wave steepness across their wave amplitude spectra.

In this study, we use the surface elevation measured at the first station and Fourier decomposition to compute S . To be consistent with our analysis of the wave group characteristics, the spectrally-weighted wave number, k_s , rather than the wavenumber associated with the center frequency of the wave group is used in the computation, $S=k_s \sum a_n$. Notice that $\sum a_n$ is the surface elevation at the focusing point according to linear wave theory. Fourier decomposition is applied to the measured signal (windowed for 40.95 s corresponding to 2^{12} points); in fact, this S definition is insensitive to the signal duration as long as all the non-zero surface elevations of the mechanically

generated wave packet are included in the determination of the amplitude spectrum, $a(f)$.

The computed global wave steepnesses for our groups are listed in Table III-1.

In the computation of S as well as the other wave group characteristics (i.e. C_{gs} and f_s), we remark that only Fourier components of frequencies in the range $[0, 10]$ Hz are included. Careful observation of the wave spectra reveals that this frequency range is sufficient to include all meaningful wave components. We further note that all wave group characteristics (i.e. C_{gs} , f_s , and $S = k_s \sum a_n$) remain virtually the same even when all Fourier components are considered. On the other hand, this is not the case for the global wave steepness defined as $S = \sum (k_n a_n)$, for which significant variation is found if higher Fourier components are included.

3.1.4 Local wave characteristics immediately prior to wave breaking

To characterize the energy dissipation rate due to wave breaking, local wave characteristics have to be determined. With the surface profile measured just before wave breaking, we use the *local wave number* definition proposed by Tian et al. (2008), who demonstrated that the wave number, $k_b = \pi/|x_{zd} - x_{zu}|$, based on consecutive zero-up (x_{zu}) and zero-down (x_{zd}) crossing points spanning the maximum surface displacement, satisfied Song and Banner's wave breaking criterion (2002). Since the wave breaking process is unsteady, x_{zu} and x_{zd} are determined from the elevation record when the wave crest front becomes vertical. Four to six observations from repeated experiments are used to minimize error. Then the corresponding angular wave frequency, ω_b , is determined using the linear finite-water-depth dispersion relation. The wave speed defined by $c_b =$

ω_b/k_b (used to estimate the energy dissipation rate due to wave breaking in section 3.3.2) is termed as the *breaking wave phase speed*, c_b . The resulting c_b are listed in Table III-1.

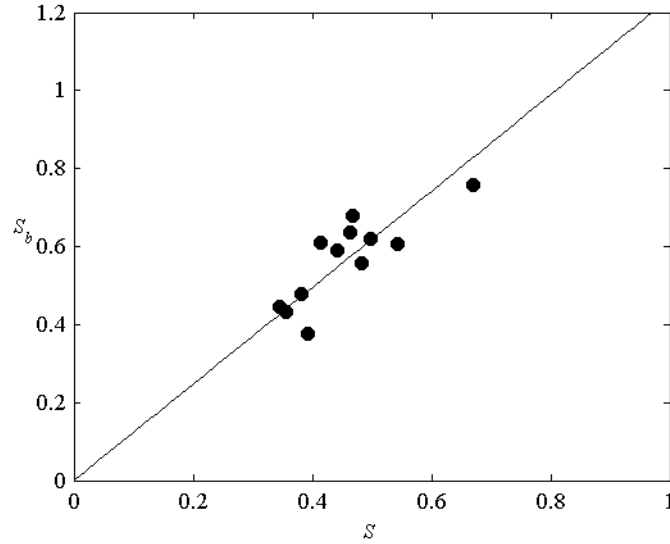


Figure III-5 Global wave steepness, S , versus local wave steepness, S_b . The solid line represents a linear least-squares fit: $S_b = 1.237S$.

We compared the wave characteristics associated with the wave group (i.e. f_s , k_s and c_s) to the local wave characteristics just prior to wave breaking (i.e. f_b , k_b and c_b) to examine the possibility of definite correlations among them. As shown Figure III-5, it is found that the *local wave steepness*, S_b , prior to wave breaking defined by $S_b = k_b \sum a_n$ is roughly a linear function of S . Any data scatter can be attributed to the fact that each wave group has different bandwidth since S_b is expected to be a function of S and bandwidth, although its dependence on bandwidth is found weak (see our discussion in section 3.2.3). For our wave groups, it is found that $S_b = 1.237S$. This implies that a wave group of relatively

large global wave steepness increases in slope immediately before wave breaking occurs, which might lead to more violent wave breaking, resulting in larger energy dissipation. In addition, the local wave speed and the local wave number can be approximated as $c_b/c_s = 0.9 \pm 0.1$ and $k_b/k_s = 1.25 \pm 0.25$, respectively.

3.1.5 Wave breaking criterion parameter

Banner and Peirson (2007) and Tian et al. (2008) reported that their *wave breaking criterion parameter* immediately prior to breaking onset, δ_{br} , is correlated strongly with the wave breaking strength. First, a parameter $\delta(t)$ is defined as $\delta(t) \equiv \frac{1}{\omega_c} \frac{D \langle \mu(t) \rangle}{Dt}$, where ω_c is the center angular wave frequency; $\langle \mu(t) \rangle$ denotes the mean of the upper and lower envelope of $\mu(t)$; and $\mu(t) \equiv [E_{max}/\rho g]k^2$. E_{max} is the local wave energy density at the maximum surface displacement (see Song and Banner, 2002 for details). In this study (including data from Tian et al., 2008), δ_{br} is set to $\delta(t)$ at breaking except that in the calculation of $\delta(t)$, the characteristic wave frequency ($\omega_s = 2\pi f_s$) instead of ω_c is used. This choice reduces data scatter for our experimental measurements. As illustrated in Table III-1 and also in Tian et al. (2008), this parameter with threshold $\delta_c = (1.4 \pm 0.1) \times 10^{-3}$ distinguishes wave groups that lead to wave breaking from those that do not.

It is of interest whether there is any correlation between S_b (or S) and Song and Banner's wave breaking criterion parameter, δ_{br} . Banner and Peirson (2007) made indirect comparisons between S and δ_{br} by correlating both parameters to the total mean energy loss. They found both δ_{br} and S increase in general as the total mean energy loss rises. As

S_b measures the local wave slope and $\mu(t) = S_b^2$, the wave breaking parameter of Song and Banner (2002) can be approximated by

$$\delta_{br} = C S_b^2 \frac{\omega_b}{\omega_s}, \quad (3.3)$$

where $\omega_b = 2\pi f_b$ and C is a proportionality constant. As shown in Figure III-6, (3.3) is indeed a good approximation to δ_{br} and, considering that S_b is linearly correlated with S , the wave breaking parameter δ_{br} can be roughly approximated by $\delta_{br} \sim \omega_b S^2 / \omega_s$. We will further examine the applicability of S_b and δ_{br} and as wave breaking strength indicators and include a detailed discussion in section 3.2.3.

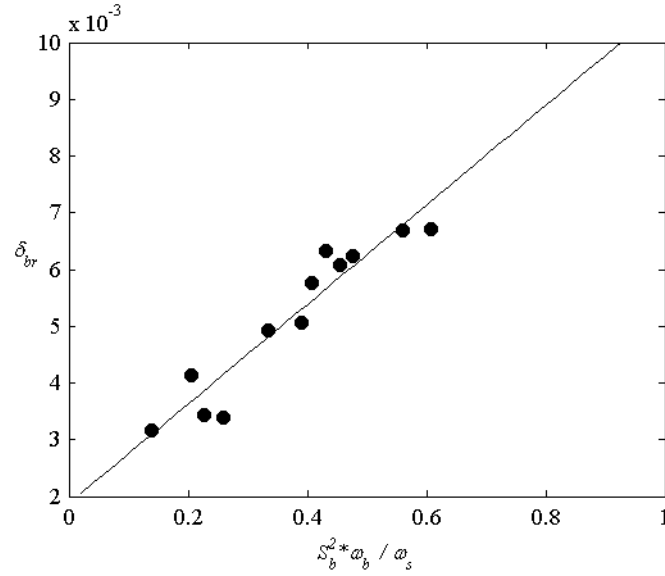


Figure III-6 Correlation between S_b and δ_{br} . The solid line represents a linear least-squares fit and the slope is 8.77×10^{-3} .

3.2 Energy loss

3.2.1 Estimation of total energy

Following Drazen et al. (2008) and Tian et al. (2008), total energy is estimated based on surface elevation measurements. The approximate total energy is obtained by time integration of the linear theory energy flux, $F(x,t)=\rho g C_{gs} \eta^2(x,t)$, at fixed spatial locations. Here, $F(x, t)$ is the energy flux; ρ is the water mass density; g is the gravitational acceleration; C_{gs} is the spectrally-weighted group velocity computed with surface elevation measurements at the first wave station; and $\eta(x,t)$ is the measured surface elevation.

This simplification based on linear theory in estimating the energy flux is valid except where nonlinearity becomes significant (e.g. close to wave breaking or focus points), and it is accurate to the second order, $O[(ka)^2]$ (Rapp and Melville, 1990), where “ a ” is the wave amplitude. Since our measurement is initiated from quiescent conditions (before wave groups arrive) and continues through quiescent conditions (after wave groups pass), the time integration of the energy flux provides the total energy, $E(x) = \langle F(x, t) \rangle$. Here, $E(x)$ is the total energy and $\langle \dots \rangle$ denotes integration with respect to time.

Figure III-7 resents the total energy as a function of position, x . Obvious in the figure are data oscillations superposed on a general decay trend. Similar observations were also made in previous studies, e.g. Rapp and Melville (1990), Kway et al. (1998) and Banner and Peirson (2007), but have not been addressed explicitly. The decrease trend of the total energy as a function of space is due mainly to surface damping, contact-line dissipation (Jiang et al., 2004), friction by tank sidewalls and the bottom, and, most

importantly, wave breaking (for breaking wave groups only). On the other hand, the smaller oscillations in regions far from wave focusing/breaking are due mainly to measurement error; meanwhile, the oscillations in wave focusing/breaking regions (where nonlinearity becomes prominent) may be attributed partially to failure of the linear assumption in estimation of the total energy.

Nevertheless, even for the non-breaking case, a significant decrease of the energy is observed and is due likely to viscous dissipation and contract-line dissipation. Therefore, non-breaking energy loss has to be estimated before energy loss due to wave breaking is computed.

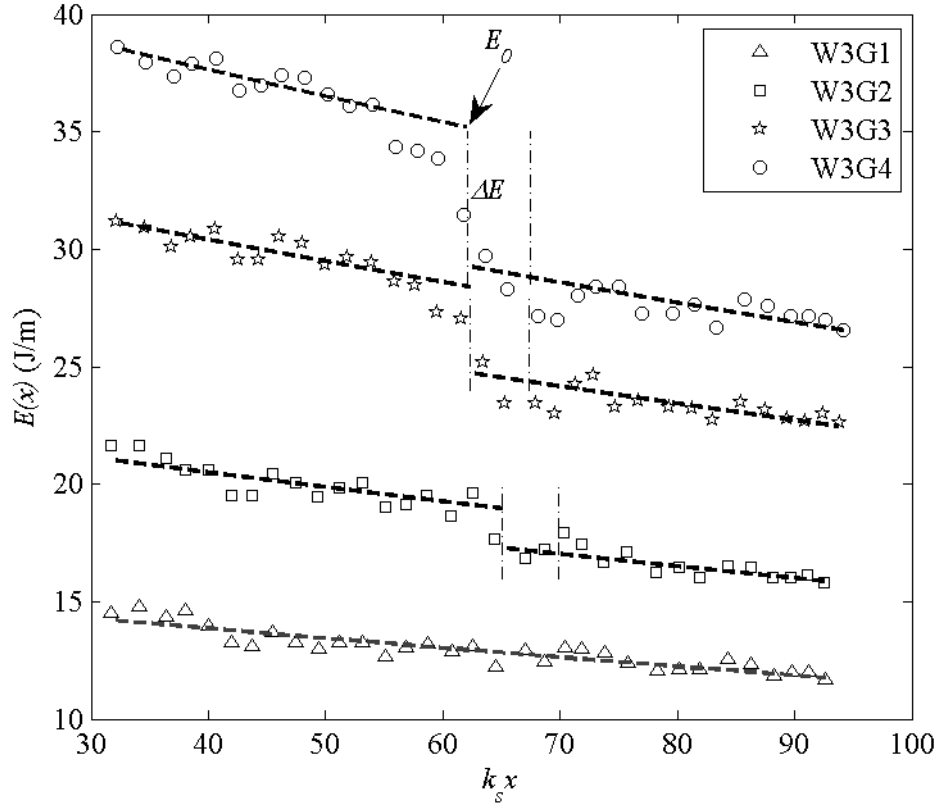


Figure III-7 Estimation of energy loss due to friction, contact-line damping, and wave breaking, shown only for Wave 3. The thick dash lines are the exponential best fits; the vertical dash dot lines denote the active breaking length scale. Non-breaking losses are estimated from the exponential fit of the non-breaking wave measurements (lowest, W3G1). E_0 is the estimated total energy just prior to wave breaking based on the exponential fit; ΔE is the estimated energy loss due to wave breaking, both shown only for W3G4.

3.2.2 Non-breaking energy loss

We assess energy loss due to viscous dissipation and contact-line damping with experimental measurements of non-breaking wave groups and previous theoretical analysis for viscous losses (Lamb, 1932; Mei, 1983; Tulin and Waseda, 1999), which demonstrate that the energy decay rate due to viscosity is exponential, $E = E_{first} \exp(-\sigma x)$. Here, σ is the spatial decay rate due to bulk viscosity and boundary layers in the free surface, sidewalls, and bottom, and E_{first} is the total energy at the first wave probe location.

An exponential best fit in the least squares sense is applied to the measured total energy of the non-breaking case to obtain the decay rate. As shown in Figure III-7, the exponential best fit is close to a straight line. Therefore, the decay may be approximated by a linear decrease (as in figure 15 of Tian et al., 2008) or by a quadratic least-squares best fit (as in figure 6 of Banner and Peirson, 2007) over a short distance. Also visible in the figure is that roughly 15% of the total energy is dissipated in a distance of 10 characteristic wave lengths. Significant energy loss was reported by Banner and Peirson (2007) also, who showed 20% of mean wave energy loss in 37 wave periods. Therefore, viscous energy dissipation is significant and should be taken into account in determining energy loss due to wave breaking.

For the wave groups considered in this study, the exponential decay rate, σ , estimated with the exponential best fit is $O(0.01)$, which is as much as 40% greater than the linear wave theory prediction (Lamb, 1932; Mei, 1983; Tulin and Waseda, 1999). This discrepancy is attributed to the nonlinearity and, more importantly, the highly dissipative

capillary waves and contact lines generated by the water-sidewall interactions (Perlin and Schultz, 2000; Jiang et al., 2004).

3.2.3 Energy loss due to wave breaking

The energy loss due to wave breaking is defined the total energy loss less the non-breaking energy dissipation. First, measurements upstream and downstream of wave breaking are fitted with the dissipation rate of the non-breaking case, respectively, to account for the non-breaking loss. Then, the energy dissipation due to wave breaking is determined from the step change between the upstream and the downstream best fits at the point where wave breaking initiates, as illustrated in Figure III-7. Details can be found in Banner and Peirson (2007) and Tian et al. (2008). We note that the best fits exclude measurements near and in the active breaking region, where total energy estimation using linear wave theory contains considerable error due to strong nonlinearity. An alternative approach to estimate energy loss would be the control volume approach suggested by Rapp and Melville (1990), where the total energy loss can be determined by the difference of total energy fluxes in and out the control volume.

The energy loss due to wave breaking as a function of S and δ_{br} is presented in Figure III-8. When non-dimensionalized by $\rho g/k_s^3$, both the estimated total energy prior to wave breaking, E_0 , and the estimated energy loss due to wave breaking, ΔE , are correlated very well with the global wave steepness, S . Therefore, the normalized energy dissipation ($\Delta E/E_0$) correlates closely with S , as in Figure III-8. The relationship can be approximated well with a linear least-squares fit, as illustrated in the figure. Alternatively, both E_0 and ΔE are well correlated with the local wave steepness, S_b .

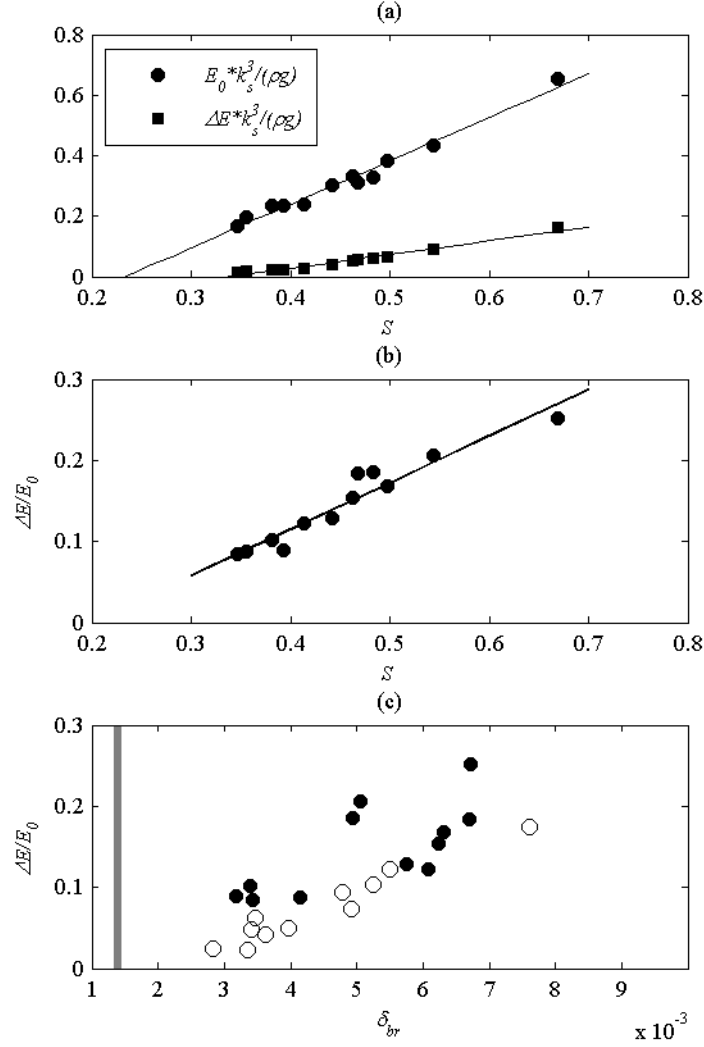


Figure III-8 Normalized energy loss versus S and δ_{br} . Banner and Peirson (2007) data (open symbols in the figure) are reproduced for comparison. The solid lines in (a) and (b) represent linear least-squares fits. The thick vertical line in (c) illustrates the threshold, $\delta_c = (1.4 \pm 0.1) \times 10^{-3}$, for wave breaking onset, as discussed in Song and Banner (2002) and Tian et al. (2008).

Both E_0 and ΔE normalized with respect to $\rho g/k_s^3$ are expected to be functions of S and $\Delta f/f_s$ from dimensional analysis (Drazen et al. 2008, section 2.1), where Δf is the frequency bandwidth associated with one-half the maximum energy wave frequencies, as shown in Table III-1. However, our results indicate that the dependence of the local energy and the energy loss on the bandwidth $\Delta f/f_s$ is weak and will be neglected. The weakness of the effect might be explained by the fact that wave breaking in our experiments is achieved mainly by linear superposition rather than a nonlinear mechanism such as the Benjamin-Feir instability where the bandwidth plays a crucial role.

On the other hand, $\Delta E/E_0$ is not well correlated with δ_{br} , while the normalized energy loss due to wave breaking in general increases with δ_{br} , as shown in Figure III-8(c). A better correlation can be found between $\Delta E/E_0$ and $(\delta_{br}\omega_s/\omega_b)^{1/2}$, which is proportional to S_b , as discussed in section 3.1.5. Our results are somewhat inconsistent with Banner and Peirson's study (2007), in which δ_{br} was shown to have a better correlation with the energy dissipation due to wave breaking. We remark that both S and δ_{br} defined in this study are different than those of Banner and Peirson (2007).

It is worthwhile to make two additional comments regarding figure 8. The first one is regarding the global wave steepness threshold, S_0 , which indicates incipient wave breaking. Our results in Table III-1 show that the threshold resides in the range [0.31, 0.35]. From Figure III-8(a), ΔE can be approximated by $\Delta E / (\rho g/k_s^3) = 0.445(S-0.339)$ and, therefore, S_0 is found roughly to be 0.339 for which $\Delta E = 0$. As described in section 3.1.4, $S_b = 1.237S$ and, therefore, the local wave slope criterion for incipient wave

breaking can be estimated by $(S_b)_0 = 0.419$, which is slightly smaller than the maximum slope of 0.441 for deep water Stokes' waves.

Previously, Rapp and Melville (1990) reported incipient breaking waves are associated with S_0 between 0.22 and 0.25. Banner and Peirson (2007) observed incipient breaking waves with S_0 as small as 0.12, much lower than previously reported even with viscous damping taken into account. (Note that Banner and Peirson (2007) obtained S with measurements just prior to breaking onset, and they reported a mean energy loss of 20% due to viscous damping. This energy loss translates to an amplitude loss around 10%. Therefore, their S could be $\sim 10\%$ larger for their upstream measurements.) In addition, the measurements by Drazen et al. (2008) show that wave breaking does not occur until S becomes approximately 0.3. We remark that this variation in S_0 may be due mainly to different definitions of S and may be related partially to different wave trains (i.e. wave spectrum shape). Although our definition of S predicts well total energy loss due to wave breaking, the applicability of S as a universal indicator of wave breaking onset needs to be further explored due to the variation of S_0 in different laboratory studies. Alternatively, the local wave steepness, S_b , might be a better parameter to understand wave breaking. Although the relationship between S and S_b might depend on particular wave trains, the local wave characteristics prior to breaking might be more universal.

The second issue is the different level of total energy loss due to wave breaking. For a comparable δ_{br} , our energy dissipation level is greater generally than that reported by Banner and Peirson (2007), whose wave groups commonly have multiple spilling breakers. Since our wave groups are essentially single plunging breakers, the discrepancy might be associated with some intrinsic difference between spilling and plunging

breakers. However, a recent study by Drazen et al. (2008, figure 14) demonstrated that spilling and plunging breakers may have the same breaking strength (i.e. b). Regardless, the cause of the discrepancy in energy dissipation is not yet well understood.

3.3 Energy dissipation rate due to wave breaking

3.3.1 Time and horizontal length scales of wave breaking

In this section, we discuss the time and length scales associated with active wave breaking in laboratory studies. These scales will be used to estimate the energy dissipation rate under the assumption that the dissipation rate is constant throughout the breaking process.

Accurate estimation of energy loss rate defined by the energy loss per unit time during wave breaking undoubtedly requires accurate estimation of the dissipation time scale, which should be obtained with detailed velocity field measurements during active wave breaking. However, this measurement proves extremely difficult due to the two-phase flow opacity, bubble scattering in the active breaking crest (Perlin et al., 1996), and the large field of view needed. To our knowledge, the dissipation time scale for energy loss due to active wave breaking based on robust and reliable measurements has not been reported. Information available for the time scale are the measurements by Rapp and Melville (1990), who reported that 90% of the total energy loss occurs within four wave periods after incipient breaking. In addition, based on their numerical study, Chen et al. (1999) reported that 80% of the total energy loss occurred within three wave periods.

In this study, the *breaking time scale*, t_{br} , used to estimate energy loss rate is defined as the time from when the wave crest begins to fall to the end of the obvious surface-disturbance front, the horizontal location of which is represented by the vertical bars in Figure III-3. This definition is in fact fairly subjective; repeated trials show that the variation of the measured time scale is limited to within $\pm 0.02\text{s}$ (i.e. less than 5% considering this time scale is on the order of one second for our wave groups). These time scales are presented in Figure III-9(a). The dissipation time scale is on the order of one characteristic wave period ($2\pi/\omega_b$). For breaking from wave groups with similar spectral shape and phase, the dissipation duration increases as breaking intensifies, or, equivalently, as S_b increases. The trend is consistent with Drazen et al. (2008).

Also shown in Figure III-9 is the *horizontal breaking length scale*, l_{br} , which is defined as the distance from incipient breaking to where the obvious surface disturbance front ends. As seen in (b) of the figure, l_{br} increases as wave breaking intensifies. In the short time, t_{br} , the “whitecap” coverage (l_{br}) can extend as far as one and a half characteristic wavelengths ($2\pi/k_b$) for the most violent breaking while other plunging breakers have length scales around one characteristic wave length, consistent with the dye patch experiments of Rapp and Melville (1990). In general, both t_{br} and l_{br} depend linearly on S_b when they are non-dimensionalized with respect to ω_b and k_b . This indicates that the breaking process is more violent as the local wave slope increases.

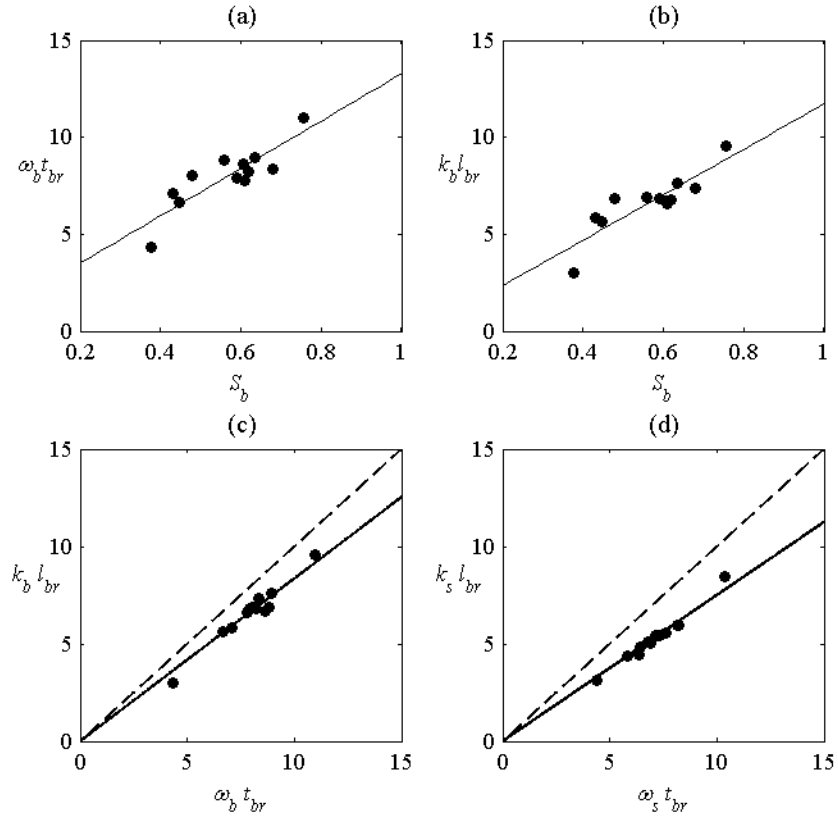


Figure III-9 Time scale t_{br} and length scale l_{br} associated with active wave breaking. ω_b and k_b are the wave frequency and the wave number associated with the breaking wave (see section 3.1.4 for details). ω_s and k_s are the spectrally-weighted wave frequency and wave number. Solid lines represent linear least-squares fits. In (c), the dash line illustrates the characteristic wave speed, c_b , based on local wave number, k_b , measurement; the solid line represents the estimated horizontal breaking crest speed as $u_{br} = 0.836c_b$. And in (d), the dash line represents the characteristic wave speed, c_s , based on the spectrally-weighted wave frequency ω_s ; the solid line represents the estimated horizontal breaking crest speed as $u_{br} = 0.750c_s$.

Since the horizontal length scale, l_{br} , is essentially the distance that the apparent surface-disturbance front travels in t_{br} , the length and the time scales are expected to be related by the *horizontal breaking wave crest speed*, $u_{br} = l_{br} / t_{br}$. Notice that the breaking crest speed is less than the linear phase speed of the breaking wave, c_b defined as $c_b = \omega_b / k_b$ in section 3.1.4. Figure III-9(c) shows our estimations of the breaking crest speed based on observed t_{br} and l_{br} . The estimation of $u_{br} \sim 0.836c_b$, represented by the solid line in the figure generally agrees with Melville and Matusov (2002), but is larger than that reported by Banner and Peirson (2007). It is interesting to note from Figure III-9(d) that u_{br} can be well estimated in terms of the spectrally-weighted wave phase speed as $u_{br} \sim 0.750c_s$.

3.3.2 Rate of energy loss due to wave breaking

Based on dimensional analysis, the *energy dissipation rate*, ε , scales to the fifth power of a characteristic speed, U :

$$\varepsilon = b\rho U^5 / g \quad (3.4)$$

where b is a dimensionless *wave breaking strength parameter* (Melville, 1994; Banner and Peirson, 2007; Drazen et al., 2008; Gemmrich et al., 2008), which might depend on global wave parameters, such as the global wave slope and the bandwidth. This equation relates the kinematics and the dynamics of wave breaking by using a wave breaking strength parameter and is expected to approximate the energy dissipation rate due to

wave breaking in spectral modeling of ocean waves (Phillips, 1985; Phillips et al., 2001; Melville and Matusov, 2002; and Gemmrich et al., 2008).

Both laboratory experiments and field measurements have been conducted to quantify the breaking strength parameter (Duncan, 1981 and 1983; Phillips, 1985; Thorpe, 1993; Melville, 1994; Phillips et al., 2001; Melville and Matusov, 2002; Banner and Peirson, 2007; Drazen et al., 2008; Gemmrich et al., 2008). The reported breaking strength parameter varies over a wide range (more than two orders of magnitudes), and generally, estimation based on field data is much less than that from well-controlled laboratory experiments. The discrepancy remains unresolved (Gemmrich et al., 2008).

It would be beneficial if a universal constant could be found for b , independent of wave parameters, for a particular choice of U , but it is not feasible. It is therefore of interest to find a form of b that correlates well with the characteristic wave parameters. Depending on the choice of the characteristic velocity, different definitions for b have been proposed. For example, Duncan (1981, 1983) used the breaking wave crest velocity, u_{br} , and defined the corresponding wave breaking strength parameter, b_{br} . To facilitate its application to the estimation of the energy-dissipation-rate of a wave spectrum, in which wave speed, c , corresponding to Fourier wave components is employed commonly, Banner and Peirson (2007) proposed to use the breaking wave phase velocity, c_b , for which b_b can be determined. As discussed in section 3.1.4, c_b exhibits an almost linear relationship with the breaking wave crest velocity, $u_{br} \sim 0.836c_b$, and b_b can be estimated as $b_b \sim 0.836^5 b_{br} = 0.408b_{br}$. This is consistent with Banner and Peirson (2007) who showed that b_b is approximately one half of b_{br} .

A straightforward method to evaluate b is based on estimation of total energy loss and direct measurements of the active breaking time (Melville, 1994; Drazen et al., 2008). First, the energy dissipation rate is estimated as $\varepsilon = -\Delta E/t_{br}$. The breaking strength parameter is then evaluated from (3.3) as $b = \varepsilon g/\rho U^5$. This method involves only local wave breaking characteristics (e.g. local energy ‘jump’ and active breaking time) and is adopted here to compute b .

Banner and Peirson (2007, Appendix A) proposed an alternative method to estimate b based on mean energy loss and mean energy propagation (i.e. temporal and spatial transfer), $b = gC_g\Delta[\hat{E}]/c_b^5$. Here, $\Delta[\hat{E}]$ is the mean energy density loss, $[\dots]$ denotes average over a wave group and $\hat{E} = g\eta^2$. This method provides an estimation of b without evaluating the breaking wave time scale t_{br} . We note that application of Banner and Peirson’s (2007) estimation scheme to our breaking waves is somewhat arbitrary as there is ambiguity in choosing the average period to obtain the mean energy loss. Therefore, their method is not adopted here.

Results of our measurements are given in Figure III-10. Obvious in the figure is the strong correlation between S_b and b_b , which implies that the energy dissipation rate increases as the local wave slope increases. As shown in Figure III-10(b), the breaking strength parameter, b_b , is also correlated with δ_{br} , as expected: a larger δ_{br} is associated with a larger dissipation rate, but the correlation between S_b and b_b appears to be stronger than that between δ_{br} and b_b . Figure III-8 and Figure III-10 imply that S_b is a more appropriate parameter to predict both energy loss and energy loss rate due to wave breaking for our wave groups than is δ_{br} . As mentioned before, this is inconsistent with the results of Banner and Peirson (2007), who observed that δ_{br} is a more fundamental

parameter to characterize both energy loss and energy loss rate due to wave breaking for their wave groups. The discrepancy is attributed mainly to different wave groups.

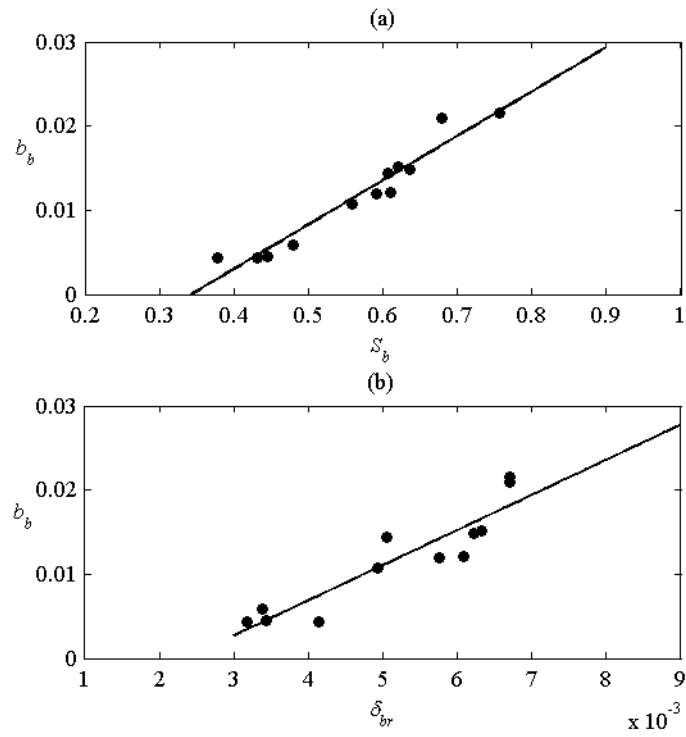


Figure III-10 Normalized energy dissipation rate versus S_b and δ_{br} . Solid lines represent linear least-squares fits.

Our estimated wave breaking strength parameter is the same order of magnitude as Melville (1994), but is about one order of magnitude larger than that of Banner and Peirson (2007). Therefore, proper comparison with the latter requires additional attention to the wave group parameters. Typical lengths of our wave group are $O(10\text{m})$ and characteristic group velocities are $O(1\text{ms}^{-1})$, which reduces our wave breaking strength parameter one order of magnitude if Banner and Peirson's method is used for the calculation. Therefore, our results are generally on the same order of magnitude as Banner and Peirson's (2007), subject to proper data interpretation. In comparison to measurements by Drazen et al. (2008), our energy dissipation rate is about one third to one half of theirs (for a comparable $S - S_0$). This discrepancy is attributed mainly to the relative short time scale used in their estimation. Different wave group structures may also contribute to this disparity.

3.4 Eddy viscosity

It is our intent to model eddy viscosity to determine the energy dissipation due to deep water breaking waves. For simplicity, a constant eddy viscosity is assumed throughout the breaking process. Dimensional analysis served as a simple yet effective way to obtain the proper time and length scales for the eddy viscosity estimation.

For a plunging breaker, we believe that the active breaking time, t_{br} , and the horizontal breaking length, l_{br} , are the proper time and horizontal length scales, respectively. As for the vertical length scale, Rapp and Melville (1990) suggested that the breaking wave penetration depth, D , is comparable with the characteristic length scale of the turbulence

generated by wave breaking; therefore, D may be employed as the vertical length scale in the analysis. Our experiments provide no measurement of the penetration depth. However, the penetration is caused mainly by the falling wave crest/water jet. Therefore, a large falling wave crest/water jet height would introduce a large breaking penetration depth, which is confirmed qualitatively with the high-speed imager in our experiments. Thus the falling wave crest/water jet height, h , as defined in Drazen et al. (2008) is used as the vertical length scale in this analysis.

For the turbulent viscous flow in breaking waves, we assume that the energy dissipation rate can be expressed as in Phillips (1977, section 3.4) with replacing the kinematic viscosity with eddy viscosity, ν_{eddy} , as

$$\frac{dE}{dt} = -\frac{1}{2} \rho \nu_{eddy} \int \left(\frac{\partial u_i}{\partial x_j} + \frac{\partial u_j}{\partial x_i} \right)^2 dA \sim \rho \nu_{eddy} \frac{c_b^2}{h^2} h l_{br}, \quad (3.5)$$

where A represents an area over which large vorticity of $O(c_b^2/h^2)$ is induced by breaking waves and is estimated by $h l_{br}$. When combined with an estimate of dE/dt as $\rho c_b^2 l_{br}^2 / t_{br}$, (3.5) yields the following estimation of eddy viscosity:

$$\nu_{eddy} = \theta h l_{br} / t_{br} \quad (3.6)$$

where θ is a proportionality coefficient and remains to be determined.

Alternatively, the eddy viscosity can be represented by $\nu_{eddy} \sim ul$ (Rapp and Melville, 1990), where u is an integral velocity scale and l is an integral length scale. Based on the

dye patch experiments by Rapp and Melville (1990), the integral length l is roughly comparable with the breaking wave penetration depth. However, as mentioned before, we choose to use the falling wave crest height, h , as the vertical length scale. As for the integral velocity, u , it is considered to be a fraction of the breaking wave phase speed, $u = \chi c_b$ (Melville, 1994), where χ is a numerical constant in the range $[0.1, 0.17]$ in his analysis, depending on the breaking strength (see Appendix C). Then, from $\nu_{eddy} \sim ul$, the eddy viscosity is estimated as

$$\nu_{eddy} = \theta' ul = \theta' \chi c_b h \quad (3.7)$$

where θ' is a proportionality coefficient and remains to be determined. Notice that (3.7) is consistent with (3.6) since l_{br}/t_{br} in (3.6) is the horizontal breaking wave crest speed, u_{br} , which is found in section 3.3.1 as a fraction of the breaking wave phase speed, c_b .

Eddy viscosities associated with different wave groups are estimated using the experimental measurements and (3.6) and (3.7) (the proportionality coefficients in the equations are determined as $\theta = 0.02$ and $\theta' = 0.10$ for our wave groups; see section 4.2 for details). As presented in Figure III-11, the two equations provide similar estimations that are on the order of $10^{-3} \text{m}^2 \text{s}^{-1}$. We remark that the kinematic viscosity of water is $O(10^{-6} \text{m}^2 \text{s}^{-1})$. Also as can be seen in the figure is that the eddy viscosity increases as wave breaking intensifies (i.e. S_b and δ_{br} increase). In the following section, the estimated eddy viscosities are implemented in numerical simulations to model energy dissipation due to wave breaking.

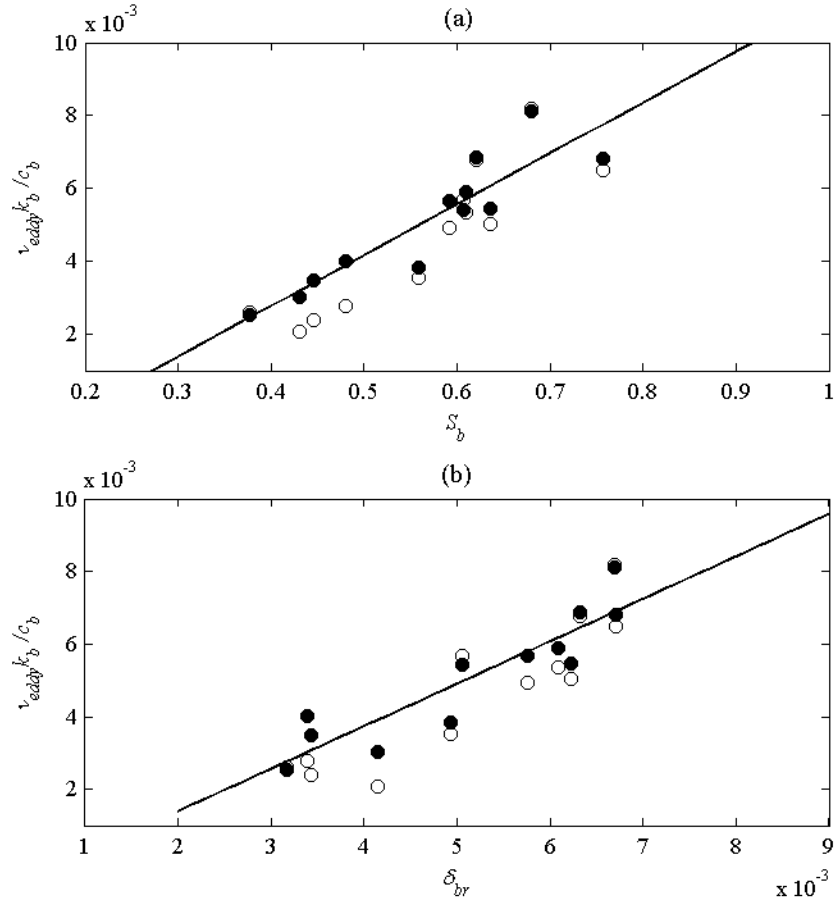


Figure III-11 Eddy viscosity as a function of the wave breaking strength is presented. Solid symbols denote estimations using (3.6) and open symbols using (3.7). The two equations provide estimations close to each other. In this study, estimations with (3.6) are used in the numerical simulations. Solid lines represent linear least-square fits (only estimations with (3.6) are included in the best fits).

4 Eddy viscosity parameterization and numerical simulations

4.1 Eddy viscosity parameterization

Ruvinsky, Feldstein and Freidman (1991) presented a system of coupled equations for weakly damped surface waves and used them to study capillary-gravity ripples riding on steep gravity-capillary waves. The derivation of the coupled equations involved separating the potential and the vortical components of the flow: $\mathbf{u} = \nabla\phi + \mathbf{u}'$ with $\mathbf{u}' = \nabla \times \boldsymbol{\psi}$. Here, ϕ is the velocity potential; $\mathbf{u} = (u, w)$, the velocity vector with u and w being the components in the x - and z -directions, respectively; $\boldsymbol{\psi}$ is a vector stream function; $\mathbf{u}' = (u', w')$, the vortical velocity vector with u' and w' being the components in the x - and z -directions, respectively. Here, x and z are, respectively, the horizontal and vertical coordinates with z defined positive upwards from the mean surface. In addition, a boundary-layer approximation similar to that used in Longuet-Higgins (1953, 1960) was adopted. When linearized, the resulting governing equations and boundary conditions can be written (Ruvinsky et al., 1991) as

$$\nabla^2 \phi = 0, \quad (4.1)$$

$$\frac{\partial \phi}{\partial t} + g\eta + 2\nu \frac{\partial^2 \phi}{\partial z^2} = 0 \quad \text{on } z = 0, \quad (4.2)$$

$$\frac{\partial \eta}{\partial t} = \frac{\partial \phi}{\partial z} + w' \quad \text{on } z = 0, \quad (4.3)$$

$$\frac{\partial \phi}{\partial z} \rightarrow 0 \quad \text{as } z \rightarrow -\infty, \quad (4.4)$$

$$\frac{\partial w'}{\partial t} = 2\nu \frac{\partial^3 \phi}{\partial x^2 \partial z} \quad \text{on } z = 0. \quad (4.5)$$

Here, g is the gravitational acceleration, η is the free surface, and ν is the kinematic viscosity. To derive the free surface boundary condition (4.2), first linearize the viscous normal stress condition to $p/\rho = 2\nu(\partial w/\partial z) = 2\nu(\partial^2 \phi/\partial z^2)$ on $z=0$, where $|\mathbf{u}'|/|\nabla \phi| = O(k\delta)$ is assumed (Lamb, 1932; Ruvinsky et al., 1991), with δ being the boundary layer thickness. Then, substitute the linearized Bernoulli equation for the pressure, p , to obtain (4.2). Equation (4.5) is obtained from the linearized boundary layer equation for the rotational velocity components combined with the tangential stress condition on $z=0$ (Ruvinsky et al., 1991; see also Appendix B).

To find the expression for w' in terms of η and ϕ , (4.5) is re-written, after using the linearized kinematic boundary condition, as

$$\frac{\partial w'}{\partial t} = 2\nu \frac{\partial^3 \phi}{\partial x^2 \partial z} = 2\nu \frac{\partial^3 \eta}{\partial x^2 \partial t} \quad \text{on } z = 0. \quad (4.6)$$

Now, integrating (4.6) in time once yields

$$w' = 2\nu \frac{\partial^2 \eta}{\partial x^2} + C(x) \quad \text{on } z = 0, \quad (4.7)$$

where, by assuming the flow is initially inviscid and irrotational, the integration “constant” $C(x)$ is set to zero. Then, the kinematic free surface boundary condition is as follows:

$$\frac{\partial \eta}{\partial t} = \frac{\partial \phi}{\partial z} + 2\nu \frac{\partial^2 \eta}{\partial x^2} \quad \text{on } z = 0. \quad (4.8)$$

And (4.2) is written as

$$\frac{\partial \phi}{\partial t} = -g\eta + 2\nu \frac{\partial^2 \phi}{\partial x^2} \quad \text{on } z = 0, \quad (4.9)$$

where $-\frac{\partial^2 \phi}{\partial z^2}$ is replaced with $\frac{\partial^2 \phi}{\partial x^2}$. Equations (4.8) and (4.9) form the closed free surface boundary conditions modified with the leading-order viscous effects and, in fact, are identical to those obtained by Dias, Dyachenko and Zakharov (2008) using the solutions of the linearized Navier-Stokes equations in the small viscosity limit.

Earlier Longuet-Higgins (1992) suggested that modified free surface boundary conditions similar to (3.8) and (3.9) may be used to represent energy dissipation due to wave breaking if the kinematic viscosity, ν , is replaced with the turbulent eddy viscosity, ν_{eddy} . This might be a reasonable eddy viscosity model when short-wavelength scale disturbances, once excited (by wave breaking here), are assumed to be dissipated in the same manner as energy dissipation by kinematic viscosity. Therefore, as a first step toward a more comprehensive parameterization for wave breaking energy dissipation, we simply replace the kinematic viscosity in (4.8) and (4.9) with the eddy viscosity estimated

from experimental measurements, as described in the preceding section and we conduct numerical simulations to test the validity of this simple idea.

4.2 Comparison of numerical solutions with laboratory measurements

The numerical model is based on an asymptotic expansion in small wave steepness (West et al., 1987; Choi 1995) which yields the following nonlinear equations for the surface elevation, $\eta(x,t)$, and the velocity potential at the free surface, $\Phi(x,t)$. When the eddy viscosity terms are included, the model can be written as

$$\frac{\partial \eta}{\partial t} = \sum_{n=1}^{\infty} Q_n [\eta, \dots] + 2\nu_{eddy} \frac{\partial^2 \eta}{\partial x^2} \quad (4.10)$$

$$\frac{\partial \Phi}{\partial t} = \sum_{n=1}^{\infty} R_n [\eta, \Phi] + 2\nu_{eddy} \frac{\partial^2 \Phi}{\partial x^2} \quad (4.11)$$

where Q_n and R_n of $O(ka)^n$ represent the n th-order nonlinear terms that can be found through explicit recursion formulas (for example, Choi et al., 2005).

In this study, the right-hand sides of the equations are truncated to the third order and the nonlinear evolution equations (4.10) and (4.11) are solved numerically with a pseudo-spectral method based on the fast Fourier transform and a fourth-order Runge-Kutta method to integrate in time. Details of the numerical method can be found in Choi et al. (2005). This numerical model has been applied to predict surface wave profiles and local kinetic energy in the breaking criterion study by Tian et al. (2008), where excellent

agreement with their measurements was shown before wave breaking occurs. In this paper, the applicability of the eddy viscosity model in (4.10) and (4.11) after wave breaking will be explored by comparing numerical solutions with laboratory experiments.

Following Tian et al. (2008), initial conditions (i.e. initial surface profile and velocity potential at $z = 0$) are generated with the first wave probe measurements and linear wave theory. Then, numerical simulations are performed in a 48 m long numerical wave channel, which is discretized with 2^{11} points. A time step of 1/50 s is employed for the simulations.

During initial numerical tests, we found that the total potential energy (i.e. $\langle \eta^2 \rangle$) at the first wave probe did not match the experimental measurements. The discrepancy was due to viscous effects and nonlinearity (i.e. the initial entire surface elevation as a function of space was generated with the first wave probe measurement and linear wave theory; then it was propagated back to the first probe with the 3rd-order model). Therefore, to match the total potential energy measured at the first wave probe, the linear model without eddy viscosity is solved over the spatial domain from the wavemaker to the location of the first wave probe. The remainder of the tank is assumed viscous and the 3rd-order model with the eddy viscosity is solved. A transition layer (\sim one meter) between the linear inviscid and the 3rd-order viscous domain is applied to avoid any transition irregularity of the surface profiles.

In the viscous non-breaking domain, an equivalent kinematic viscosity is applied to the free surface boundary conditions ((4.8) and (4.9)) to account for the free surface damping and the friction and contact-line loss due to the side walls and the tank bottom. For each

of the five wave groups, the equivalent kinematic viscosity is estimated with the surface elevation measurements of the non-breaking trains and linear wave theory (i.e. exponential decay prediction, Lamb, 1932; Mei, 1983; Tulin and Waseda, 1999).

During active wave breaking (i.e. for t_{br}), a breaking region based on experimental measurements (i.e. l_{br}) is defined so that the estimated breaking eddy viscosity can be applied to the free surface boundary conditions. To obtain the eddy viscosity with (3.6) and (3.7), the proportionality coefficients have to be determined. However, our experimental measurements provide no information on the coefficient estimation. To determine the coefficients, θ and θ' , one wave group (W1G3, Table III-1) is used for a trial test. The proportionality coefficients are set to one; then the trial eddy viscosities estimated with (3.6) and (3.7) are used to run the simulation. Next numerical results of the total potential energy as a function of space are compared to the experimental measurements. The coefficients are adjusted systematically till good agreement between the numerical and the experimental results are achieved. As mentioned previously, the proportionality coefficients are determined as $\theta = 0.02$ and $\theta' = 0.10$ for wave group W1G3. Finally, these two coefficients are applied to other wave groups to test their applicability. As shown subsequently, good agreement between the numerical and experimental results suggests that the proportionality constants determined from a particular wave group are valid for all our wave groups.

As (3.6) with $\theta = 0.02$ and (3.7) with $\theta' = 0.10$ provide similar estimations of the eddy viscosity (see Figure III-11) and our tests show that numerical simulations with either eddy viscosity provide virtually the same energy dissipation, we present results of numerical simulations with the eddy viscosity estimated by (3.6). As shown in Figure

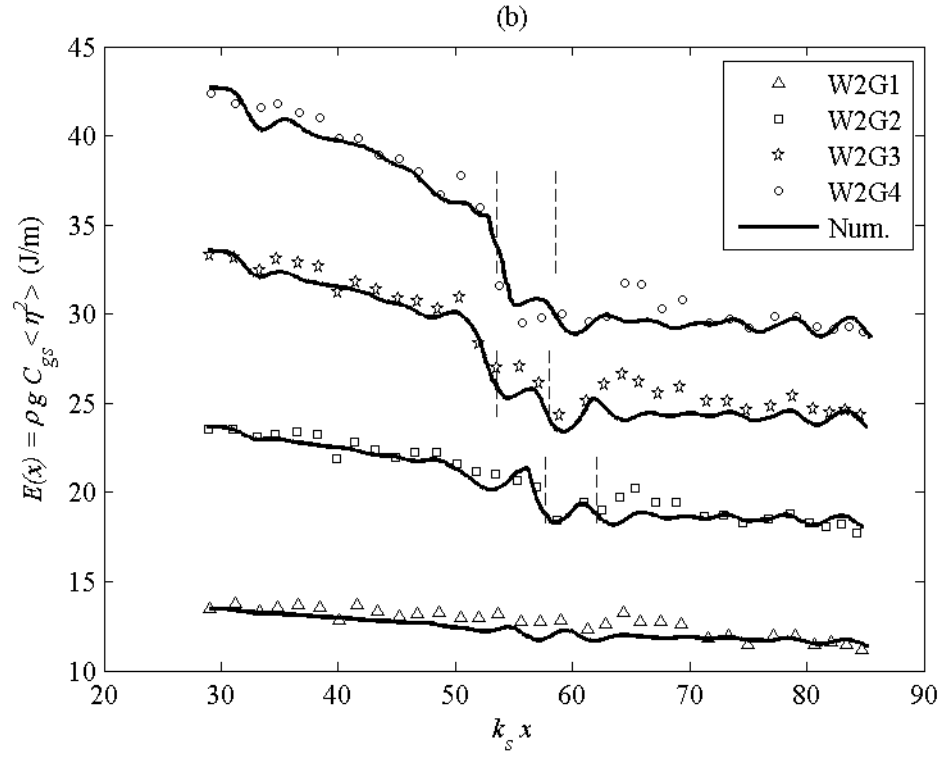
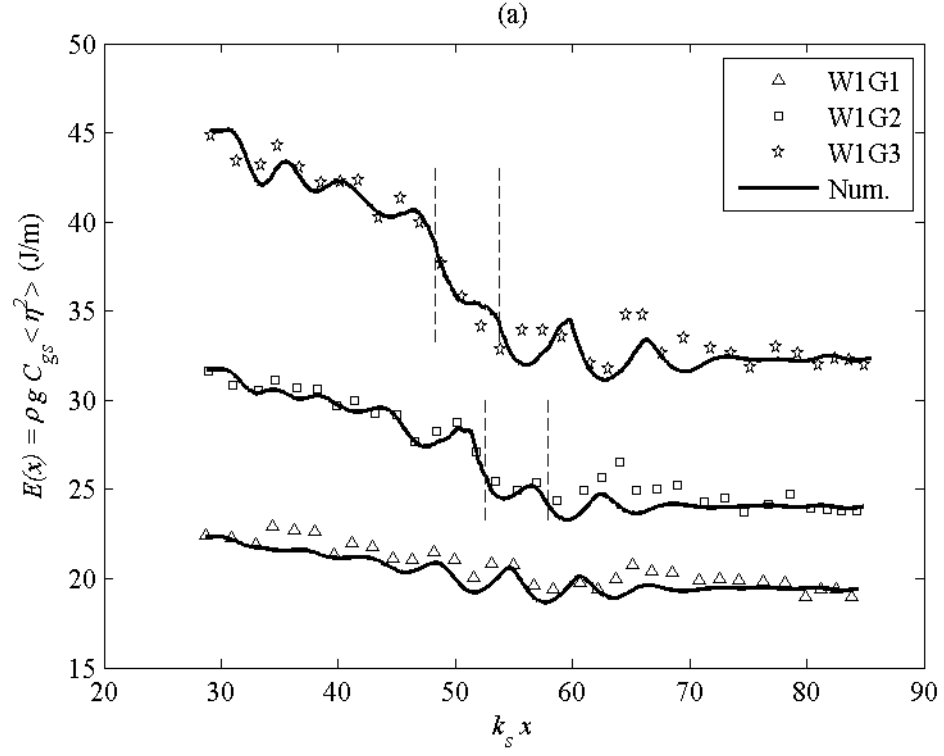
III-12, both the magnitude and the trend of the total energy measured in the experiments as a function of space are approximated reasonably well by the numerical results. Most importantly, the numerical results capture the measured energy loss due to wave breaking.

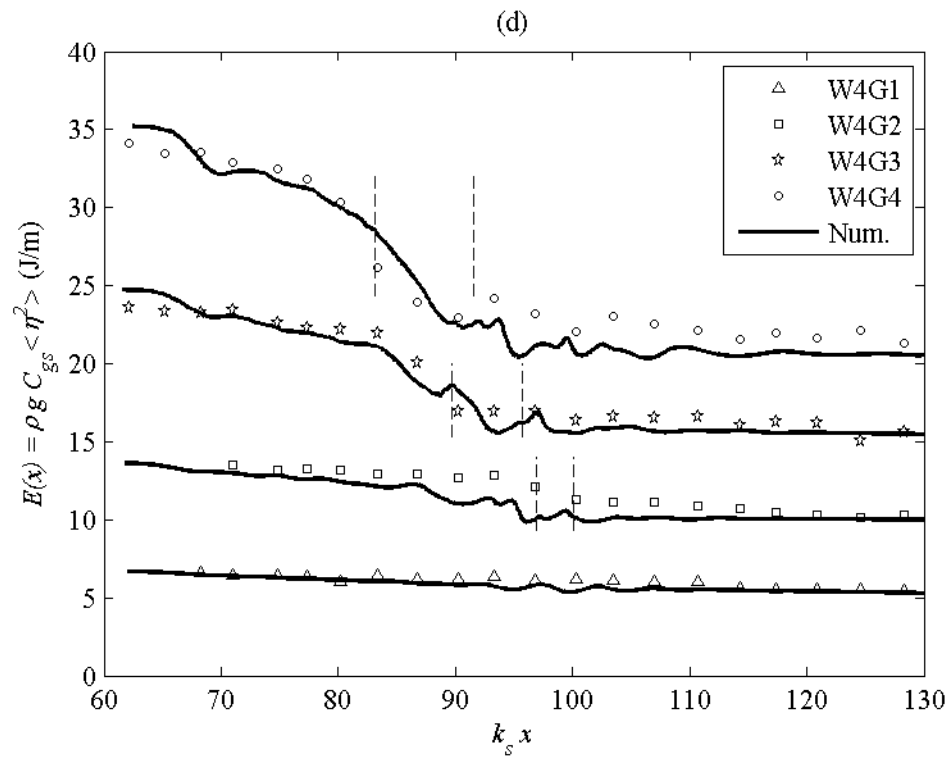
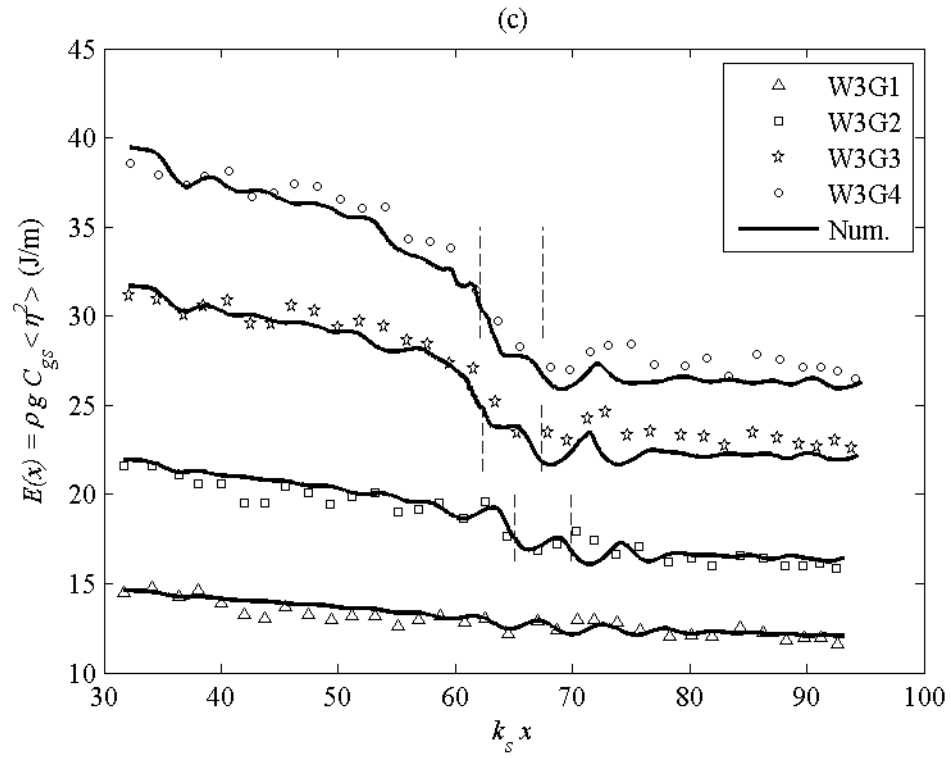
The data oscillations in Figure III-12 are worth mentioning. As discussed in section 3.2.1, these oscillations in the experimental results are due partially to failure of the linear assumption to estimate the total energy using $\langle \eta^2 \rangle$. We examined numerically the total energy, $E(t)$, as a function of time for a non-breaking wave group and found that both the total potential energy, $E_p(t)$, and the total kinetic energy, $E_k(t)$, demonstrate a general decay trend with oscillations present in wave focusing/breaking regions; however, the oscillations of $E_p(t)$ and $E_k(t)$ are 180° out of phase; therefore, the total energy decays monotonically. This finding indicates that the oscillations in the focusing/breaking regions are due mainly to failure of the linear assumption in estimating the total energy, as expected.

The surface elevation comparison downstream of wave breaking is also of obvious interest. Figure III-13 presents the surface elevation measured at three wave stations along the wave tank: one upstream and two downstream locations relative to wave breaking. For reference, measurements for a non-breaking wave group are provided also. In the figure, dimensional variables are used for a straightforward comparison. Notice that our experimental and numerical results show very good agreement not only in the wave amplitude, but also in phase. Some small local discrepancies also appear in the comparisons. For example, the second major peak of the numerical surface elevation at $x = 15.42\text{m}$ (W1G3, Figure III-13(a)) is reduced by a significant amount. Although its

cause is not known yet, we believe this is not caused by the eddy viscosity model as a similar reduction is present in the non-breaking wave group, too.

Our numerical study suggests that the simple eddy viscosity model works reasonably well for deep-water breaking waves in terms of energy dissipation. The model is based on simple dimensional analysis, in which a wave breaking time scale, t_{br} , a horizontal wave breaking length scale, l_{br} , and a vertical length scale (breaking wave crest falling height), h , are used. However, to apply this model to numerical simulation, the eddy viscosity has to be determined a priori with experimental measurements, and applied in the proper location and during the correct time with both known in advance. These requirements are obviously demanding. Fortunately, our study shows that the local wave steepness S_b and the breaking strength parameter, δ_{br} , proposed by Song and Banner (2002) demonstrate strong correlation with the energy dissipation rate, b_b , and the eddy viscosity, ν_{eddy} . In addition, based on Figure III-9, t_{br} and l_{br} depend on S_b or δ_{br} ; and, for a rough estimation, one may infer the breaking time and the horizontal length based on S_b or δ_{br} . In simulating an individual wave breaking event, for example, the local wave steepness S_b can be computed and monitored throughout the numerical simulation. Once S_b approaches $(S_b)_0$, the eddy viscosity may be implemented (i.e. prior to a numerical disaster).





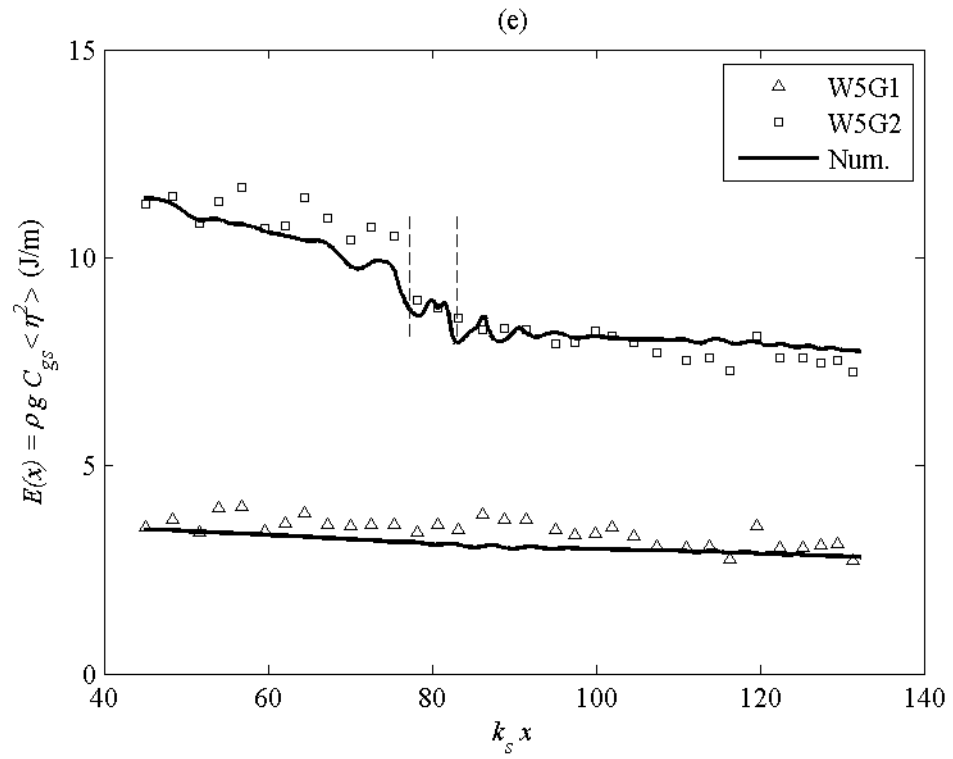
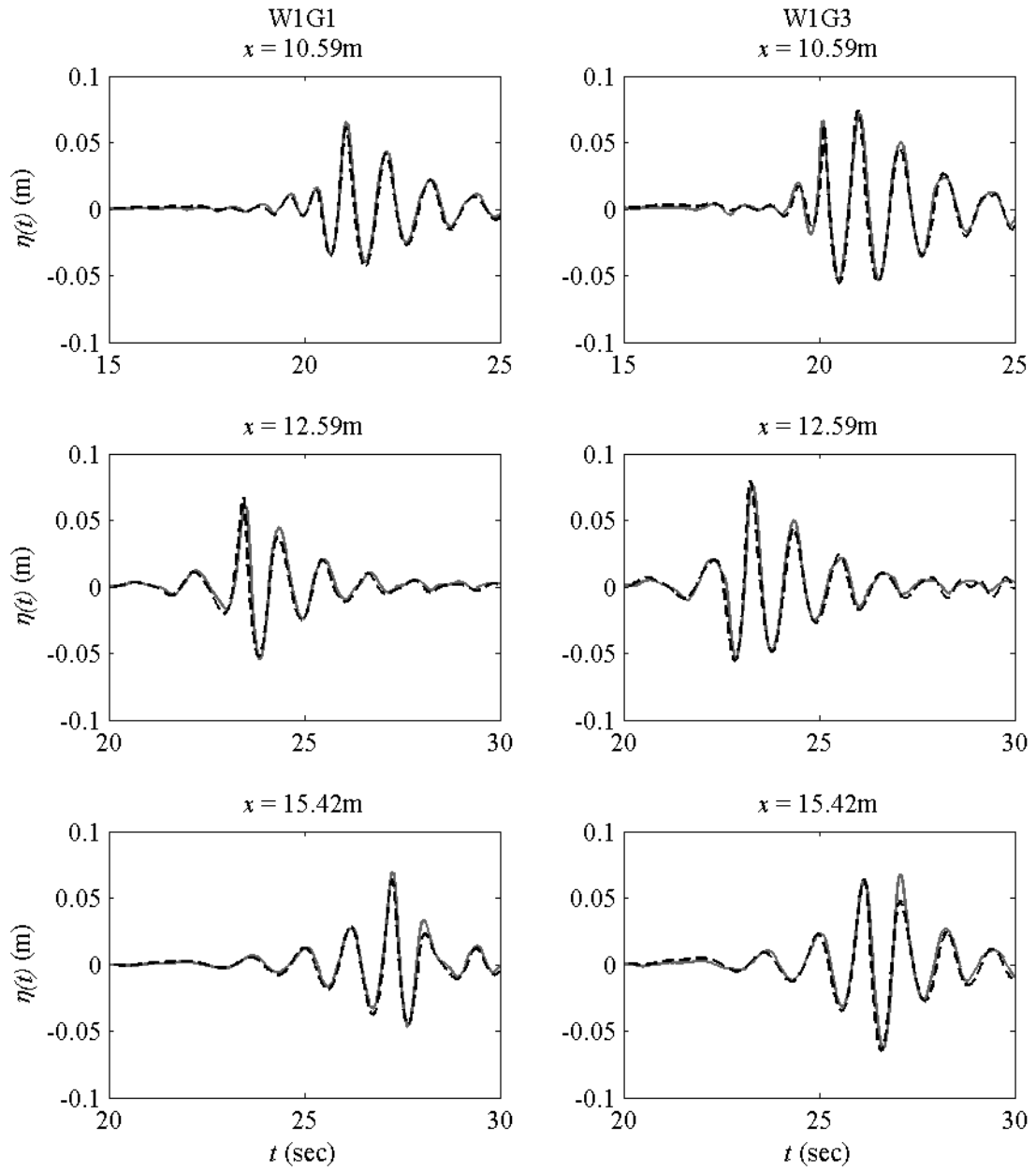
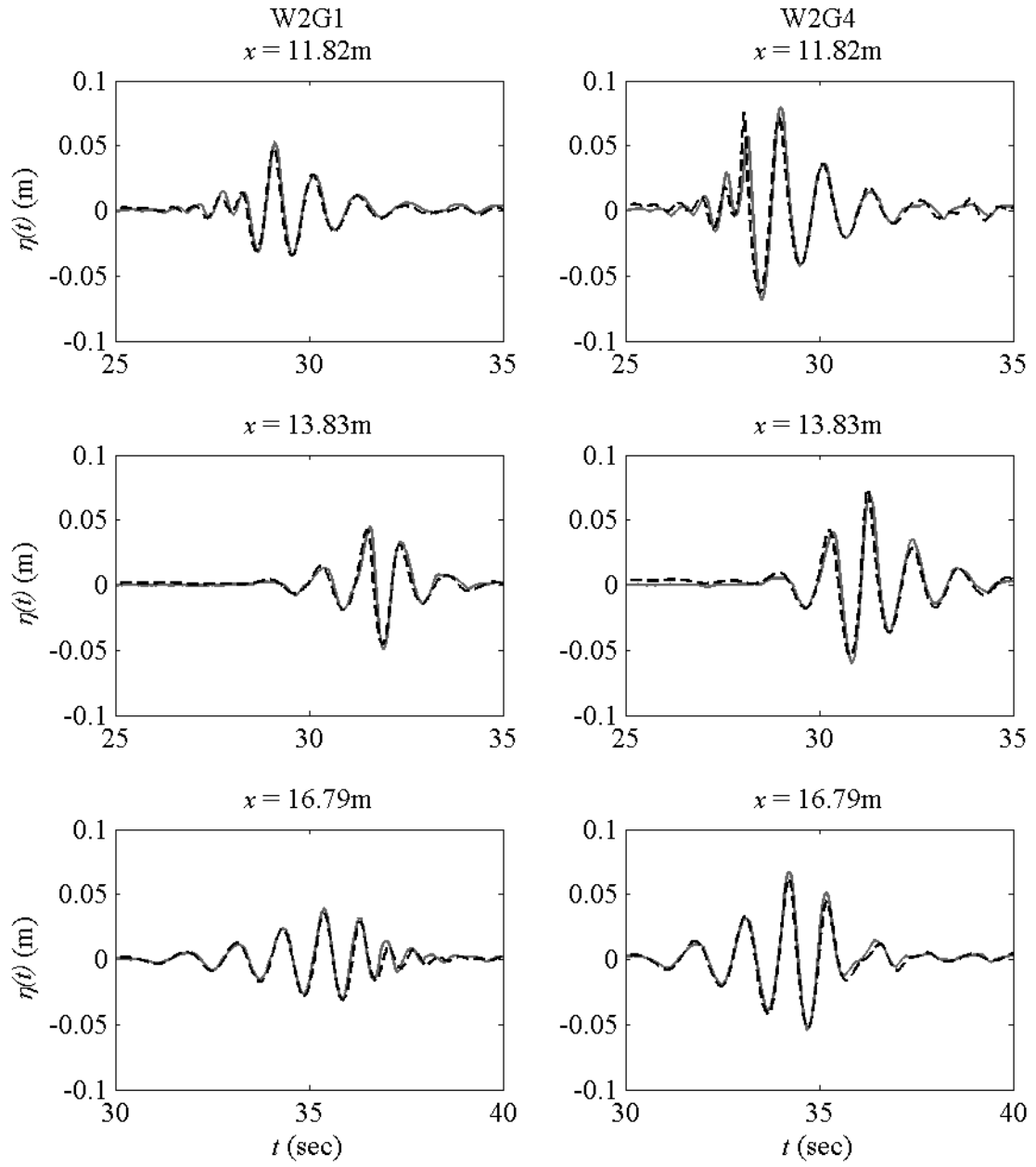


Figure III-12 In graphs (a - e), comparisons of the total energy as a function of space are presented. Symbols represent experimental measurements and solid lines represent numerical results. The vertical dash lines indicate the wave breaking region.

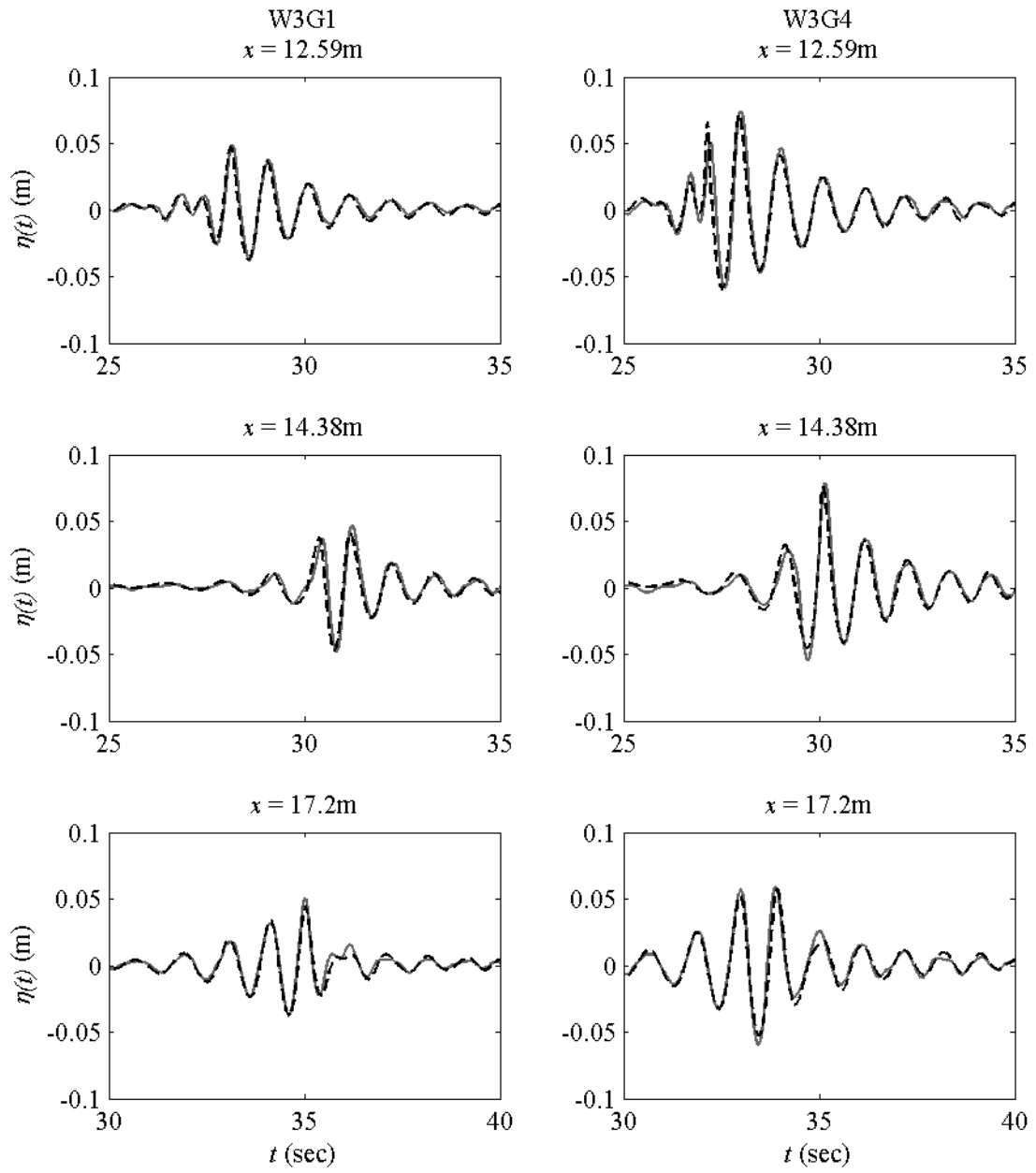
(a)



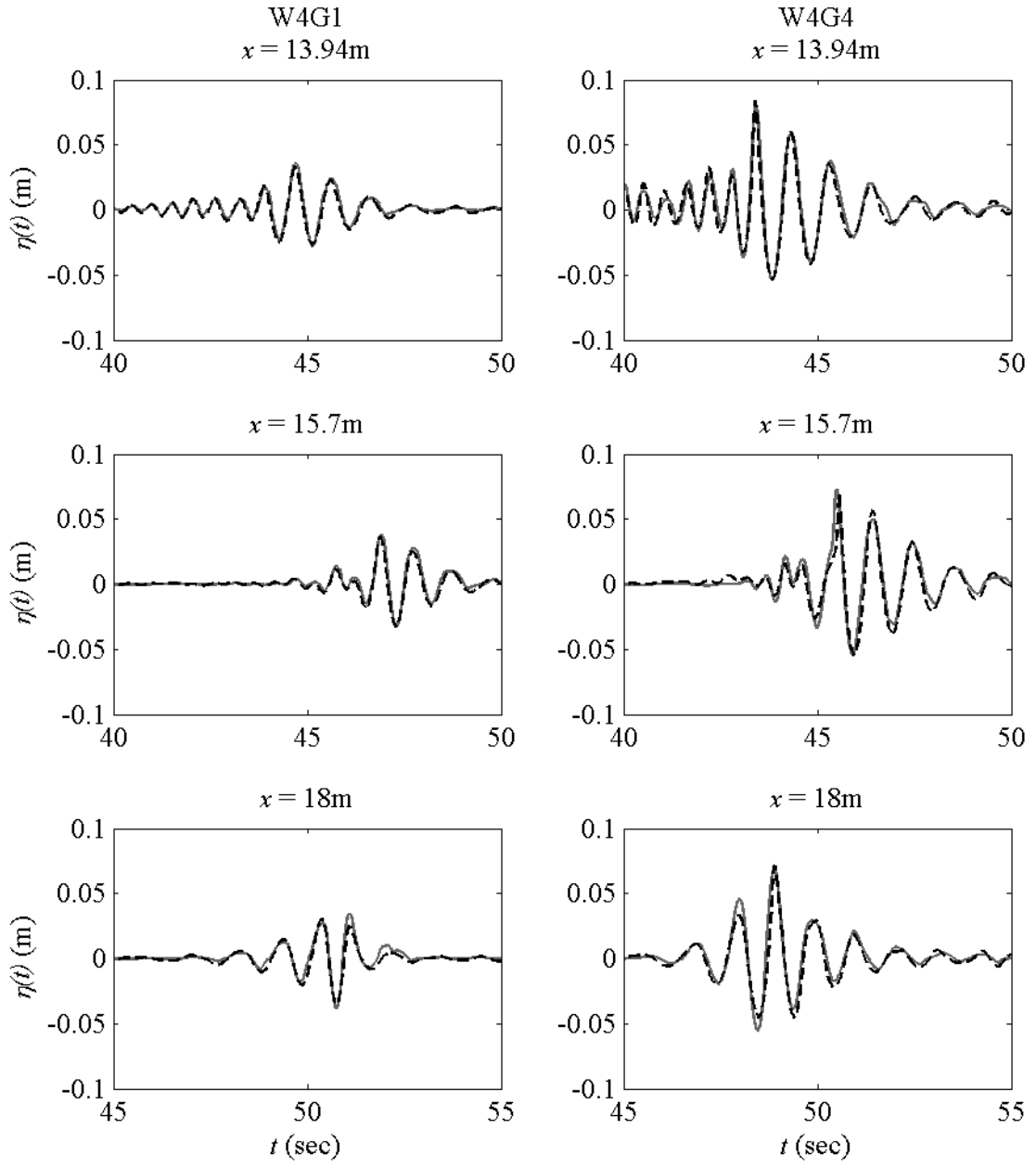
(b)



(c)



(d)



(e)

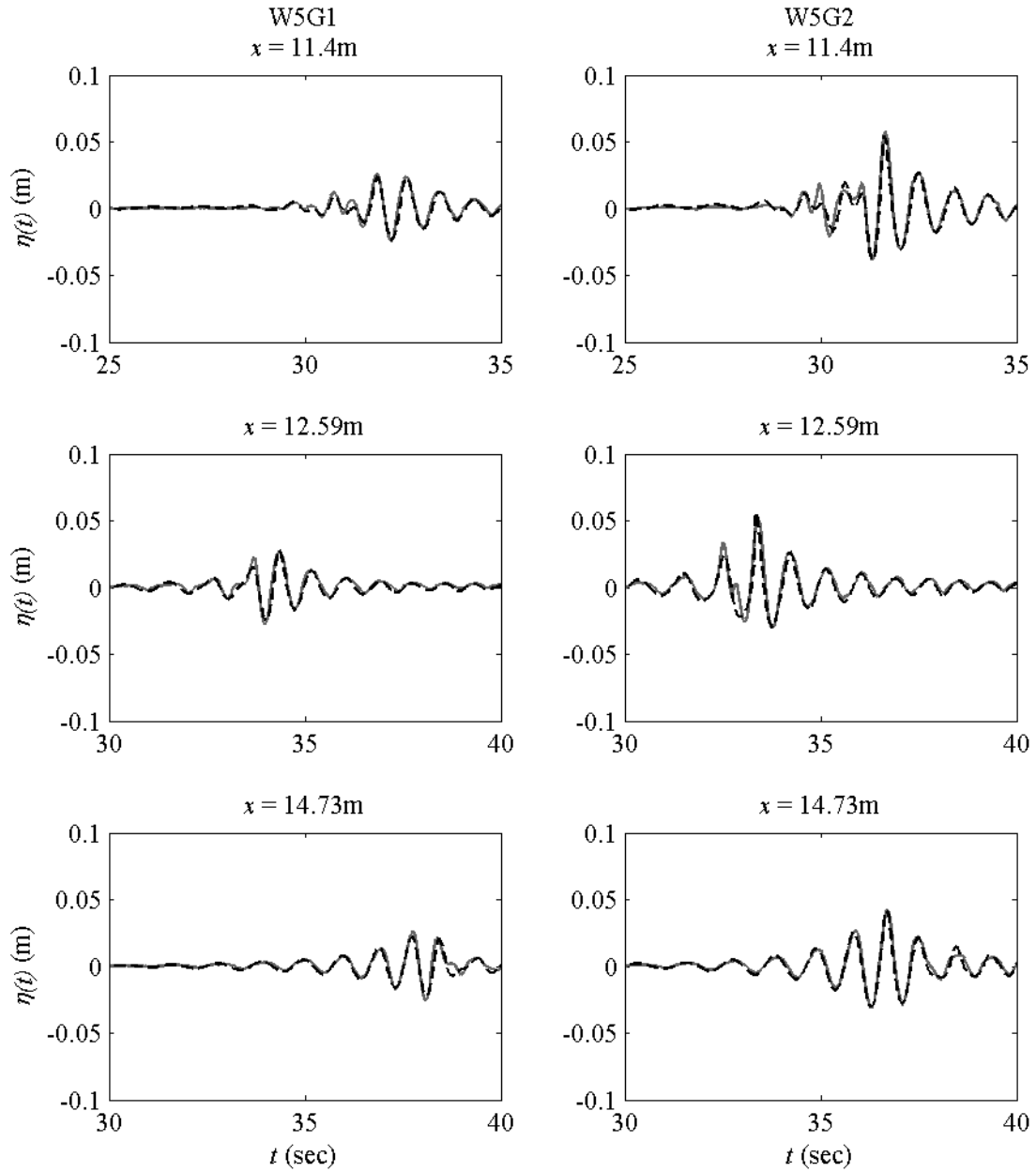


Figure III-13 (a - e) show the comparison of surface elevations measured from three wave stations. Solid line: experimental measurements; dash line: numerical results. In each of the five sets of graphs, figures in the left column are from the nonbreaking wave groups; figures of the most violent breaking wave groups are in the right column. Breaking regions are: [11.28 m, 12.57m] for W1G3 in (a), [12.53m, 13.71m] for W2G4 in (b), [13.09m, 14.24m] for W3G4 in (c), [14.11m, 15.54m] for W4G4 in (d), and [11.72m, 12.59m] for W5G2 in (e).

5 Conclusions

An experimental study of the kinematics and the dynamics of two-dimensional unsteady plunging breakers has been reported. In addition, an eddy viscosity model is proposed to simulate the energy dissipation due to wave breaking and the model is validated with our experimental results.

In our experiments, wave surface elevations are measured with both wave probes and high-speed imaging. With the wave probe measurements, wave characteristics associated with the wave group (i.e. S , f_s , k_s , c_s and C_{gs}) are defined and determined. While the center wave frequency and the associated linear group velocity in a wave group are considered commonly the group characteristics, our study illustrates that the spectrally-weighted wave frequency (and wave number) and group velocity better represent the characteristic properties for wave groups (with constant wave steepness distribution across their amplitude spectra). Based on surface profiles (just prior to wave breaking onset) measured with high-speed imaging, local breaking wavenumber, k_b , local wave steepness, S_b , and breaking wave phase speed, c_b , are determined. We find a strong connection between our wave group characteristics and the local breaking wave parameters (i.e. $S_b/S = 1.237$, $c_b/c_s = 0.9 \pm 0.1$ and $k_b/k_s = 1.25 \pm 0.25$). To our knowledge, these links have not been reported before.

Surface elevation measurements with wave probes are used also to estimate the total energy and the total energy loss. We find that energy loss due to surface damping, contact-line dissipation, and friction by the tank sidewalls and the bottom is non-negligible as compared to energy loss due to wave breaking that ranges from 8% to 25%

of the total pre-breaking energy. More interestingly, both estimated total pre-breaking energy and energy loss due to wave breaking are found to scale accurately with the wave group characteristics (i.e. $E_0 k_s^3 / (\rho g)$ versus S and $\Delta E k_s^3 / (\rho g)$ versus S). Good correlations are observed also when both the energy and the energy loss are scaled with local wave characteristics (i.e. $E_0 k_b^3 / (\rho g)$ versus S_b and $\Delta E k_b^3 / (\rho g)$ versus S_b). Based on a linear least-square fit between $\Delta E k_s^3 / (\rho g)$ and S , the threshold of S that predicts wave breaking onset is estimated as $S_0 = 0.339$ and hence, $(S_b)_0 = 0.419$ for the same purpose. However, the application of S or S_b as a universal indicator to predict wave breaking and breaking strength needs to be explored further due to the variation of S_0 in different laboratory studies. While the local wave steepness parameter, S_b , seems to be a more universal wave breaking indicator, its performance needs to be further investigated.

Surface profile measurements using high-speed imaging are utilized to determine the breaking criterion parameter, $\delta(t)$, and its magnitude just prior to wave breaking. Our study justifies Song and Banner's (2002) wave breaking criterion which states that $\delta(t)$ with threshold $1.4 \pm 0.1 \times 10^{-3}$ distinguishes wave groups that lead to breaking from those that do not. The breaking parameter immediately before wave breaking (i.e. δ_{br}) increases in general as the energy loss due to wave breaking increases. In addition, δ_{br} can be expressed analytically with the local wave slope, S_b ; and the relationship is supported by our experimental results.

Breaking time scale and breaking horizontal length scale are defined and obtained with high-speed imaging measurements. The time and length scales depend approximately linearly on S_b , indicating that the breaking process is more violent as S_b increases. The two scales are then used to determine the horizontal breaking wave crest speed, u_{br} ,

which is shown to correlate strongly with the breaking wave phase speed, c_b , and the spectrally-weighted wave phase speed, c_s .

The energy dissipation rate in the plunging breakers is determined as the ratio of the total energy loss due to wave breaking to the measured breaking time. This estimation method assumes a constant dissipation rate and it involves only local wave parameters. The normalized energy dissipation rate (i.e. b_b) is on the order of 10^{-3} , which in general is consistent with previous results, subject to proper data interpretation. Although both S_b and δ_{br} correlate well with b_b , indicating both parameters can be used to indicate wave breaking strength, S_b appears to have a stronger correlation.

An eddy viscosity model obtained from the viscous free surface boundary conditions for weakly damped surface waves is adopted and tested numerically with laboratory measurements for energy dissipation due to wave braking. The eddy viscosity is estimated by both dimensional analysis and turbulent energy dissipation rate analysis with measured breaking time and length scales. The two estimations are very close, both on the order of $10^{-3} \text{ (m}^2\text{s}^{-1}\text{)}$. The estimated eddy viscosity also illustrates close correlation with the energy dissipation rate, b_b , and the wave breaking strength parameters, S_b and δ_{br} . The estimated eddy viscosity is employed in simulations that aim to reproduce the experimental tests numerically. Good agreement in energy dissipation obtained from the numerical simulations and the experimental measurements is found and this indicates that the eddy viscosity model could be an effective tool in simulating the energy dissipation in plunging breakers and post-breaking wave profiles.

Appendix A Nonlinear group velocity

The rate of change of total energy, dE/dt , inside a control volume between two vertical planes bounded by a free surface and a flat bottom is given (Wehausen and Laitone 1960, section 8) by

$$\frac{dE}{dt} = F_1 - F_2 \quad \text{with } F = -\rho \int_{-h}^{\eta} \frac{\partial \phi}{\partial t} \frac{\partial \phi}{\partial x} dz, \quad (\text{A.1})$$

where F_1 and F_2 represent the energy fluxes per unit length through two vertical planes at x_1 and $x_2 = x_1 + \Delta x$, the left and right-hand side boundaries, respectively. By substituting into (A.1) Stokes' wave solutions correct to the third order in wave steepness (Wehausen and Laitone 1960, section 27):

$$\begin{aligned} \phi &= ac_0 e^{kz} \sin kx + \dots, \\ \eta &= a \left[\cos(kx) + \frac{1}{2} ka \cos(2kx) + \frac{3}{8} (ka)^2 \cos(3kx) + \dots \right], \\ c &= c_0 \left[1 + \frac{1}{2} (ka)^2 + \dots \right], \end{aligned}$$

the energy flux averaged over a wavelength $2\pi/k$, \bar{F} , can be expanded as

$$\bar{F} = \overline{\rho c \int_{-h}^{\eta} \left(\frac{\partial \phi}{\partial x} \right)^2 dz} = \frac{1}{4} \rho g c_0 a^2 \left(1 + \frac{5}{2} k^2 a^2 + \dots \right),$$

where $c_0^2 = g/k$ and a is the wave amplitude. The averaged energy flux can be also written as the product of the total energy density and the (nonlinear) group velocity, $\bar{F} = e C_g$, where the total energy density averaged over a wavelength is

$$e = \frac{1}{2} \rho g \eta^2 + \frac{1}{2} \rho \overline{\int_h^\eta \left[\left(\frac{\partial \phi}{\partial x} \right)^2 + \left(\frac{\partial \phi}{\partial z} \right)^2 \right] dz} = \frac{1}{2} \rho g a^2 \left(1 + \frac{3}{4} k^2 a^2 + \dots \right).$$

Then, from the two different expressions of \bar{F} , the group velocity C_g correct to $O(k^2 a^2)$ can be found as

$$C_g = \frac{1}{2} c_0 \left(1 + \frac{7}{4} k^2 a^2 + \dots \right).$$

When the effect of nonlinearity is included, this nonlinear group velocity measuring the speed at which energy propagates is different from the classical nonlinear definition of the group velocity (from the kinematic consideration), which can be written as

$$\frac{\partial \omega}{\partial k} = \frac{1}{2} c_0 \left(1 + \frac{5}{2} k^2 a^2 + \dots \right).$$

Appendix B Derivation of (4.5)

When linearized, the tangential stress condition at $z=0$ is given by

$$\frac{\partial u}{\partial z} + \frac{\partial w}{\partial x} = 0 \quad \text{on } z = 0. \quad (\text{B.1})$$

After writing $\mathbf{u} = \nabla \phi + \mathbf{u}'$ and assuming $|\mathbf{u}'|/|\nabla \phi| = O(k\delta)$ (Lamb 1932; Ruvinsky et al., 1991) and $|w'|/|u'| = O(k\delta)$ from boundary layer scaling, the leading-order approximation in $k\delta$ of the linearized tangential stress condition yields

$$\frac{\partial u'}{\partial z} = -2 \frac{\partial^2 \phi}{\partial x \partial z} \quad \text{on } z = 0. \quad (\text{B.2})$$

On the other hand, the rotational horizontal velocity satisfies the following (linearized) boundary layer equation:

$$\frac{\partial u'}{\partial t} = \nu \frac{\partial^2 u'}{\partial z^2}. \quad (\text{B.3})$$

By differentiating (B.3) with respect to x and using the continuity equation

$\partial u'/\partial x + \partial w'/\partial z = 0$, we have

$$\frac{\partial}{\partial z} \left(\frac{\partial w'}{\partial t} \right) = \nu \frac{\partial^3 w'}{\partial z^3}, \quad (\text{B.4})$$

which can be integrated to obtain (4.5):

$$\frac{\partial w'}{\partial t} = \nu \frac{\partial^2 w'}{\partial z^2} = -\nu \frac{\partial^2 u'}{\partial z \partial x} = 2\nu \frac{\partial^3 \phi}{\partial x^2 \partial z} \quad \text{on } z = 0, \quad (\text{B.5})$$

where the continuity equation for \mathbf{u}' and the tangential stress condition (B.2) have been used for the last two expressions, respectively.

Appendix C Integral velocity estimation based on the turbulent energy dissipation analysis by Melville (1994)

Based on the analysis by Melville (1994), the total energy loss rate, ε , in the assumed triangular turbulent region due to wave breaking can be approximated by

$$\varepsilon = \rho u^3 l_{br} / 2, \quad (C.1)$$

where l_{br} is the length of turbulent “whitecap”, and is comparable to one characteristic wave length (see section 3.3.1 and figure 9(b)); therefore, $l_{br} \sim c_b^2/g$. Hence, the dissipation rate can be rewritten as

$$\varepsilon = \rho (\chi c_b)^3 (\gamma c_b^2 / g) = (\gamma \chi^3) \rho c_b^5 / g. \quad (C.2)$$

Here γ is a constant and can be deduced from experimental measurements and $u = \chi c_b$ has been used. Recognizing that the term $(\gamma \chi^3)$ represents b_b , we can evaluate the coefficient $\chi = (b_b/\gamma)^{1/3}$. Figure III-14 provides the estimation versus wave breaking strength, b_b . As expected, χ increases as wave breaking intensifies and it agrees well with the estimations by Melville (1994). Therefore, eddy viscosity can be estimated roughly as $\nu_{eddy} \sim \chi c_b h$, (3.7).

With the inertial scaling analysis by Drazen et al. (2008), who proposed that $b_b = \alpha(k_b h)^{5/2}$, one may write the eddy viscosity as a function of b by substituting $\chi = (b_b/\gamma)^{1/3}$

and $h = (b_b/\alpha)^{2/5}k_b$ into the above equation; further manipulation gives the eddy viscosity as

$$\nu_{eddy} = \beta b_b^{11/15} c_b / k_b, \quad (C.3)$$

where β is a proportionality coefficient. With a least-squares analysis, the proportionality constant, β , is determined to be 0.13 for our wave groups. In addition, this power law relationship between ν_{eddy} and b_b can be replaced approximately with a linear one (Figure III-11(b)).

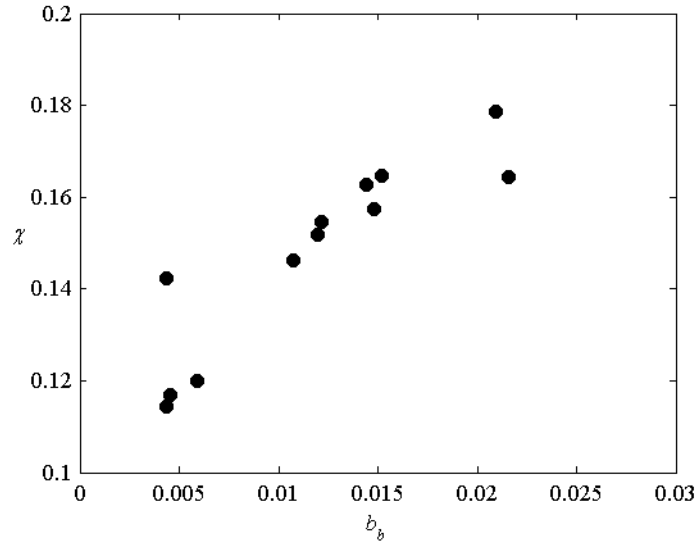


Figure III-14 Normalized integral speed ($\chi = u/c_b$) as a function of wave breaking strength, b_b . As expected, the integral speed increases as wave breaking intensifies.

References

- BANNER, M. L. & PEIRSON, W. L. 2007 Wave breaking onset and strength for two-dimensional deep-water wave groups. *J. Fluid Mech.* **585**, 93-115.
- BANNER, M. L. & PEREGRINE, D. H. 1993 Wave breaking in deep-water. *Annu. Rev. Fluid Mech.* **25**, 373-397.
- BANNER, M. L. & TIAN, X. 1998 On the determination of the onset of breaking for modulating surface gravity water waves. *J. Fluid Mech.* **367**, 107-137.
- BONMARIN, P. 1989 Geometric properties of deep-water breaking waves. *J. Fluid Mech.* **209**, 405-433.
- CHANG, K. A. & LIU, P. L. F. 1998, Velocity, acceleration and vorticity under a breaking wave. *Phys. Fluids* **10**, 327-329.
- CHEN, G., KHARIF, C., ZALESKI, S. & LI, J. 1999 Two-dimensional Navier-Stokes simulation of breaking waves. *Phys. Fluids* **11** (1), 121-133.
- CHOI, W. 1995 Nonlinear evolution equations for two-dimensional surface waves in a fluid of finite depth. *J. Fluid Mech.* **295**, 381-394.
- CHOI, W., KENT, C. P. & SCHILLINGER, C. 2005 Numerical modeling of nonlinear surface waves and its validation. *Advances in Eng. Mech.* 94-110, World Scientific
- DIAS, F., DYACHENKO, A. I. & ZAKHAROV, V. E. 2008 Theory of weakly damped free-surface flows: A new formulation based on potential flow solutions. *Phys. Letters A* **372**, 1297-1302.
- DIAS, F. & KHARIF, C. 1999 Nonlinear gravity and capillary-gravity waves. *Annu. Rev. Fluid Mech.* **31**, 301-46.
- DOMMERMUTH, D. G., YUE, D. K. P., LIN, W. M., RAPP, R. J., CHAN, E. S. & MELVILLE, W. K. 1988 Deep-water plunging breakers: a comparison between potential theory and experiments. *J. Fluid Mech.* **189**, 432-442.
- DRAZEN, D. A., MELVILLE, W. K. & LENAIN, L. 2008 Inertial scaling of dissipation in unsteady breaking waves. *J. Fluid Mech.* **611**, 307-332.
- DUNCAN, J. H. 1981 An experimental investigation of breaking waves produced by a towed hydrofoil. *Proc. R. Soc. London Ser. A* **377**, 331-348.
- DUNCAN, J. H. 1983 The breaking and non-breaking wave resistance of a two-dimensional hydrofoil. *J. Fluid Mech.* **126**, 507-520.
- DUNCAN, J. H. 2001 Spilling breakers. *Annu. Rev. Fluid Mech.* **33**, 519-547.

- DUNCAN, J. H., QIAO, H. B., PHILOMIN, V. & WENZ, A. 1999 Gentle spilling breakers: crest profile evolution. *J. Fluid Mech.* **379**, 191-222.
- GEMMRICH, J. R., BANNER, M. L. & GARRETT, C. 2008 Spectrally resolved energy dissipation rate and momentum flux of breaking waves. *J. Phys. Oceanog.* **38**, 1296-1312.
- GRUE, J. CLAMOND, D., HUSEBY, M. & JENSEN, A. 2003 Kinematics of extreme waves in deep water. *Appl. Ocean Res.* **25**, 355-366.
- GRUE, J. & JENSEN, A. 2006 Experimental velocities and accelerations in very steep wave events in deep water. *Eur. J. Mech. B/Fluids* **25**, 554-564.
- HARA, T. & MEI, C. C. 1991 Frequency downshift in narrowbanded surface waves under the influence of wind. *J. Fluid Mech.* **230**, 429-477.
- JIANG, L., PERLIN, M. & SCHULTZ, W. W. 2004 Contact-line dynamics and damping for oscillating free surface flows. *Phys. Fluids* **16** (3), 748-758.
- KWAY, J. H. L., LOH, Y. S. & CHAN, E. S. 1998 Laboratory study of deep water breaking waves. *Ocean Eng.* **25**, 657-676.
- LAKE, B. M., YUEN, H. C., RUNGALDIER, H., & FERGUSON, W. E. 1977 Nonlinear deep-water waves: theory and experiment. Part 2. Evolution of a continuous wave train. *J. Fluid Mech.* **83**, 49-74.
- LAMB, H. 1932 *Hydrodynamics*. 6th ed. Cambridge Univ. Press.
- LAMARRE, E. & MELVILLE, W. K. 1991 Air entrainment and dissipation in breaking waves. *Nature* **351**, 469-472.
- LOEWEN, M. R. & MELVILLE, W. K. 1991 Microwave backscatter and acoustic radiation from breaking waves. *J. Fluid Mech.* **224**, 601-623.
- LONGUET – HIGGINS, M. S. 1953 Mass transport in water waves. *Phil. Trans. R. Soc. Lond. A* **245**, 535-581.
- LONGUET – HIGGINS, M. S. 1960 Mass transport in the boundary – layer at a free oscillating surface. *J. Fluid Mech.* **8**, 293-306.
- LONGUET – HIGGINS, M. S. 1992 Theory of weakly damped Stokes waves: a new formulation and its physical interpretation. *J. Fluid Mech.* **235**, 319-324.
- LONGUET – HIGGINS, M. S. & COKELET, E. D. 1976 The deformation of steep surface waves on water. I. A numerical method of computation. *Proc. R. Soc. London A*. **350**, 1-26.
- MEI, C. C. 1983 *The Applied Dynamics of Ocean Surface Waves*. Wiley-Interscience, 385.

- MELVILLE, W. K. 1982 The instability and breaking of deep-water waves. *J. Fluid Mech.* **115**, 165-185.
- MELVILLE, W. K. 1994 Energy-dissipation by breaking waves. *J. Phys. Oceanogr.* **24**, 2041-2049.
- MELVILLE, W. K. 1996 The role of surface-wave breaking in air-sea interaction. *Annu. Rev. Fluid Mech.* **28**, 279-321.
- MELVILLE, W. K. & MATUSOV, P. 2002 Distribution of breaking waves at the ocean surface. *Nature* **417**, 58-63.
- MELVILLE, W. K., VERON, F. & WHITE, C. J. 2002, The velocity field under breaking waves: coherent structures and turbulence. *J. Fluid Mech.* **454**, 203-233.
- NEPF, H. M., WU, C. H. & CHAN, E. S. 1998 A comparison of two- and three-dimensional wave breaking. *J. Phys. Oceanogr.* **28**, 1496-1510.
- PERLIN, M., LIN, H. J. & TING, C. L. 1993 On parasitic capillary waves generated by steep gravity waves: An experimental investigation with spatial and temporal measurements. *J. Fluid Mech.* **255**, 597-620.
- PERLIN, M., HE, J. H. & BERNAL, L. P. 1996 An experimental study of deep water plunging breakers. *Phys. Fluids* **8** (9), 2365-2374.
- PERLIN, M. & SCHULTZ, W. W. 2000 Capillary effects on surface waves. *Ann. Rev. Fluid Mech.* **32**, 241-274.
- PHILLIPS, O. M. 1977 *The dynamics of the upper ocean*. Cambridge University Press.
- PHILLIPS, O. M. 1985 Spectral and statistical properties of the equilibrium range in wind-generated gravity-waves. *J. Fluid Mech.* **156**, 505-531.
- PHILLIPS, O. M., POSNER, F. L. & HANSEN, J. P. 2001 High range resolution radar measurements of the speed distribution of breaking events in wind-generated ocean waves: surface impulse and wave energy dissipation rates. *J. Phys. Oceanogr.* **31**, 450-460.
- RAPP, R. J. & MELVILLE, W. K. 1990 Laboratory measurements of deep-water breaking waves. *Phil. Trans. R. Soc. Lond. A.* **331**, 735-800.
- RUVINISKY, K. D., FELDSTEIN, F. I. & FREIDMAN, G. I. 1991 Numerical simulations of the quasi-stationary stage of ripple excitation by steep gravity-capillary waves. *J. Fluid Mech.* **230**, 339-353.
- SCHULTZ, W. W., HUH, J. & GRIFFIN, O. M. 1994 Potential energy in steep and breaking waves. *J. Fluid Mech.* **278**, 201-228.
- SKYNER, D. 1996 A comparison of numerical predictions and experimental measurements of the internal kinematics of a deep-water plunging wave. *J. Fluid Mech.* **315**, 51-64.

- SONG, J. B. & BANNER, M. L. 2002 On determining the onset and strength of breaking for deep water waves. Part I: Unforced irrotational wave groups. *J. Phys. Oceanog.* **32**, 2541–2558.
- STANSELL, P. & MACFARLANE, C. 2002 Experimental investigation of wave breaking criteria based on wave phase speeds. *J. Phys. Oceanog.* **32**, 1269–1283.
- STOKES, G. G. 1880 Supplement to a paper on the theory of oscillatory waves. *Math. Phys. Papers* **1**, 314–326.
- SULLIVAN, P. P., MCWILLIAMS, J. C. & MELVILLE, W. K. 2004 The oceanic boundary layer driven by wave breaking with stochastic variability. Part 1. Direct numerical simulations. *J. Fluid Mech.* **507**, 143–174.
- THORPE, S. A. 1993 Energy-loss by breaking waves. *J. Phys. Oceanog.* **23**, 2498–2502.
- TIAN, Z. G., PERLIN, M. & CHOI, W. 2008 Evaluation of a deep-water wave breaking criterion. *Phys. Fluids* **20** (066604), 1–13.
- TRULSEN, K. & DYSTHE, K. 1997 Frequency downshift in three-dimensional wave trains in a deep basin. *J. Fluid Mech.* **352**, 359–373.
- TULIN, M. P. & WASEDA, T. 1999 Laboratory observations of wave group evolution, including breaking effects. *J. Fluid Mech.* **378**, 197–232.
- WEHAUSEN, J. V. & LAITONE, E. V. 1960 *Surface waves*. Handbook of Physics, Vol. 9. Springer (also available at <http://www.coe.berkeley.edu/SurfaceWaves/>).
- WU, C. H. & NEPF, H. M. 2002 Breaking criteria and energy losses for three-dimensional wave breaking. *J. Geophys. Res.-Oceans* **107** (C10), 3177.
- YAO, A. F. & WU, C. H. 2005 Incipient breaking of unsteady waves on sheared currents. *Phys. Fluids* **17** (082104), 1–10.

Chapter IV

Wave Spectra Evolution of Two-Dimensional Unsteady Breaking Waves

Abstract

An experimental study on spectral evolution of laboratory generated breaking waves is presented. Spatial evolution of wave frequency spectra and temporal evolution of wavenumber spectra of breaking wave groups are examined. Spectral content following energy dissipation due to wave breaking is presented.

Spatial evolution of wave frequency spectra is examined for non-breaking wave groups. Nonlinear energy transfer across the frequency spectra is obvious as wave groups focus and defocus. A large energy loss due to viscous effects and contact-line damping is observed in the non-breaking wave groups. Depending on spectral bandwidth, 20% to 70% of this non-breaking energy loss is from the spectral peak region ($f/f_p = 0.95 \sim 1.1$). Here, f_p is the peak energy frequency. In addition, the energy loss near the spectral peak rises as frequency spectral bandwidth decreases. To the best of our knowledge, a similar observation has not been reported previously.

Observations of the evolution of the frequency spectra for breaking wave groups are also reported. From these the spectral distribution of energy dissipated due to wave breaking

is determined then as the spectral difference between the before and after wave breaking value less the corresponding spectral difference of the non-breaking wave group. Wave components in the frequency range $1.1 f_p$ to $2.0 f_p$ lose significant energy, which contributes to most of the energy loss due to wave breaking; wave components between $0.65 f_p$ and $0.95 f_p$ gain to 50% of the energy loss in the higher frequency band. The ratio of the energy gain to loss across the wave spectrum due to wave breaking shows no apparent dependence on breaking strength, and is higher than others, previous experimental results. Due to wave breaking, energy near the spectral peak may increase or decrease, depending on the initial wave frequency spectrum.

Surface profile measurement is used to examine the temporal evolution of the wavenumber spectra before and after breaking. Consistent with the observation on the frequency spectra, shorter wave components ($k/k_p = 1.2 \sim 4.0$) lose energy during wave breaking while longer wave components ($k/k_p = 0.4 \sim 0.9$) gain energy. Here, k_p is the wavenumber associated with the peak frequency component. Surface elevation measurements and the linear dispersion relation are used to transform the wave frequency spectra to wavenumber spectra. As nonlinearity increases, as expected, the transformed wavenumber spectra demonstrate larger discrepancies from the measured ones, indicating that not surprisingly this transformation has limited application for highly nonlinear and breaking wave groups.

Numerical tests using a simple eddy viscosity model to simulate energy dissipation in breaking waves are conducted. Although the eddy viscosity model fails to simulate detailed spectral changes after wave breaking, the character of the energy loss and gain across the spectrum is captured.

1 Introduction

Breaking waves play an important role in upper ocean dynamics. Wave breaking limits wave height and dissipates wave energy. It also enhances gas and heat exchange between air and sea by entraining air bubbles into the water, spray into the stmosphere, and generating surface turbulence.

Our understanding of breaking waves has been advanced through numerous studies (e.g. Rapp and Melville, 1990; Perlin et al., 1996; Melville et al., 2002; Banner and Peirson, 2007; Drazen et al., 2008; Tian et al., 2008 & 2009). Lab experiments serve as the most reliable method in the study of breaking waves, as numerical simulations fail or cannot fully represent the physics subsequent to wave breaking, and field observations lack the control required for detailed studies. In lab experiments, breaking waves are generated often by focusing wave energy at desired time and space (e.g. Rapp and Melville, 1990) and by Benjamin-Feir (1967) instability (e.g. Tulin and Waseda, 1999). Both methods use wave-wave interaction, but the intrinsic governing mechanism for wave breaking may be different. In this study, we will focus mainly on breaking waves generated by frequency focusing wave groups in lab experiments.

Energy dissipation due to wave breaking is a fascinating subject. Previous studies typically include quantification of the total energy dissipated and parameterization of the energy dissipation rate (e.g. Duncan, 1981 & 1983; Rapp and Melville, 1990; Melville, 1994; Nepf et al., 1998; Wu and Nepf, 2002; Banner and Perison, 2007; Drazen et al., 2008; Tian et al., 2009). One may be also interested in how energy is dissipated across a

wave spectrum, which is often obtained with surface elevation measurements and subsequent fast Fourier transform (FFT).

Rapp and Melville (1990) examined evolution of wave frequency spectra of breaking wave groups and observed that most of the energy dissipated is from the high frequency end of the first harmonic band (i.e. $f/f_p = 1 \sim 2$). Kway et al. (1998) made similar observations for breaking wave groups of three types of wave spectra (i.e. constant-amplitude, constant-steepness, and Pierson-Moskowitz). Both studies made no attempt to quantify the spectral change due to wave breaking or the viscous related dissipation, which was shown to be significant in the determination of energy loss in breaking waves (Banner and Peirson, 2007; Tian et al., 2009).

Meza et al. (2000) estimated the free-wave energy dissipation in laboratory generated breaking waves. They argued that wave spectra close to breaking are affected likely by bound waves. Therefore, a nonlinear deterministic decomposition method was applied to try to remove bound wave effects from the wave spectra. Spectral distribution of free-wave energy dissipation was quantified by comparing directly the wave spectra before and after wave breaking. They found that almost all energy dissipation is from wave components higher than the peak frequency and a small portion ($\sim 10\%$) of the energy lost from the higher frequency wave components is gained by lower frequency components. No significant change in the vicinity of the spectral peak after breaking was observed. Energy dissipation due to viscous effects was neglected in their study.

Yao and Wu (2004) reported an experimental study on energy dissipation of unsteady wave breaking in the presence of currents. To minimize the bound wave effects on the

wave spectra, surface elevations measured far from breaking were used. In addition, measurements of incipient breaking wave groups were made to estimate energy dissipation due to friction on the tank bottom and side walls. Findings on energy loss and gain across the wave spectra due to wave breaking were generally consistent with previous studies. For breakers on strong opposing currents, lower frequency wave components were reported to gain to 40% of the energy lost in the higher frequency wave components for breakers on strong opposing currents. Little energy change at the spectral peak was observed.

The above mentioned studies on spectral change in breaking waves are based on observations of wave frequency spectra. Evolution of wavenumber spectra in breaking waves is also of interest. Often wavenumber spectra are determined from frequency spectra using the linear dispersion relation; however, the transformation may be somewhat unreliable due to the high nonlinearity present in breaking waves. Alternatively, wavenumber spectra can be measured with scanning slope sensors (Hwang et al., 1996) and of course can be computed directly from spatial measurement of surface profiles and FFT, as shown later.

In this study, observations on the evolution of both wave frequency and wavenumber spectra of breaking waves are presented. The remainder of this paper is organized as follows. Section 2 describes our experimental setup for both surface elevation measurement by wave probes and surface profile measurement with high-speed imaging. Section 3 presents our experimental results and observations on wave spectra evolution. Numerical simulations are provided in Section 4. The last section presents our conclusions.

2 Experiments

Experiments are conducted in a two-dimensional wave flume at the University of Michigan. The wave flume is 35 m long, 0.70 m wide, and filled with tap water to a depth of 0.62 m. A servo-controlled wedge-type wavemaker with auxiliary electronics is located at one end of the flume to generate wave trains; two stacks of “horsehair” mats are placed at the other end to help damp incident waves. Figure IV-1 presents a sketch of the experimental setup.

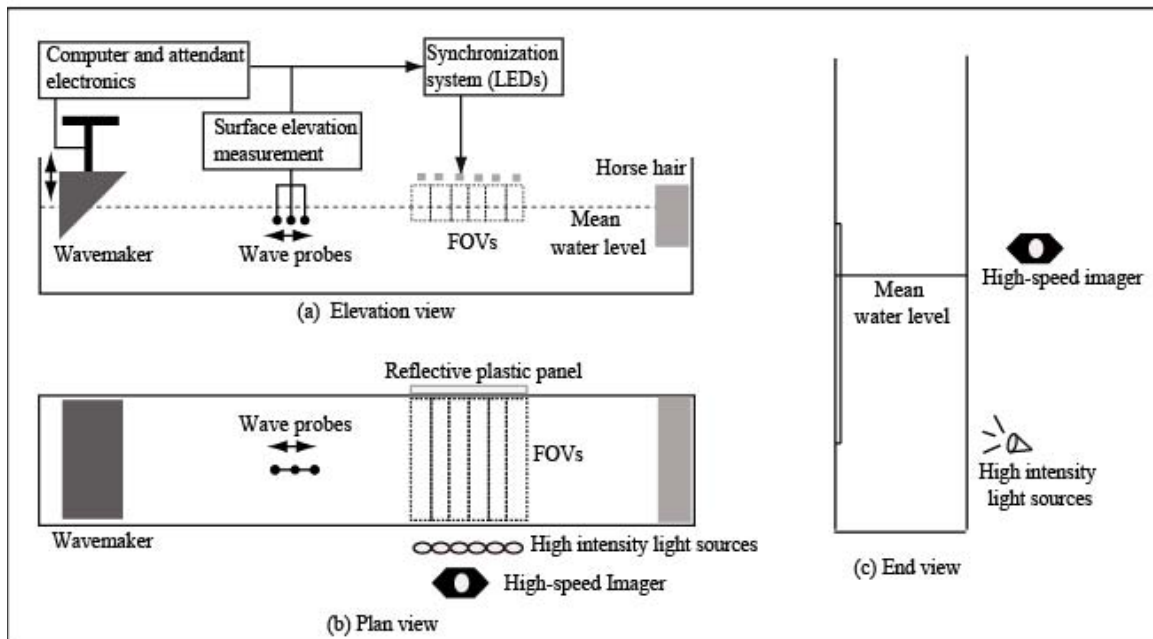


Figure IV-1 Sketch of the experimental setup (not to scale).

Frequency focusing wave groups are generated with a technique similar to that in Perlin et al. (1996). The resulting wave groups have approximately constant steepness wave spectra. By adjusting the gain (i.e. relative voltage) of the input signal to the wavemaker, both non-breaking and breaking waves can be generated. Most of our wave groups that lead to breaking have one single plunger, though very limited spilling occurs either upstream, or of less importance downstream in some cases. As shown in Tian et al. (2008, 2009), wave groups generated with this technique demonstrate high temporal and spatial repeatability. Table IV-1 presents some key parameters of the generated wave groups. As listed in the table, wave groups are categorized into five wave *packets* (i.e. W1, W2, W3, W4 and W5) based on wave group structure and center wave frequencies specified in the input signal to the wavemaker; gain values (e.g. G1 and G2) are used to distinguish a wave group from others in each of the five wave packet. In this way, each wave group is designated uniquely (e.g. W1G3 and W2G4). We note gains (e.g. G1) in one wave packet is not necessarily the same as that in another wave packet.

Temporal variation of surface elevations at desired locations along the wave flume are recorded by capacitance wave probes, along with other assisting hardware. Wave probes have two copper wires 25 cm long. The wire that senses surface elevation is located within a 1.5 mm diameter glass tube; the other is placed directly in water. Electronic circuits are designed and used to detect capacitance between the sensing wire and the water. Dynamic calibration is employed to transfer measured electric signal (i.e. volts) to surface displacement. Sampling rate for the wave probes in this measurement is set to 100Hz. Figure IV-2 presents time series of some typical surface elevation measurements.

Surface profiles as a function of time and space are measured with a Phantom high-speed imager (Model 9.1), which has a full resolution of 1632×1200 pixels and can capture images to 144k frames per second (fps) with reduced resolution (1,000 fps at full resolution). In the experiment, a backlit technique is used to illuminate the water-air interface to facilitate the measurement. The imager records surface profiles at 100 fps with a field of view of approximately 1.1 m by 0.2 m (1632×304 pixels). With a precise target of known geometry, the spatial resolution is determined to be 0.683 mm/pixel while image distortion is shown to be negligible. Figure IV-3 presents some typical images recorded in the experiment.

Only three wave probes and one high-speed imager are available during the experiment. However, surface elevation measurements by wave probes are desired at more than 30 points along the tank; in addition, surface profile measurements in a spatial domain over 10 meters is necessary to capture the complete surface profile of a wave group. Therefore, we rely on the high repeatability of the experiment (Tian et al., 2009) and a synchronizing system consisting of LEDs that is designed to align measurements from repeated runs. With a total of more than 450 runs, we achieved surface elevation measurements at 33 wave stations along the wave flume and surface profile measurements in a domain of approximately 10 meters. Additionally, we extended the spatial measurement of wave packet W4 so that the complete profiles of these wave groups are captured after wave breaking.

Most of the measured surface elevations and profiles have been used to study wave breaking criteria and kinematics and dynamics of breaking waves by Tian et al. (2008, 2009). Details of the experiment are referred to these two references. In this study, we use

the measurements to further study wave breaking onset and to quantify wave spectra change in breaking waves.

Table IV-1 Summary of primary wave parameters. f_c : center wave frequency specified in the input signal to the wavemaker; f_p : peak wave frequency; Δf : frequency bandwidth based on one-half the maximum energy associated frequencies; f_s : spectrally-weighted wave frequency (for definition see Chapter III, equation (3.2) on page 85) ; k_s : spectrally-weighted wave number; $S = k_s(\sum a_n)$: global wave steepness; $k_s x_b$: wave group focusing/breaking point relative to the mean position of the wavemaker; $f_s t_b$: wave group focusing/breaking time relative to the initial motion of the wavemaker; ν_{eddy} : estimated eddy viscosity used in the numerical simulations.

Wave Packet	Wave group ID	f_c (Hz)	f_p (Hz)	$\Delta f/f_p$	f_s (Hz)	k_s (rad/m)	S	$k_s x_b$	$f_s t_b$	$\nu_{eddy} \times 10^3$ (m ² /s)
W1	W1G1				1.019	4.223	0.315	57.8	25.6	–
	W1G2	1.105	0.952	0.307	1.022	4.247	0.381	52.5	23.5	1.011
	W1G3				1.026	4.279	0.463	48.3	21.8	1.196
W2	W2G1				1.024	4.263	0.268	57.0	31.9	–
	W2G2	1.232	0.903	0.351	1.021	4.239	0.346	57.7	31.6	0.855
	W2G3				1.023	4.255	0.413	53.5	30.1	1.174
	W2G4				1.025	4.271	0.468	53.5	30.1	1.651
W3	W3G1				1.073	4.662	0.293	69.8	32.9	–
	W3G2	1.238	1.025	0.214	1.073	4.662	0.356	65.1	31.9	0.706
	W3G3				1.080	4.721	0.442	62.3	30.6	1.122
	W3G4				1.082	4.738	0.497	62.1	30.6	1.499
W4	W4G1				1.192	5.727	0.277	99.5	59.6	–
	W4G2	1.50	1.025	0.381	1.192	5.727	0.393	96.9	57.7	0.615
	W4G3				1.201	5.813	0.544	89.7	54.4	1.027
	W4G4				1.210	5.900	0.669	83.8	53.0	1.234
W5	W5G1	1.552	1.245	0.196	1.282	6.618	0.263	85.0	44.4	–
	W5G2				1.295	6.752	0.483	79.1	42.4	0.549

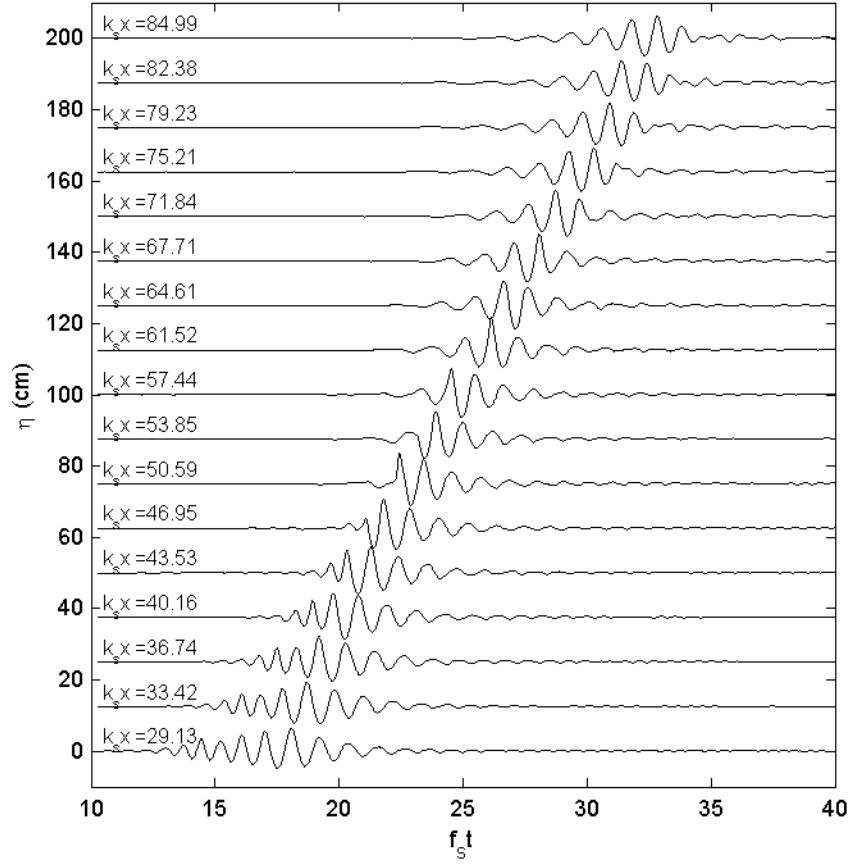


Figure IV-2 Typical surface elevations measured with wave probes along the tank (W1G3). The horizontal axis is normalized time, $f_s t$. Locations of measurements, $k_s x$, are shown on the figure. Here, f_s is the characteristic wave frequency; k_s is the characteristic wavenumber; x is the horizontal distance to the wavemaker's front face intersection with calm water. For clarity, an increment of 12.5 cm is applied to the ordinate to separate different measurements.

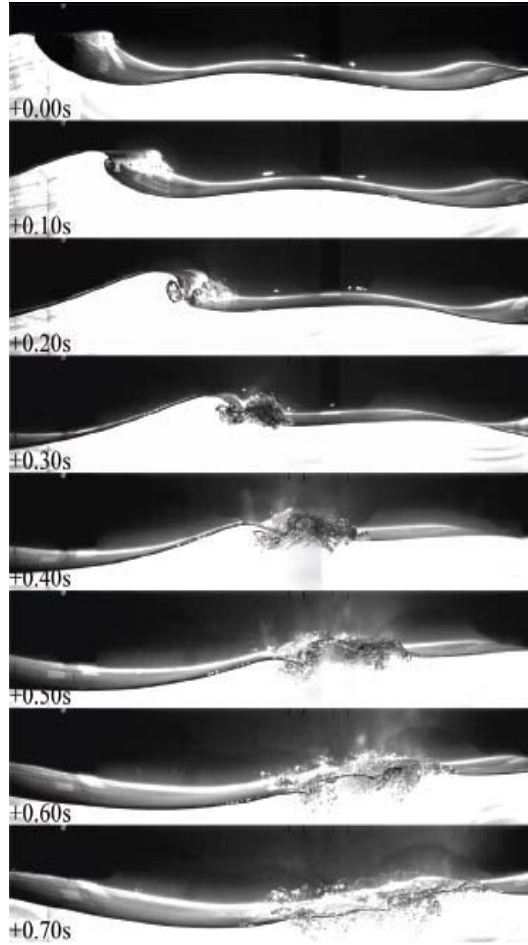


Figure IV-3 Examples of recorded image for surface profile measurement (W4G3). The time stamps referenced to the top image. For images without breaking crests, the water-air interface is well defined and can be easily tracked with a simple MATLAB program (after some brightness and contrast ratio adjustments). When active breaking crests are present, a ‘mean’ water-air interface is also obvious. However, the entrained bubbles/air clouds have to be manually removed to use the MATLAB program to detect the surface profile.

3 Experimental results

3.1 Spatial evolution of wave frequency spectra

3.1.1 Non-breaking wave groups

Surface elevations measured at wave stations along the wave tank and FFT are used to obtain the wave energy density spectrum, or wave frequency spectrum for simplicity, $S(f)$. Sampling time is truncated to 40.95 s, corresponding to 4096 points, and the mean of the measurements is subtracted before applying the FFT. The forward transformation used is:

$$N(f) = \int_t^{t+T} \eta(t) e^{-2\pi i f t} dt. \quad (3.1)$$

Here, $N(f)$ is the Fourier transform of surface elevation $\eta(t)$. The wave frequency spectrum is then computed as $S(f) = 2|N(f)|^2/T$. Note $S(f)$ is a single-sided wave spectrum. At each station, three repeated measurements are used to find an average spectrum. Then, following Rapp and Melville (1990), the obtained wave frequency spectrum is smoothed by averaging over four adjacent spectral components.

Figure IV-4 (a) exhibits a typical set of wave spectra evolution for a non-breaking wave group (W1G1). As the wave group focuses, nonlinearity becomes prominent and the nonlinear wave energy transfer across the wave spectra is obvious: energy gain in the higher frequency components is significant. This rapid growth of the higher frequency wave components may be critical to the generation of steep/breaking waves. This spectral change is attributed mainly to nonlinear energy transfer and may also be related to bound wave effects.

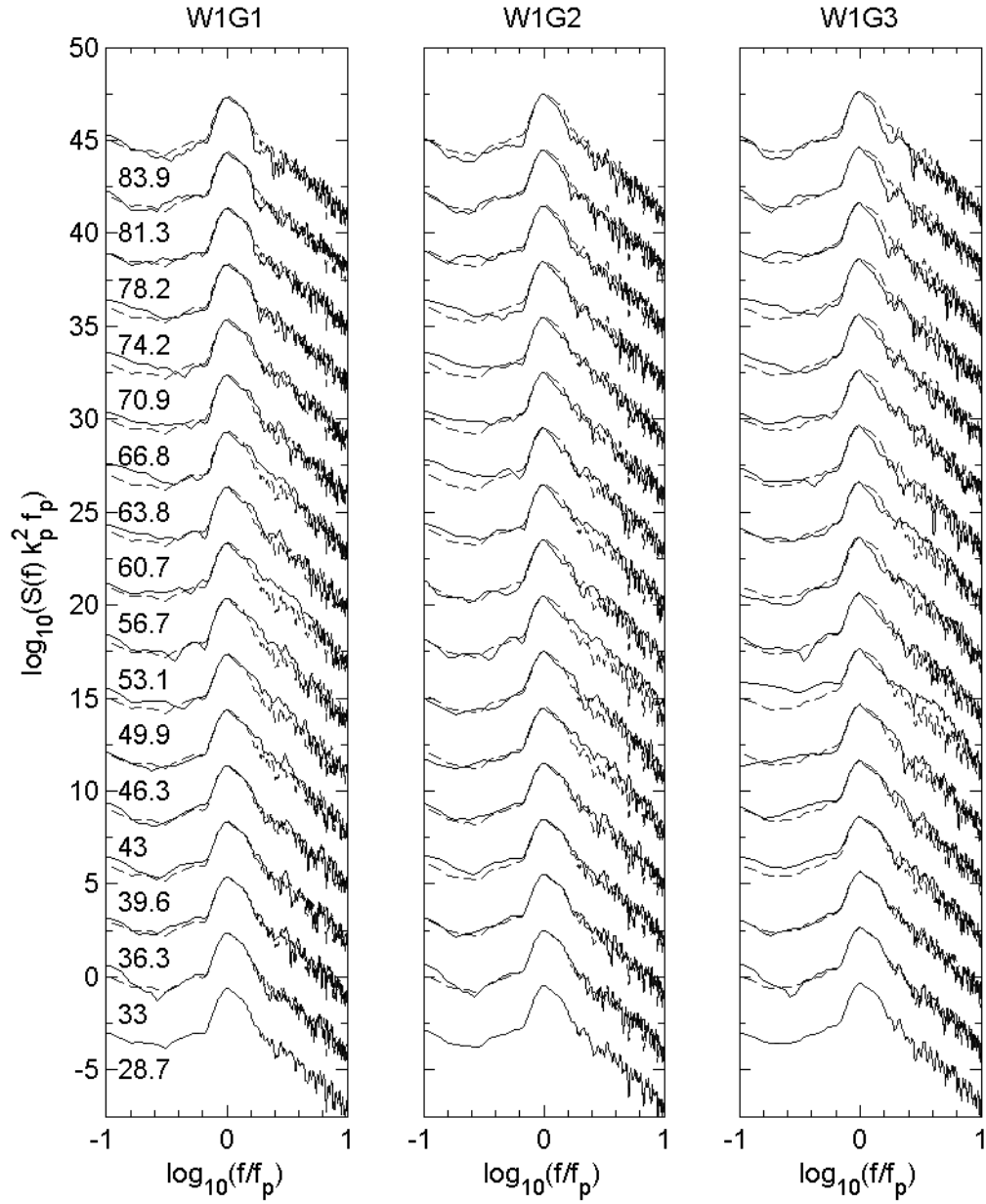


Figure IV-4 Wave frequency spectra of typical non-breaking (first column) and breaking wave groups. Locations of measurements, $k_s x$, are shown in the first column of the figure. The dash lines indicate the reference spectrum measured at the first wave station ($k_s x = 28.7$ for this case). For clarity, an increment of three is applied along the ordinate to separate the wave spectra at different locations.

We observed some energy variation in low frequency wave components ($f/f_p < 0.5$); however, no definite conclusions on energy change in this frequency range can be made based on our measurements. On the other hand, Rapp and Melville (1990) observed considerable energy gain in the low frequency components as wave groups approach the focal point and described it as ‘growth of the forced wave at the low frequencies’.

As downstream defocusing progresses, the spectral shape eventually recovers approximately its upstream reference level, indicating the reversibility of energy transfer due to nonlinearity. Some energy dissipation, especially near the spectral peak, is noticeable and slight energy loss is present at the higher end of the first harmonic band (i.e. $f/f_p = 1 \sim 2$). The latter was observed also in Rapp and Melville (1990); on the other hand, the noticeable spectral reduction near the spectral peak was barely discussed. Here, f_p is the peak frequency. This *non-breaking* energy dissipation is attributed mainly to viscous effects and the generation of contact lines on the sidewalls (Jiang et al., 2004).

We now quantify the non-breaking dissipation by integrating the wave frequency spectrum at each wave station to determine the total energy change as a function of space. Careful observations reveal that frequencies of meaningful wave components are less than 10 Hz. Therefore, our integration excludes components with frequencies higher than 10 Hz. In addition, we examine the energy in the vicinity of the spectral peak ($f/f_p = 0.95 \sim 1.1$) and term the energy dissipation in this frequency region as the *spectral peak dissipation*. The arbitrary frequency band $f/f_p = 0.95 \sim 1.1$ is chosen based on the fact that wave breaking introduces relatively less energy change in the frequency range (as shown later in Figure IV-9). Note that spectral peak dissipation is part of non-breaking energy dissipation. Figure IV-5 presents our results for the non-breaking waves. We can see that

the total non-breaking dissipation can be to 20% of the total initial energy after a distance of roughly 10 wave lengths. Also obvious in Figure IV-5 is that, in the defocusing process, the energy near the spectral peak appears to dissipate at a slower rate than the total energy. This fact is due to the nonlinear energy transfer from the higher frequency components back to the spectral peak.

One comment on the magnitude of the total non-breaking energy loss: viscous dissipation based on linear theory, i.e. exponential decay prediction (Mei, 1983), accounts for only half of the total non-breaking dissipation observed (Rapp and Melville, 1990; Tian et al., 2009). While Rapp and Melville (1990) attribute their underestimation to nonlinearity and measurement errors, Tian et al. (2009) argued that the discrepancy may be mainly due to nonlinearity and highly dissipative contact-lines and capillary waves generated by water-sidewalls interaction (Perlin and Schultz, 2000; Jiang et al., 2004).

In addition, after approximately 10 characteristic wave lengths, the total spectral peak dissipation contributes more than 20% of the total non-breaking energy dissipation. Interestingly, a much larger contribution ($\sim 70\%$) from the spectral peak is observed in wave groups W3G1 and W5G1. The variation in the contribution of the spectral peak dissipation to the total non-breaking dissipation may be related to spectral bandwidth. As shown in Figure IV-6, the total spectral peak dissipation contributes less to the total non-breaking dissipation as the wave frequency bandwidth increases. This observation indicates that, in terms of non-breaking energy dissipation, wave groups with narrow-band spectra behave more like the peak frequency wave component while each individual wave component in wave groups with broadband spectra plays an approximately equal role (see the more uniform spectral distribution of non-breaking dissipation for W4G1 in

Figure IV-8). To the best of our knowledge, a similar observation on the frequency bandwidth effect on spectral peak dissipation has not been reported previously.

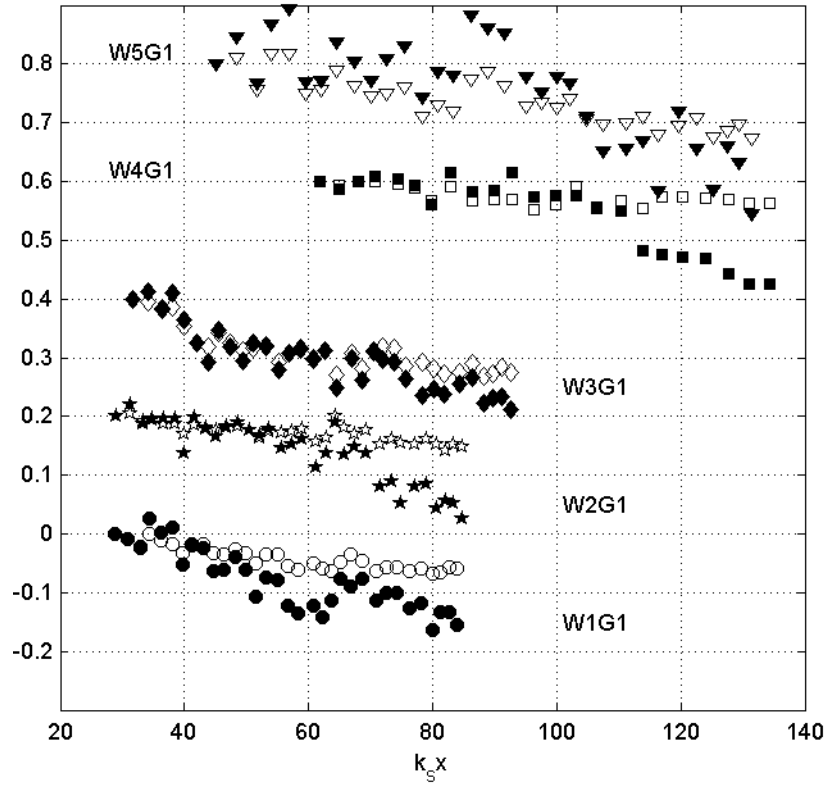


Figure IV-5 Energy dissipation as a function of space for non-breaking wave groups. Solid symbols: $\Delta E_0(x)/E_0(x_1)$; open symbols: $\Delta E_1(x)/E_0(x_1)$. Here, $\Delta E_i(x) = E_i(x) - E_i(x_1)$ with $i = 0$ and 1 . $E_0(x)$ and $E_1(x)$ are the total energy and the energy near the spectral peak ($f/f_p = 0.95 \sim 1.1$), respectively. x_1 indicates the location of the first measurement station. For clarity, an increment of 0.2 is applied to separate different wave groups along the ordinate.

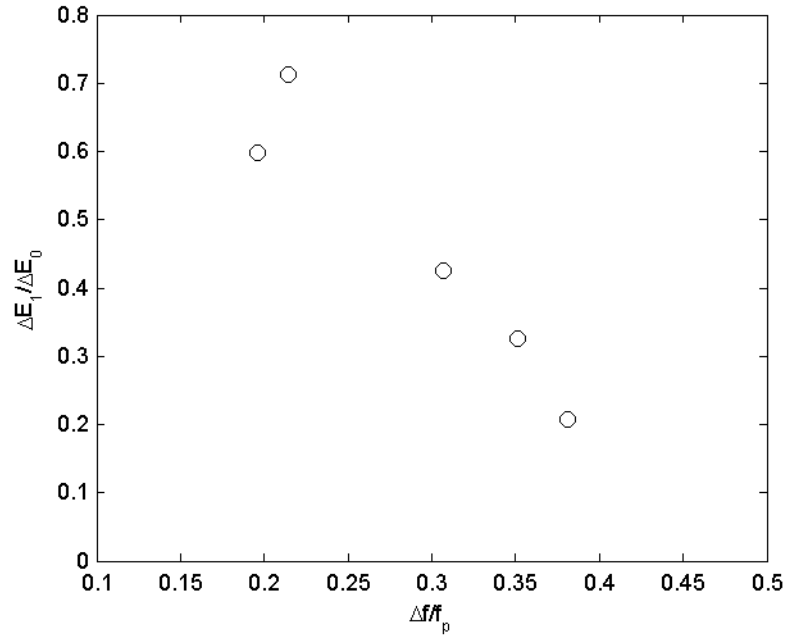


Figure IV-6 Frequency bandwidth effect on spectral peak dissipation. ΔE_l and ΔE_0 are the total spectral peak dissipation and the total non-breaking dissipation, respectively, both averaged over the last four measurements for each non-breaking wave group in Figure IV-8.

3.1.2 Breaking wave groups

Figure IV-4 (b) and (c) present typical wave frequency spectra evolution of two breaking wave groups (W1G2 and W1G3). As the wave groups approach breaking, similar spectral change is observed to that of a non-breaking wave group. However, when wave groups propagate downstream after breaking, their spectral shape does not return to the upstream reference level. Wave components of frequencies higher than the spectral peak appear to lose energy, as a result of both non-breaking loss (i.e. viscous damping and contact-line dissipation) and wave breaking. As wave breaking intensifies (e.g. W1G3 versus W1G2),

more energy loss is observed. While the energy loss near the spectral peak ($f/f_p = 0.95\sim 1.1$) may be mainly due to viscous and contact-line dissipation, the energy loss of the higher frequency wave components ($f/f_p = 1.1\sim 2.0$) may be attributed primarily to wave breaking. Rapp and Melville (1990), for example, observed that most of the total energy loss was in the higher frequency end of the first harmonic band (i.e. $f/f_p = 1 \sim 2$) and the second harmonic band (i.e. $f/f_p = 2 \sim 3$). The study of free wave energy dissipation of laboratory breaking waves (Meza et al., 2000) showed that most energy dissipation comes from wave components of frequencies between $1.0 f_p$ and $3.25 f_p$ for spilling breakers and $1.2 f_p$ and $2.5 f_p$ for plungers. In a more recent study, Yao and Wu (2004) observed significant energy loss in the frequency range between $1.2 f_p$ and $2.5 f_p$ due to breaking waves on currents. In contrast to the higher frequency bands, our measurements show that lower frequency wave components ($f/f_p = 0.65\sim 0.95$) may gain some energy after wave breaking.

We quantify the energy change in the two frequency bands for the breaking wave groups: the first one is the frequency range $f/f_p = 0.65\sim 0.95$ and the second one is $f/f_p = 1.1\sim 2.0$. The arbitrary divisions are based mainly on the observations discussed above. Figure IV-7 provides energy changes in the two frequency bands for five violent breaking wave groups. For comparison, the corresponding energy changes of five non-breaking wave groups also are presented. In general, for the non-breaking wave groups, the energy variation in the two frequency bands remains relatively small in comparison with the total energy loss. For breaking wave groups, the total energy loss increases significantly after wave breaking, confirming that breaking dissipates considerable amounts of energy in addition to the non-breaking dissipation. The higher frequency band obviously loses large

amount of energy immediately after wave breaking and the loss is nearly that of the total energy dissipated. On the other hand, the lower frequency band appears to gain some energy (a few percent of the total energy) after breaking. Note that the overall energy dissipation by viscous damping and breaking exceeds $1/3$ in some violent cases.

An interesting observation for some breaking wave groups is that, compared to the dissipation rate of the non-breaking wave groups and measurements upstream of breaking, the total energy, as well as energy in the higher frequency band, appear to be dissipated at a much lower rate after wave breaking. The same phenomenon can be seen in the experiments by Rapp and Melville (1990, e.g. Figure 11 and Figure 13), although they did not mention this. We are not sure about what causes the decrease in the dissipation rate after wave breaking, but the obvious choice is the reduction in nonlinearity.

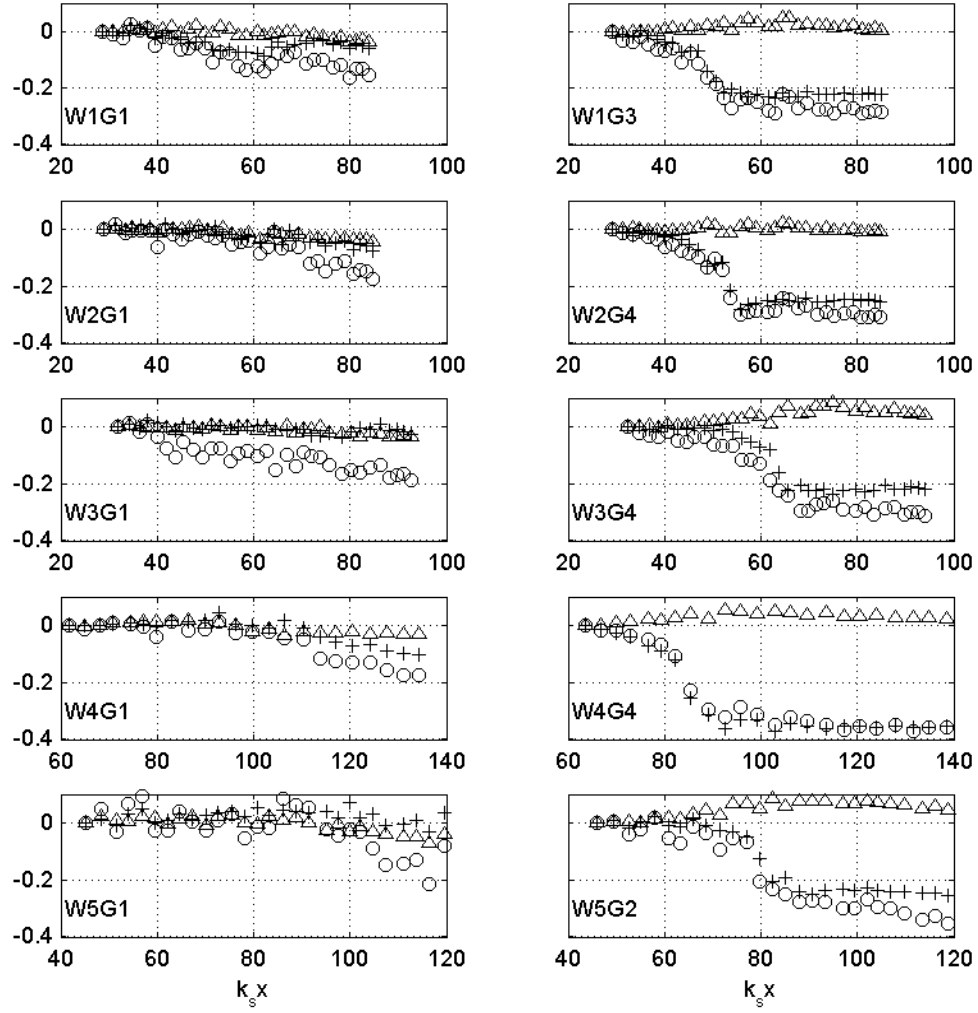


Figure IV-7 In the right column of the figure, energy dissipation as a function of space for breaking wave groups (only five most violent breaking wave groups) are shown. For comparison, results of the non-breaking wave groups are also provided (left column). Open circles: $\Delta E_0(x)/E_0(x_1)$; triangles: $\Delta E_2(x)/E_0(x_1)$; plusses: $\Delta E_3(x)/E_0(x_1)$. Here, $\Delta E_i(x) = E_i(x) - E_i(x_1)$ with $i = 0, 2$ and 3 . $E_0(x)$: the total energy; $E_2(x)$: energy in frequency range $f/f_p = 0.65 \sim 0.95$; $E_3(x)$: energy in frequency range $f/f_p = 1.1 \sim 2.0$. x_1 indicates the location of the first measurement station.

3.1.3 Spectral distribution of energy dissipation by frequency

In this study, surface elevations measured at stations before and after wave breaking are used to determine the spectral distribution of energy dissipated due to wave breaking. One may obtain this spectral distribution by comparing wave frequency spectra immediately upstream and downstream of breaking. Non-breaking dissipation has minimal effect over this short distance; ignoring this minimal change was adopted by Meza et al. (2000). According to Meza et al. (2000), wave spectra at locations near breaking vary considerably in lower and higher frequencies due to bound waves. Therefore, special treatment, i.e. bound wave removal, is necessary. Alternatively, Yao and Wu (2004) proposed to use wave frequency spectra measured far from breaking, where they assumed few bound waves were present. In this method, the spectral distribution of the non-breaking dissipation of an incipient breaking wave group is estimated first. Then the spectral difference of a breaking wave group, representing both non-breaking and breaking dissipation, is estimated accordingly. Finally, the spectral distribution of energy dissipation due to wave breaking can be determined by comparing the two estimations.

We employ the second technique to determine the spectral distribution of energy dissipated due to wave breaking. Accordingly, we first present the frequency spectra difference for the five non-breaking wave groups in Figure IV-8. In these estimations, measurements at the first three upstream and the last three downstream wave stations, far from focusing points, are used. Details of the locations of the wave stations are provided in Figure IV-14 later. The mean spectral difference is found as:

$$\Delta S(f) = \frac{S_N(f) + S_{N-1}(f) + S_{N-2}(f) - S_1(f) - S_2(f) - S_3(f)}{3}. \quad (3.2)$$

Here, the subscript represents the station number where N represents the last station. The estimated mean spectral difference is normalized by the spectral peak of the upstream reference spectrum. As shown in Figure IV-8, the energy of wave components just above the peak decreases significantly (to 25%), indicating that non-breaking energy dissipation is not negligible. In addition, most non-breaking energy loss appears in the vicinity of the spectral peak ($f/f_p = 0.95 \sim 1.1$) for wave groups with narrower bandwidth (e.g. W3G1 and W5G1); on the other hand, for wave groups W2G1 and W4G1, non-breaking energy loss distribution is relatively more uniform across the frequency spectrum, ranging from $0.75 f_p$ to $2.0 f_p$. As mentioned before, this may be related to the frequency bandwidth effect.

Similarly, the spectral difference for the breaking groups is estimated with the first and the last three wave probe measurements. Following Yao and Wu (2004), we subtract the non-breaking dissipation distribution shown in Figure IV-8 from the spectral difference of the corresponding breaking wave groups and the spectral distribution of energy dissipated due to wave breaking is isolated approximately and provided in Figure IV-9. In general, wave breaking is an overall energy sink that causes wave components in the higher frequency range (roughly $f/f_p = 1.1 \sim 2.0$) lose significant energy, and the lower frequency wave components ($f/f_p = 0.65 \sim 0.95$) gain some energy as a result of wave breaking. These conclusions are qualitatively consistent with previous studies (Meza et al, 2000; Yao and Wu, 2004).

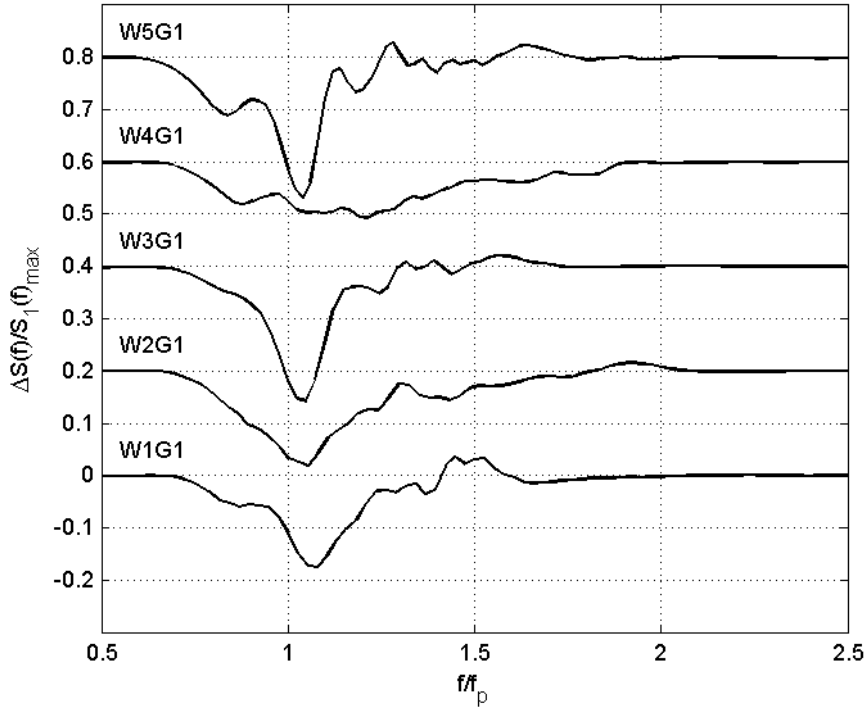


Figure IV-8 Spectral distribution of the non-breaking dissipation. $S_1(f)_{max}$ indicates the spectral peak of the reference wave spectrum measured at the first wave station. For clarity, an increment of 0.2 is applied to separate different wave groups.

On the other hand, our results shows that energy change near the spectral peak ($f/f_p = 0.95 \sim 1.1$) due to wave breaking is less predictable. As shown in the figure, the spectral peak itself does not gain or lose significant amounts of energy for most wave groups except W5G2, whose spectral peak is reduced by more than 10% due to wave breaking while there is minimal energy change at $f/f_p \approx 0.95$. In laboratory experiments, this loss in the spectral peak is seldom reported, but it is common in field measurements (e.g. Young and Babanin, 2006). We are not sure about the cause(s) but mention that the downstream wave spectra demonstrate a large spectral peak downshift for wave group W5G2. Another interesting observation is that there is an energy gain above the spectral peak (f/f_p

= 1.0~1.1) for some wave groups, e.g. wave packet W2. No similar observations have been reported before and this is not understood.

Based on Figure IV-9, total energy dissipation due to wave breaking, as well as energy gain and loss across the spectrum, are estimated and listed in Table IV-2. Surprisingly, we find that 20% to 50% of the energy dissipated in the high frequency wave components transfers to the lower frequency waves. The energy gain-loss ratios are generally greater than those of previous studies (Meza et al., 2000; Yao and Wu, 2004). We note that Meza et al. (2000) focused on free wave energy dissipation in breaking waves while Yao and Wu (2004) were interested in energy dissipation of unsteady breaking waves on currents. In addition, more surprising, the energy gain-loss ratios seem to have no apparent dependence on wave breaking strength. Although the details of the energy losses and gains are not well understood, the trends are the same. And the fact that the magnitudes do not track with breaking intensity, as is evident in Table IV-2, is assumed related to the focusing process itself.

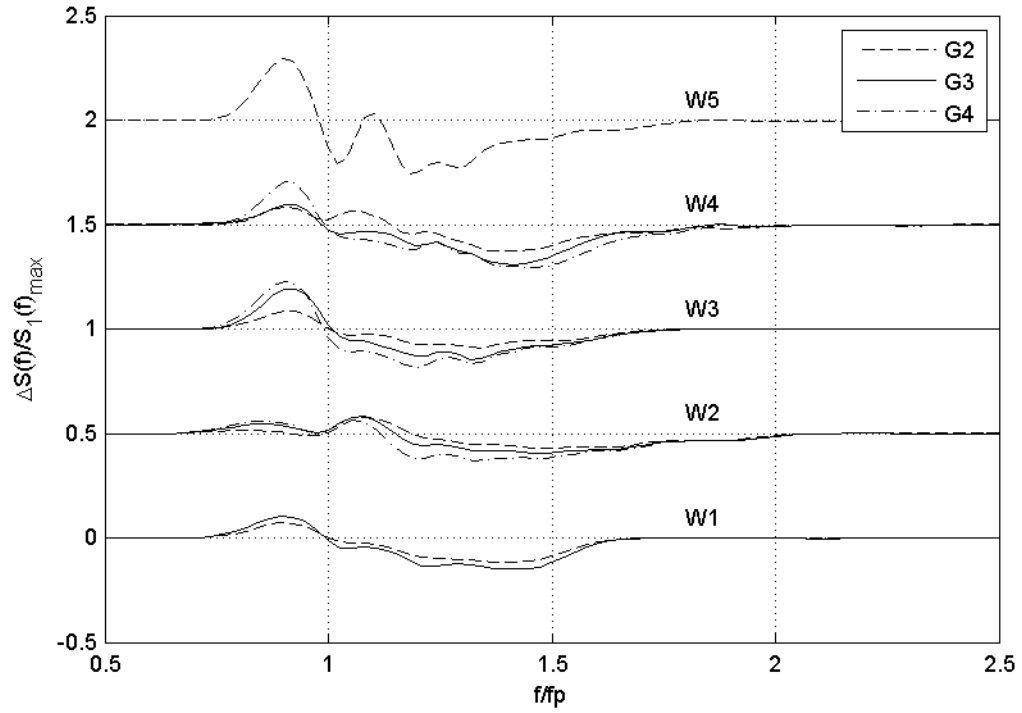


Figure IV-9 Spectral distribution of energy dissipation due to wave breaking. $S_1(f)_{max}$ indicates the spectral peak of the reference wave spectrum measured at the first station. For clarity, an increment of 0.5 is applied to separate the five wave packets. Results of wave groups in each wave packet are plotted together and distinguished by the gain value, i.e. G2, G3 and G4.

Table IV-2 Normalized energy loss and gain due to wave breaking. ΔE_{pos} represents integration of the positive portion of the spectral distribution of energy dissipated due to wave breaking (essentially all energy gain in low frequency band) and ΔE_{neg} for negative portion (essentially all energy loss in high frequency band). ΔE_{tot} represents the overall energy loss due to wave breaking. ΔE_{pos} , ΔE_{neg} and ΔE_{tot} are all normalized by the total energy at the reference wave station, $E_0(x_1)$.

Wave groups	ΔE_{pos} (%)	ΔE_{neg} (%)	$\Delta E_{tot} = \Delta E_{pos} + \Delta E_{neg}$ (%)	$R = -\Delta E_{pos} / \Delta E_{neg}$ (%)
W1G2	3.07	-12.77	-9.70	24.03
W1G3	4.41	-17.34	-12.93	25.42
W2G2	2.76	-8.83	-6.07	31.23
W2G3	3.86	-12.45	-8.59	31.03
W2G4	3.82	-17.13	-13.31	22.28
W3G2	4.15	-11.79	-7.65	35.17
W3G3	8.35	-17.33	-8.97	48.21
W3G4	9.48	-22.12	-12.65	42.84
W4G2	4.10	-11.78	-7.68	34.79
W4G3	3.45	-19.17	-15.72	17.99
W4G4	6.54	-24.61	-18.07	26.59
W5G2	11.17	-27.00	-15.83	41.38

3.2 Temporal evolution of wavenumber spectra

Surface profiles measured with high-speed imaging are used to examine the temporal evolution of wavenumber spectra. For this purpose, complete surface profiles of a wave group (from the wave group front to the trailing end) have to be measured. Due to the time consuming tedious effort required, this measurement is conducted for wave groups W4G1, W4G2, W4G3 and W4G4 only. Wavenumber spectra are obtained by applying the fast Fourier transform to the measured surface profile (2048 spatial points are used and the mean of the record is subtracted before applying the FFT).

Figure IV-10 provides the temporal evolution of the wavenumber spectra for one non-breaking and three breaking wave groups. As the non-breaking wave group propagates, energy changes of the shorter wave components in the spectra are observed; however, the changes are less evident as compared to the obvious wave frequency spectra variations. After the wave group focuses, the wavenumber spectrum recovers approximately to the reference spectrum, though some difference in the shorter wave components is present (at time $f_s(t-t_b) = 3.6$ as shown in the figure. Here, t_b is the time when waves focus/break; see Table IV-1 for details). For the two stronger breaking wave groups, W4G3 and W4G4, shorter wave components ($k/k_p = 1.2 \sim 4.0$) lose noticeable amounts of energy and longer wave components ($k/k_p = 0.4 \sim 1.0$) gain some energy. As for the less violent breaking group, W4G2, the energy loss in the shorter wave components is noticeable but the energy gain in the longer wave components is not immediately evident, primarily due to the fact that the viscous dissipation of these longer wave components is greater than their energy gain from the shorter wave components in this case (see comments on Figure IV-11 in the next paragraph).

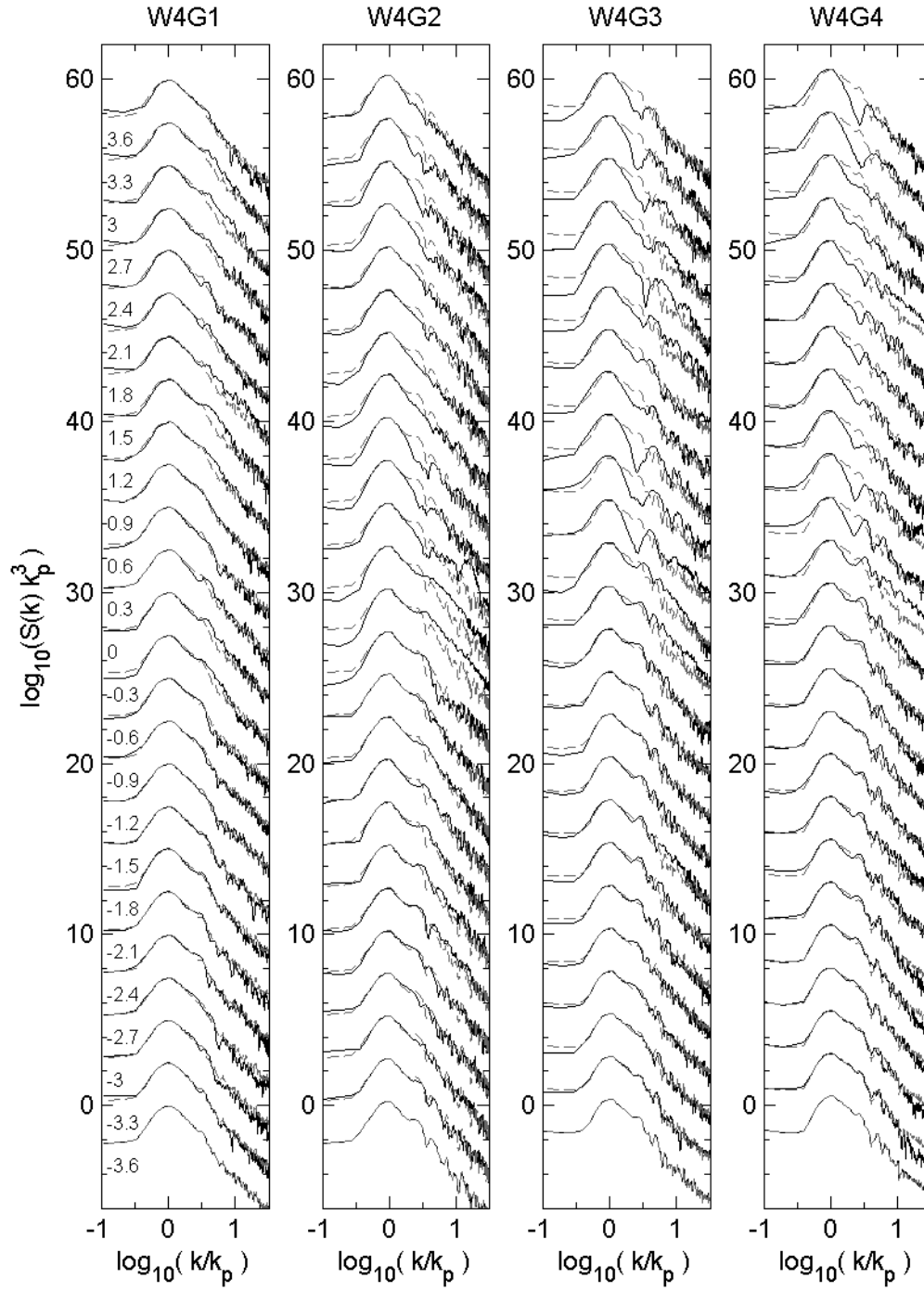


Figure IV-10 Temporal evolution of the measured wavenumber spectra. Nondimensional time relative to wave breaking/focusing, i.e. $f_s(t-t_b)$, is provided and shown in the results of W4G1. Here, t_b represents wave breaking/focusing time. Dash lines represent the reference wavenumber spectra measured at $f_s(t-t_b) = -3.6$. For clarity, an increment of 2.5 is applied to the ordinate values to separate the measured spectra.

To determine the mean spectra difference we use the spectra before and after wave breaking/focusing. First, wavenumber spectra are averaged over one characteristic wave period ($f_s(t-t_b) = -3.6 \sim -2.6$ and $f_s(t-t_b) = 2.6 \sim 3.6$), respectively. Then the wavenumber spectral redistribution due to viscous effects and wave breaking is the difference between the two averaged wave spectra. They are presented in Figure IV-11. As shown, the two stronger breaking groups exhibit similar results while the mild breaking and the non-breaking cases resemble each other; however, it appears that the mild breaking case is as expected shifting toward the two stronger breaking conditions. Also obvious in the figure is that the longer waves in the range of $k/k_p = 0.4 \sim 1.0$ gain some energy for two stronger breaking groups, W4G3 and W4G4, while the shorter waves in $k/k_p = 1.2 \sim 4.0$ lose energy. The mild breaking wave group, W4G2, showed much less energy loss in the longer wave components than the non-breaking wave group, W4G1, indicating that the longer wave components in the mild breaking condition also gained energy from the shorter waves as a result of wave breaking.

Since the surface profiles are measured near wave breaking/focusing ($f_s(t-t_b) = \pm 3.6$), we expect the presence of bound waves in the wavenumber spectra. Therefore, these spectral differences may not represent the wavenumber spectral distribution of energy dissipated due only to wave breaking.

As we have both spatial and temporal spectra information of four wave groups, we choose to investigate the transformation from one to the other, i.e. we examine the functionality of the transformation from wave frequency to wavenumber spectrum using the linear dispersion relation. We attempted first to conduct the transformation with a more pedestrian approach, i.e. multiplying the wave frequency spectrum by the group

velocity to obtain the wavenumber spectrum (see Ochi, 1998, page 24). However, we observed large discrepancies on a frequency-by-frequency basis, although the total energy is the same across the temporal and spatial spectra as it must be.

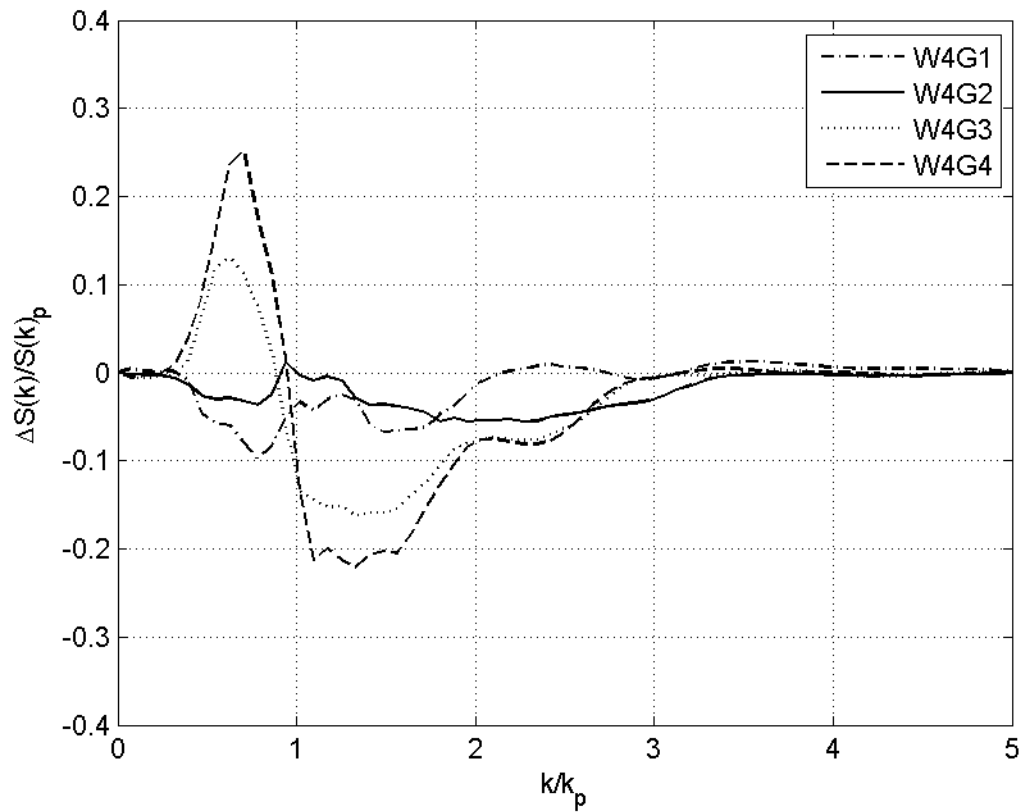


Figure IV-11 Mean wavenumber spectral differences before and after wave breaking/focusing. $S(k)_p$ represents the mean of the wavenumber spectral peak before wave breaking.

Therefore, we used a second technique for the transformation. Surface profiles as a function of time and space are generated numerically using the wave probe measurements, the linear finite water-depth dispersion relation and Fourier analysis (for details, see Tian et al, 2008). For a fair comparison, wave probe locations for surface elevation measurement are related to the time when spatial surface profiles are measured, i.e. $t = (x_p - x_b)/C_{gs} + t_b$. Here, x_p represents the spatial locations of the wave probe measurements; x_b represents the wave breaking/focusing locations; C_{gs} is the characteristic wave group velocity; t_b represents wave breaking/focusing time. Figure IV-12 presents a comparison of the measured and the predicted surface profiles for W4G4. The comparison is reasonable considering the high nonlinearity present and that a violent plunging breaker was present during the wave group evolution.

Wavenumber spectra are obtained then with the predicted surface profiles and FFT (termed *transformed* wavenumber spectra), $S(k) = 2|N(k)|^2/L$. Here, the spatial domain is discretized to 2048 points for FFT. Note that $S(k)$ is a single sided wavenumber spectrum and $N(k)$ is the Fourier transform of the surface elevation $\eta(x)$, similar to Equation (3.1) but in the spatial domain. Then the wavenumber spectra are compared with the ones based on the measured surface profiles (termed *measured* wavenumber spectra). Figure IV-13 presents a comparison of the measured and the transformed wavenumber spectra before and after wave breaking/focusing. In general, as nonlinearity is increased (i.e. larger gain), as expected, the discrepancy becomes larger between the transformed and the measured wavenumber spectra. Comparing to the measured wavenumber spectra, the transformed ones have a smaller energy density in the range $k/k_p = 1.0 \sim 3.0$. This discrepancy is attributed mainly to nonlinearity and it may indicate that this

transformation underestimates sharp wave crests (i.e. high frequency components in the Fourier domain), as demonstrated in Figure IV-12. Not surprisingly, our observation suggests that this transformation of wave frequency to wavenumber spectrum may have very limited application for breaking wave groups.

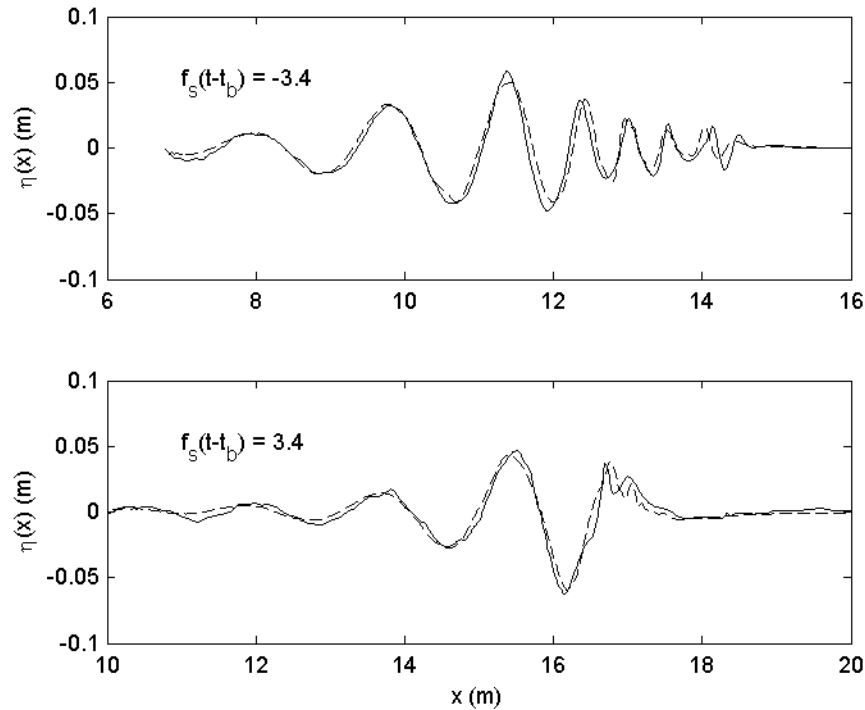


Figure IV-12 Comparison of the measured and the linear-wave-theory-predicted surface profiles before and after wave breaking for W4G4. Nondimensional time relative to wave breaking/focusing is provided on each figure. Solid lines are the measured profile at these nondimensional times and dash lines are the predicted profile at corresponding spatial locations. The profiles are used as input to the Fourier analysis, which give the wave number spectra shown later. The peaks in the linear-wave-theory predictions have been aligned to the measurements for these figures; however this does not affect the wavenumber spectra based on linear-wave-theory predictions.

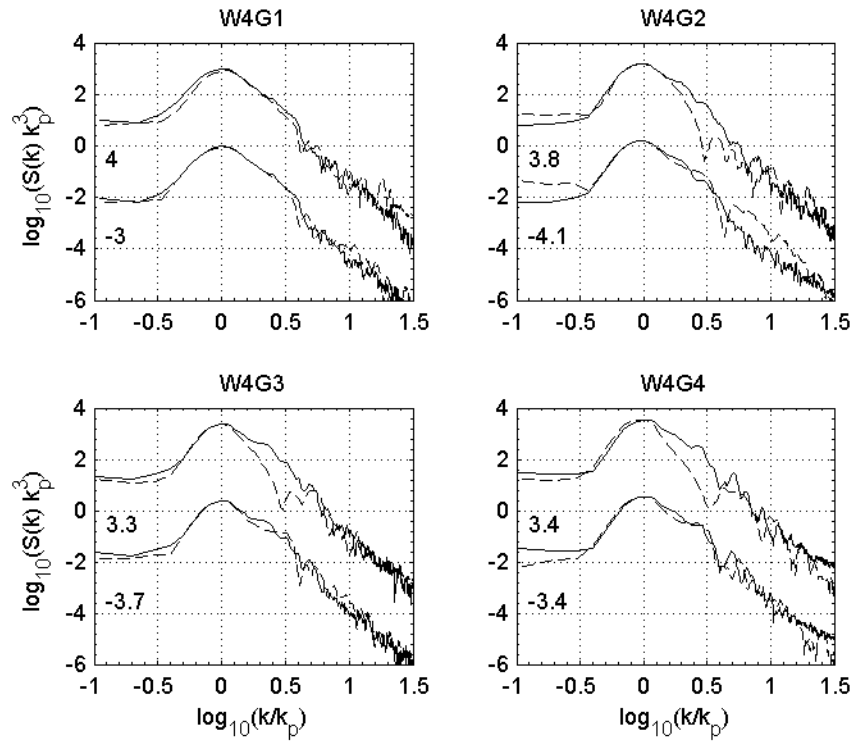


Figure IV-13 Comparison of the measured (solid lines) and the transformed (dash lines) wavenumber spectra before and after wave breaking/focusing. Nondimensional time is shown on the graphs. For clarity, an increment of 3 is applied to the ordinates in each of the four graphs.

4 Numerical Simulations

4.1 The eddy viscosity model for breaking waves

Tian et al. (2009) proposed an eddy viscosity model to simulate energy dissipation due to unsteady plunging breakers. For completeness, their model is described briefly as follows. As demonstrated in their study, under the small viscosity assumption, the leading-order (molecular) viscous effect can be incorporated into free surface boundary conditions, (4.1) and (4.2):

$$\frac{\partial \eta}{\partial t} = \frac{\partial \phi}{\partial z} + 2\nu \frac{\partial^2 \eta}{\partial x^2} \quad \text{on } z = 0 \quad (4.1)$$

$$\frac{\partial \phi}{\partial t} = -g\eta + 2\nu \frac{\partial^2 \phi}{\partial x^2} \quad \text{on } z = 0. \quad (4.2)$$

Here, ϕ is the velocity potential; g is the gravitational acceleration. η is the free surface, and ν is the kinematic viscosity. x and z are, respectively, the horizontal and vertical coordinates with z defined positive upwards from the mean surface.

Tian et al. (2009) used the two free surface boundary conditions to represent energy dissipation due to wave breaking by replacing the kinematic viscosity, ν , with the turbulent eddy viscosity, ν_{eddy} . To apply this model, they first estimated the magnitude of the eddy viscosity with wave breaking time and length scales based on dimensional analysis,

$$\nu_{eddy} = \theta h l_{br} / t_{br} . \quad (4.3)$$

Here, h is the height of the falling breaking crest as defined by Drazen et al. (2008); l_{br} is a horizontal breaking length scale; t_{br} is a breaking time and θ is a proportional constant, $\theta = 0.1$ as determined in Tian et al. (2009). The estimated eddy viscosity is on the order of $10^{-3} \text{ (m}^2\text{s}^{-1}\text{)}$ and shows a strong dependence on wave breaking strength, as listed in Table IV-1.

The eddy viscosity model is incorporated then into a numerical model based on an asymptotic expansion in small wave steepness (Choi, 1995). The following two nonlinear equations for the surface elevation, $\eta(x,t)$, and the velocity potential at the free surface, $\Phi(x,t)$ are obtained when the eddy viscosity terms are included:

$$\frac{\partial \eta}{\partial t} = \sum_{n=1}^{\infty} Q_n [\eta, \dots] + 2\nu_{eddy} \frac{\partial^2 \eta}{\partial x^2}, \quad (4.4)$$

$$\frac{\partial \Phi}{\partial t} = \sum_{n=1}^{\infty} R_n [\eta, \Phi] + 2\nu_{eddy} \frac{\partial^2 \Phi}{\partial x^2}, \quad (4.5)$$

where Q_n and R_n of $O(ka)^n$ are the n th-order nonlinear terms that can be found through explicit recursion formulas (e.g. see Choi et al., 2005). The right-hand sides of equations (4.4) and (4.5) are truncated to the third order here and are solved numerically with a pseudo-spectral method based on the fast Fourier transform and a fourth-order Runge-Kutta method to integrate in time.

Tian et al. (2009) demonstrates that the eddy viscosity model works well in simulating total energy loss due to wave breaking and predicts well the surface elevation after wave breaking. Details can be found in the reference.

4.2 Evolution of the wave spectra

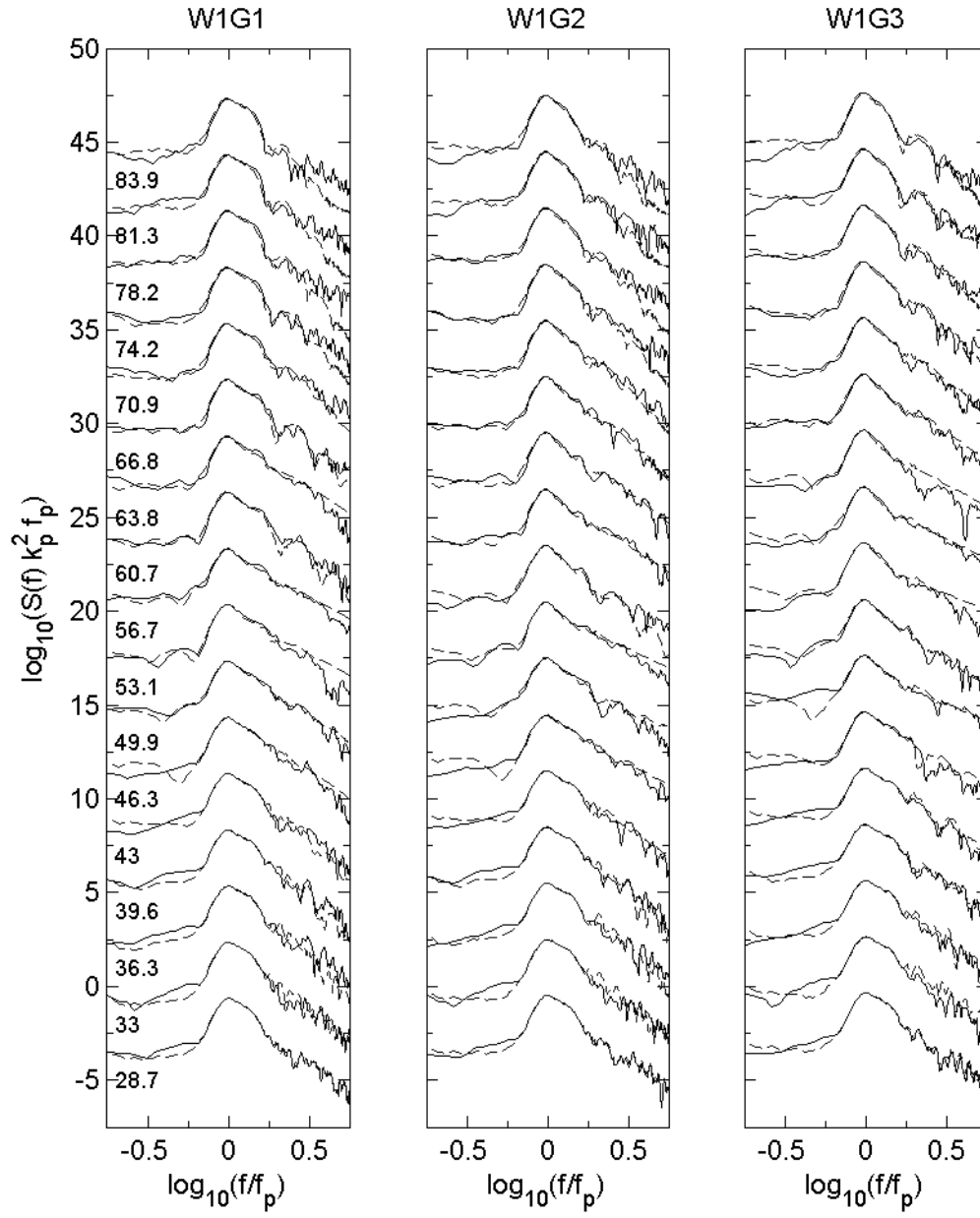
In this study, we evaluate the eddy viscosity model and its ability to predict the spectral evolution of nonlinear and breaking waves. Based on wave probe measurements and Fourier analysis, initial conditions that match our experiments are generated to run the numerical tests. Only the first 512 Fourier components (corresponding to frequencies less than 12.5 Hz) are included in the initial conditions, as the higher frequency components carry negligible energy and have little effect on the wave group dynamics. Details on the generation of the initial conditions can be found in Chapter II. Comparisons of the experimental and the numerical results follow.

Figure IV-14 presents a comparison of the evolution of the wave frequency spectra based on the experimental measurements and the numerical simulations. In general, the numerical results match well the experimental measurements before and after wave breaking/focusing; the agreement near the spectral peak is better than those in other frequency ranges. Specifically, similar to the experimental measurements, significant energy increase in the high frequency components is observed as wave groups approach focusing/breaking, possibly due to nonlinear energy transfer and generation of bound waves. Just prior to wave breaking/focusing, the energy increase in the numerical results is greater typically than the measurements. As wave groups propagate further downstream beyond breaking, the numerical simulations capture major spectral changes due to viscous effects and wave breaking. However, the prediction near the spectral peak with the eddy viscosity model can be as much as 15% different from that of the measurements. Of course this discrepancy can be minimized to a low level (less than 5%) by adjusting the magnitude of the estimated eddy viscosity.

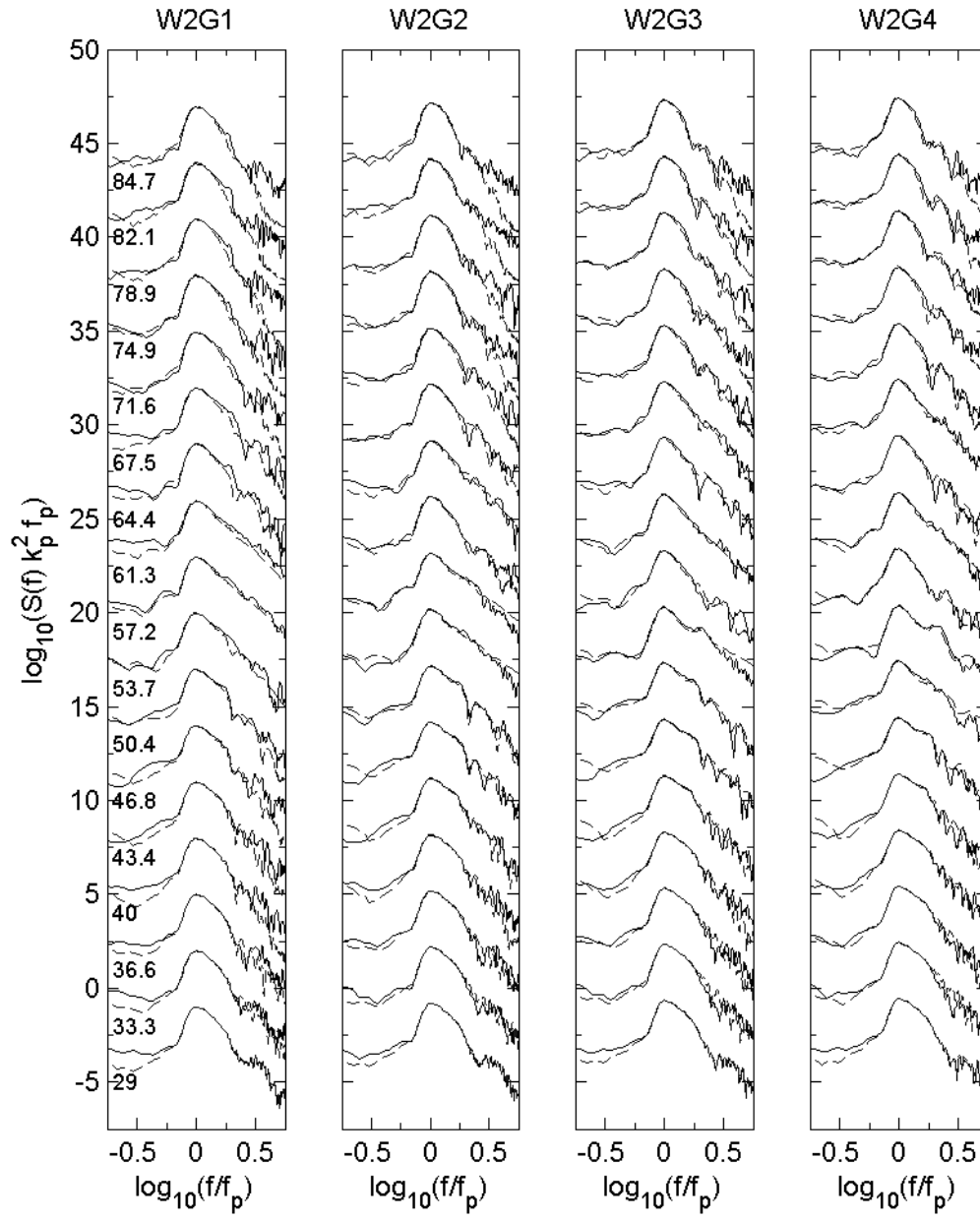
We compare the experimental and the numerical results of the wavenumber spectra evolution in Figure IV-15. In general, the numerical model captures the main characteristics of the wavenumber spectra during their evolution. However, detailed spectral changes, e.g. some discrepancy in the high wavenumber range for the most violent breaking wave group W4G4, is not captured in the numerical simulations.

We further examined numerical results of the spectral distribution of energy dissipated due to wave breaking, and these are shown in Figure IV-16. We found that the numerical results are similar in energy loss and gain behavior, but with a larger magnitude in general than the experimental results in the higher ($f/f_p > 1.1$) and the lower ($f/f_p = 0.65 \sim 0.95$) frequency ranges. In the vicinity of the spectral peak, numerical results demonstrate relatively large discrepancy from the measurements. For most wave groups (except wave packet W4), the spectral peak loses noticeable amounts of energy in the numerical prediction. These discrepancies indicate that the eddy viscosity model works effectively only in modeling the general behavior of the energy gain and loss across the wave spectrum. Considering the complicated kinematics and dynamics involved in breaking waves, the performance of this simple eddy viscosity model is much better than expected.

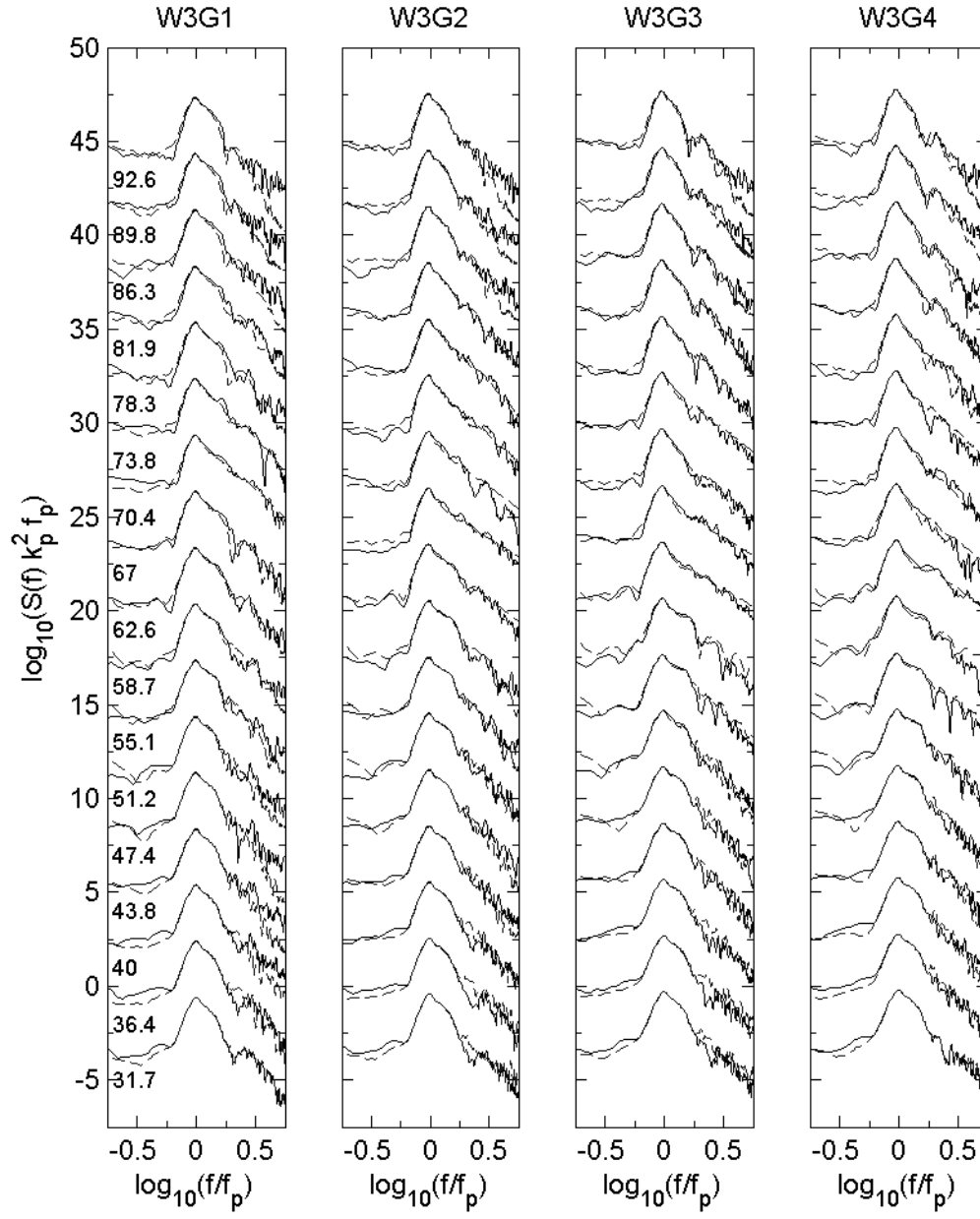
(a)



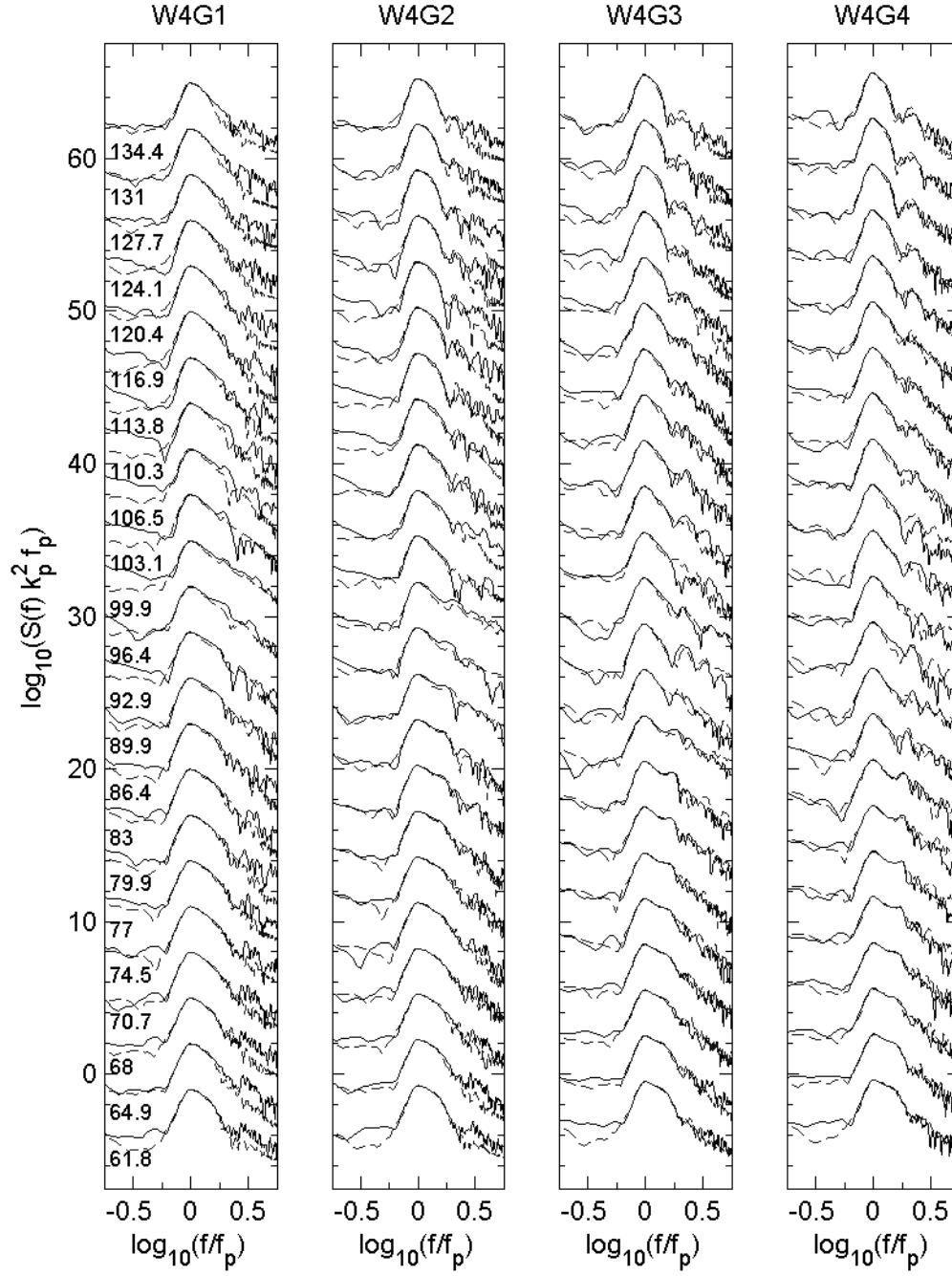
(b)



(c)



(d)



(e)

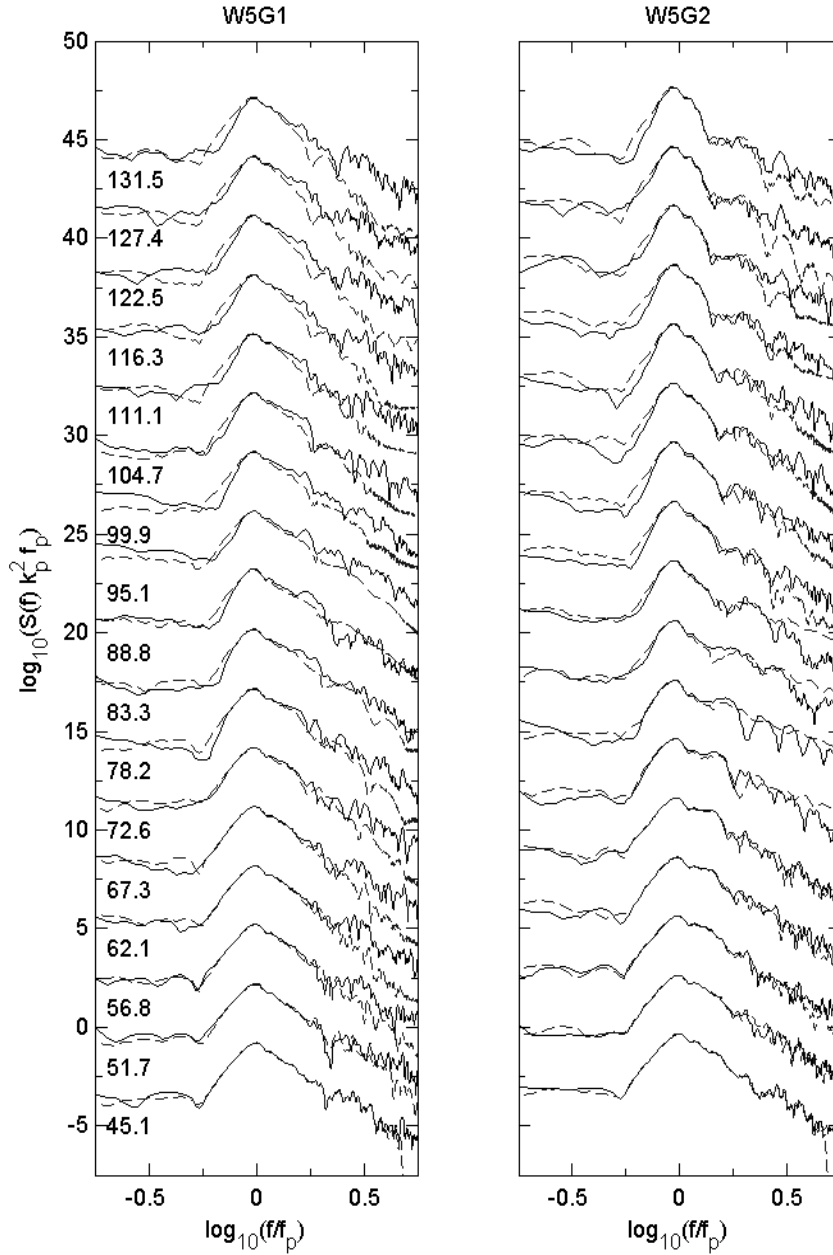


Figure IV-14 (a) through (e) provide a comparison of all the wave frequency spectra. Solid lines are based on probe measurements and dash lines are the numerical results. Nondimensional locations of the probes are provided and shown in the first column of the figures. For clarity, an increment of three is applied to the ordinates to separate the frequency spectra.

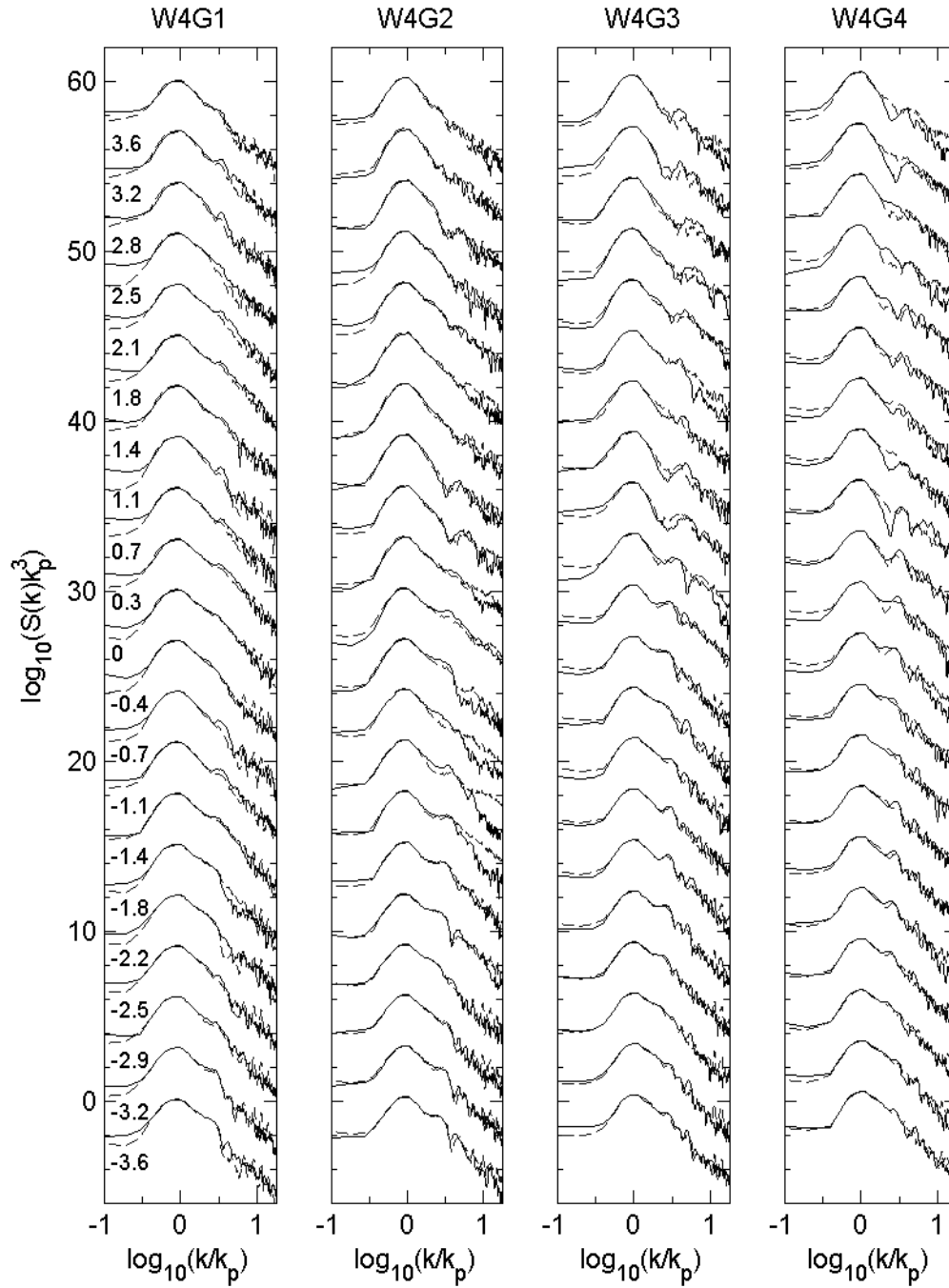


Figure IV-15 Comparison of the wavenumber spectra evolution. Solid lines are the experimental measurements and dash lines are the numerical results. Nondimensional time relative to wave breaking/focusing are provided and shown in W4G1. For clarity, an increment of three is applied to the ordinates to separate the wavenumber spectra.

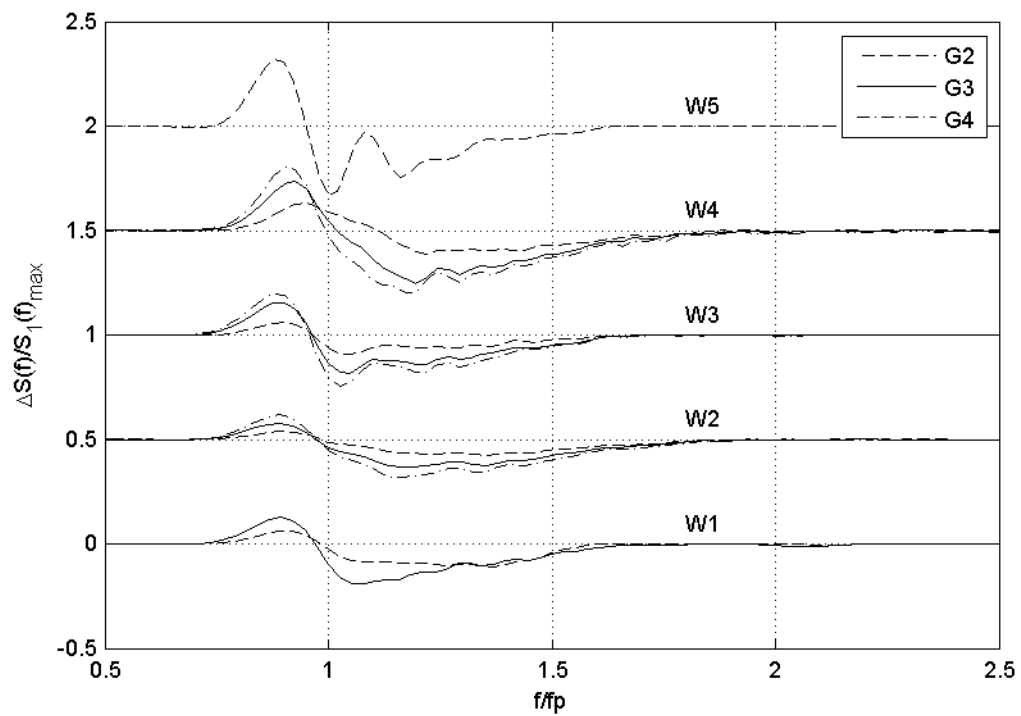


Figure IV-16 Same as Figure IV-9 but based on numerical simulations.

5 Conclusions

An experimental study on the spectral evolution of laboratory generated breaking waves is presented. Surface elevation and surface profile measurements are used to examine wave spectral evolution, and to determine spectral distribution of energy dissipated in breaking waves.

In the experiments, wave breaking is generated using frequency focusing. Temporal variation of the surface elevation is measured with wave probes at fixed locations along the wave flume while spatial variation of surface profiles is recorded with high-speed imaging.

Spatial evolution of wave frequency spectra is examined. Nonlinear energy transfer across the frequency spectra is obvious during wave focusing and defocusing. Significant energy loss due to viscous effects and contact-line damping is observed in non-breaking wave groups. More than 20% of the non-breaking energy loss is from the vicinity of the spectral peak ($f/f_p = 0.95 \sim 1.1$). More interestingly, energy loss near the spectral peak appears to depend on the frequency spectral bandwidth. To the best of our knowledge, a similar observation has not been reported previously.

Observations of frequency spectra evolution in breaking wave groups is documented also. Spectral distribution of energy dissipated due to wave breaking is determined then as the difference before and after breaking less the corresponding difference of a non-breaking wave group. Wave components in the frequency range from $1.1 f_p$ to $2.0 f_p$ lose significant energy, which contributes to most of the energy loss due to wave breaking; wave components between $0.65 f_p$ and $0.95 f_p$ appear to gain to 50% of the energy loss in

the high frequency band. The energy gain-loss ratio has no apparent dependence on breaking strength and is higher than previous laboratory results. The energy near the spectral peak may increase or decrease due to wave breaking, depending on the initial wave frequency spectrum. This finding differs from previous laboratory results but agrees with some field observations.

Spatial surface profile measurement is used to examine the temporal evolution of wavenumber spectra before and after wave breaking. Consistent generally with the observations for the frequency spectra, shorter wave components ($k/k_p = 1.2 \sim 4.0$) lose energy in breaking waves and longer wave components ($k/k_p = 0.4 \sim 0.9$) gain some energy. Wave probe measurements and the linear dispersion relation are used to transform wave frequency spectra to wavenumber spectra. As nonlinearity increases, as expected the results exhibit larger discrepancy from the measured wavenumber spectra, indicating this linear transformation has limited application for highly nonlinear breaking wave groups.

Numerical tests with a simple eddy viscosity model to simulate the energy dissipation in breaking waves are conducted. Although the eddy viscosity model fails to simulate detailed spectral change throughout the breaking process, numerical results capture the major characteristics of energy loss and gain across the spectrum, and are consistent in general with the evolution of the measured wave frequency and wavenumber spectra. Considering the complicated kinematics and dynamics in breaking waves, the performance of this simple eddy viscosity is much better than expected.

References

- BANNER, M. L. & PEIRSON, W. L. 2007 Wave breaking onset and strength for two-dimensional deep-water wave groups. *J. Fluid Mech.* **585**, 93-115.
- BENJAMIN, T. B. & FEIR, J. E. 1967 Disintegration of wave trains on deep water. 1. Theory. *J. Fluid Mech.* **27**, 417-430.
- CHOI, W. 1995 Nonlinear evolution equations for two-dimensional surface waves in a fluid of finite depth. *J. Fluid Mech.* **295**, 381-394.
- CHOI, W., KENT, C. P. & SCHILLINGER, C. 2005 Numerical modeling of nonlinear surface waves and its validation. *Advances in Eng. Mech.* 94-110, World Scientific
- DRAZEN, D. A., MELVILLE, W. K. & LENAIN, L. 2008 Inertial scaling of dissipation in unsteady breaking waves. *J. Fluid Mech.* **611**, 307-332.
- DUNCAN, J. H. 1981 An experimental investigation of breaking waves produced by a towed hydrofoil. *Proc. R. Soc. London Ser. A* **377**, 331-348.
- DUNCAN, J. H. 1983 The breaking and non-breaking wave resistance of a two-dimensional hydrofoil. *J. Fluid Mech.* **126**, 507-520.
- HWANG, P. A., ATAKTURK, S., SLETTEN, M. A. & TRIZNA D. B. 1996 A study of the wavenumber spectra of short water waves in the ocean. *J. Phys. Oceanogr.* **26**, 1266-1285.
- JIANG, L., PERLIN, M. & SCHULTZ, W. W. 2004 Contact-line dynamics and damping for oscillating free surface flows. *Phys. Fluids* **16** (3), 748-758.
- KWAY, J. H. L., LOH, Y. S. & CHAN, E. S. 1998 Laboratory study of deep water breaking waves. *Ocean Eng.* **25**, 657-676.
- MEI, C. C. 1983 *The Applied Dynamics of Ocean Surface Waves*. Wiley-Interscience, 385.
- MELVILLE, W. K. 1994 Energy-dissipation by breaking waves. *J. Phys. Oceanogr.* **24**, 2041-2049.
- MELVILLE, W. K. 1996 The role of surface-wave breaking in air-sea interaction. *Annu. Rev. Fluid Mech.* **28**, 279-321.
- MELVILLE, W. K., VERON, F. & WHITE, C. J. 2002 The velocity field under breaking waves: coherent structures and turbulence. *J. Fluid Mech.* **454**, 203-233.
- MEZA, E., ZHANG, J. & SEYMOUR, R. J. 2000 Free-wave energy dissipation in experimental breaking waves. *J. Phys. Oceanogr.* **30**, 2404-2418.

- NEPF, H. M., WU, C. H. & CHAN, E. S. 1998 A comparison of two- and three-dimensional wave breaking. *J. Phys. Oceanog.* **28**, 1496-1510.
- OCHI, M. K. 1998 *Ocean waves: The stochastic approach*. Cambridge University Press, 24.
- PERLIN, M., HE, J. H. & BERNAL, L. P. 1996 An experimental study of deep water plunging breakers. *Phys. Fluids* **8** (9), 2365-2374.
- RAPP, R. J. & MELVILLE, W. K. 1990 Laboratory measurements of deep-water breaking waves. *Phil. Trans. R. Soc. Lond. A.* **331**, 735-800.
- SONG, J. B. & BANNER, M. L. 2002 On determining the onset and strength of breaking for deep water waves. Part I: Unforced irrotational wave groups. *J. Phys. Oceanog.* **32**, 2541–2558.
- TIAN, Z. G., PERLIN, M. & CHOI, W. 2008 Evaluation of a deep-water wave breaking criterion. *Phys. Fluids* **20** (066604), 1-13.
- TIAN, Z. G., PERLIN, M. & CHOI, W. 2009 Energy dissipation in two-dimensional unsteady plunging breakers and an eddy viscosity model. *J. Fluid Mech.* (accepted)
- TULIN, M. P. & WASEDA, T. 1999 Laboratory observations of wave group evolution, including breaking effects. *J. Fluid Mech.* **378**, 197–232.
- WU, C. H. & NEPF, H. M. 2002 Breaking criteria and energy losses for three-dimensional wave breaking. *J. Geophys. Res.-Oceans* **107** (C10), 3177.
- YAO, A. F. & WU, C. H. 2004 Energy dissipation of unsteady wave breaking on currents. *J. Phys. Oceanog.* **34**, 2288-2304.
- YOUNG, I. R. & BABANIN, A. V. 2006 Spectral distribution of energy dissipation of wind-generated waves due to dominant wave breaking, *J. Phys. Oceanog.* **36**, 376-394.

Chapter V

Conclusions

In this study, experiments are conducted to investigate two-dimensional unsteady breaking waves generated by frequency focusing wave groups in finite-depth water in laboratory. An eddy viscosity model to simulate the energy dissipation in two-dimensional unsteady plunging breakers is developed. Numerical simulations are performed to facilitate the comparison to the experimental results. Major findings and conclusions are summarized as follows.

In Chapter II, an experimental and numerical study of the wave breaking criterion proposed by Song and Banner is presented by examining the growth rate of the breaking parameter, $\delta(t)$, constructed from the evolution of the total local energy density and the local wave number at the maximum surface displacement of wave groups. It is found that the breaking criterion of Song and Banner is sensitive to the choice of the local wave number, but that a particular local wave number based on local wave geometry distinguishes wave groups leading to breaking from wave groups that do not break.

The breaking/non-breaking wave generation technique used in the experiments is capable of producing wave groups with reasonable spatial and temporal repeatability. The repeatability of the generated wave groups enables us to divide the spatial domain into

smaller sub regions, each of which can be measured individually. Measurements from different runs are combined to obtain the surface elevation spatial profile during the final stages of breaking. Error analysis showed that the measurement technique can provide reasonable precision.

Local wave number computation based on both the Hilbert transform and the local wave profile is discussed; using one of the wavenumber construction techniques and the local wave profile in conjunction with the Song and Banner parameter produced reliable wave breaking predictions for our wave groups. Ratios of local potential energy to local total energy at crest maxima and trough maxima are obtained based on numerical simulations. The ratios at crest maxima decrease as the wave groups focus, while there is little variation of the ratios at trough maxima. Local energy at wave maxima for the experimental study is inferred based on numerical simulations.

For the criterion based on local wave geometry, measured surface profiles just prior to incipient breaking are used to determine the local wave steepness. Results show that the wave steepness criterion is unable to differentiate wave breaking from non-breaking for our wave groups. For Song and Banner's criterion, experimental results illustrate that the energy convergence rate at the maxima increases, and that the corresponding wave geometry steepens. The breaking parameter, $\delta(t)$, constructed from the energy convergence rate and the local wave geometry decreases after it achieves a maximum, which is smaller than the threshold for non breaking waves; on the other hand, the parameter continues growing once it surpasses the threshold for breaking conditions.

It is shown that the lead time between the parameter exceeding the threshold and incipient wave breaking increases as wave breaking intensifies. The total energy loss is related strongly to this parameter immediately prior to breaking. A similar relationship exists between the total energy loss and the value of the breaking parameter just prior to wave breaking.

In Chapter III, an experimental study of the kinematics and the dynamics of two-dimensional unsteady plunging breakers has been reported. In addition, an eddy viscosity model is proposed to simulate the energy dissipation due to wave breaking and the model is validated with our experimental results.

In our experiments, wave surface elevations are measured with both wave probes and high-speed imaging. With the wave probe measurements, wave characteristics associated with the wave group (i.e. S , f_s , k_s , c_s and C_{gs}) are defined and determined. While the center wave frequency and the associated linear group velocity in a wave group are considered commonly the group characteristics, our study illustrates that the spectrally-weighted wave frequency (and wave number) and group velocity better represent the characteristic properties for wave groups (with constant wave steepness distribution across their amplitude spectra). Based on surface profiles (just prior to wave breaking onset) measured with high-speed imaging, local breaking wavenumber, k_b , local wave steepness, S_b , and breaking wave phase speed, c_b , are determined. We find a strong connection between our wave group characteristics and the local breaking wave parameters (i.e. $S_b/S = 1.237$, $c_b/c_s = 0.9 \pm 0.1$ and $k_b/k_s = 1.25 \pm 0.25$). To our knowledge, these links have not been reported before.

Surface elevation measurements with wave probes are used also to estimate the total energy and the total energy loss. We find that energy loss due to surface damping, contact-line dissipation, and friction by the tank sidewalls and the bottom is non-negligible as compared to energy loss due to wave breaking that ranges from 8% to 25% of the total pre-breaking energy. More interestingly, both estimated total pre-breaking energy and energy loss due to wave breaking are found to scale accurately with the wave group characteristics (i.e. $E_0 k_s^3 / (\rho g)$ versus S and $\Delta E k_s^3 / (\rho g)$ versus S). Good correlations are observed also when both the energy and the energy loss are scaled with local wave characteristics (i.e. $E_0 k_b^3 / (\rho g)$ versus S_b and $\Delta E k_b^3 / (\rho g)$ versus S_b). Based on a linear least-square fit between $\Delta E k_s^3 / (\rho g)$ and S , the threshold of S that predicts wave breaking onset is estimated as $S_0 = 0.339$ and hence, $(S_b)_0 = 0.419$ for the same purpose. However, the application of S or S_b as a universal indicator to predict wave breaking and breaking strength needs to be explored further due to the variation of S_0 in different laboratory studies. While the local wave steepness parameter, S_b , seems to be a more universal wave breaking indicator, its performance needs to be further investigated.

Surface profile measurements using high-speed imaging are utilized to determine the breaking criterion parameter, $\delta(t)$, and its magnitude just prior to wave breaking. Our study justifies Song and Banner's (2002) wave breaking criterion which states that $\delta(t)$ with threshold $1.4 \pm 0.1 \times 10^{-3}$ distinguishes wave groups that lead to breaking from those that do not. The breaking parameter immediately before wave breaking (i.e. δ_{br}) increases in general as the energy loss due to wave breaking increases. In addition, δ_{br} can be expressed analytically with the local wave slope, S_b ; and the relationship is supported by our experimental results.

Breaking time scale and breaking horizontal length scale are defined and obtained with high-speed imaging measurements. The time and length scales depend approximately linearly on S_b , indicating that the breaking process is more violent as S_b increases. The two scales are then used to determine the horizontal breaking wave crest speed, u_{br} , which is shown to correlate strongly with the breaking wave phase speed, c_b , and the spectrally-weighted wave phase speed, c_s .

The energy dissipation rate in the plunging breakers is determined as the ratio of the total energy loss due to wave breaking to the measured breaking time. This estimation method assumes a constant dissipation rate and it involves only local wave parameters. The normalized energy dissipation rate (i.e. b_b) is on the order of 10^{-3} , which in general is consistent with previous results, subject to proper data interpretation. Although both S_b and δ_{br} correlate well with b_b , indicating both parameters can be used to indicate wave breaking strength, S_b appears to have a stronger correlation.

An eddy viscosity model obtained from the viscous free surface boundary conditions for weakly damped surface waves is adopted and tested numerically with laboratory measurements for energy dissipation due to wave braking. The eddy viscosity is estimated by both dimensional analysis and turbulent energy dissipation rate analysis with measured breaking time and length scales. The two estimations are very close, both on the order of $10^{-3} \text{ (m}^2\text{s}^{-1}\text{)}$. The estimated eddy viscosity also illustrates close correlation with the energy dissipation rate, b_b , and the wave breaking strength parameters, S_b and δ_{br} . The estimated eddy viscosity is employed in simulations that aim to reproduce the experimental tests numerically. Good agreement in energy dissipation obtained from the numerical simulations and the experimental measurements is found and this indicates that

the eddy viscosity model could be an effective tool in simulating the energy dissipation in plunging breakers and post-breaking wave profiles.

In Chapter IV, an experimental study on the spectral evolution of laboratory generated breaking waves is presented. Surface elevation and surface profile measurements are used to examine wave spectral evolution, and to determine spectral distribution of energy dissipated in breaking waves.

In the experiments, wave breaking is generated using frequency focusing. Temporal variation of the surface elevation is measured with wave probes at fixed locations along the wave flume while spatial variation of surface profiles is recorded with high-speed imaging.

Spatial evolution of wave frequency spectra is examined. Nonlinear energy transfer across the frequency spectra is obvious during wave focusing and defocusing. Significant energy loss due to viscous effects and contact-line damping is observed in non-breaking wave groups. More than 20% of the non-breaking energy loss is from the vicinity of the spectral peak ($f/f_p = 0.95 \sim 1.1$). More interestingly, energy loss near the spectral peak appears to depend on the frequency spectral bandwidth. To the best of our knowledge, a similar observation has not been reported previously.

Observations of frequency spectra evolution in breaking wave groups is documented also. Spectral distribution of energy dissipated due to wave breaking is determined then as the difference before and after breaking less the corresponding difference of a non-breaking wave group. Wave components in the frequency range from $1.1 f_p$ to $2.0 f_p$ lose significant energy, which contributes to most of the energy loss due to wave breaking;

wave components between $0.65 f_p$ and $0.95 f_p$ appear to gain to 50% of the energy loss in the high frequency band. The energy gain-loss ratio has no apparent dependence on breaking strength and is higher than previous laboratory results. The energy near the spectral peak may increase or decrease due to wave breaking, depending on the initial wave frequency spectrum. This finding differs from previous laboratory results but agrees with some field observations.

Spatial surface profile measurement is used to examine the temporal evolution of wavenumber spectra before and after wave breaking. Consistent generally with the observations for the frequency spectra, shorter wave components ($k/k_p = 1.2 \sim 4.0$) lose energy in breaking waves and longer wave components ($k/k_p = 0.4 \sim 0.9$) gain some energy. Wave probe measurements and the linear dispersion relation are used to transform wave frequency spectra to wavenumber spectra. As nonlinearity increases, as expected the results exhibit larger discrepancy from the measured wavenumber spectra, indicating this linear transformation has limited application for highly nonlinear breaking wave groups.

Numerical tests with a simple eddy viscosity model to simulate the energy dissipation in breaking waves are conducted. Although the eddy viscosity model fails to simulate detailed spectral change throughout the breaking process, numerical results capture the major characteristics of energy loss and gain across the spectrum, and are consistent in general with the evolution of the measured wave frequency and waveumber spectra. Considering the complicated kinematics and dynamics in breaking waves, the performance of this simple eddy viscosity is much better than expected.

In Appendix 1, an experimental study on wave breaking prediction of laboratory generated breaking waves is presented. A coefficient that accounts for wave spectral shape is proposed and used to modify a global wave steepness, which was shown to relate closely to total energy loss due to wave breaking, but has different wave breaking onset threshold for different wave spectra. After modification, the global steepness has a threshold close to 0.25 for wave breaking onset prediction, and correlates approximately linearly with energy dissipation due to wave breaking for wave groups with both constant amplitude and constant steepness wave spectra.

In Appendix 2, our observations demonstrate that separations of air flow over steep yet non-breaking wave crests indeed occur, implying that wave breaking is not necessary for the air flow separation over water waves. In addition, as compared to separation over breaking waves, higher wind speed is necessary for non-breaking wave crests, indicating that as expected a robust air flow separation criterion likely depends on both the local wave crest geometry and the wind speed above the wave crest. To the best of our knowledge, such a criterion has not been identified and validated in laboratory studies, despite the fact that determination of the criterion is of great importance to the numerical study of wind-wave interactions.

Appendix 1

Wave Breaking Onset Prediction Using a Modified Global Wave Steepness

1 Introduction

Breaking waves play an important role in upper ocean dynamics. Wave breaking limits wave height and dissipates wave energy. It also enhances gas and heat exchange between air and sea by entraining air bubbles into the water and generating surface turbulence.

Wave breaking onset prediction is obviously an interesting topic in the study of breaking waves. Many wave breaking criteria based on local wave geometry and wave kinematics and dynamics have been proposed; however, predicting breaking onset is nontrivial and few criteria are universal due to the complicated processes that wave breaking involves, such as wave-wave, wave-current, and wave-wind interactions.

An energy-convergence based breaking criterion proposed by Song and Banner (2002) seems very promising. They constructed a parameter, δ_{max} , based on local energy convergence rate and showed that δ_{max} with threshold $(1.4 \pm 0.1) \times 10^3$ is effective in predicting breaking onset. The criterion was also shown to be valid in the presence of wind-forcing and surface shear (Banner and Song, 2002). Subsequent studies (Banner

and Peirson, 2007; Tian et al., 2008 & 2009) provided experimental validations of the criterion for two-dimensional unforced, irrotational wave groups. The criterion involves tracking surface displacement maxima during wave group evolution, computing local wave energy density and local wave number at the maxima, and differentiating mean energy growth with respect to time to find the mean energy convergence rate. Therefore, determination of δ_{max} is computationally demanding.

A less demanding wave breaking criterion proposed by Rapp and Melville (1990) has been the focus of several studies (Rapp and Melville, 1990; Kway et al., 1998; Drazen et al., 2008; Tian et al., 2009). A global wave steepness, $S = k_c(\sum a_n)$, was defined and employed as a predicting parameter by Rapp and Melville (1990). Here, k_c is the wave number of the center frequency wave in a wave group; a_n is the amplitude of the n th wave component and a total of 32 waves were used in the original definition. Later studies modified this definition slightly based on considerations of wave group spectra, e.g. $S = \sum(k_n a_n)$ (Drazen et al., 2008) and $S = k_s(\sum a_n)$ in Tian et al. (2009). Here, k_n is the wave number of the n th wave component; k_s is a characteristic wave number computed with a spectrally-weighted wave frequency, f_s , and the linear dispersion relation; and f_s is defined as

$$f_s = \frac{\sum (f_n a_n^2)(\Delta f)_n}{\sum (a_n^2)(\Delta f)_n}, \quad (\text{A1.1})$$

where f_n is the frequency of the n th component of in a wave train. $(\Delta f)_n$ is the frequency difference between components. Note f_s equals the center wave frequency, f_c , for a constant amplitude wave spectrum. The global wave steepness, S , demonstrates a very

good relationship with the energy dissipation due to wave breaking; however, the estimated threshold for wave breaking onset prediction varies significantly in different experiments reported previously.

In this study, measurements from Tian et al. (2008 & 2009) are used to develop further the global wave steepness so that it can be applied to predict wave breaking onset and breaking strength for focusing wave groups with both constant amplitude and constant steepness wave spectra. Details of the experiments can be found in the two references.

2 Wave breaking onset and breaking strength prediction

As mentioned in the introduction, a global wave steepness proposed by Rapp and Melville (1990) has demonstrated a strong correlation with energy dissipation due to wave breaking in these studies, e.g. Figure 15 of Rapp and Melville (1990) and Figure 8 of Tian et al. (2009). However, as shown in Figure A1-1, the observed threshold value, S_0 , of the global wave steepness for breaking onset prediction varies significantly. Although the variation may be related partially to different definitions of S , we believe the difference in wave spectral shape primarily contributes to the discrepancy. The effect of wave spectral shape on S_0 was also noticed in Wu and Nepf (2002), and influence of a mean wave spectral slope on energy loss due to wave breaking was discussed in Yao and Wu (2004).

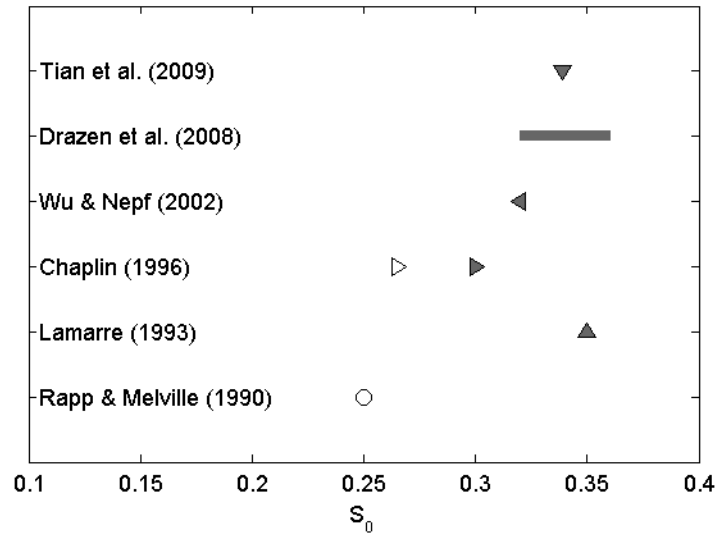


Figure A1-1 Observed global wave steepness of two-dimensional incipient wave breaking, S_0 . Open symbols indicate wave breaking is produced by focusing wave groups with constant amplitude wave spectra; solid symbols are used for constant steepness wave spectra. S_0 from Drazen et al. (2008) are based on our observations of their figure 8.

Figure A1-1 suggests that a wave spectrum whose high-frequency wave components contain relatively more energy, e.g. constant amplitude versus constant steepness wave spectrum, is likely associated with a smaller threshold, S_0 . To understand better the wave spectral shape effect on S , we first examined a constant steepness wave spectrum and obtained its global wave steepness. Based on conservation of energy, we then computed an equivalent spectrum with constant amplitude within the same wave frequency range. We found that this change resulted in an increase of the global wave steepness (more than 30% for the case considered). This finding indicates that wave groups with constant amplitude wave spectra are in general more likely to experience energetic breaking than those with constant steepness spectra (i.e. the former has a smaller S_0) and is consistent with Figure A1-1.

According to the discussions above, wave spectral shape shall be considered in applying the global wave steepness as a parameter for wave breaking and breaking strength prediction for focusing wave groups. For this purpose, we define an *equivalent* global wave steepness, $S_{eqv} = \alpha S$. Here, S is the *apparent* global wave steepness that is defined as $S = k_s(\sum a_n)$ and computed directly from a given wave spectrum, $S(f)$. And α is a coefficient that represents the difference of $S(f)$ relative to a constant amplitude wave spectrum as described later; $\alpha = E_p/E_{ref}$. E_p is the integration of the given wave spectra in a frequency band determined by the one-half maximum energy density associated frequencies,

$$E_p = \int_{f_1}^{f_2} S(f) df . \quad (A2.1)$$

Here, $S(f_1) = S(f_2) = S(f)_{max}/2$. A reference wave spectrum is defined so that it has a constant amplitude, $S(f)_{max}$, across the frequency band $[f_1, f_2]$. This definition results in a reference energy, $E_{ref} = S(f)_{max} * (f_2 - f_1)$. We note that α accounts implicitly for wave spectrum bandwidth. An illustration of the α determination for wave group W1G1 is presented in Figure A1-2. Clearly, for constant amplitude wave spectra, the apparent global wave steepness becomes the equivalent global wave steepness with $\alpha = 1$; for wave groups with constant steepness wave spectra in Tian et al. (2009), α is in the range of $[0.75, 0.82]$ with an average of 0.78.

The more closely a given wave spectrum approaches the reference spectrum described above, the larger the apparent global wave steepness and the coefficient α , resulting an even greater S_{eqv} . Relatively more energy in a focusing wave group with larger equivalent

global wave steepness is expected to produce a more violent breaking; thus, the focusing wave group may lose more energy due to wave breaking.

Figure A1-3 shows the correlation between energy dissipation due to wave breaking and the equivalent global wave steepness, S_{eqv} . Despite slight differences in the definitions of S and variations in different publication in presenting energy loss due to wave breaking, resulted S_{eqv} are comparable and show a strong correlation with the energy loss due to wave breaking. As expected, energy loss due to wave breaking increases as S_{eqv} increases. In addition, $S_{eqv0} = 0.25$ appears to predict wave breaking onset for wave groups with either constant amplitude or constant steepness wave spectra. Therefore, S_{eqv} may be considered a more universal parameter for wave breaking and breaking strength prediction for focusing wave groups.

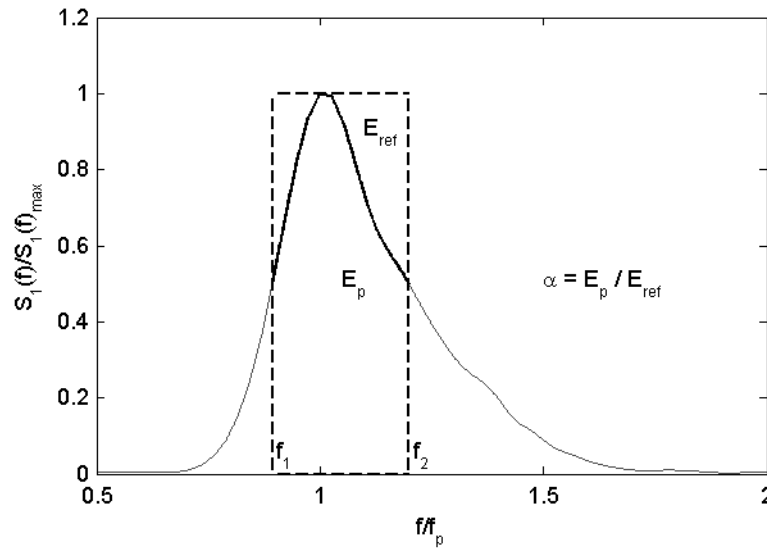


Figure A1-2 Illustration of the determination of α for W1G1. The area under the thick solid line represents E_p and the area within the box defined by the dash lines represents E_{ref} . f_1 and f_2 are the one-half maximum energy associated frequencies.

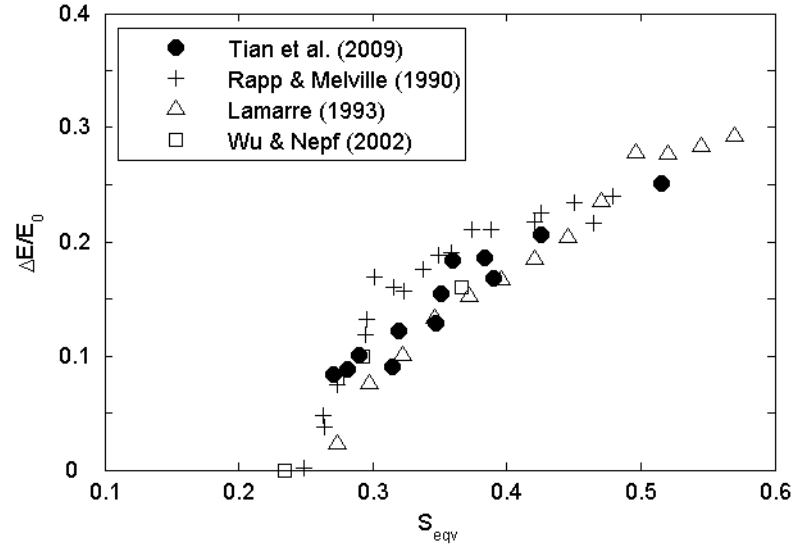


Figure A1-3 Energy loss due to wave breaking as a function of S_{eqv} . Results from Rapp and Melville (1990) are reproduced with data from their Figure 15; only measurements for wave groups with center frequency 1.08 Hz and 1.28 Hz are shown, as both center frequencies are comparable to ours; non-breaking energy loss is deducted from their measured total energy loss to obtain energy loss due to wave breaking. Results from Lamarre (1993) are based on their Figure C.3 and their wave spectrum in Figure 3.2, which gives $\alpha \approx 0.77$. Results from Wu and Nepf (2002) are obtained from their Tables 2 and 3 and their wave spectrum in Figure 3(b), which produces $\alpha \approx 0.73$.

Nonetheless, further study is necessary to examine the performance of S_{eqv} , as this conclusion is based on limited data from the literature and only two types of wave spectra were considered. We intended to include some recent results from Drazen et al. (2008) but did not have enough data on their wave spectra to reproduce S_{eqv} . However, estimated S_{eqv0} based on an assumption that $\alpha \sim 0.75$ for their wave spectra (constant steepness) is in the range of [0.23, 0.27], close to the threshold $S_{eqv0} = 0.25$. In addition, Banner and

Pierson (2007) conducted an experimental study on breaking onset and strength prediction. Their breaking wave groups have global wave steepnesses much smaller than 0.25 (as low as 0.12). We note that most of their breaking waves are results of Benjamin-Fair instability, indicating that the proposed global wave steepness may not be applicable to predict wave breaking due to the Benjamin-Feir instability.

3 Conclusions

An experimental study on wave breaking prediction of laboratory generated breaking waves is presented. A coefficient that accounts for wave spectral shape is proposed and used to modify a global wave steepness, which was shown to relate closely to total energy loss due to wave breaking, but has different wave breaking onset threshold for different wave spectra. After modification, the global steepness has a threshold close to 0.25 for wave breaking onset prediction, and correlates approximately linearly with energy dissipation due to wave breaking for wave groups with both constant amplitude and constant steepness wave spectra.

References

- BANNER, M. L. & PEIRSON, W. L. 2007 Wave breaking onset and strength for two-dimensional deep-water wave groups. *J. Fluid Mech.* **585**, 93-115.
- CHAPLIN, J. 1996 On frequency-focusing unidirectional waves, *Int. J. Offshore Polar Eng.* **6**(2), 131.
- DRAZEN, D. A., MELVILLE, W. K. & LENAIN, L. 2008 Inertial scaling of dissipation in unsteady breaking waves. *J. Fluid Mech.* **611**, 307-332.
- KWAY, J. H. L., LOH, Y. S. & CHAN, E. S. 1998 Laboratory study of deep water breaking waves. *Ocean Eng.* **25**, 657-676.
- LAMARRE, E. 1993 An experimental study of air entrainment by breaking waves, Ph.D. thesis, Mass. Inst. of Technol., Cambridge.
- RAPP, R. J. & MELVILLE, W. K. 1990 Laboratory measurements of deep-water breaking waves. *Phil. Trans. R. Soc. Lond. A.* **331**, 735-800.
- SONG, J. B. & BANNER, M. L. 2002 On determining the onset and strength of breaking for deep water waves. Part I: Unforced irrotational wave groups. *J. Phys. Oceanog.* **32**, 2541-2558.
- TIAN, Z. G., PERLIN, M. & CHOI, W. 2008 Evaluation of a deep-water wave breaking criterion. *Phys. Fluids* **20** (066604), 1-13.
- TIAN, Z. G., PERLIN, M. & CHOI, W. 2009 Energy dissipation in two-dimensional unsteady plunging breakers and an eddy viscosity model. *J. Fluid Mech.* (submitted)
- WU, C. H. & NEPF, H. M. 2002 Breaking criteria and energy losses for three-dimensional wave breaking. *J. Geophys. Res.-Oceans* **107** (C10), 3177.
- YAO, A. F. & WU, C. H. 2004 Energy dissipation of unsteady wave breaking on currents. *J. Phys. Oceanog.* **34**, 2288-2304.

Appendix 2

Observation of Air Flow Separation over Steep Wave Crests

1 Introduction

The dynamics of air flow over water waves has received much attention recently due to its important role in the momentum transfer across the air-sea interface (Kawai, 1982; Banner, 1990; Kharif et al., 2008; Reul et al., 1999 & 2008, to name a few). A very interesting topic is the air flow separation over water waves (e.g. Wu, 1969; Banner and Melville, 1976; Kawai, 1981; Donelan et al., 2006).

Wu (1969) proposed that air flow separation over water waves with a following wind occurs when the shear velocity is greater than the wave phase velocity. This criterion was based on general physical arguments and had no direct experimental support (Wu, 1969). This work is one of the first studies on an air flow separation criterion.

A more comprehensive study on the air flow separation was presented by Banner and Melville (1976), which argued that air flow separation occurs only in the presence of breaking waves. In this study, they demonstrated analytically that a stagnation point, in a frame of reference in which the air-water interfacial boundary retains a steady shape (i.e.

a quasi-steady model), is required for air flow separation. They argued that the presence of the stagnation point in the case of wind wave interaction corresponds to wave breaking onset. In addition to the analytical argument, they managed to observe air flow separation over a steady breaking crest as well as a non-separated flow over an unbroken, steady wave by means of smoke visualization. The air flow separation criterion was based on a quasi-steady analysis and the experimental evidence was obtained with a steady wavy air-water interface generated with hydrofoils in a channel.

Later, Kawai (1981) questioned Banner and Melville's criterion by arguing that their experiments validated only the fact that air flow separation and wave breaking occurred simultaneously at a steady wavy interfacial boundary. The study (Kawai, 1981) suggested the possibility of air flow separation over non-breaking wind waves. To visualize the air flow over actual wind waves, a smoke wire was attached to a wave follower and was used in their experiments. Under a wind speed of 6 ms^{-1} and a fetch of 3.8 m in their wave tunnel, air flow separations were observed over actual wind wave crests that were not accompanied by noticeable air entrainment. As they could not determine whether incipient breaking occurred (In the study, breaking waves were identified as breaking processes with air entrainment) when the air flow separation was observed, we can draw no conclusions that contradict or support Banner and Melville's criterion.

In a second study by Kawai (1982), air flow over wind waves was visualized with Zinc Stearate particles and illuminating light sources. Based on observations of 79 tests with a free stream wind speed of 7 ms^{-1} and a fetch 3.7 m, they concluded that a maximum local gradient of the surface along the crest greater than 0.6 is a sufficient condition for air flow to separate over wind wave crests.

On the other hand, in the study of Kharif et al. (2008), a device composed of hot and cold wires was used to detect air flow separation over frequency focusing wave groups and a critical local wave slope, $(\partial\eta/\partial x)$, close to 0.35 was determined to indicate the onset of air flow separation. Kharif et al. (2008) further noted that the air flow separation was accompanied generally with breaking waves.

In a recent field measurement of the spectral function of the wind-input to the wave field, Donelan et al. (2006) identified the full air flow separation over non-breaking waves (here full separation means that “the streamlines detach from the flow at the steep crest and do not reattach until well up the windward face of the preceding wave toward its crest”) and argued that the air flow separation may depend on the force balance over the wave crests: the vertical gradient of pressure, proportional to $(U-c)(ka)^2$, shall match the centripetal acceleration, proportional to $\frac{\partial^2\eta}{\partial x^2}$, required to keep the streamlines in contact with the wave surface. Here, U is the wind speed measured at one-half wave length above the wave crest; c is the wave phase speed; η is the surface elevation. The finding suggests that the criterion proposed by Banner and Melville (1976) may not be applicable to unsteady water waves. The study considered, for the first time, the wind speed effect on the air flow separation over water wave crests.

Recent particle image velocimetry (PIV) measurements (e.g. Reul, 1999 & 2008) have advanced our understanding of the dynamics of the air flow structure over water wave crests. Unfortunately, no such measurements have been used to identify a robust criterion for the air flow separation over unsteady steep wave crests. The criterion may be expected to depend on both the local wave crest geometry and the wind speed.

In this study, as a preliminary step toward a more comprehensive study of identifying such an air flow separation criterion, we conduct flow visualization experiments of the air flow over mechanically generated waves. In fact, to the best of our knowledge, direct observation of the air flow separation over mechanically generated, steep yet non-breaking wave crests have not been reported before. After this introduction, a brief description of the experimental set-up is presented in section 2. Section 3 provides some preliminary observations on the air flow separation over steep wave crests. The final section provides conclusions and possible future works.

2 Experiments

Experiments are performed at the University of Michigan in a two-dimensional wind wave tunnel with glass bottom and sidewalls, as well as removable glass panels on the top. The tunnel is 35 m long, 0.7 m wide, and has a water depth as used of 0.68 m. Water waves are generated with a servo-controlled wedge-type wavemaker and auxiliary electronics located at one end of the facility. Wind is generated with a 40 horsepower suck-down flow loop (open) that is capable of producing air flow to 30 ms^{-1} . The air flow passage height where incident on the mean water elevation is 0.84 m as used. The cross-sectional area of the air flow increases slightly downstream to balance the growing boundary layer. Figure A2-1 provides a sketch of the wind wave channel.

In the experiments, we examine the wind speed effect on the air flow separation over wave crests by using four wind speeds, $U_0 = 4.2, 5.4, 6.6$ and 7.8 ms^{-1} as measured with a Pitot-static tube in the free stream. To investigate the effects of the wave steepness on the

air flow separation, regular waves of different frequencies with different amplitudes are produced by adjusting both the frequency and the gain (i.e. relative voltage) of the electric signals sent to the wavemaker.

To visualize the air flow over wave crests, water particles produced with a high-pressure spray gun (KARCHER, model K3.68M) are used to seed the air. The particles are injected into the open loop inlet against the wind so that they flow downstream with a zero initial horizontal speed. An argon-ion laser (Coherent Innova 90), 6W, is used to produce the light source in the flow visualization. A laser light sheet of approximately 1.5 mm thick is generated through a series of mirrors, spherical and cylindrical lenses to illuminate the seeded air flow at fetch close to 6 m. A high-speed imager (Phantom V9.1) is used to record the illuminated air flow at 100 fps and the exposure time used is 4 ms. The field of view is approximately 33 cm by 24 cm (1632×1200 pixels). Figure A2-2 provides an illustration of the experimental set-up for the flow visualization.

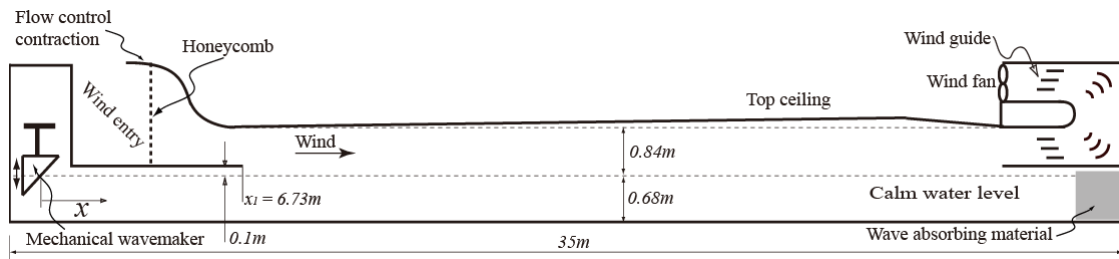


Figure A2-1 Sketch of the wind wave tunnel (not to scale).

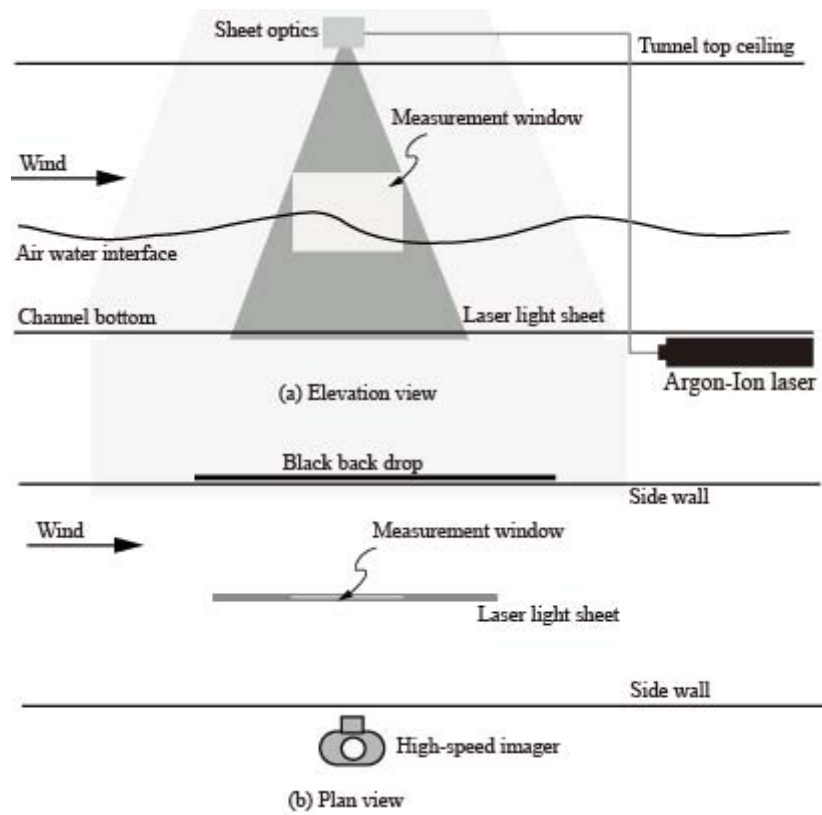


Figure A2-2 Experimental set-up for flow visualization (not to scale).

3 Preliminary observations

Figure A2-3 provides four typical images recorded during the tests. Clearly, the air flow pattern is visualized successfully through the traces of the water particles. Note that Particle Tracking Velocimetry (PTV) may be applied to these data. In the figure, (a) shows no air flow separation over a low steepness non-breaking wave crest; on the other hand, air flow separation over a steep yet non-breaking crest is observed in (b). Compared with (a), higher wind speed and increased local wave steepness are needed to initiate the air flow separation in (b), as expected. Figure A2-3 (c) shows the air flow separation over an incipient breaking wave crest at a lower wind speed compared to (b). In (d), a breaking crest introduced an air flow separation under an even lower wind speed, the lowest in the four wind speed considered in the experiments.

The preliminary observations showed 1) air flow separation occurs over breaking wave crests; 2) separation of air flow indeed occurs over steep yet non-breaking wave crests; 3) high wind speed and increased local wave steepness is necessary to introduce the air flow separation over non-breaking wave crests

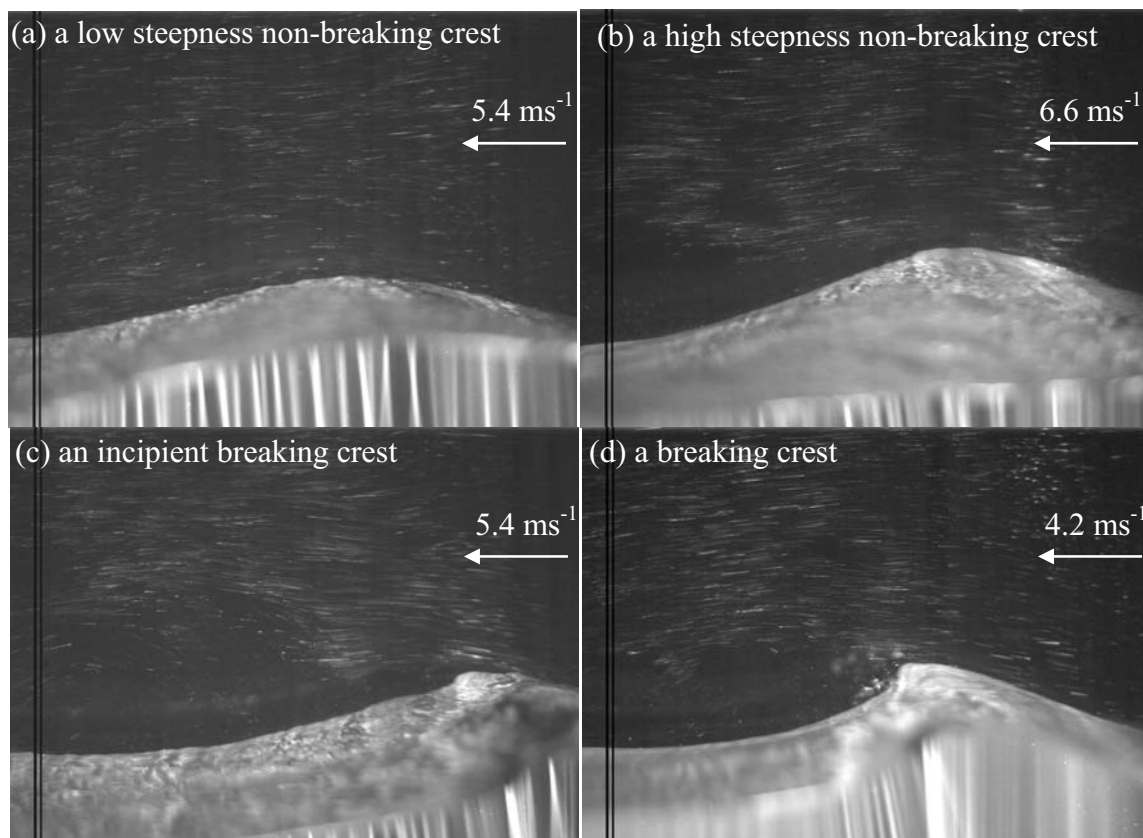


Figure A2-3 (a) through (d) are four typical images recorded during the experiments. The air flow direction and wind speed are shown on the images. These waves are generated by driving the wavemaker with a sinusoidal electric signal of frequency 1.8 Hz with different strokes. Waves are traveling in the same direction as the wind. The two vertical black strips on the left side of each image are due to a malfunction of the CCD in the imager.

4 Conclusions and future work

Our observations demonstrate that separations of air flow over steep yet non-breaking wave crests indeed occur, implying that wave breaking is not necessary for the air flow separation over water waves. In addition, as compared to separation over breaking waves, higher wind speed is necessary for non-breaking wave crests, indicating that as expected a robust air flow separation criterion likely depends on both the local wave crest geometry and the wind speed above the wave crest. To the best of our knowledge, such a criterion has not been identified and validated in laboratory studies, despite the fact that determination of the criterion is of great importance to the numerical study of wind-wave interactions.

As a first step to identify such a separation criterion, further air flow visualization tests over a larger wind speed range are necessary. In addition, to examine the wave group effects on the flow separation, flow visualization over irregular wave groups (e.g. frequency focusing wave groups) is needed. And finally, PIV or PTV measurements are necessary to facilitate our understanding of the physics involved in the separation process.

References

- BANNER, M. L. 1990 The influence of wave breaking on the surface pressure distribution in wind-wave interactions. *J. Fluid Mech.* **211**, 463-495.
- BANNER, M. L. & MELVILLE, W. K. 1976 On the separation of air flow over water waves. *J. Fluid Mech.* **77**, 825-842.
- DONELAN, M. A., BABNIN, A. V., YOUNG, I. R. & BANNER, M. L. 2006 Wave-follower field measurements of the wind-input spectral function. Part II: parameterization of the wind input. *J. Phys. Oceanog.* **36**, 1672-1689.
- KAWAI, S. 1981 Visualization of airflow separation over wind-wave crests under moderate wind. *Boundary-Layer Meteorol* **21**, 93-104.
- KAWAI, S. 1982 Structure of air flow separation over wind wave crests. *Boundary-Layer Meteorol* **23**, 503-521.
- KHARIF, C., GIOVANANGELI, J. P., TOUBOUL, J., GRARE, L. & PELINOVSKY, E. 2008 Influence of wind on extreme wave events: experimental and numerical approaches. *J. Fluid Mech.* **594**, 209-247.
- REUL, N., BRANGER, H. & GIOVANANGELI, J. P. 1999 Air flow separation over unsteady breaking waves. *Phys. Fluids* **11**, 1959-1961.
- REUL, N., BRANGER, H. & GIOVANANGELI, J. P. 2008 Air flow structure over short-gravity breaking water waves. *Boundary-Layer Meteorol* **126**, 477-505.
- WU, J. 1969 Laboratory studies of wind-wave interactions. *Tellus* **21**, 708-713.